THE UNIVERSITY *of* EDINBURGH

Novel active magnetic bearings for direct drive C-Gen linear generator

José Ignacio Barajas Solano

Doctor of Philosophy

The University of Edinburgh

2017

Für Elisa…und Damian

For believing in me, even more than I believe in myself.

You are the reason I can say my life is beautiful.

Abstract

This document presents a novel active magnetic levitation system. In the pursued of this endeavour different topics related with wave energy were explore.

Climate change and energy security are the main motivation to pursued new options for non-fossil fuels energy generation. An overview of renewable energy and specifically of wave energy was presented. The potential for wave energy in The United Kingdom turn out to be 75 TWh/year from wave energy, 3 times more of what wind energy has produced in 2013. This means a massive impact on the energy market and emission reduction.

In order to achieve this, improvements on wave energy devices have to be done. An overview of wave energy converters was covered selecting the C-Gen as the generator topology this document will base its studies.

Linear generator bearings are desired to have long lifespan with long maintenance intervals. The objective is to come with an active magnetic levitation design that can replace traditional bearings augmenting the reliability of the system.

Therefore magnetic bearings option have been reviewed and simulation experimentations has resulted in a novel active magnetic levitation system using an air-cored coils Halbach array acting over a levitation track. The configuration would generate bi directional repulsion forces with respect of the levitating body.

Different software were used to analyse the magnetic field and forces generation. Additionally a prototype was built and tested to corroborate the results. As part of the modelling a mathematical model was explored and robust control implementation was also realised.

Finally a scalability study of the device as well as a reliability analysis was done. Although the reliability studies shows an increase of ten times of the mean time to failure, the concept is not able to endure the loads acting on the generator unless the

magnetic bearings became bigger than the generator and therefore economically unfeasible.

Declaration

I hereby declare that the work contained in this thesis is my own, any additional source has been referenced properly. Furthermore, I confirm that this document has not been submitted for any other degree or professional qualification.

José Ignacio Barajas Solano

Acknowledgements

Along five years there are so many people I would like to add in this section, but I will try to make it brief.

I would like to acknowledge the support from CONACYT and SuperGen Marine. Without the support of these organisations many students like me would not be able to follow their goals. Also, I would like to thank my supervisor Markus Mueller, for his guidance and patience. Generally I would like to express my gratitude to the IES staff for all the help, especially to Douglas Carmichael.

As well, thanks to my brothers far away in body but not in spirit “Sopitas” and “Perkins”, the brothers that I had the luck to find in my life path. Likewise to the ones that shared a home far away from our home, Marisol Ochoa, Manuel Sanchez and Adriana Contreras.

To my other colleagues and friends sharing the workplace that are always there to share their knowledge and their good vibes, Kaswar Mostafa, Alberto Perez, Jen Hao Wu, Ozan Keysan and Monika Kreitmair, but especially to Siraj Sabihuddin and Joseph Burchell. Thanks for your time, your energy and your laugh.

Finally I want to thank my Son’s Godmother Damaris Medina, and my beloved Elisa Kappe and Damian Barajas Kappe for brightening my days. I am grateful for my family and my extended “Kappe” Family, always in my mind and my heart.

For you, I would like to cite Mercedes Sosa “Thanks to life, which has given me so much”

“Gracias a la vida que me ha dado tanto”

Table of Contents

Table of figures

Symbol	Description
D_{co}	Outer Diameter of a coil
D_{ci}	Inner diameter of a coil
h_c	Length/height of a coil
B	Magnetic flux density
μ_0	Permeability of free space
N	Number of turns in a coil
I	Current
l_c	Coil length
R_{loop}	Resistance of a single loop track
L_{loop}	Inductance of a single loop track
B_0	Halbach array Peak magnetic field
w_t	Track width
d_m	Thickness of the permanent magnet(cube)
z_g	Gap between Halbach array and levitation track
M	Number of element per wavelength in a Halbach array
λ	wavelength
v	Velocity of the translator
f_c	Current frequency
ω_f	Angular frequency
$a_1, b_1, c_1;$	Dimensions Element 1 and 2 of a Halbach array.
a_2, b_2, c_2	
x_p, y_p, z_p	Point of study coordinates in a 3D space.
J	Current density
r_c	Circular loop radius
ρ_{cu}	Resistivity of the material
l_{tot}	Length of the material(track)
d_s	Diameter of the material.
k_s	Depends on the construction of the conductor
n	Number of elements in a Litz wire.
D	Distance between the centre of one wire thread of a Litz compound to the next one.
$i\{n\}$	Track rung currents

Symbol	Description
$\mathcal{L}$	Inductance Matrix
$\mathcal{R}$	Resistance Matrix
L_{wt}	Inductance window track
L_{Litz}	Inductance Litz track
R_{dc}	Direct current resistance
s_1	Length window shaped track coil
s_2	Height window shaped track coil
t_{th}	Thickness window shaped track coil cross sectional area
t_w	Width window shaped track coil cross sectional area
B_z	Magnetic flux density in "z"
B_y	Magnetic flux density in "y"
E_n	Magnetic field time derivative crossing a loop area od the nth loop
R_r	Resistance of a rung
R_b	Resistance of the side bar
L	Self-inductance
M_n	Mutual inductance to the nth rung
i_{rung}	Current in the rung
i_n, i_{n-1}	Current in loop nth, or nth-1
F_{yn}	Force on the "y" axis at loop n
F_{zn}	Force on the "z" axis at loop n
ρ	State vector
u	Input vector
$y(\rho)$	Output vector
R	Euler angular description
a_t, b_t, c_t	Translator dimensions for control
m_t	Mass of the translator
j_θ	Inertia
$C_{ij}; Z_{0i}; k_i$	Control coefficients.
D_{cylo}	Outer diameter of the cylinder enclosing the C-Gen generator.
D_{cyli}	Inner diameter of the cylinder enclosing the C-Gen generator.

Symbol	Description
h_t	Translator height
h_s	stator height
d_t	Translator depth
d_s	Stator depth
ρ_{sw}	Density of sea water
ρ_{pm}	Density of permanent magnets
ρ_s	Density of mild steel
ρ_{pol}	Density of cylinder's polyurethane
g	Gravity
C_d	Drag coefficient
C_m	Inertia coefficient
H	Wave height
T	Wave period
P	Power
F_{th}	Thrust Forces from the generator
W_{trans}	Translator weight
$\mathrm{V_{core}}$	Core volume
$\mathrm{V_{pm}}$	Permanent magnet volume
$\mathrm{V_{cylo}}$	Volume of outside cylinder
$\mathrm{V_{cyli}}$	Volume of inside cylinder
$F_{z\_mor\_t}$	Z Forces on the translator due to the waves movement
B_{cyl}	Generator Cylinder buoyancy
$F_{x\_mor\_t}$	X Forces on the translator due to the waves movement
W_{cyl}	Generator Cylinder weight
$F_{x\_mor\_s}$	X Forces on the stator due to the waves movement
M_{wec}	Mass of the moving part(translator + cylinder)
a_{wec}	Acceleration of the moving part(translator + cylinder)
ρ_{sw}	Salt water density
l_s	Stator length
$a_{r1}, b_{ri1}, b_{ro1}, c_{r1};$	Rectangular coils dimensions
$a_{r2}, b_{ri2}, b_{ro2}, c_{r2}$	

1 Introduction

1.1 Renewable Energy

There are two main reasons renewable energy has been attracting more attention in recent years, namely climate change and energy security. In the following section the situation of the world's energy usage and production is introduced as well as climate change and current international eco-politics.

1.1.1 Climate change effects on the world

The rises in temperature and sea level have been a general concern to the international community. More extreme seasonal changes along with stronger natural disasters can be seen each year. Flooding and extended dry seasons occur around the globe affecting food production, fresh water resources allocation, and impacting health in general. In order to solve these problems the causes need to be understood. The rise of global air and ocean temperature is undeniable, causing melting of snow and ice and rising sea levels[1].

The scientific community attributes global warming to greenhouse gases in the atmosphere. Green House Gases(GHG's) reflect some of the solar rays back to the earth surface, increasing the average temperature of the earth [2] which is called the greenhouse effect. The most important anthropogenic emitted greenhouse gas is Carbon Dioxide (CO_2). Its emission has grown by 80% since the 1970's and the rate of growth was higher from 1995-2004 than in the previous 25 years. Most of these emissions comes from energy supply, transportation and industry [1].

The industrial revolution in the 19^{th} century and the rapid growth in heavy industry and population in the 20^{th} century led to a rapid increase in energy demand supplied by fossil fuelled power stations and the subsequent increase in emission[3].

The effect of the steam engine invention by James Watt can be noted in Figure 1.1, where coal production and CO_2 emissions in the UK seem to follow a similar pattern through time. After the UK, many other countries followed the industrial revolution and its mass production behaviour [3].

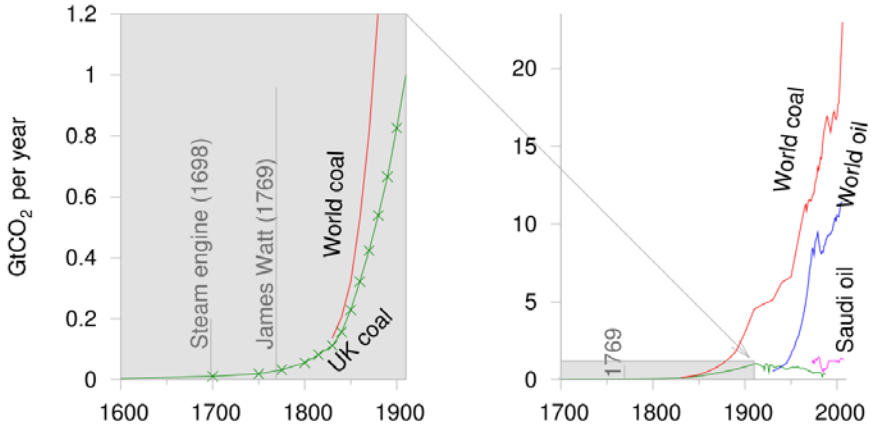

Fig. 1.1. Effect of industrial revolution in Coal and oil world production[3].

The production of GHG is not only affected by economic activity but also by population growth and lifestyle as mentioned in [4]. A clear pattern between GHG emissions, population and temperature rise is shown in Figure 1.2.

Fig. 1.2. Relationship between Population, CO_2 concentration and Global Temperature[4].

The Intergovernmental Panel on Climate Change (IPCC) has projected different scenarios where CO_2 emissions continue to increase at different rates. In these scenarios the projected temperature will rise over the next century, causing more frequent and longer heat waves and, in the same way, more common and stronger extreme precipitations. The ocean level will continue to rise, higher ocean temperature are expected as well as further acidification of waters. The changes in temperature and weather will consequently affect nature and hence, human life. The risks listed by the same report are[1],[5]:

Possible extinction and re-allocation. Due to extreme weather changes, plants which cannot adapt to changing conditions fast enough will perish, small fresh water mammals and mollusc might face the same situation and marine life will be affected due to the low levels of oxygen and higher acidification rates. Consequently organisms sensitive to sea level such as coral reef will be affected, and as a result coral ecosystems will be put at risk. Those natural cycles' changes are likely to affect food security. Activities such as fishery and agriculture productivity will change due to species redistribution.

Water access scarcity. Competition for water resources is projected to intensify between agriculture and other productive sectors. Decrease in wheat and maize crop production are expected if an increase of 2˚C is registered. As a result displacement of people from rural to urban areas due to extreme weather or lack of resources is predicted.

Health problems. Another expected outcome from climate change is the higher incidence of health problems particularly in developing countries with low income. High temperature combined with humidity might favour spread of diseases. Thus health issues will compromise human productive activities, as mentioned before exacerbating the aforementioned economic, logistics and infrastructure problems in these areas.

The mentioned scenarios highlight the potential for climate change to generate geopolitical stress creating or emphasising conflicts around the world. Diminished food production and reduced access to water are likely to create social issues causing violence, in other words a global humanitarian crisis[6].

1.1.2 Energy security

The second reason for the interest in renewable energy is energy security. Since human beings started living as a society, energy has been required to process food, transport materials and generally fulfill productive activities. In the past, civilizations located close to water to exploit potential and kinetic energy. Later people settled in the proximity of coal with the start of the industrial revolution. In present times, oil has become the preferred fossil fuel consumed by the planet. Therefore it is highly

important to be familiar with the limitations of this resource and especially to the concept of peak oil.

The term peak oil was coined by Marion King Hubbert as early as the 1950's, referring to the moment in which oil production reaches its maximum and then declines to zero in a bell shaped curve. Peak oil is currently expected during the early part of the 21st century. As with oil, fossil fuels are considered a finite resource and are projected to run out.

The depletion of oil and fossil fuels would carry huge changes for the economy and society as a whole. First world countries with high energy demand, developing countries with high intensity manufacturing industries and countries whose economy is based on oil would be affected when fossil fuels run out.

The potential consequences of the depletion of traditional energy sources highlight the need to diversify energy production in a more mixed and environmentally friendly way in order to ensure energy security [7][8].

1.1.3 Worlds situation & Kyoto's Protocol

As an international effort to tackle climate change the Kyoto protocol was signed by many countries around the world. The agreement exhorts nations around the world to reduce the GHG emissions on average by 5% by 2012 compared to levels reached in 1990. Different nations have different mitigation goals depending on their economical and socio-political conditions. In the case of the UK the goal was set to 8%[9]. After 2012 Doha Amendment [10]settled a second round target which is expected to be acting from 2013 to 2020. Additionally a mitigation plan post 2020 has been set in the Paris agreement in December 2015[11].

UK Goals. The UK reported that by 2009 a 21% reduction of 1990's emissions, was achieved, setting a new target of decreasing emissions to 80% by 2050. To achieve this the Government launched a Low Carbon Five point plan which includes plans to generate 30% of electricity through a combination of renewable energy sources, new nuclear power stations and carbon capture installations by 2020 [12]. The "UK Renewable Energy Roadmap" [13] includes Marine Energy and highlights that it has the potential to make a substantial input to the UK's renewable energy goal.

1.1.4 Global Marine Energy

In [14] it is noted that the higher power rate points of energy are situated on the west cost of continents towards the poles. In the northern hemisphere they are allocated along Scotland and Ireland latitude in Europe, whilst Alaska, British Colombia and Oregon latitude had the peak of resources in North America. In the case of the southern Hemisphere the peaks are allocated in New Zealand, Australia in Oceania, South Africa in the African continent and Chile in South America (see Figure 1.3).

Specifically in the UK, the potential of wave energy is extraordinary. It is shown in Figure 1.3 a) an annual net theoretical coastal power of >60kW/m in the North Atlantic. Although in Figure 1.3 b) it can be observed that this resource can be highly seasonal [14]. More information about this is presented in section 1.2.

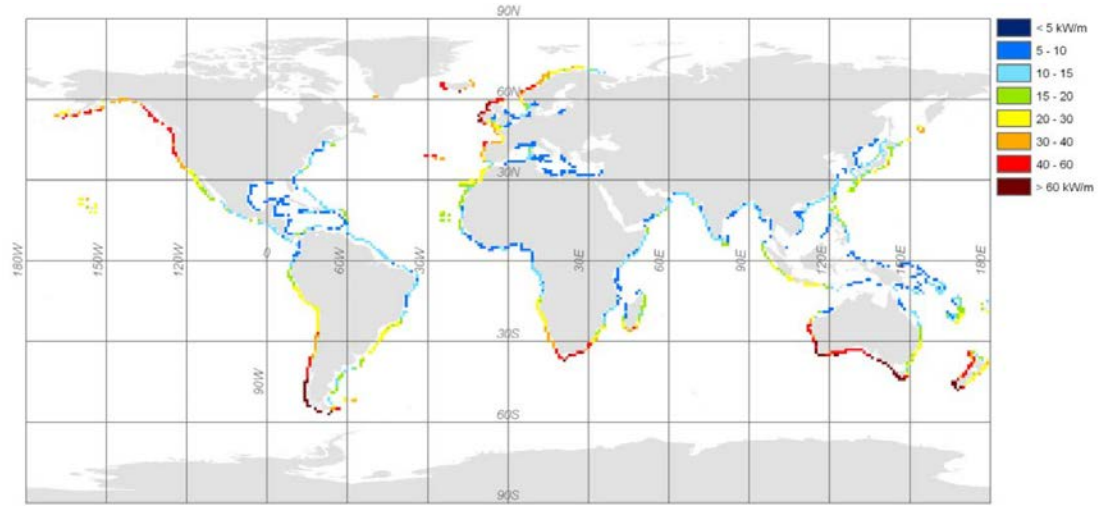

a)

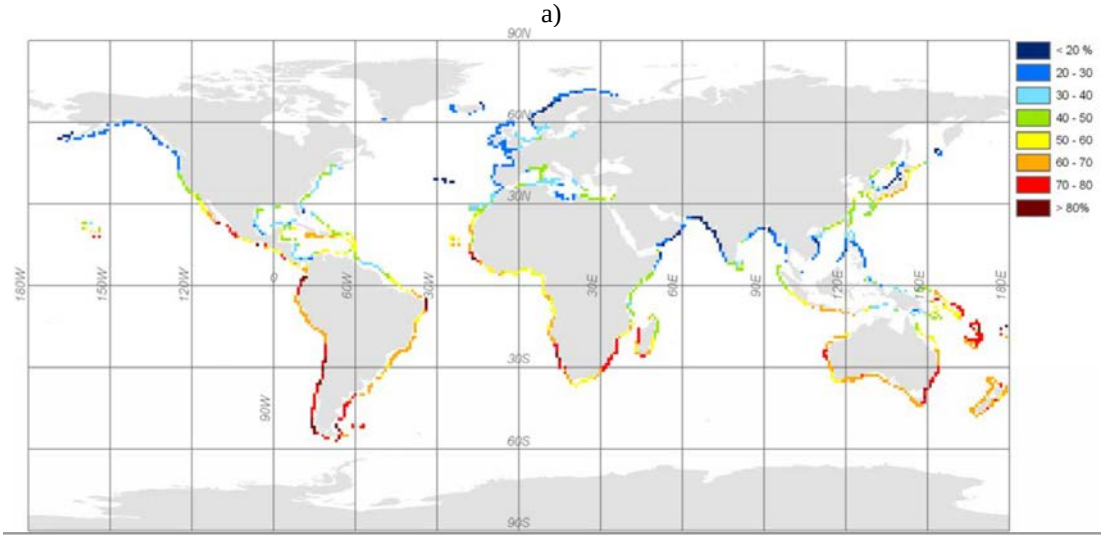

b)

Fig. 1.3. a) Annual global gross theoretical wave power for all World Waves grid points

1.1.5 Near future scenario for Marine Energy in the UK

According to a RenewableUK report [15] the marine renewable industry, wave and tidal, projected value is £6.1 billions and is predicted to create around 20,000 jobs in the UK by 2035. For this to happen certain policy and economic conditions need to be achieved.

A total of 12 large-scale prototypes were deployed in 2012 in the UK, surpassing the total of projects in the rest of the world combined.

The development of marine projects with a strong commitment from the government resulted in world leading technologies built and demonstrated in the UK by national

and international companies using local supply chains. Investments from different European and UK organizations have led the Wave and Tidal sectors to gain confidence and experience on the deployment of new devices. Thus, developers such as MeyGen, ScottishPower Renewables, Andritz Hydro Hammerfest and others, are planning to install to arrays of devices in UK waters. RenewableUK has predicted a deployment time line for viable projects shown in Figure 1.4[15]. On wave energy, companies such as ASX-listed, Carnegie Clean Power and GWave LLC are preparing to deliver wave energy devices arrays in the near future according to [16].

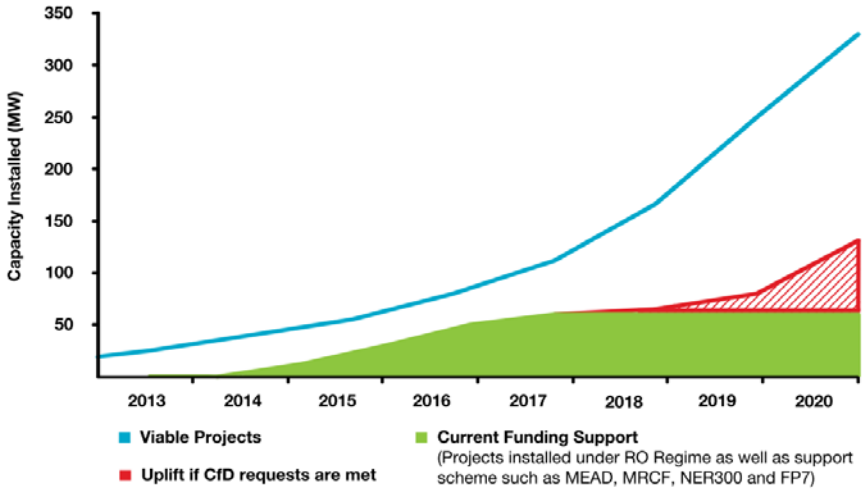

Fig. 1.4. Likely deployment for UK Wave and Tidal energy[15].

Nevertheless the main obstacle this industry faces in the following years is the transition from Renewable obligations certificates (ROC's) to the new Contract for Difference (CfD) regime which will take place from 2014 to 2017.

In the ROC scheme an accredited renewable energy supplier can trade the certificate to an energy supplier so they can prove that they have met their obligations. If the supplier fails to meet their obligation in a report period, they would need to pay the equivalent amount.

On the other hand Contract for Difference (CFD) is a contract between a low carbon electricity generator and the Low Carbon Contracts Company (LCCC). The contractor and LCCC agree on a strike price for the length of the contract. If the market price for electricity generated by the contractor is below the strike price a payment will be made by the LCCC to the contractor, if the case is the opposite the contractor would have to pay the LCCC [1] [2].

As a result of the uncertainty surrounding this transition, investors seem to be focusing on the industry after 2017 or when ROC scheme ends.

RenewableUK[15] document also mentioned that this transition has the possibility to either stop or stimulate the marine energy industry. In order to act as a springboard, an initial strike price of 280-320 £/MWh would be required. These projects need time to become cost convergent, and so contracts must be at least 20 years long. Contradictory to this the new CfD contracts are reduced to 15 years.

New technologies need a longer time to establish and should not be considered equally to other more developed renewable energy sources such as wind, since the state of maturity for marine energy hasn't reach the same level. However, if CfD assures 20 year contracts for novel projects, this would create more certainty for investors. Then projects where risk can be manageable will become more attractive to investment.

In order to keep developing the energy industry a robust risk management and a close working relationship between private sector, academia and government needs to be achieved in programmes like CATAPULT [15].

Climate change possible scenario has been presented as well as the need for a mix of energy production in order to avoid fossil fuel dependency.

Although a certain level of CO_2 mitigation has been achieved by the UK a more ambitious goal has been set by the UK Government. To reach the 80 % reduction on CO_2 emissions (compared to levels of 1990) every low carbon energy generation technology must be utilized.

Having said that, Marine energy presents a large potential of energy generation, with thousands of projected job created in the near future[15]. This would make tidal and wave energy an attractive area for investors if the uncertainties of the current market and legislation are removed.

1.2 Wave energy in the UK

The following section is based on two documents exploring wave energy resources. A UK Carbon trust report was summarized for the first part [17] 1.2.1 whilst the

legal and market scenario for the near future is presented as a summary of a RenewableUK document[15] in 1.2.2.

1.2.1 Wave energy potential exploitation in the UK

The total wave energy resource is derived as the amount of energy that reaches the UK from the Atlantic ocean passing by a series of frontages. Nevertheless these frontages are not always the most practical location. Therefore the calculation of wave energy resources must be focused on sites where energy can be harvested and also where real wave energy converters can be used. Figure 1.5 shows the wave energy recources around the UK [1].

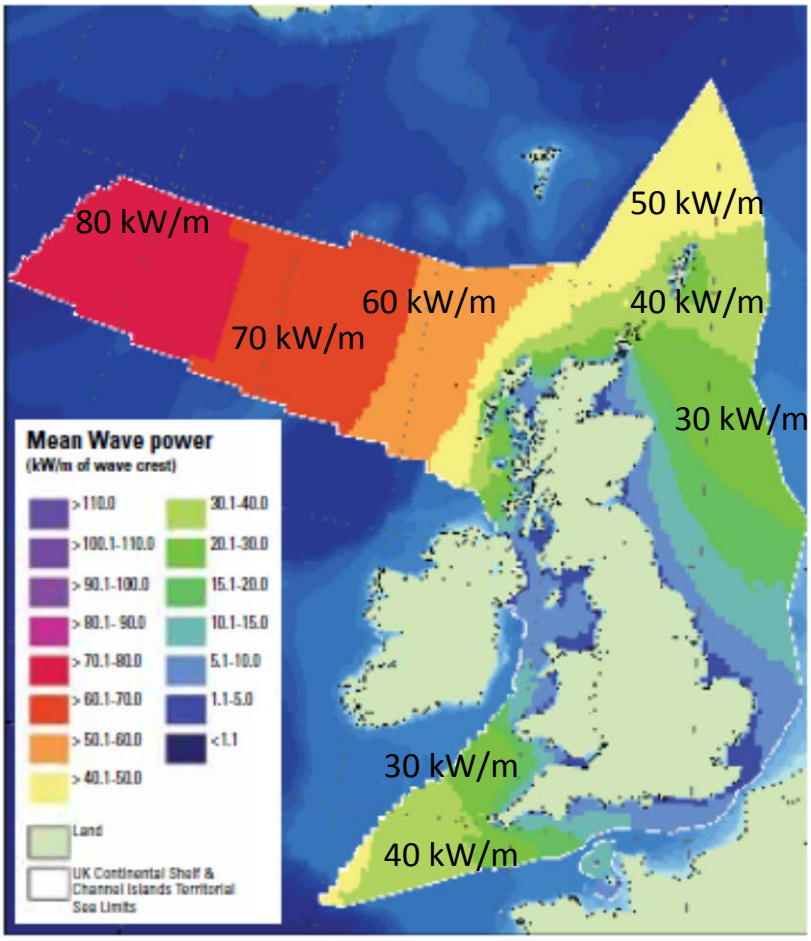

Fig. 1.5. Wave energy resources in the UK [1]

For the UK the least cost sites are on the west coast of Scotland and at the edge of UK waters in the southwest as seen in Figure 1.6.

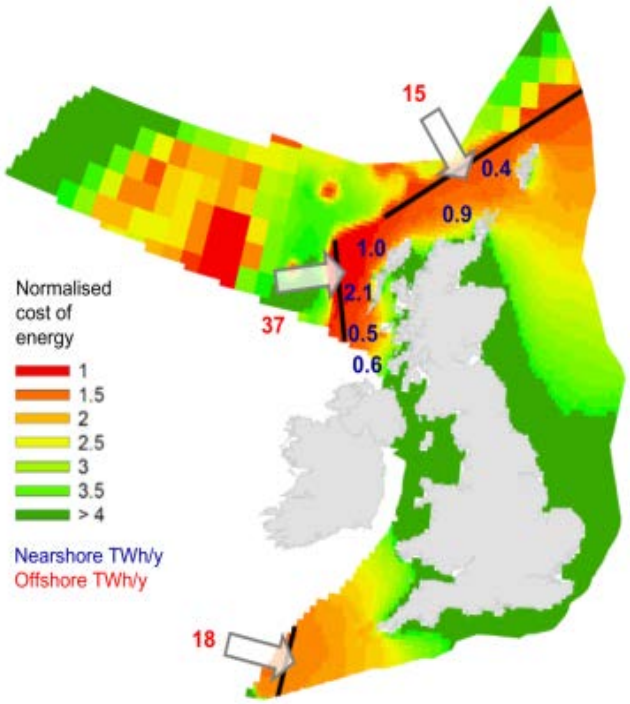

Fig. 1.6. Cost of Wave energy in the UK [1]

Not only the location but the distribution and orientation of the Wave Energy Converters (WEC's) might affect energy production. In wave farms the first incident device row absorbs some energy which reduces the energy available to the next row of devices in a farm. In the same way directionality might be an issue for non-omnidirectional absorbers.

In addition, any location will present an energy distribution depending on wave height and periods. Likewise waves with different periods and directionality might converge in a specific point containing high energy at different wave periods (see wave directionality in Figure 1.7). Hence the wave energy convertor must not only be able to absorb energy but it should be designed to have a wide natural hydrodynamic spectral response or be able to tune to the differing wave patterns.

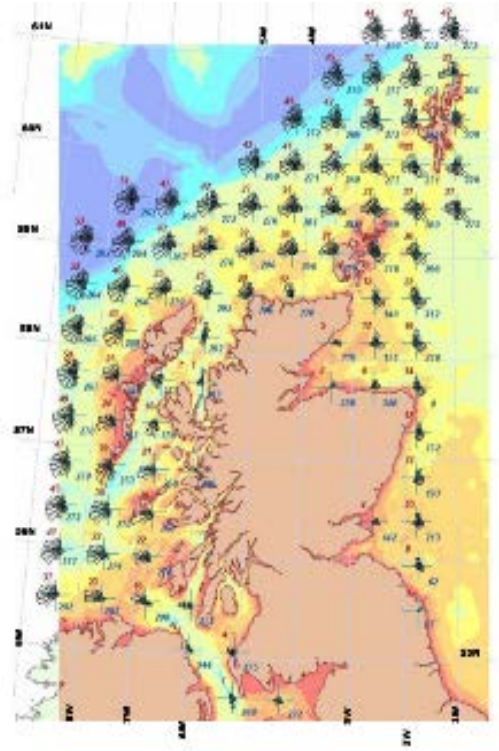

Fig. 1.7. Wave directionality around the Scottish coast [1]

In short, not only the characteristics of the waves, and resource, but practicability, and competition of economically feasible zones against other commercial activities and protected zones influences the potential resource extracted from waves. Examples of constraints can be special areas of conservation, military areas, shipping routes and fishing areas along with birds, mammals and other environmental conditions. The latter are not well mapped yet.

The Carbon Trust predicted that the total UK wave resources is 230 TWh/year. However this does not take into account the aforementioned issues. In order to come to a more realistic estimate, the restricted technical and practical resource has to be considered, with the following definitions:

Theoretical resources: refers to the maximum energy accessible from specific locations based on areas expected to have the most competitive low cost of energy.

Technical resources: Is derived from the theoretical resources that can be extracted using foreseen technology options.

Practical Resource: This is obtained from the technical resource available considering location limitations.

The total resource calculated by the Carbon Trust document is broken down in Figure 1.8 as theoretical, technical and practical. It is worth to notice that these resources are not strictly additive; the reason being that if the entire resource is extracted offshore none of it would arrive to the shore. However both kinds of devices can coexist if the offshore extract waves with certain characteristic leaving the rest for the nearshore devices.

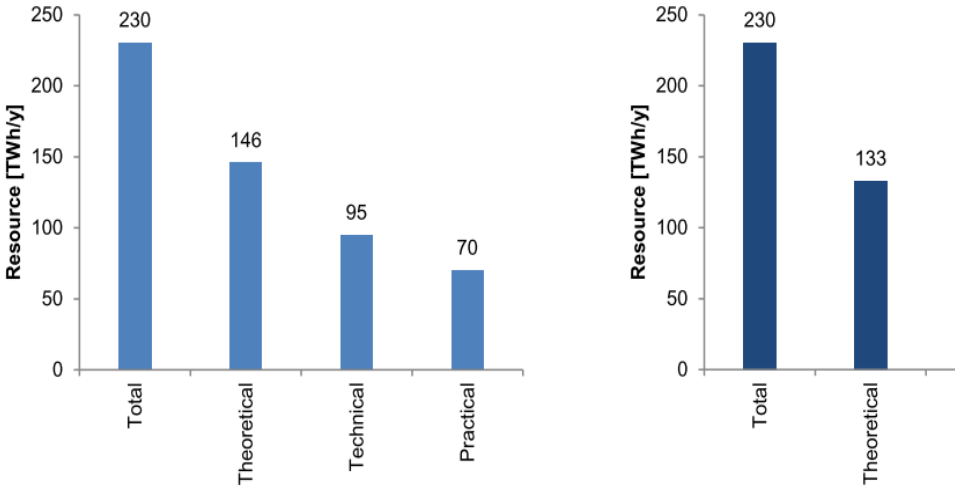

Fig. 1.8. Summary of resource estimate for wave energy farms: a) Offshore; b) Nearshore[17]

Applying the constraints results in the practical resource being 70 TWh/y for the offshore resource and 5.7 TWh/y for the nearshore. The total resources for both near shore and offshore. From the 70 TWh/y only 42 TWh/y would be at a cost ratio of 3, meaning three times below the cost of energy (revenue potential) [17].

It is also important to highlight that the potential practical resources coming from wave energy represents 3 times more than the production from wind farms in 2013 (25TWh/year) [13], which signifies a massive step towards the UK goals on CO_2 mitigation.

1.3 Chapter summary and thesis layout

This first part of the document highlights the wave energy potential in the UK. The practical energy generation mentioned in this section is outstanding even in comparison with other more mature kinds of renewable energy such as wind. This is the reasons the object of study for the following chapters is wave energy converters, their advantages, challenges and how to overcome them.

The following chapter focuses on a brief introduction and overview of different power take offs (PTO's) and compares a few of them. This chapter notes the importance of a reliable system, especially in offshore, for marine applications, and concludes that robust, reliable direct drive linear generators could be the technology which is best suited to these applications.

Chapter 3 highlights the problems associated with linear rolling element bearings for linear direct drive generators. Magnetic bearings are highlighted as a plausible solution. Subsequently a literature review of magnetic bearings is covered. A short introduction of different magnetic bearing configurations, as well as their classification by material used, control system and application is realized.

Chapter 4, explains concepts presented at EWTEC 2013 which were primarily designed for linear direct drive generators. The chapter also compares the concepts and simulates different magnetic configurations for an active magnetic bearing.

Chapter 5 presents a novel magnetic bearing topology utilizing the concept of "Inductrack" used for MagLev trains but replacing the permanent magnets by air-cored coils. Changing from permanent magnets to electromagnets allows full control of the magnetic field amplitude, frequency and the direction of the forces generated. The chapter calculates the magnetic field of the Halbach array considering two geometries. Also mathematical models based on two authors Post and Storset obtain the lifting and dragging forces are explored. The second part of the chapter presents the experiments performed to probe the concept, its challenges and setbacks.

In Chapter 6, the active magnetic bearing size is calculated for a 1MW generator, under the premise that, at this scale an optimised magnetic bearing will be cost

effective. Also a reliability study was completed comparing active magnetic bearings against traditional rolling element bearings.

Chapter 7 comprises the outcomes from the previous chapters listing the improvements areas and recommendations.

2 Wave energy converters

Wave energy converters extract energy from the oceans by interacting with waves, reducing the amount of energy in the sea. The author at [18] mentions that a good energy convertor must be able to generate a wave that can destructively interact with the one it is trying to absorb. This is not always completely effective and many other characteristics must be taken into account to achieve a total transformation of energy. Additionally a generator design with high reliability is pursued. High reliability translates to less down-time, and O&M cost. For a wave energy converter project, a device that requires fewer maintenance stops is essential, since undersea location requires specialized equipment and skills to access.

In order to make the most of wave energy converters several challenges have to be solved. Intermittent oscillating loads with slow frequencies have to be converted. Thus generators with special characteristics are needed. In the UK the most common offshore waves to be converted are close to the British Isles and have a range of 30-70 kW/m. However, wave energy converters might experience rare extreme waves of 2000 kW/m. These extreme waves as well as other environmental conditions will affect materials and consequently the overall performance of wave energy converters and the level of economic competitiveness compared to other forms of generation.

2.1 Classifications of Wave Energy Converters

The classification of wave energy converters varies from one author to the other. The next section describes classifications by location, by operation as well as classification by different power take-off (PTO).

According to [19], Wave Energy Converters can be classified

- By location:
    - **Shoreline devices:** Advantages of shoreline devices are proximity to the grid, easy maintenance, and low probability to be damaged in extreme weather. Disadvantages include low

wave power due to the location in shallow waters and limited number of sites.

- **Near shore devices:** These devices are placed on a depth of less than a quarter of wavelength, which can be considered shallow waters. Also they are anchored to the seabed, having stationary point of reference from where an oscillating body can harvest energy. Higher concentration of energy than shoreline devices. Disadvantages include reduced power limiting harvesting and higher cost of installation.
- **Offshore devices:** Benefits include the potential for greater energy production (see figure 2.1 [1]and 2.2 [3]) but due to its installation in deep water, installation, operation and maintenance cost increases.

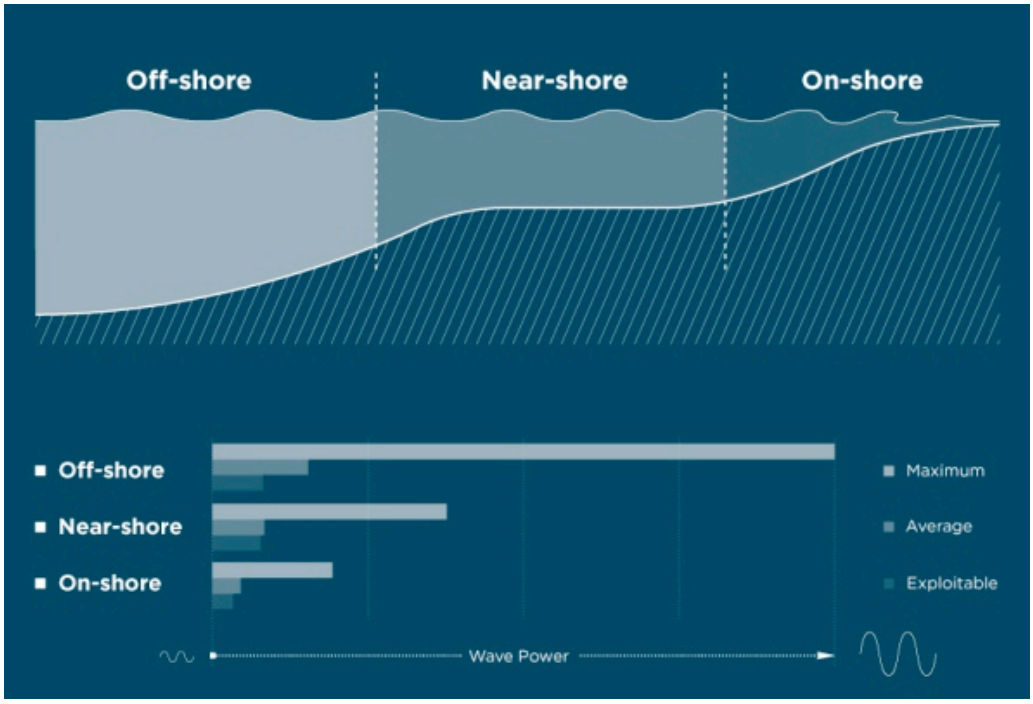

Fig. 2.1. Energy density location

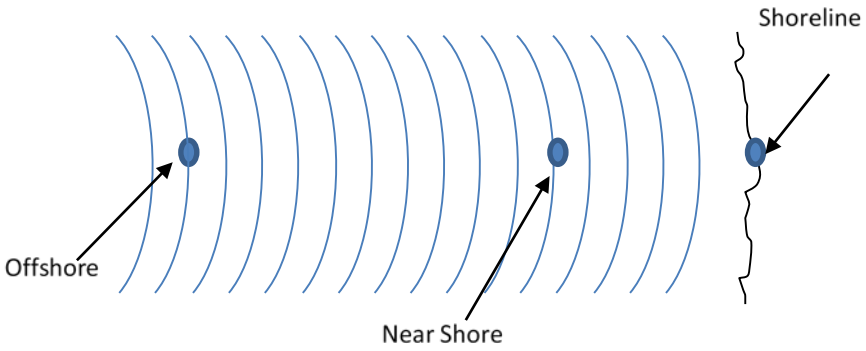

Fig. 2.2. Wave Energy Converters classification by location.

- by type:
  - **Attenuator:** Situated perpendicular to predominant wave direction.
  - **Point absorber:** Small dimensions relative to the incident wavelength. Floating structures that heave up and down.
  - **Terminator:** Situated parallel to the wave front intercepting the wave

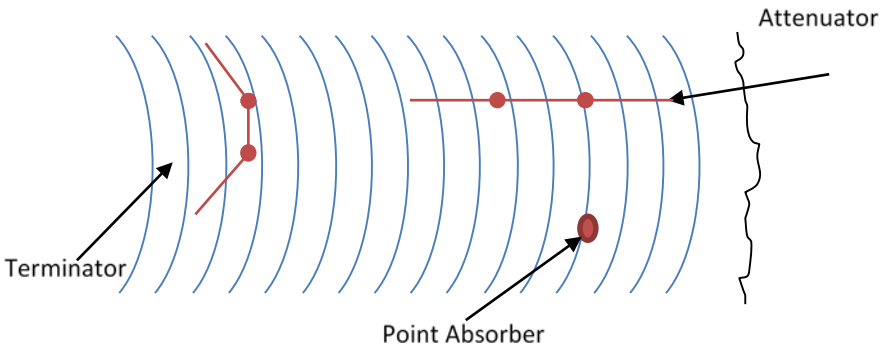

Fig. 2.3. Wave Energy Converters classification by type.

- by operation:
  - **Submerged pressure differential:** The oscillating hydrodynamic pressure produced by the wave's movement creates a vertical force over the floating body that reduce once the wave has passed over the device.

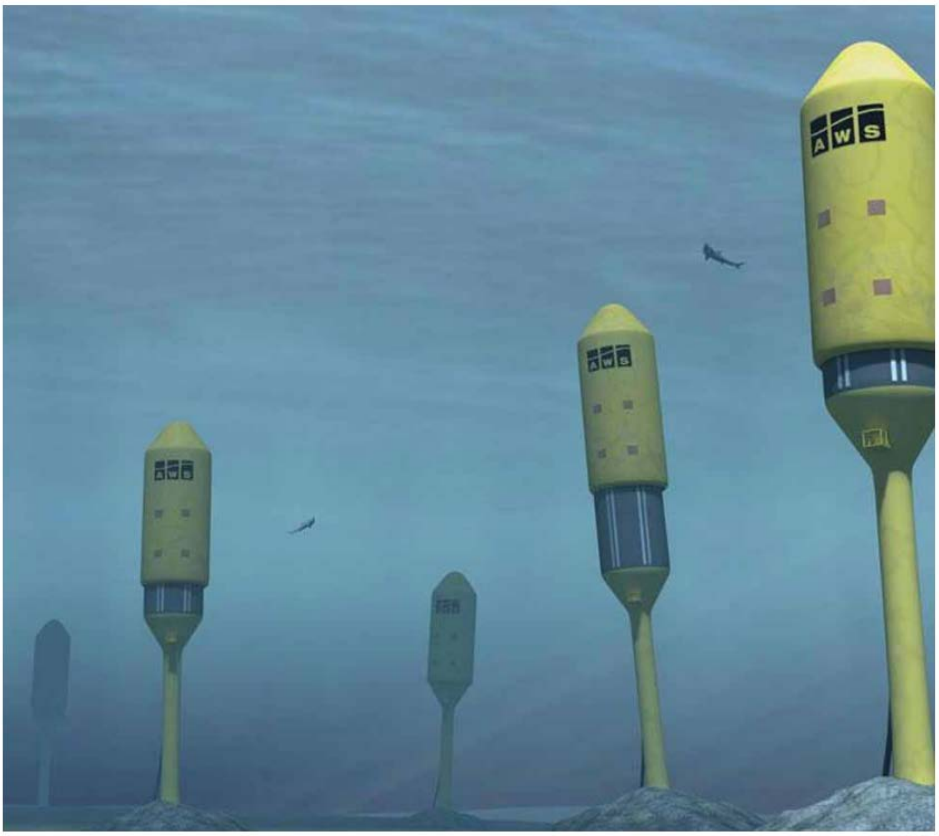

Fig. 2.4. Submerged pressure differential WEC. The Archimedes Wave Swing[19].

- **Oscillating wave surge converter:** Generally a hinged deflector acting as a terminator, it moves back and forth.

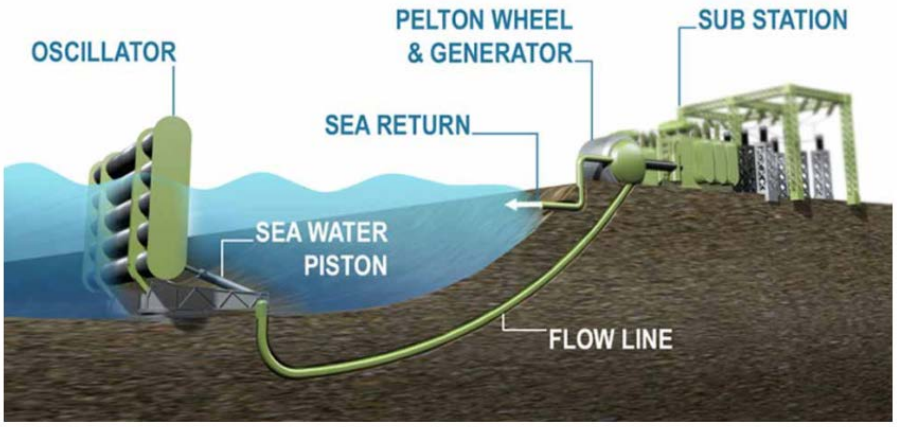

Fig. 2.5. Oscillating wave surge Converter: Aquamarine Power Oyster [19].

- **Oscillating water column:** Enclosed chamber with an outlet directed into a turbine. A Bi-directional air-flow is produced due to the rising and falling motion of the waves. The air-flow drives an air turbine, with the Wells turbine being the most popular because it rotates in one direction regardless of the direction of air-flow.

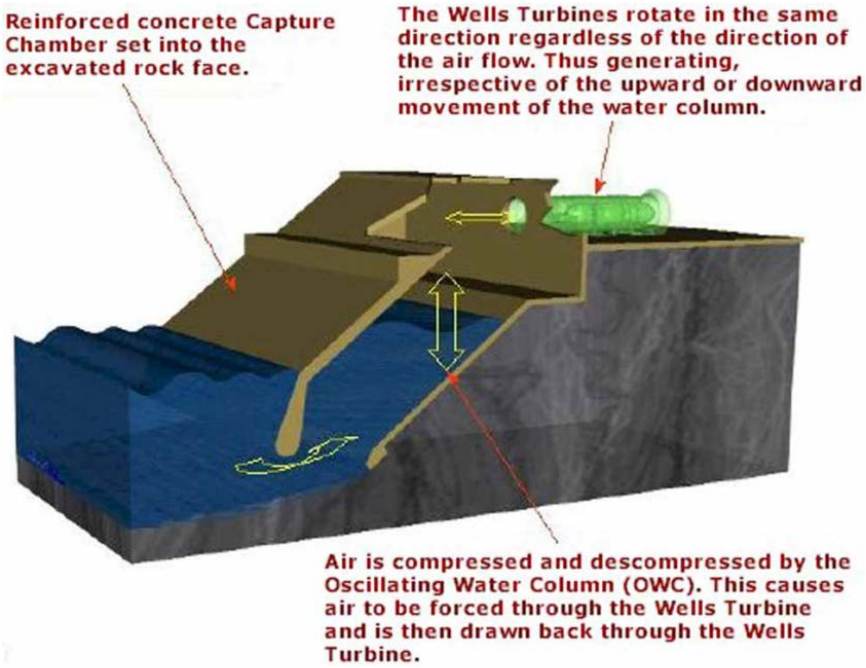

Fig. 2.6. Oscillating water column: The Limpet [19].

- **Overtopping device:** Captures sea water to build up a water head, releasing this once it is enough to run a turbine.

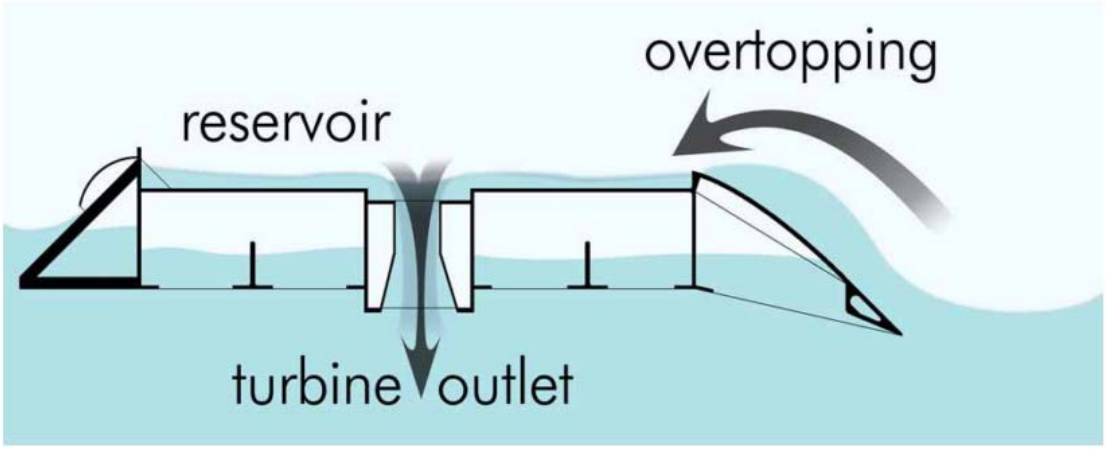

Fig. 2.7. Overtopping Wave Energy Converter[19].

2.2 Electric Power Take Off

In [20] devices are classified depending on power take-off for the most advanced wave energy converters. The PTO's are classified as:

- **Oscillating Water Column (OWC):** The previously mentioned movement of air in an OWC, increases the fluid speed and makes air pass through a rotational generator coupled to a Wells turbine. Energy extraction efficiency is around 40% therefore the electric conversion must be highly efficient.
- **Hydraulic Pumps:** The constant motion of waves is used to pump a fluid transforming mechanical movement to axial displacement at rams. This pumps oil and drives a hydraulic motor coupled to a generator. An advantage from this PTO is that it can drive a generator at synchronous speed, eliminating the use of power electronics although the speed must be fixed. However hydraulics take-off systems like Artemis Intelligent Power have achieved variable speed meaning more design flexibility[21]. Issues such as seal failure can cause malfunctioning of the device as well as environmental contamination.

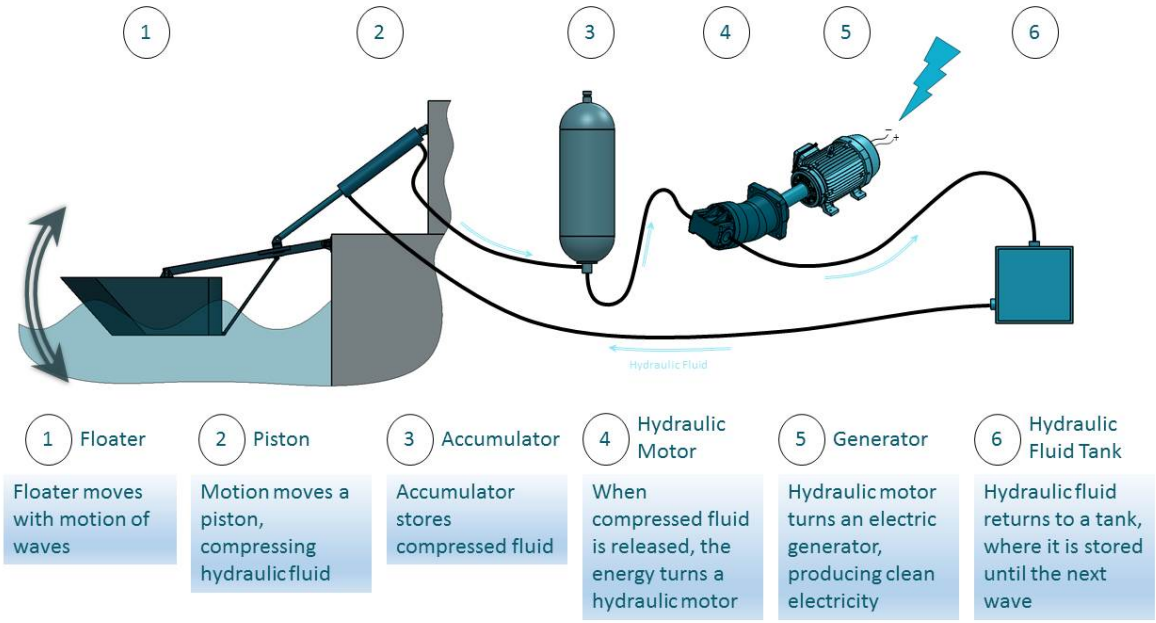

Fig. 2.8. Hydraulic system schematic [4]

- **Water Turbines:** Same principle used by low head hydro systems. Waves crash into the device flooding a constrained area (dam). Subsequently, this water is released driving a turbine. The main advantages of these kind of schemes are built-in energy storage, few moving parts and the use of a mature technology principle for energy conversion (See Fig.2.7).
- **Direct Drive:** In these systems there is no mechanical interface linking the prime mover to the generator (no gearbox or hydraulic system). As a result, a reduction in parts is achieved as well as a simpler system, which could potentially translate to lower maintenance costs and a more efficient system. However direct drive iron-cored generators are large in weight and size due to the low speed of operation, typically 0.5 to 2 m/s. A direct drive linear permanent magnet machine was used in the Archimedes Wave Swing(AWS) device shown in Figure 2.9, from which the scale of the generator can be seen with respect to the two people in the photo. Direct drive generators are typically large in dimension and mass. For instance the 2MW AWS device at 2m/s will need a surface airgap

area of 25 m^2. Also in iron-cored designs, attraction forces between the permanent magnet and iron core make the assembly difficult and imbalance airgap in the manufacture can lead to unbalanced forces adding undesired loads to the system.

Fig. 2.9. Archimedes Wave Swing Linear Direct Drive Generator [20]

As can be seen from the outlined classifications, selecting and designing the right wave energy converter is a complex process. In an attempt to develop a standardised method to compare generators, [22] considered different WEC's and with appropiate weighting, one would be able to relate each generator with the cost of energy to compare them. On the other hand [23] highlighted that energy production is not only related to the technical aspects of the PTO or the location, but also to non-technical barriers listed in [24] as regulatory, logistical and financial.

2.3 Reliability in generators.

The majority of literature about renewable energy generators has focused on wind turbines. However these generators can be translated to other energy sectors such as tidal or wave energy. Hence the following subsection will cover reliability issues in

wind turbine generators on the understanding that the same topic can be applicable to wave energy converters.

As mentioned before a high reliability generator is preferred for wave energy converter. In [25], Pinar highlighted the gearbox as one of the most problematic parts of the generators. Pinar also showed that although direct drive suffers from more frequent electric and electronic faults, geared options suffer from longer down time.

In [26] Delorm compare reliability of different types of wind turbines generators including Squirrel Cage Induction Generator(SCIG)/three-stage gearbox, Doubly fed induction generator(DFIG)/three-stage gearbox, Permanent magnet generator(PMG)/one or two stage gearbox and Direct Drive Permanent magnet Generator(DDPMG). Permanent magnet direct drive generators show a similar level of reliability compared to squirrel cage induction generators or doubly fed induction generators. This seems contradictory to the simpler system from direct drive generators. However this is believed to be caused by a more mature and well established industry in SCIG and DFIG than for DDPMG.

Also by eliminating the gearbox, the total cost of the device could be reduced, energy conversion efficiency could be enhanced and improvement of the availability of the energy converter could be achieved according to Grauers [27]. In order to accomplish this, the design of the generator must be improved since Direct Drive generators are typically large in mass, operating with high torques and at low speed. Hence novel designs must be explored.

Furthermore, Bang[28] investigates different direct drive generator topologies and compares them with other geared options. The authors highlight the superior reliability, energy yielding and decrease in maintenance of the permanent magnet direct drive generator and conclude that permanent magnet synchronous direct drive generators show higher energy yield in comparison to wind turbine systems using a DFIG system or an electrically excited synchronous generator direct drive system. However, the previously mentioned permanent magnet generators are larger in mass and their relative cost is higher. For this reason, solutions on the structure and electromagnetic design must be explored in order to make the most of this kind of generator.

2.4 Direct Drive Generators in Wave Energy

After the classification of wave energy converters, three main areas have to be settled, power take off type, movement of the generator, and kind of absorber. Between different power take offs direct drive generators are built with fewer pieces making them simpler and more reliable systems. A linear configuration also translates in a simpler way to absorb wave energy due to the movement of waves. Finally a point absorber is chosen due to its ability to obtain energy in any direction and their ability to combine several devices in one wave length. The following section presents a brief introduction of different novel concepts of direct drive linear generators.

2.4.1 Linear Generators in Wave energy

Although rotary machines are common in electricity generation, linear generators are more suitable for point absorber wave energy convertors due to their simplicity and their ease to translate heave movement of waves into linear movement at the translator.

Any rotary machine type can be used as a linear machine, simply by cutting open the stator and rotor, and then unrolling the components to give a linear planar machine as shown in Figure 2.10. Such a machine is single-sided, but there are issues of magnetic attraction forces between the stator and rotor, which will try to close the gap. By adopting a double-sided configuration the attraction forces will cancel, and even if there is an offset in one of the airgaps, the net force will still be low. Alternatively the unrolled machine can then be rolled along its central axis to form a tube, resulting in a so-called tubular machine, Figures 2.13 and 2.14.

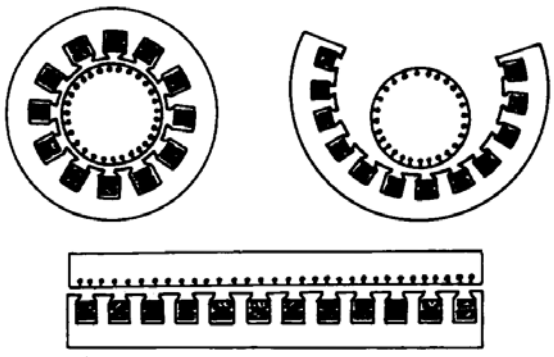

Fig. 2.10. Splitting and unrolling a rotary machine to create a linear motor[94].

2.4.1.1 Iron-cored coil

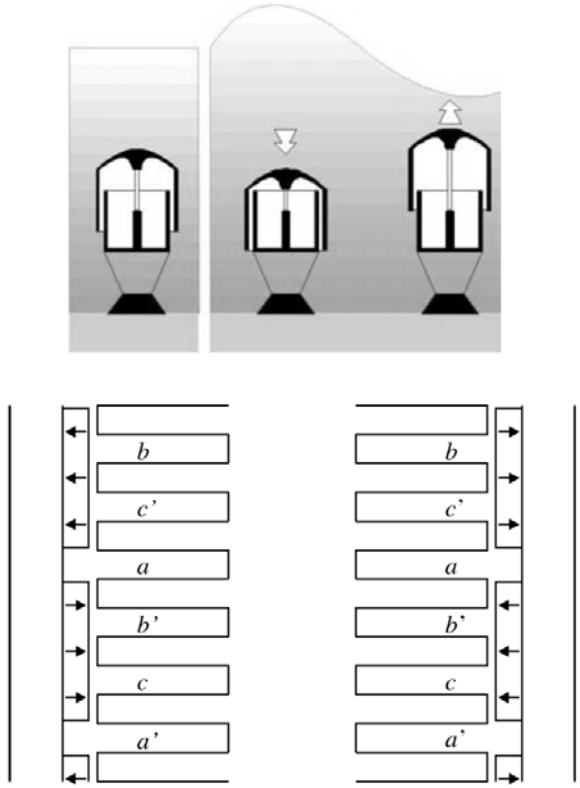

Fig. 2.11. Archimedes Wave Swing iron cored linear generator[29].

In [29] (Figure 11) the author compares five kinds of linear generators: linear induction machines and PM synchronous machines in combination with both iron and air-cores and switched reluctance machines. The comparison shows that the best cost/kW rate and most efficient generator is the Permanent magnet Iron cored generator for the Archimedes Wave Swing.

However the generator presents some mechanical engineering challenges. Attraction forces between the permanent magnets and the iron, at low speed and irregular motion signify a complex selection process for the bearing. A large balanced, and constant airgap surface area along the generator length is a manufacturing challenge. In addition attraction forces between the magnets increase the assembly process complexity. The same author explores the implications of designing this kind of generator in [30] and [31], where the importance of maintenance-free bearings is

mentioned. However Polinder mentions that the major issues are still size and weight[32],[33].

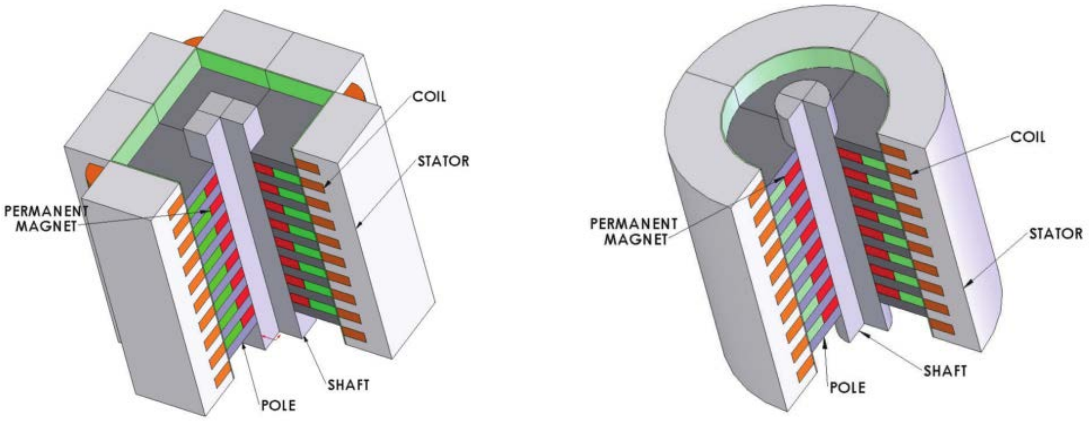

a) b)

Fig. 2.12. a) four-side linear generator b) tubular linear generator.

In order to address the bearing problem other designs of linear generators have been tried. The author mentions that this problem can be solved having a tubular design instead of the original 4-side design proposed in the same document (see Figure 2.12). Even if the electric performance of both generators are highly similar the tubular design is lighter, although it was concluded that due to the complex manufacturing process the 4-sided design would be preferred for energy production [34].

Another example of a tubular iron-cored linear generator is presented in [35] and shown in Figure 2.13, although the study does not show interaction between permanent magnets and iron cored coils, or their bearings.

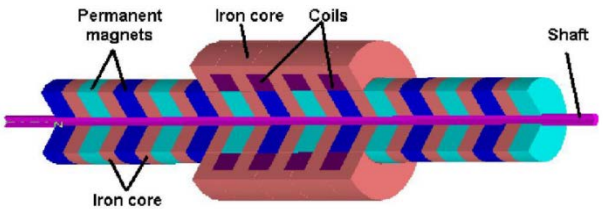

Fig. 2.13. Iron-cored tubular linear generator[35].

2.4.1.2 Air-cored coil

An alternative solution to eliminate normal forces between permanent magnets and the stator core is to use air-cored coils. This kind of generator use a non-ferromagnetic material as a core material for the coils, therefore permanent magnets do not attract any ferromagnetic material generally used to guide the magnetic lines through the coils.

The basic concept is to create a magnetic path that crosses the air-cored coils in order to generate a changing magnetic field inducing a voltage.

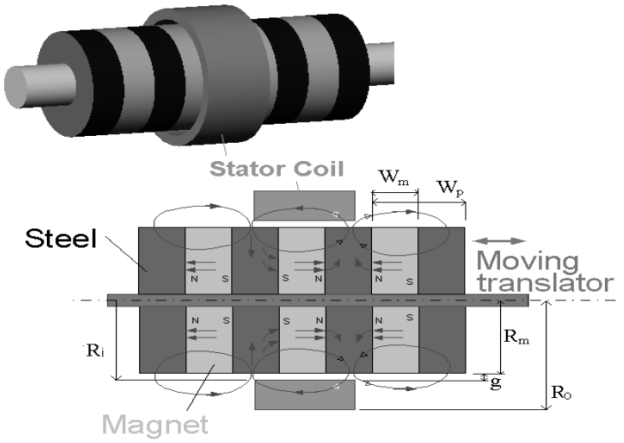

Fig. 2.14. Air-cored Permanent magnet tubular machine[20].

A tubular air-cored linear generator was presented in [20] and is shown in Figure 2.14. It can be observed in the image that the permanent magnet and steel material form a magnetic circuit going out of the moving translator and crossing the air-cored coil stator.

Another interesting tubular design is presented in [36]. Again the coils are in the stator and the traveling packed permanent magnets in the translator create a magnetic circuit alternating the magnetic field. The concept is shown in the following Figure 2.15.

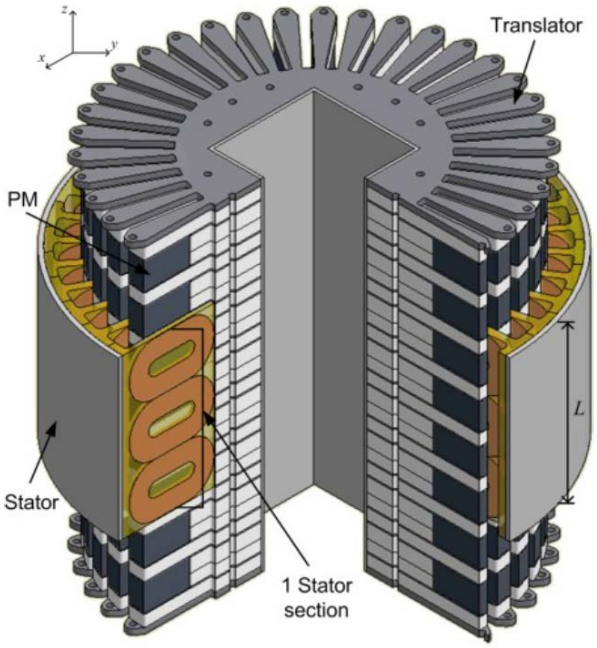

Fig. 2.15. Cut-out view of a novel air cored Permanent magnet linear generator from the University of Stellenbosch[36].

Finally an air-cored generator design developed at the University of Edinburgh is studied. The novel design called C-Gen is presented in [37] along with the functionality explanation and its structural analysis.

The authors mentioned the challenges that large attraction forces between the permanent magnets and iron-cored stator in generators create. The bearings must endure large loads and the mechanism must be stiff and precise enough to allow the translator to move freely with small air gaps between moving parts. The challenge to design bearings that can tolerate these complex loads has been noted in several linear iron-cored generator documents. Consequently a generator that eliminates said attraction forces is desired.

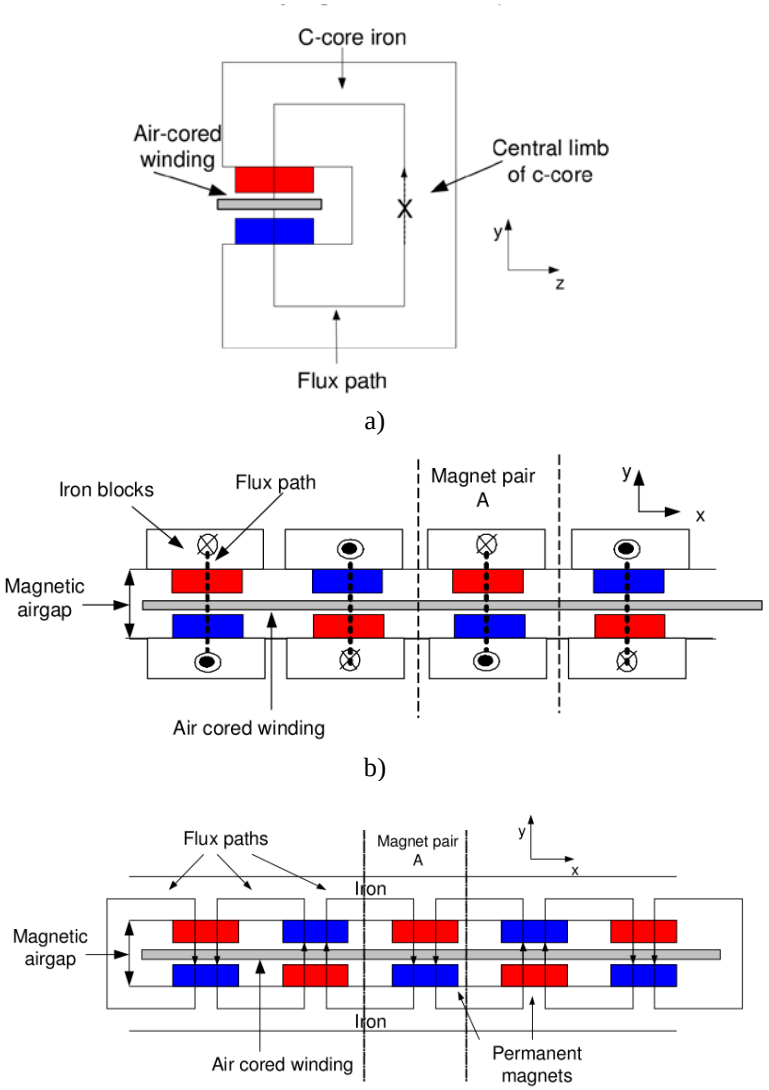

Fig. 2.16. a) C-Gen section, magnetic flux acting on the y-z plane. b) C-Gen front view. c) C-Gen front view magnetic flux acting on the y-x plane[38].

The C-Gen permanent magnets are placed so that the magnetic flux flows around the C-Core and forms a continuous circuit crossing the airgap. The windings are located within this airgap, packed in a non-ferrous material as seen in Figure 2.16 a) and b). The figures demonstrate that the flux is traveling on the z-y plane. If another "magnet pair" section is added to the device making contact and alternating the poles of the magnets, a secondary magnetic circuit is created traveling on the x-y plane as seen in Figure 2.16 c)[38].

The extra path makes it possible to reduce the C-Core thickness according to [37]. The magnetic flux path can be seen in Figure 2.17[39]. The document explores the application of a rotary C-Gen topology in marine energy. According to the authors

the C-Gen permanent magnet generator can reduce the mass by 50% compared with Iron-Cored permanent magnets. The author also mentions that even if the electromagnetic performance of the device is not as good as its iron-cored counterpart, the advantages of this topology outweigh its disadvantages for large generator projects.

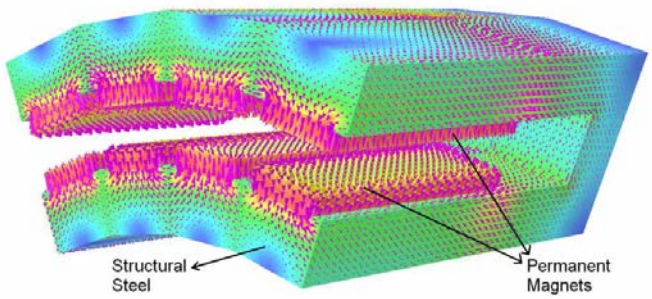

Fig. 2.17. Flux paths in a radial flux C-Core rotary machine[39].

Figure 2.18, taken from [38], shows the linear configuration of C-Gen permanent magnets. It is noted that the translator part is composed of two C-Gen modules with one pair of magnets. In other word the C-Core is closed in both ends.

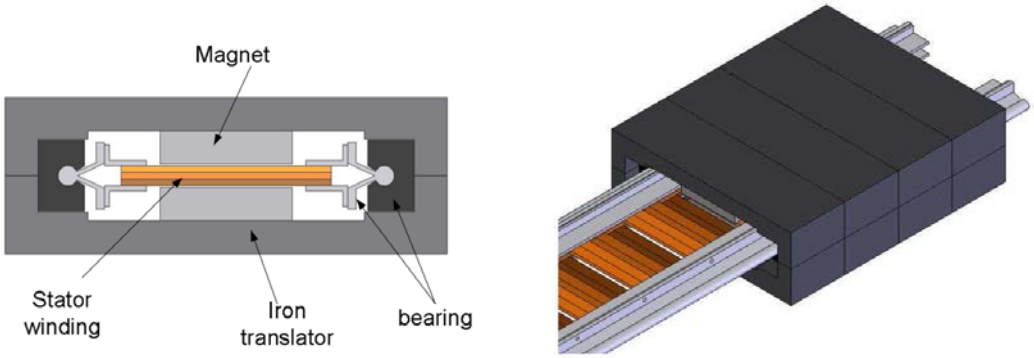

a) b)

Fig. 2.18. C-Gen's linear configuration: a) Cross section; b) Isometric view[38].

The same document compares this design with a tubular air-cored coil machine and points out a reduction in permanent magnet material which leads to reducing the overall cost while keeping the mass almost identical.

Summarizing the advantages of C-Gen mentioned in different documents the following list has been created[37]-[40]:

- Mass reduction of the device.

- Easy process of manufacturing and assembling.
- No normal forces between stator and translator.
- Higher thrust per watt of copper loss (efficiency increases).
- Potential lower Operation & Maintenance costs.
- Simpler system, potentially leading to higher reliability.

2.4.1 Novel developments

High Temperature Super Conductor (HTSC) generators are a variation of synchronous generators using HTSC coils to create superconductor magnets instead of utilising permanent magnets. In this way the generator's power density increases, although this type of machine requires special equipment to reach and maintain temperatures in which superconductivity is achieved. Therefore cryostat, rotor cooling system and electromagnetic shield play a role on the cost benefit trade off[41].

The use of superconductors in generators is reviewed in [42]. The author notes that the use of superconductor materials in generators can reduce the volume three times compared to traditional generators. In addition, a theoretical increase of 99% in efficiency compared with PM Generators is highlighted, resulting in a reduction of 50% of losses in some cases. The authors also mention that High Temperature Superconductors Generators (HTSG) might have better grid performance.

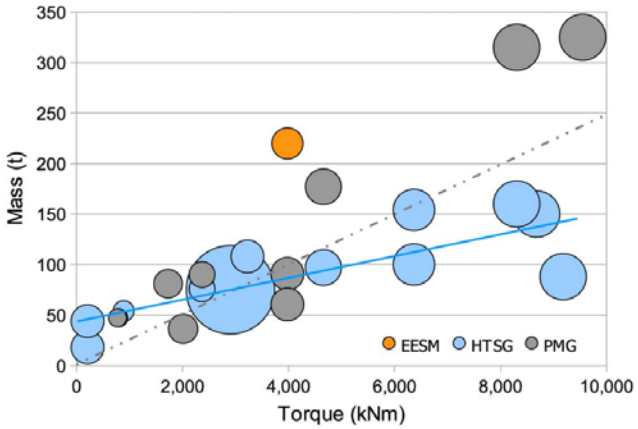

Fig. 2.19. Mass torque relationship in Wind Turbine Generators. Electrically Excited synchronous Machine (EESM) High Temperature Superconductor Generator (HTSG) and Permanent Magnet Generator (PMG). The size of the bubble represent power rating[43].

Keysan proposes the use of HTSG for large offshore wind turbines[43]. It is mentioned as well that the mass of the generator can be reduced as depicted in Figure 2.19, reducing the cost of installation.

It is proposed that a full superconductor generator would result in higher power density, however alternating fields from superconducting coils (reaching 17 Teslas) would potentially generate large current related losses. For this reason superconducting magnets and traditional copper coils are combined in the mentioned document. However, Keysan finds some disadvantages of HTSG. The large attraction forces of this kind of superconductor materials that are generated once magnetised make the assembly of the superconductor extremely difficult. Consequently an in situ magnetization device is preferred, although the use of this limits the characteristics of the winding. Even though these generators are highly efficient, reliability related to the cryogenic system might reduce the interest of manufacturers.

Transverse flux generators. This is another non- typical design, suitable for direct drive implementation. They present high forces density, considerably low copper losses and simple winding topologies [28]. Polinder [32]explored a double sided transverse flux generator design, claiming that this design is cheaper than a permanent magnet synchronous machine but more efficient. Nevertheless Polinder also pointed out the challenging manufacturing process for its design.

Keysan mixed the double sided transverse flux design adding HTS to it. In the end the author proposes an axial transverse flux homopolar topology for a low-speed and high torque generator using a stationary (DC) magnetic field.

As an example of rotary to linear electric machines adaptation in Figure 2.20 a generator presented in [44] is shown. As the cross section view (a) of the figure demonstrates even this HTSG can be adapted to a linear configuration[21]. In this design, there is a HTS material ring while the change of the magnetic field is a result of the transverse flux of the core.

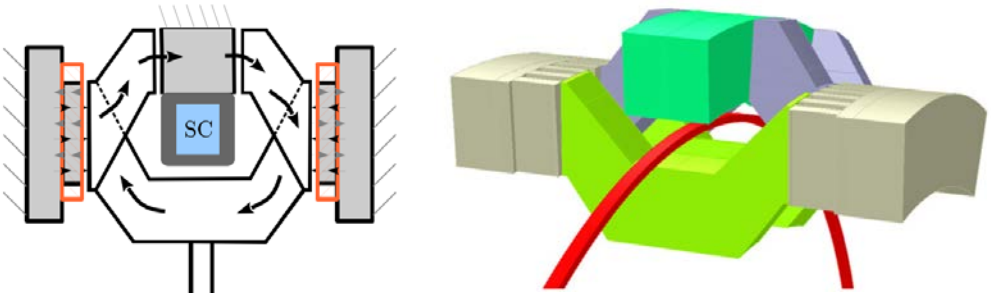

b) b)

Fig. 2.20. a) double-sided claw pole view cross section view; b) Section of the machine isometric view[44].

The linear version of the transverse flux HTS generator or claw pole machine is presnted in Figure 2.21.

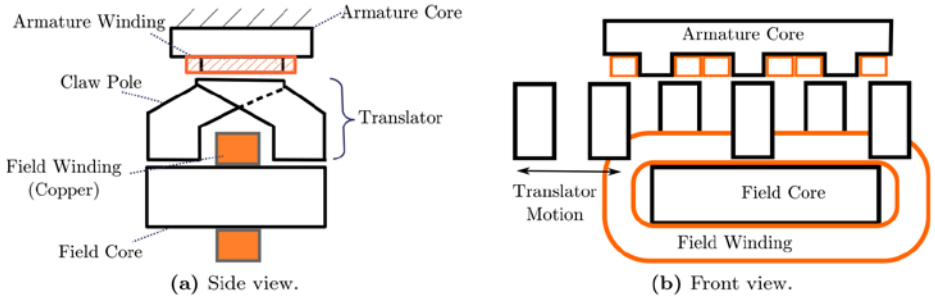

Fig. 2.21. Linear claw pole machine schematic[21]

2.5 Summary and conclusion

In this section a brief introduction and explanation of existing wave energy converters was presented as well as their classification by location, type and power take off.

Reliability plays an important part of any renewable energy project, but even more in projects where access is difficult as in offshore applications. Direct drive linear generators represent a simpler solution for wave energy exploitation and potentially a more reliable one.

Linear direct drive wave energy converters were covered, listing different devices found in the literature review. The Permanent magnet Iron-Cored linear generator is noted as the generator with better cost/kW ratio, although mechanical engineering issues, and size and weight make it less attractive than its air-cored counterpart.

Air-cored options were particularly attractive, especially the C-Gen air-cored generator. Since there is not iron in the coils the generator doesn't have to deal with large attraction forces between stator and translator usually present in iron-cored designs. Also since the permanent magnets sections are separated in pairs, attraction forces between the permanent magnets is neutralized making it not only able to separate in modules but easier to assemble. Summarising, this design presents advantages such as mass reduction, ease of manufacture and assemble, increased efficiency, and potential increases in reliability due to a simpler design. Hence the C-Gen design has been selected as the object to base this study, on.

A common challenge for direct drive wave energy linear generator designs are the bearings, as can be noted in section 2.4.

Therefore this document's objective is the study and design of a suitable magnetic bearing that, could potentially improve the overall performance of the generator, whilst aiming to be competitive against traditional bearings. Therefore a reliability study and a cost benefit analysis of the system must be carried out.

The proposed design must endure the operational conditions for a submerged G-Gen Wave Energy Converter without affecting the operation of the power take-off. The concept's prototype will be tested and compared against mathematical models and finite element models.

3 Introduction to Magnetic Bearings

Bearings are an essential part of any mechanism constraining movement to specific dimensions whilst facilitating the desired motion and interaction between moving parts, thus minimizing friction and consequently wear between parts. Magnetic bearings especially assist when the surrounding environment is extreme, hard to access, or requires specific conditions.

As mentioned in section 2, linear generators for wave energy converters have a challenge to design bearings with long life time and long maintenance intervals [45]. Likewise the design must tolerate complex loads and slow speeds in the case of direct drive generators.

The most common failures for rolling element bearings, besides the ones related with improper lubrication, are caused by vibrations, either generated by improper mounting or external causes [46]. Similarly, some of the most common failures of rolling element linear bearings are highlighted by [47], and can be grouped as, rolling element, rail and carriage (due to contact between parts) failure, and recirculation channel plugging (failure due to contamination). From here it is easy to identify 3 main areas of failure on traditional bearings, vibration, lubrication, and contact wear.

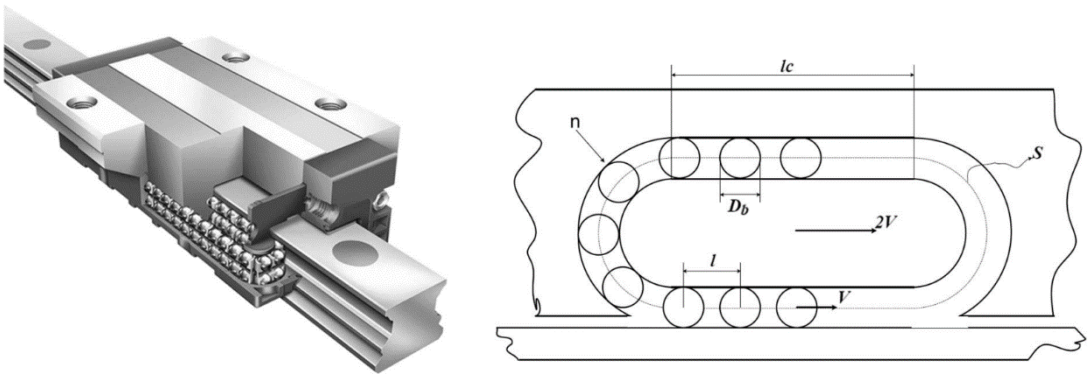

a) b)

Fig. 3.1.Rolling element linear bearing: a)Cutaway view; b)simplified model[47]

Specifically in linear bearings Caraher mentioned the short lifespan of conventional bearings in wave energy applications and investigated polymer composite bearings. At the beginning this author explored the use of oil as lubricant but due to the risk of leakage she decided to change her research to sea-water as the interacting fluid between moving parts for this application[48]. In the same way Prudell uses sea water as a lubricant for a rolling element bearing[49], the disadvantage in this case is that mechanical constraints result in a higher air gap compared to a machine with conventional bearings.

In the following section a literature review of magnetic bearings and their applications is presented. This will result in a broad comprehension of the devices, selection criteria and design.

3.1 Literature Review of Magnetic Bearings

Similar to the previously mentioned case of linear generators, applications with uncommon conditions require special bearings. This section reviews the different types of Magnetic Bearings (MB's), how they are formed and the materials used in their production. In addition summarised information of the documents read in the literature review is presented.

3.1.1 History of Magnetic bearings

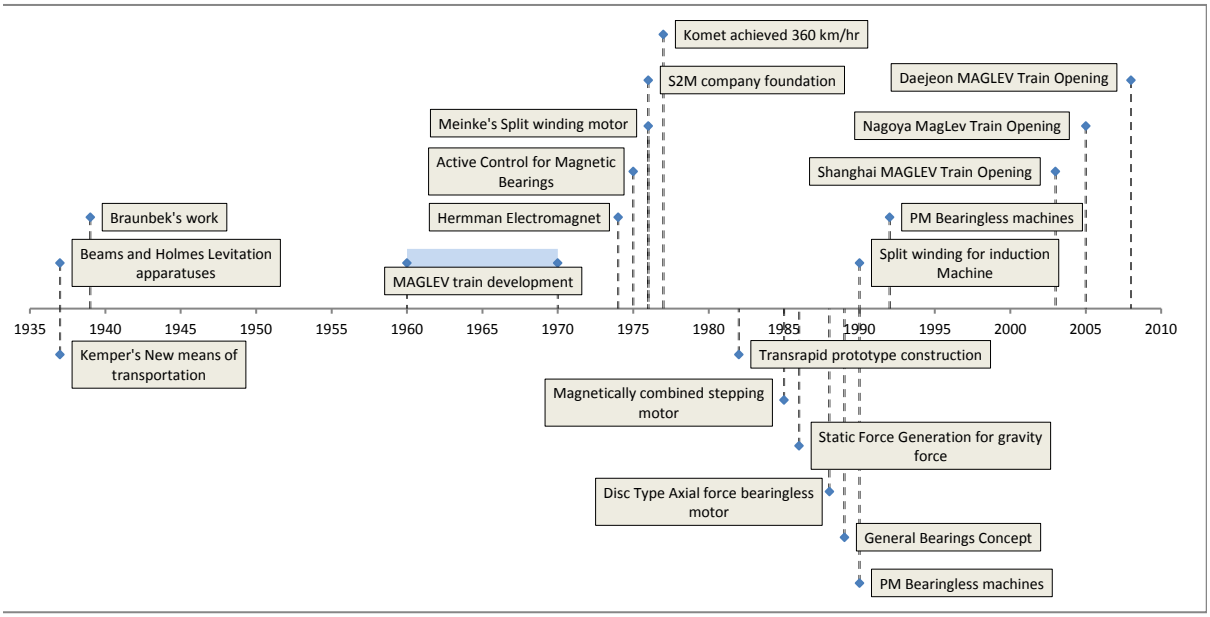

Fig. 3.2. Magnetic Bearing Time Line

Reference [1] notes that the first recorded documentation on magnetic levitation was presented by Earnshaw in 1842. A compilation of magnetic bearing development over time is shown in Fig. 3.2 [50],[51]. Linear magnetic bearings came into providence in the twentieth century and are now most popularly used in MagLev train applications. Most current reviews of linear magnetic bearings are therefore focused on transportation systems such as[52]–[54]. However the configurations and strategies mentioned in these documents can be applicable to almost any other linear device. Professor Eric R. Laithwaite is considered the father of MagLev for his work in the 1960's in the UK, but since then the technology has been refined and pursued in other countries, most notably the USA, Germany, Japan, and China [52].

The application of magnetic bearings has diversified over the years and a list of these applications is highlighted in section 3.2.4.

3.1.2 Main Advantages of Magnetic Bearings

A comparison between traditional bearings and magnetic bearings is presented in [55]. The most noticeable advantages are the lack of contact (no lubricant use), vibration suppression, active control of different levitation characteristics (position, stiffness, etc), as well as condition monitoring, the last two in the case of Active Magnetic Bearings. In the same way, these characteristics increase the life-cycle of a device and the Mean Time between Failures (MTBF), therefore leading to a reduction in Operation and Maintenance (O&M) costs.

Magnetic bearings are favoured over more conventional bearings in industries where contamination of the product is an issue, e.g. pharmaceutical and the food industry. Similarly magnetic bearings are also chosen in extreme condition applications, like ultra-low or high temperature, high vacuum, toxic environment, radiation, and remote or difficult to access areas such as under water or outer space applications[50]. Wave energy converters operate in a harsh environment, making magnetic bearings an attractive option.

3.2 Magnetic Bearing classifications

3.2.1 Passive Magnetic Bearings and Active Magnetic Bearings

Magnetic bearings can be separated into Active Magnetic Bearings (AMB) and Passive Magnetic Bearings (PMB). The first type implies higher costs and complex mechatronic systems (amplifiers, processors, software, sensors), but through the application of control offers accurate positioning, damping and vibration control as well as high stiffness. On the contrary PMB do not require any extra energy, hardware or software, but stiffness and damping are lower. Also control of position and velocity is not possible and condition monitoring would require an external system[56][57].

3.2.2 Basic Principles of Magnetic Bearings

In order to generate suspension forces magnetic levitation systems can be classified in two groups according to Schweitzer[51], reluctance force and Lorentz force.

Reluctance force can be calculated as the mechanical energy converted from the stored energy in the magnetic field. The force is derived from the principle of virtual work as presented in equation 3.1.

$$f_r = {}^{\partial W}/_{\partial s} \qquad \textit{Eq. 3.1}$$

Where W represents the field energy and δs the hovering body's virtual displacement.

This kind of force increases in accordance to the difference in permeability of the materials interacting in the magnetic circuit. In the case of ferromagnetic material the permeability is greater than the permeability of free space thus $\mu_r >> 1$. To give a better explanation of this, consider reluctance as a kind of magnetic resistance. Then reluctance forces tend to reduce said resistance which is inversely proportional to the permeability. A common example of devices using this concept is reluctance motors. Flux always wants to flow in the path of least reluctance so forces are produced to reduce reluctance. They tend to work on basis of attraction forces, and tend to be nonlinear, therefore difficult to control. This is commonly used in electromagnetic

levitation explained later in subsection 2.2.3.4. A good example of applications using this kind of forces is switched reluctance motor, presented in figure 3.3.

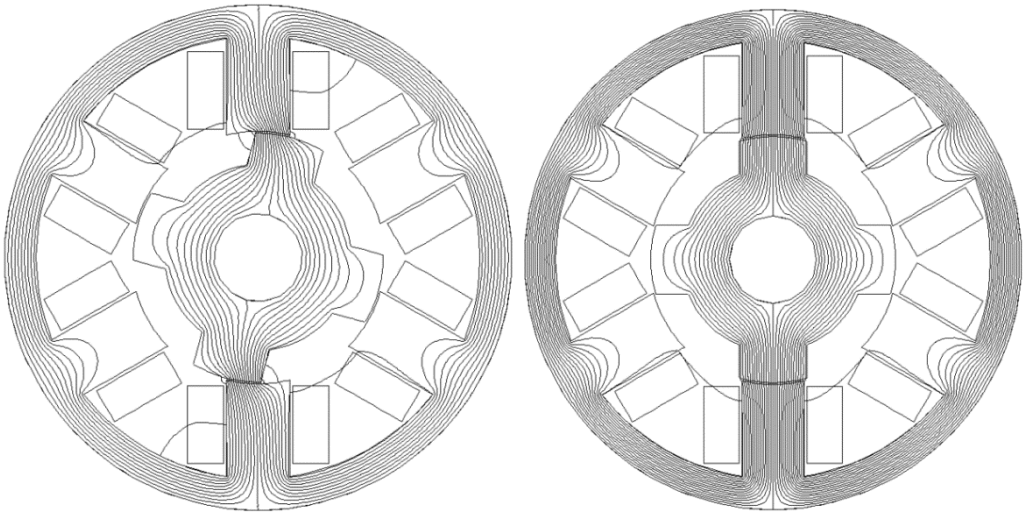

Fig. 3.3. Switched reluctance motor [193]

The other group mentioned by Schweiter is the Lorentz force. The following equation shows the resulting forces acting on a charge *Q*:

$$f_l = q(E + v \times B) \qquad \textit{Eq. 3.2}$$

Where *E* is electric field, *Q* is the charge moving at velocity *v* in a magnetic flux density *B*. *E* can be overlooked since the effect of it is 100 times smaller than the second part of the equation, consequently the expression can be simplified to equation 3.3 considering $i = qv$: A diagram of the relationship between the direction of B field current, I, and Force is shown in figure 3.4. An induction machine is a common example where this kind of force is used.

$$f_l = i \times B \qquad \textit{Eq. 3.3}$$

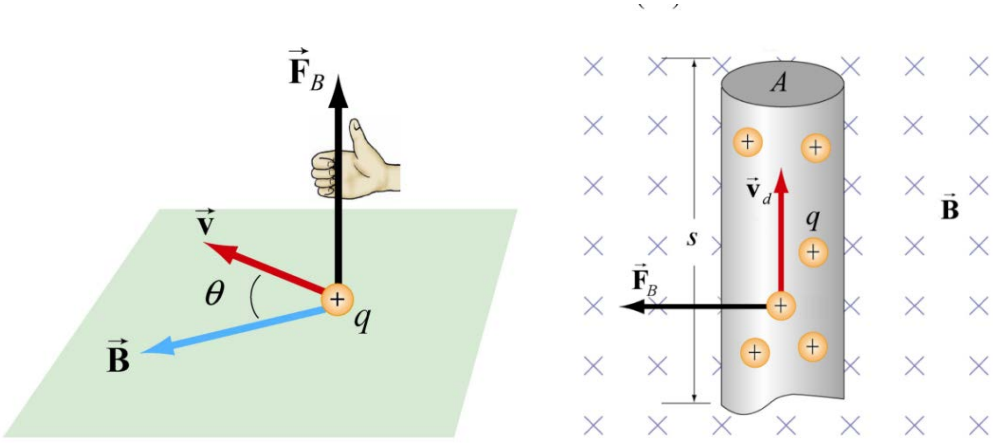

a) b)

Fig. 3.4. a) Lorentz force cross product diagram; b)Lorentz force on a conducting wire [194]

Both of the forces mentioned here depend on the combination of materials and the magnetic field interaction between them. In the following sections a deeper description of existing magnetic bearing configurations is presented.

3.2.3 Magnetic configurations for levitation

A brief introduction of the main materials utilised in magnetic bearings followed by an explanation of common configurations and classification of documents covered in the literature review is provided in the following sections.

3.2.3.1 Materials in magnetic bearings

The choice of materials is important to ensure an optimal design for either a passive or active magnetic bearing. Essentially these materials can be grouped into ferromagnetic, permanent magnets, superconductors and non-ferromagnetic conductor materials.

Ferromagnetic materials (Electrical steels)

Electric steels are used mainly in AMB as a magnetic core, with a coil wound around it to give a so called electromagnet. A current passed through the coil wound around the core causes an attraction force between the electromagnet and a ferromagnetic material. Electrical steels are laminated and alloyed with silicon to minimise losses due to eddy currents, and magnetic hysteresis [58].

Non-ferromagnetic conductive materials

Non-ferromagnetic conductive materials can be found in the examples mentioned previously since these materials are used to form the coils in which the current will flow. However, the forces generated due to the magnetic field on non-ferromagnetic conductive materials are different. If a changing magnetic field passes through these materials, repulsive forces, in reference to the source coil, are generated due to eddy currents induced in the conductive material.

Permanent Magnets

Many magnetic bearing devices use permanent magnets in order to have a source of magnetic field without any external energy use. Rare earth permanent magnets such as NdFeB are preferred in many recent applications due to the following advantages they present over other permanent magnets materials such as Alnicos and Ferrites (see figure 3.5):

- Higher , B_r(Remanence).
- Superior room temperature magnetic properties.
- Improvement against material corrosion, due to the addition of a coating.
- Very high Coercivity.

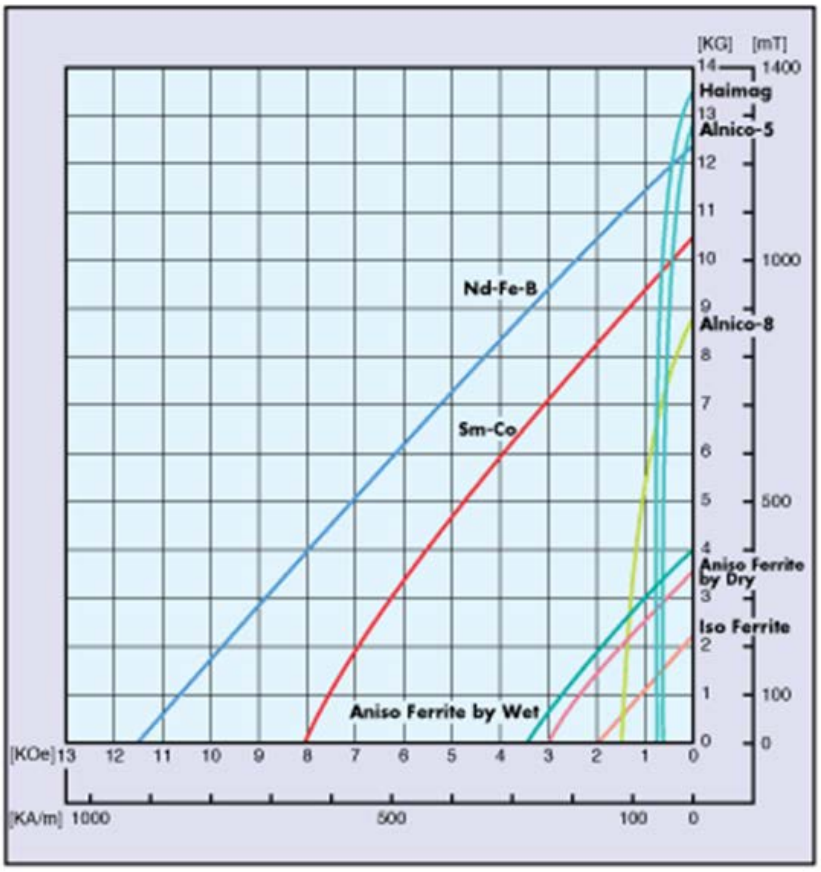

Fig. 3.5. B-H curves of different permanent magnets. “x” axis is coercivity and “y” axis is magnetic field strength [1]

Despite such positives characteristics it is worthwhile mentioning that it is still difficult for engineers to achieve the production of a proper NdFeB magnet with all the favourable conditions[58] [59].

Furthermore, in [60] two arrays for magnetic levitation, NdFeB-YBCO (superconductor) versus Ferrite magnets-YBCO (superconductor) are compared, resulting in a favourable resolution for the NdFeB combination. This material generates 10 times the levitation force generated by the ferrite magnet as can be seen in Figure 3.6.

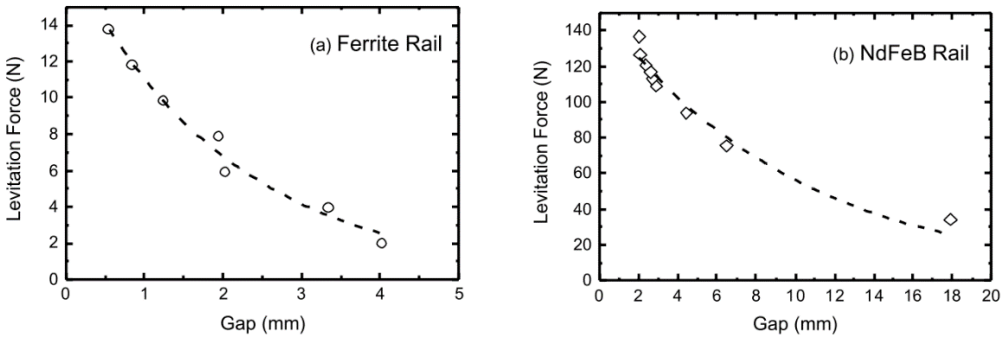

Fig. 3.6. Ferrite rail vs NdFeB rail force comparison [60].

Superconductors

The resistivity of these materials drops to zero when they reach certain low temperature (see Figure 3.7 a)). This temperature varies depending on the material (or compound) and is called the critical temperatures (T_c). In order to make the most of the characteristics of these materials different compounds and techniques are being tested to achieve a commercial competitive and compact product that can operate at higher temperatures[61] [62] [63]. Many authors claim the energy used to cool down these compounds is less than the energy used in any other active magnetic bearing. For this reason superconductive materials are desired when a passive magnetic levitation is pursued and energy usage is to be minimised (Flywheel Energy storage, Train, etc.).

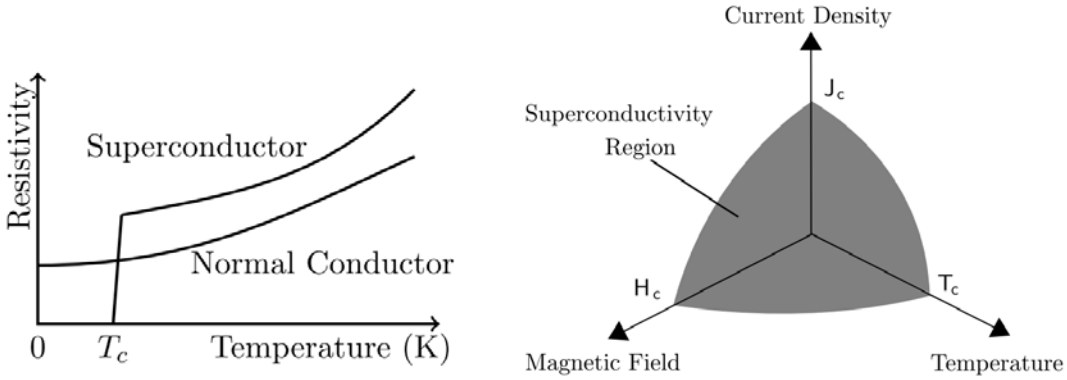

a) b)

Fig. 3.7. Superconductivity boundaries. Temperature and current density dependency [21].

3.2.3.2 Magnetic bearing configuration classification

The classification of systems made in this section is based on Lee's document with a few adaptations, since Lee has focused only on maglev train cases. Lee considered three main suspension types, Electromagnetic Suspension (EMS), Electrodynamic Suspension (EDS) and Hybrid Electromagnetic Suspension (HEMS)[64]. The change made from Lee's classification is made on the third group of systems. While Lee calls it HEMS this document refers to said group as Hybrid Magnetic Suspension (HMS) since many of the documents reviewed are a combination of EDS and EMS and not simply an enhanced EMS as Lee described in his article. The concepts are explained in more detail as follows:

Electromagnetic suspension (EMS): The principle of EMS is based upon attraction forces between a ferromagnetic material and an electromagnet which creates the levitation effect. The magnetic field at the electromagnet is generated by an electric current flowing through a wound coil, and passes through the ferromagnetic material (FM) generating a force of attraction. The most common configuration is composed of an electromagnet, floating body, distance sensor, controller and power electronics as shown in Figure 3.8 [65]. This kind of system presents non-linear attraction forces dependent on airgap and electromagnet currents thus a controller is needed to achieve stable levitation.

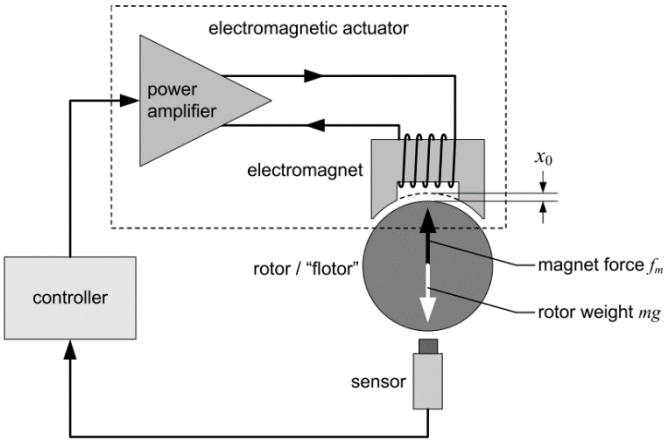

Fig. 3.8. Basic Magnetic Bearing Control Loop[65].

Electrodynamic suspension (EDS): Repulsive forces are utilised in electrodynamic suspension. These forces are due to characteristics of the materials interacting

between the stator and the rotor (or translator). Most of the literature is divided into different material combinations, for example, High Temperature Superconductors (HTSC)-Permanent Magnets (PM), PM-PM, or PM-Conductor Material (CM). Basic diagrams of each case are presented below.

Permanent magnet-HTSC

Superconducting materials must be operated at extremely low temperatures, 4.3-77˚K, depending upon the type of material, as mentioned in [66],[67],[61],[68],[63], to acquire the superconducting characteristics for operation. Not only the critical temperature but the critical current density and critical magnetic field defines the superconductivity state (ideally null resistance). These systems exploit either Meissner Effect or Quantum locking, depending on whether they are type I or II HTSC [69][70] (See Figure 3.9)

Type I: expel the magnetic field up to H_c when the temperature is below critical Temperature T_c.

Type II: has a region between H_{c2} and H_{c1} where the effect is a mix between a normal state and the Meissner effect. As can be seen in Figure 3.9 in the area below H_{c1} the Meissner effect is presented as in the material type I. This mixed effect gives stability to the levitation. In other words the Meissner effect levitates the compound while the flux-spinning locks the material in a position.

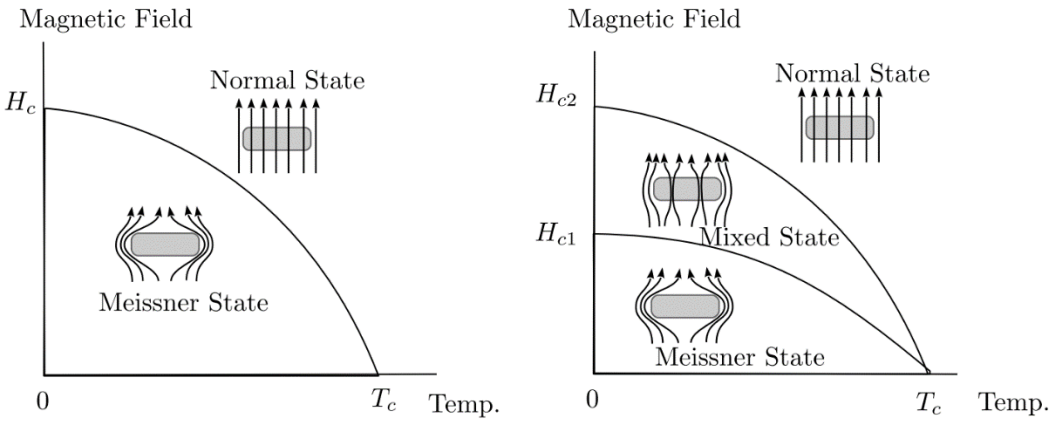

Fig. 3.9. Superconductor Materials: a)Type I ; b) Type II[69][70].

Permanent Magnets – PM-PM interaction

PM-PM interaction (Figure 3.10[71]) has been studied in [72][73][74] by Janssen and Yonnet. PM-PM interaction provides limited stiffness, and the movement of the PM-PM bearing must be constrained in order that the magnets do not flip over to join with another magnet of opposite polarity.

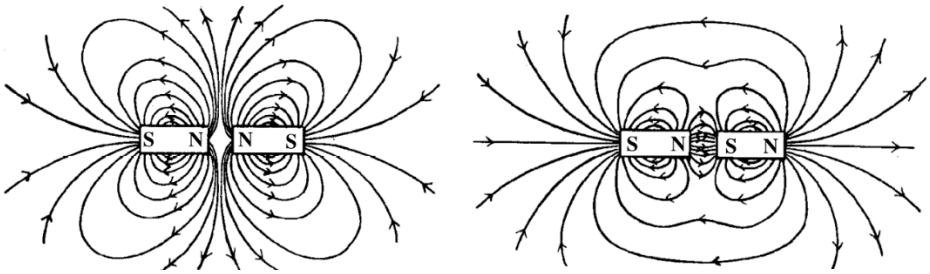

Fig. 3.10. PM's interaction[71].

Permanent Magnet-Conductor Material (PM-CM)

An example of EDS "PM-CM" is explained in [75], [76]. The concept described by the author is shown in Figure 3.11. When the array is in motion it induces currents in the conducting track, due to the changing magnetic field along the movement direction of the array. The induced currents in the track produce repelling forces between the magnetic field source and the conductive material. The intensity and shape of the magnetic field array depend upon the geometry of the magnets and the number of pieces within the Halbach array wavelength (e.g. 2, 4, 8 pieces).

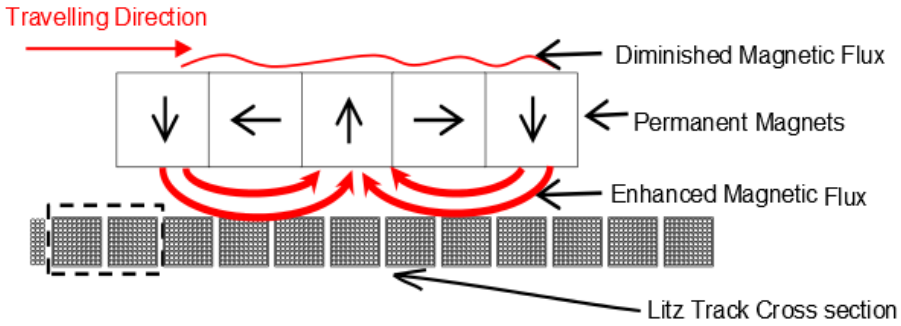

Fig. 3.11. "Inductrack" Concept

Hybrid Electromagnetic Suspension (HEMS): According to Lee [64] a HEMS system is a modified form of Electromagnetic Suspension(EMS), and thus relies on attractive forces. In this kind of system, the only difference is the use of Permanent

Magnets (PM) in the design in order to have a source of magnetic field besides the one created by the electromagnet hence using less control current (see Figure 3.12). Also according to [77] this kind of system improves the dynamic characteristics in comparison with EMS devices.

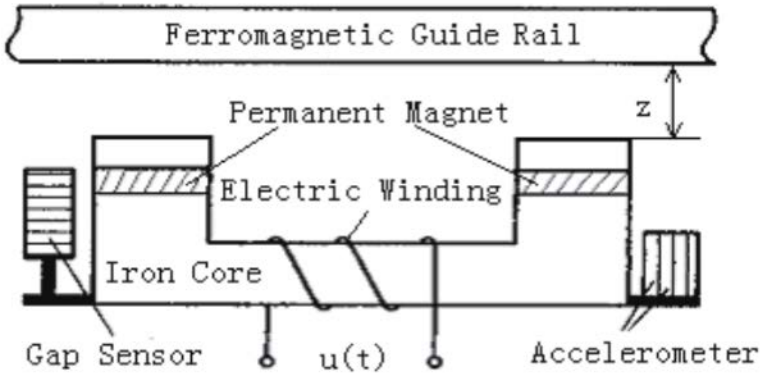

Fig. 3.12. HEMS example[77].

This group has been substituted in the present thesis by a group called Hybrid Magnetic Suspension or HMS. This group includes all the configurations where they combine EDS and EMS.

Therefore from the list of documents reviewed the different configurations are grouped as shown in Figure 3.13. A more detailed classification of levitation systems is presented in the following section.

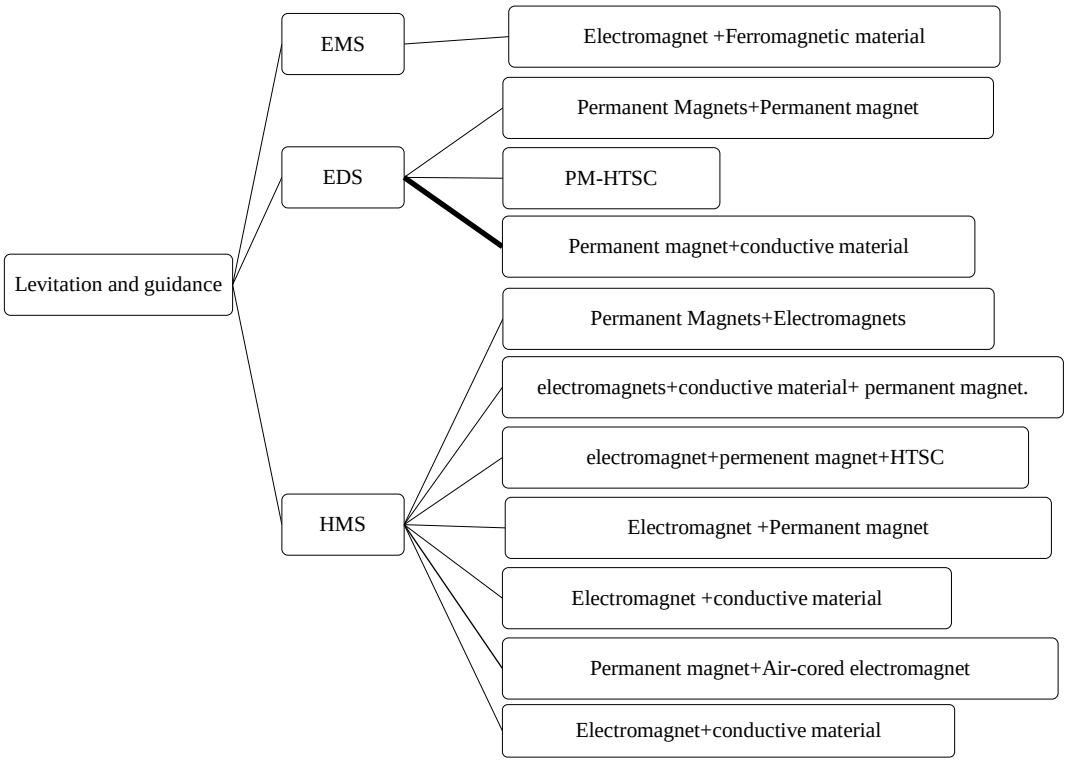

Fig. 3.13. Levitation and guidance classification

A list of the legends with the different material combinations revised in the literature review is presented in Table 3-1.

TABLE 3-I
MAGNETIC BEARING CLASSIFICATION LEGENDS BY MATERIAL COMBINATION

Symbol	Meaning	SYMBOL	Meaning
EM-FM	Electromagnet-Ferromagnetic material	PM-HTSC	Permanent Magnet-HTSC
EM-PM	Electromagnet-Permanent Magnet	PM-CM	Permanent Magnet-Conductor Material
EM-FM-PM	Electromagnet-Ferromagnetic material-Permanent Magnet	PM-PM'	Permanent Magnet-Permanent Magnet
PM-CM-EM	Permanent Magnet-Conductor Material-Electromagnet	EM-CM	Electromagnet-Conductor Material'
PM-ACEM	Permanent Magnet-Air Cored Electromagnet	*ACEM-CM*	Air Cored Electromagnet-Conductor Material
PM-HTSC-EM	Permanent Magnet-HTSC-Electromagnet		

Figure 3.14 shows a general distribution of the cases in various material configurations and their classification according to the previously mentioned EMS, EDS and HMS. Note that EMS is exclusively formed by a combination of ferromagnetic materials and electromagnets. EDS is formed by three different

combinations: permanent magnet-permanent magnet, permanent magnet-HTSC material, and permanent magnet-conductor material combination. Finally HMS is a combination of the two concepts.

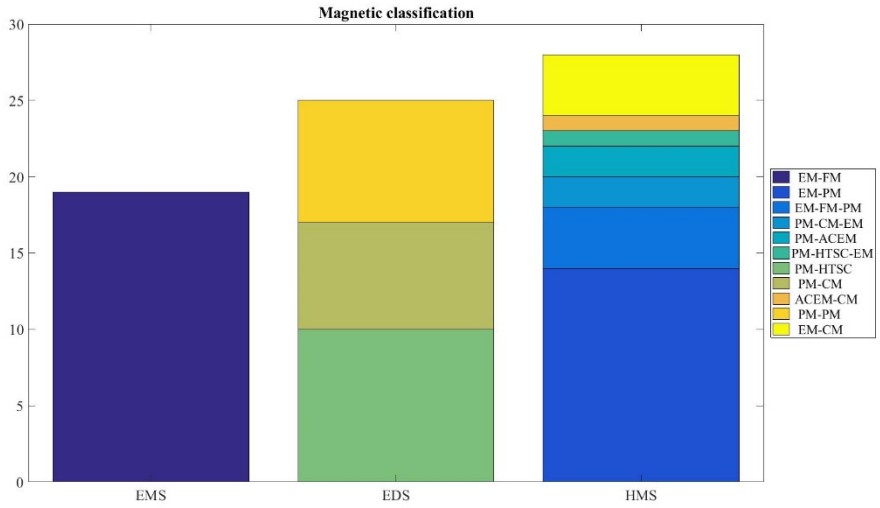

Fig. 3.14. Classification of magnetic bearing by material combination.

3.2.4 Topology and Application of Magnetic bearings

Besides their magnetic configuration, magnetic bearings can be also classified by the movement of the floating body. Thus two basic topologies have been identified: where the main action of the floating part is to turn about an axis, it can be called a rotary configuration, and where the main movement is translation over a plane (or group of planes) the configuration can be called a linear bearing.

Figure 3.15 shows the percentage of reviewed cases divided as linear and rotary configurations. Additionally Figure 3.16 shows the percentage of cases by application, transportation being the largest group followed by fine positioning if the “others” group is set aside since this last one groups several categories. The “others” groups different applications that are not that common such as measurement systems, indoor transportation, experiments and educational applications. This group will be explained in more detail in later sections.

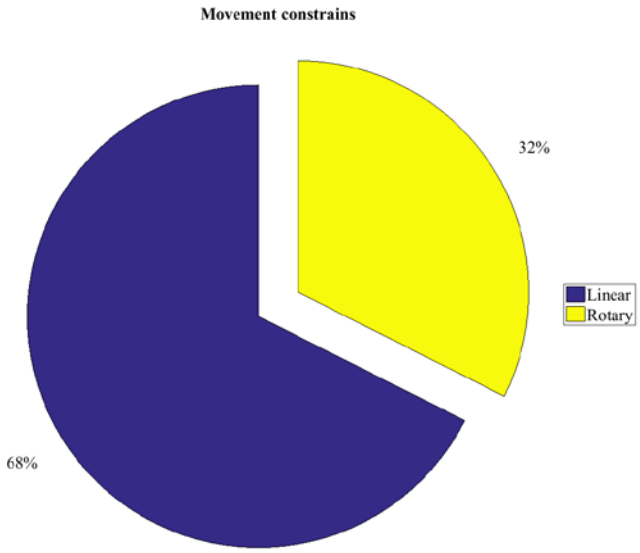

Fig. 3.15. Classification by magnetic bearing movement

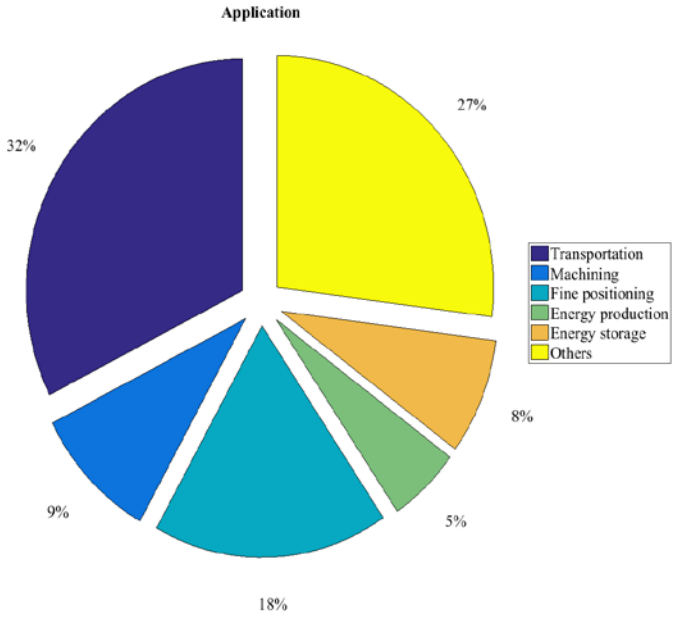

Fig. 3.16. Percentages of reviewed cases according to their application

As this project aims to find a solution for linear generators, the majority of cases reviewed are in a linear configuration.

3.2.4.1 Rotary configurations

Rotary magnetic bearings are mainly used for applications where it is desirable to avoid negative effects like vibrations and shaft deflection. At the same time these devices can be separated into vertical and horizontal. It is common to find thrust bearings which constrain certain bearing movement in this kind of magnetic bearings as shown in Fig. 3.17[50].

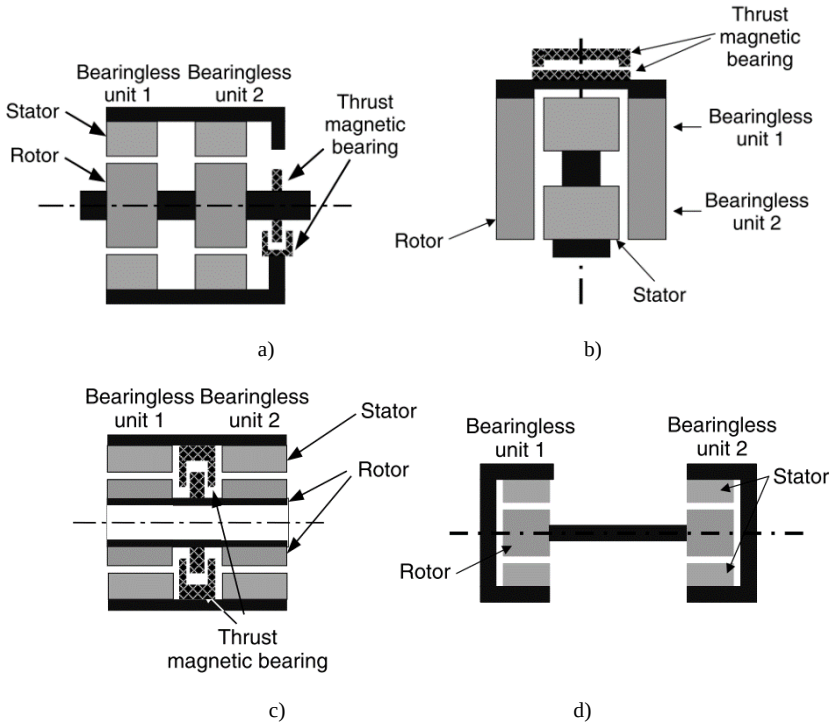

Fig. 3.17. Rotary Magnetic Bearings: a) inner rotor; b)outer rotor; c) hollow rotor; d) load machine space on the shaft centre[50].

Figure 3.18 lists examples of different EMS and HMS rotary configurations. From top to bottom a simple EMS used for machining applications [78] is shown in a), followed by two configurations using HMS where PM's have been added to enhance the magnetic field and therefore use less energy to generate attraction force in b) and c). The middle illustration corresponds to a machining application[79] while the final image indicates a flywheel [80].

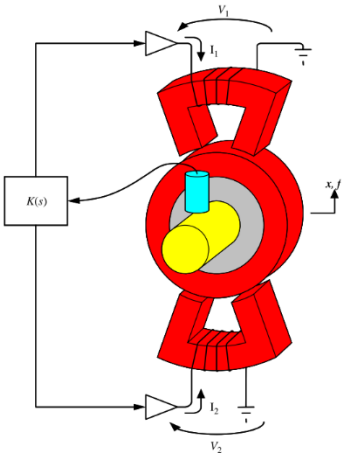

a)

b)

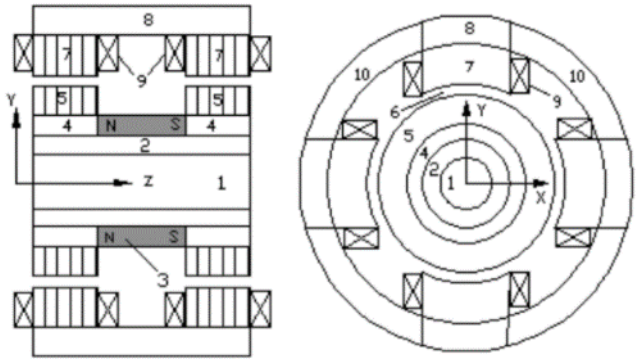

c)

Fig. 3.18. Rotary Magnetic Bearings: a)EMS; b)-c) HMS [78]- [80].

Figure 3.19 shows EDS configurations. The first one, presented in a), shows two permanent magnets arrays facing each other in order to generate repulsion and allow a machining tool to spin[81], while in the following images b) and c), type II superconductor material is being used for a flywheel[82][83].

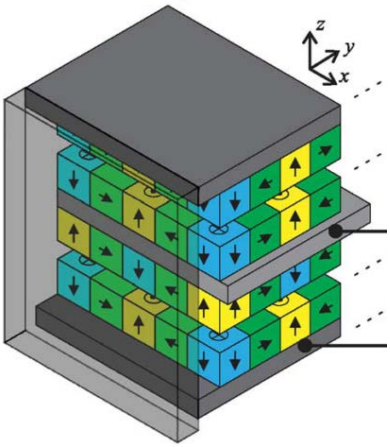

a)

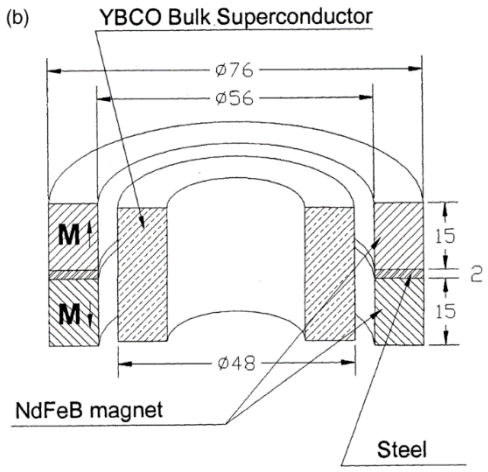

b)

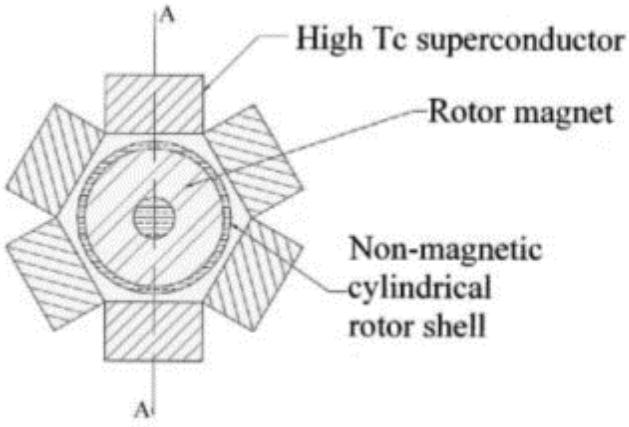

c)

Fig. 3.19. Rotary Magnetic Bearings using EDS. a) PM-PM ; b and c) PM- HTSC

Applications

Figure 3.20 classifies magnetic bearings according to application, magnetic configuration (previously mentioned) and control strategy. In this figure the number

of cases with a common combination is shown in the form of a bubble, the number and diameter of said circle represent the number of cases with the respective specific combination. For a better understanding of the distribution, each one of the planes in figure 3.20 was separated into Figures 3.21, 3.22 and 3.32. A list of the legends of the control classification is presented in Table 3-II. The reader should take in account that Tables 3-I and 3-II apply to both rotary and linear configuration section.

The applications were grouped into transportation, machining, fine positioning, energy production, energy storage and others. The “others” group include different instrumentation devices, laboratory prototypes, and educational demonstration experiments.

Figure 3.20 indicates that high speed machining and flywheel energy storage are the most popular applications for this specific topology.

Rotary tools with speeds that regular bearings cannot tolerate, ranging from 10000 rpm to 150000 rpm, were grouped in *machining* [78], [79], [81], [84], [85],[86], [87].

On the other hand magnetic levitated *flywheels* for energy storage or aircraft instrumentation are commonly found in literature. These devices claim to have reduced mechanical losses due to the lack of contact, although most of them are constrained by the cooling system [80] [82] [83] [88] [89] [90] [91].

Due to several issues related with complex loads on the bearings and Operation & Maintenance(O&M), applications in gas and wind turbines have also been proposed in [92], [93].

TABLE 3-II
CONTROL CLASSIFICATION LEGENDS

Symbol	Meaning	Symbol	Meaning	Symbol	Meaning
PID	Proportional Integral Derivative	*RA*	*Robust Adaptive*	*LQG*	Linear quadratic Gaussian
ZPC	Zero Power Control	*SMC*	Sliding Mode Control	*H∞,μ-synthesis*	*H∞,μ-synthesis*
FTC	Fault Tolerant control	*LL*	*Lead-Lag*	*FNN*	Fuzzy Neural Network
LQR	Linear Quadratic Regulator	*NP*	*Network predictive*	*P*	*Passive*

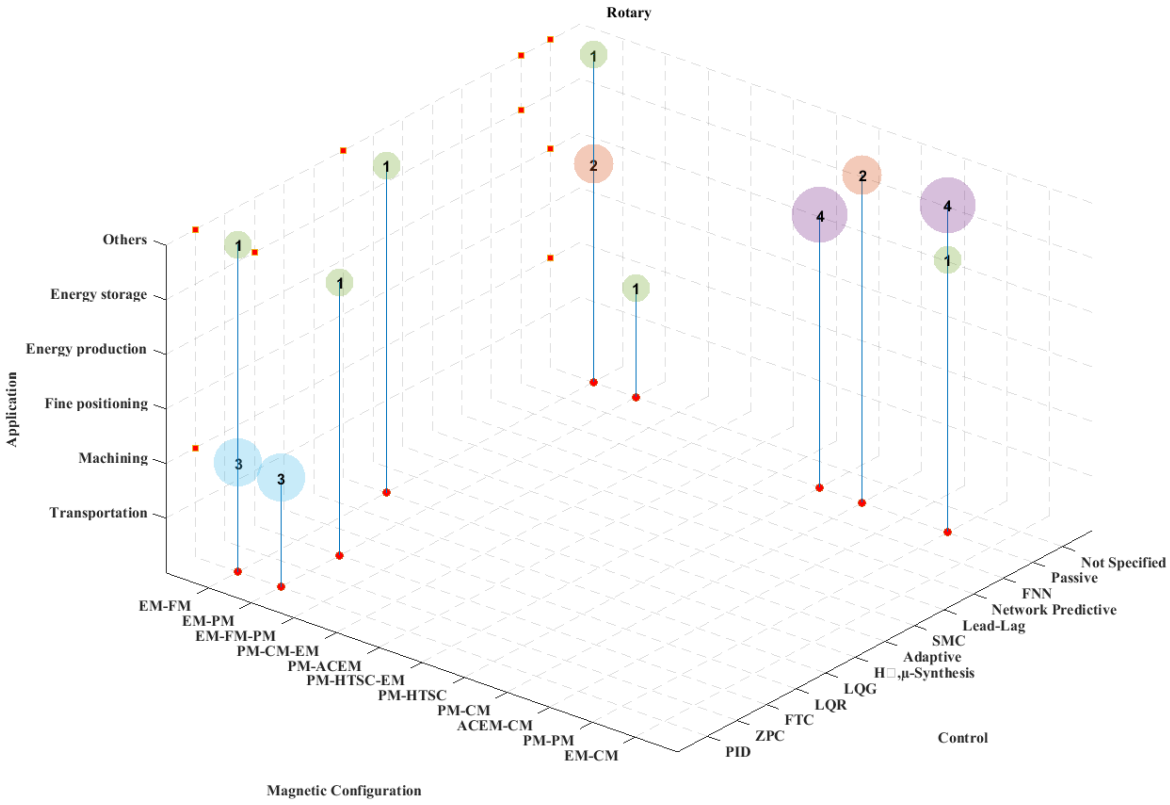

Fig. 3.20. Rotary Magnetic Bearings classification: Application, magnetic configuration and control

In Figure 3.21 applications using EDS (PM-PM, PM-CM, PM-HTSC) configurations are mainly energy storage with passive or no control system (see figure 3.22). Passive Magnetic Bearings are used generally because this comes as a solution for energy efficiency. Nonetheless the consumption of energy by the cooling devices, in HTSC systems could decrease the energy efficiency and reliability of the overall system.

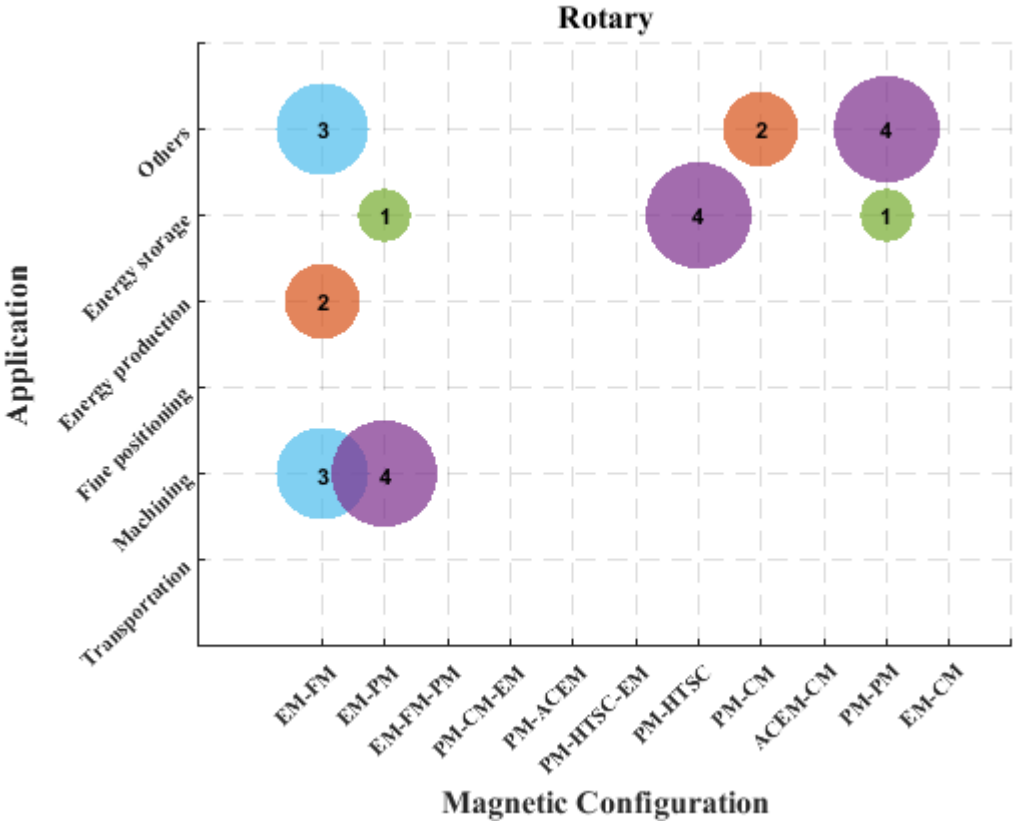

Fig. 3.21. Rotary Magnetic Bearings classification: Application-magnetic configuration

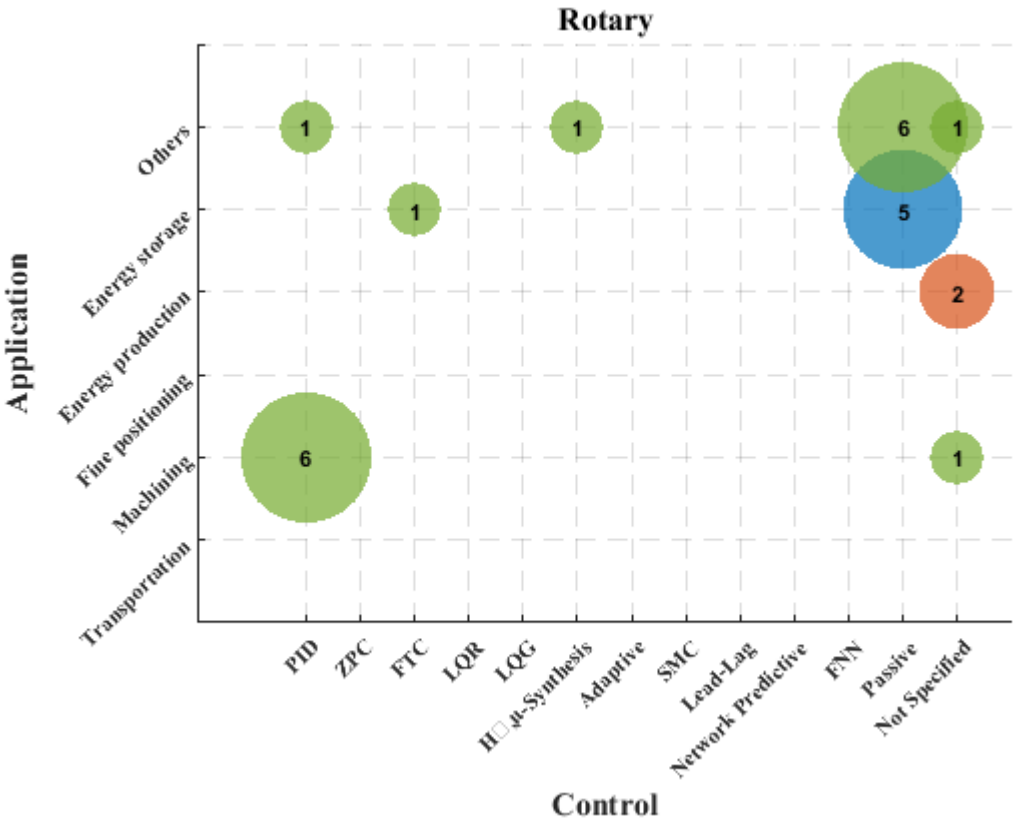

Fig. 3.22. Rotary Magnetic Bearings classification: Application-control

3.2.4.2 Linear configuration:

The previously mentioned “Father of MagLev”, Eric Laithwaite, presented his review on linear electric machines in1975 [94]. Although he mentions that at that point most of the designs were induction machines he also listed various topologies different in shape, material combination, and applications. Since then, magnetic levitation devices have evolved. This section will classify linear magnetic levitation cases found during the literature review that correspond to more recent developments.

Figure 3.23 indicates the different linear configurations currently in use. EMS can be seen in the top and middle illustration (a and b) and HMS adding permanent magnets to the magnetic circuit can be seen in c). Both of the examples are taken from a MagLev transportation application[95], [96].

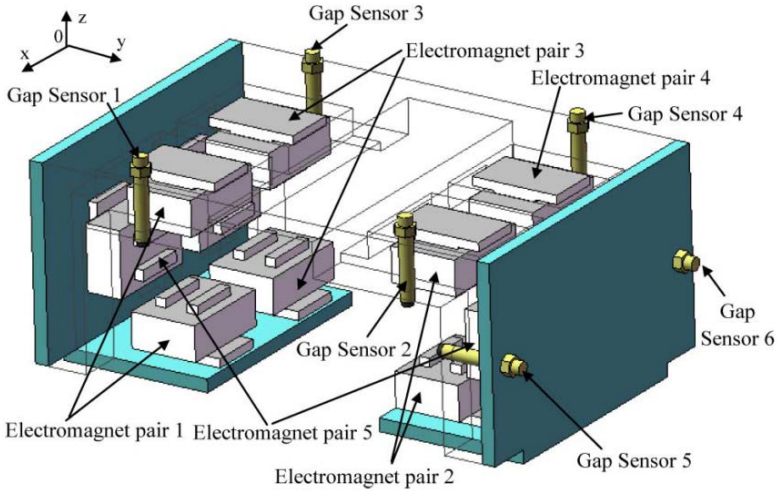

a)

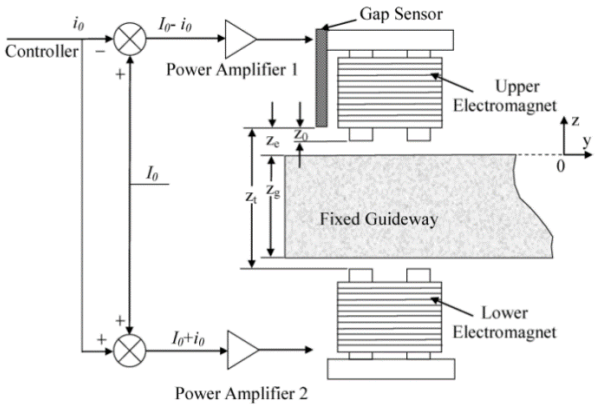

b)

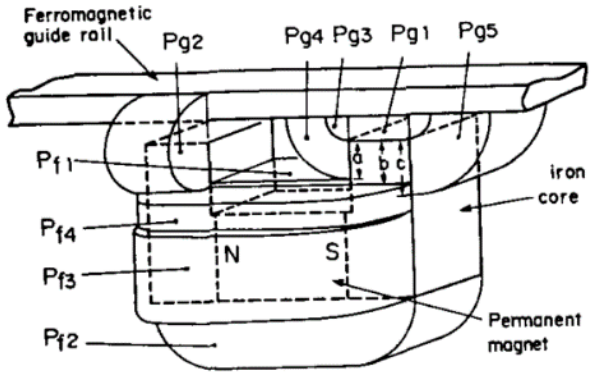

c)

Fig. 3.23. Linear Magnetic Bearings:a-b) EMS; c)HMS

A classic case of EDS composed of PM-HTSC is presented in Fig.3.24 at the top part of the picture a) [97]. A different type of EDS is on the middle part b)where the

permanent magnet arrangement over a conductor circuit creates repulsive forces [98]. Additionally in c) the oscillation of a magnetic field over a conductor material generates repulsion. In this case AC current generates repulsion against a conductor material self-centring the translator[99].

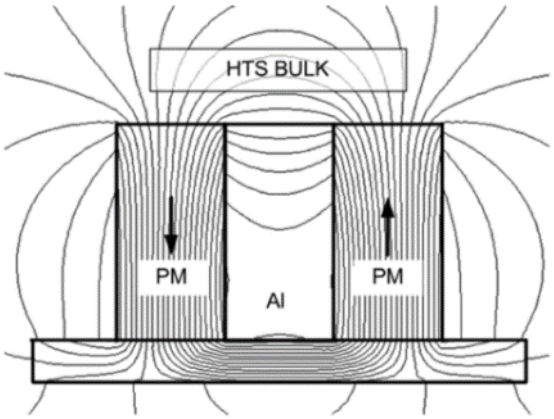

a)

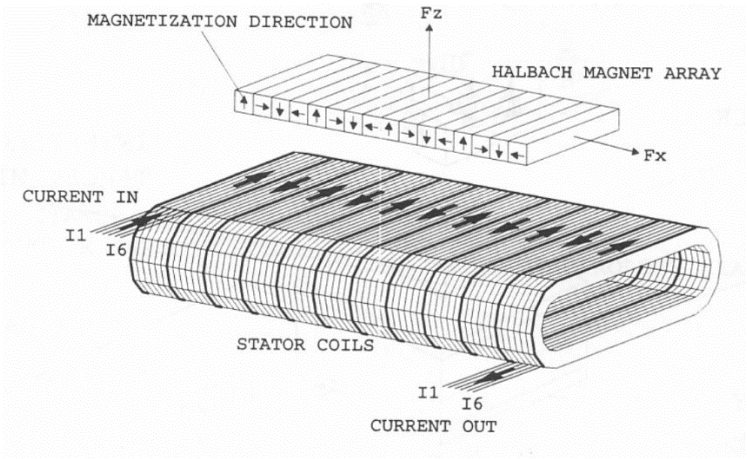

b)

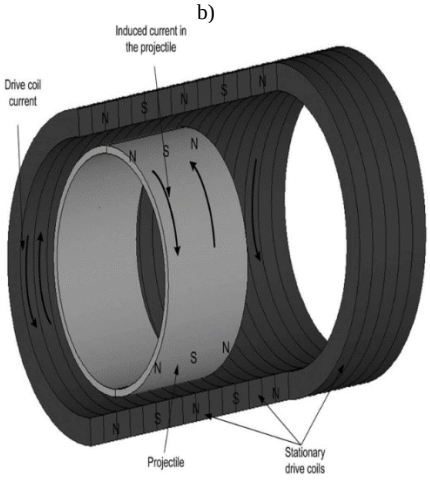

c)

Fig. 3.24. Linear Magnetic Bearings: EDS linear applications.a)PM-HTSC; b) PM-CM ; c) ACEM- CM

Applications

Linear magnetic bearing applications are design to mitigate effects like vibrations, to improve overall efficiency and precision just like rotary magnetic bearings.

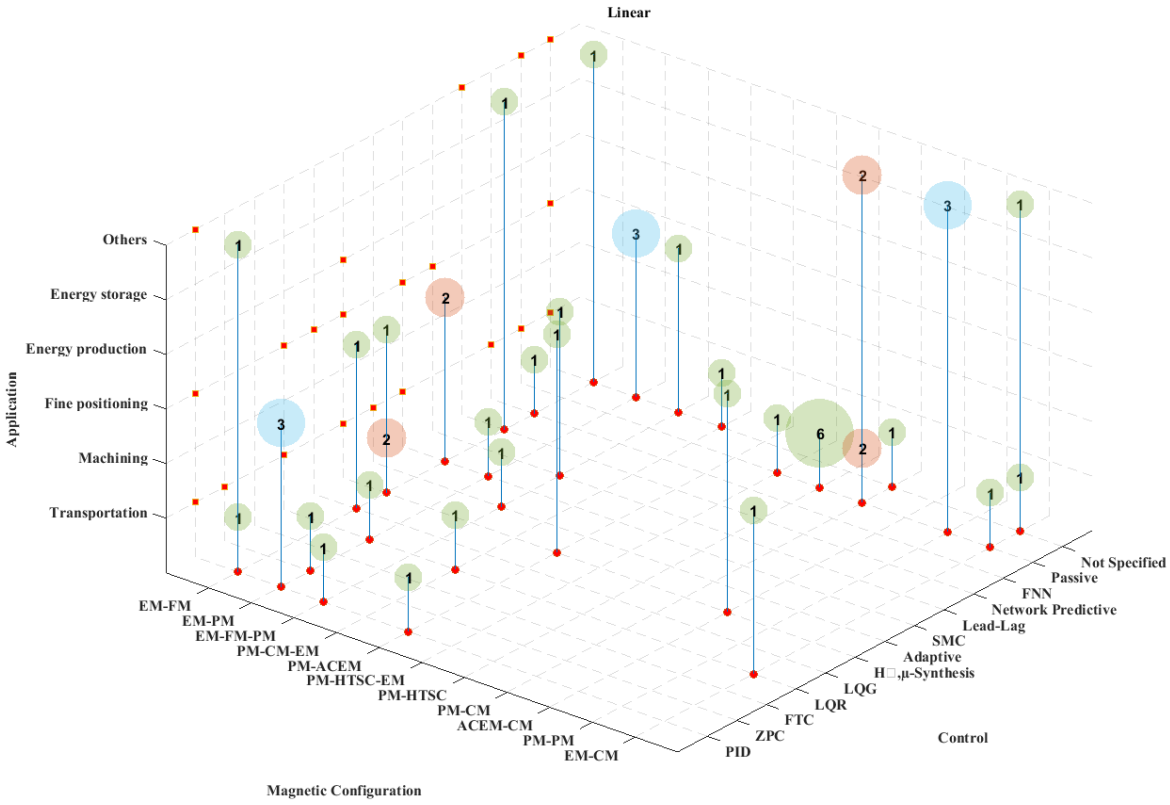

Fig. 3.25. Linear Magnetic Bearings classification: Application, magnetic configuration and control

Besides transportation, another popular application is ultra-fine positioning. Again, different configurations are presented, Electromagnets (EM) [100] [101], PM-EM [102] [103] [104] [105] [106] [107] [108] and PM-Halbach array-EM [109] [110] [111]. These applications rely more on EMS because they intrinsically need active control.

Some other examples of less widespread applications are linear generators [40][112], force measuring MEMS devices [113], conveyor transportation [114], lift systems[115] [116], photolithography[117], and control strategies experimentation[118] [119]. These applications are grouped under “others”.

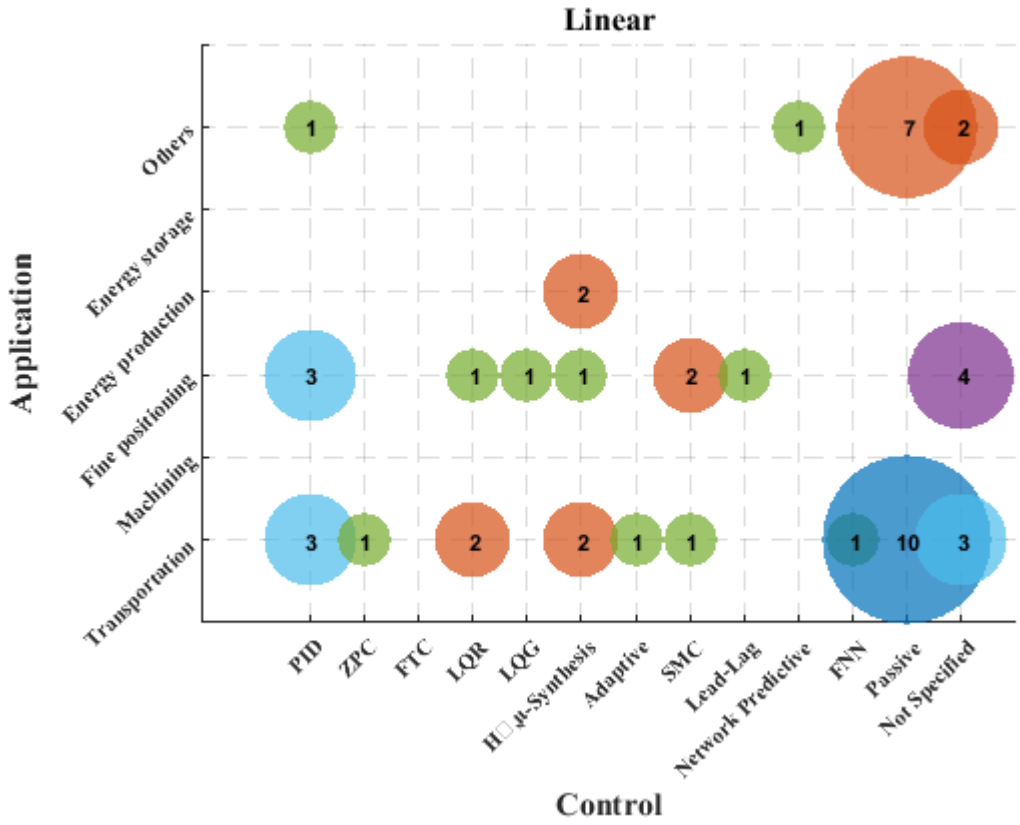

Fig. 3.26. Linear Magnetic Bearings classification: Application, magnetic configuration and control

Figure 3.26 shows a high concentration of passive systems in transportation, this can be matched to the use of HTSC and other kinds of passive systems using EDS in Figure 3.27. Also in figure 3.26 the most common control strategy is PID control, similar to rotary applications, although it is thought to be due to the simplicity of implementation. Many authors have noted the need for robust control strategies in magnetic levitation systems and consequently a large number of these kinds of systems can be observed. The result of this literature review highlights that strategies such as sliding mode control (SMC) and H_∞, μ-synthesis can be found in this area of research. The advantages and disadvantages of the different control strategies are covered in section 3.4.

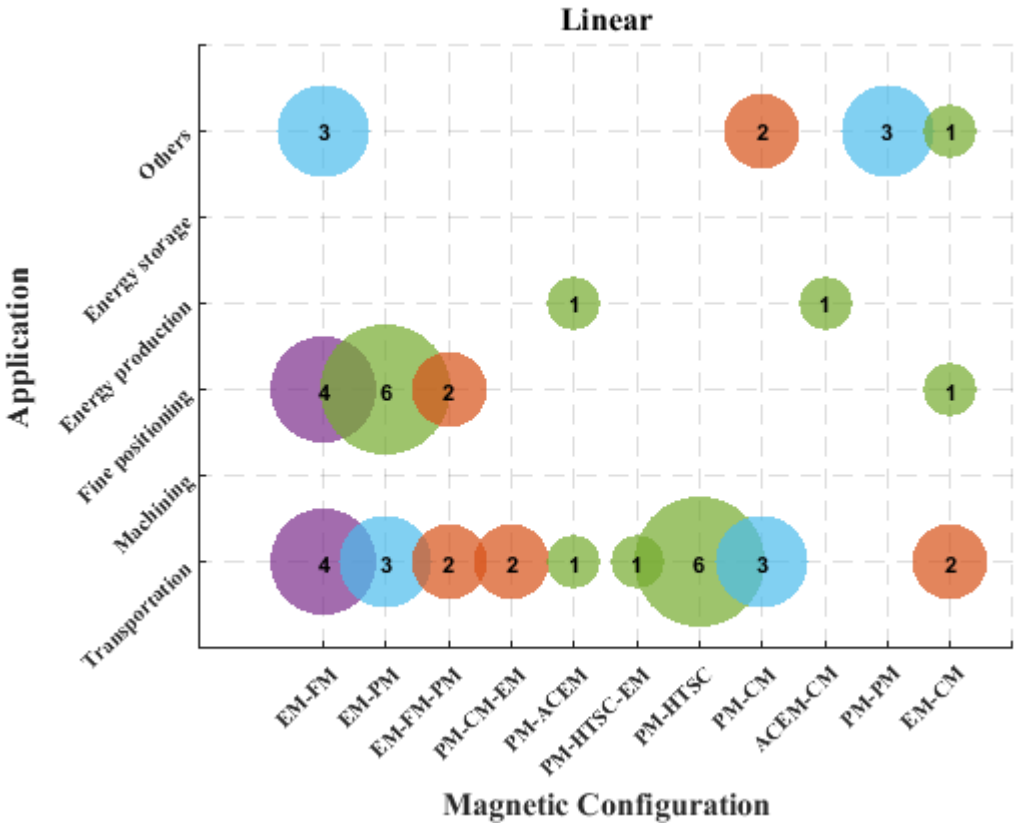

Fig. 3.27. Linear Magnetic Bearings classification: Application-magnetic configuration

MagLev Trains

One of the most popular linear magnetic bearing applications is MagLev trains as can be seen in Figures 3.26 and 3.27. MagLev systems have been highlighted as a new option for mass-transportation, offering the following advantages over traditional train systems:

- Reduction of maintenance cost, due to the lack of wheel and track wear.
- Reduction of the guide way construction cost.
- Due to the guide way design, MagLev train is highly improbable to derail.
- The absence of contact and parts diminishes the amount of noise and vibration.
- No sliding and slipping during operation.
- Greater range of acceleration.

- Less affected by weather conditions[64].

Despite the benefits mentioned there are only a few systems open to the public, such as “The Transrapid” in Shanghai in operation since 2003, the HSST in Nagoya opened in 2005[64] and the Daejeon demonstration line which opened in 2008 in Korea [120]. However, due to the difficulties presented in the switching and branching, as well as the capacity of the electromagnets needed for lifting large loads this medium of transportation is still not suitable for freight.

While companies like Transrapid use configurations such as EMS or HEMS, similar to ones presented in [95] [96] [77], [121], [122], other researchers are more focused on EDS, [97] [123] [124] [125] [68] and specifically on the interaction of HTSC and different kinds and configurations of PM. This last configuration (HTSC-PM) needs a special cryogenic system, with some examples shown in Figure 3.28.

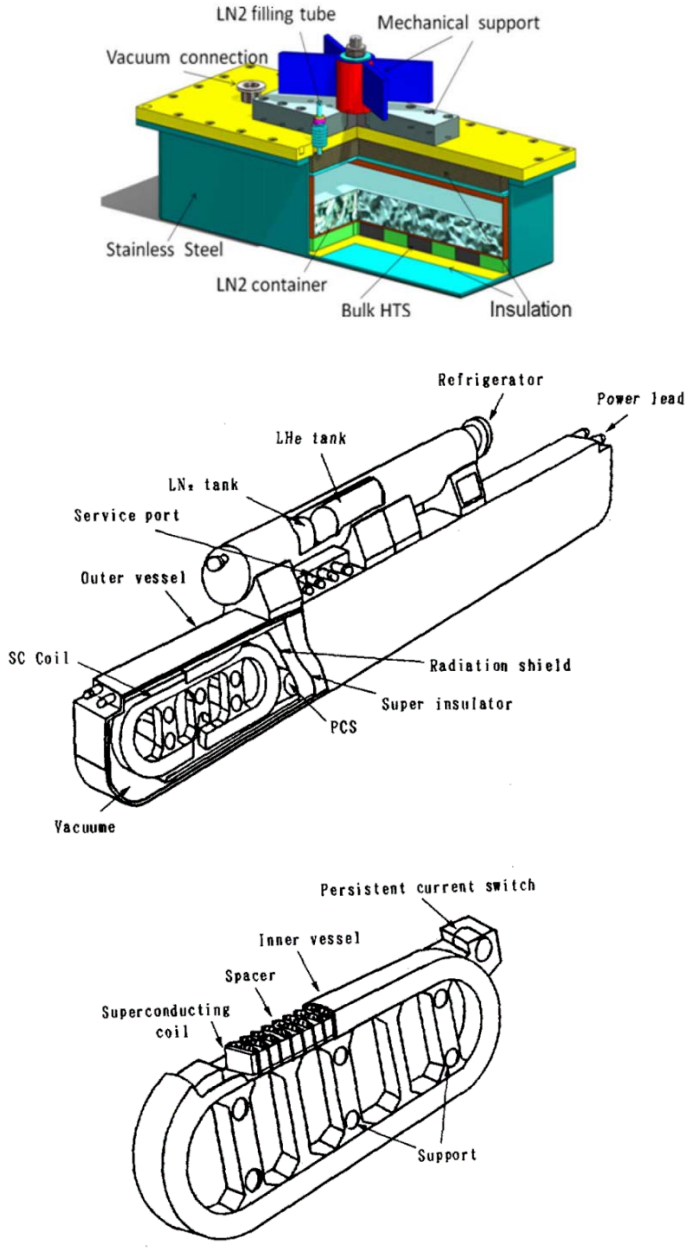

Fig. 3.28. Cryogenic cooling devices

Although HTS are highly efficient once they are in “working conditions”, cooling systems need to recharge nitrogen to function. Some researchers declare that some cryogenic devices can operate 20-24 hours between nitrogen recharges[63], making this attractive for locations where the infrastructure for cooling fluid can be installed.

As stated previously there are some concepts for current induction levitation EDS systems. A topology for levitation due to current induction is presented in [99] and

[126], where using the concept of a coil gun [127] or an air-cored coil [128] over a conductive material is presented. This is a concept which some suggest can easily produce levitating and guidance forces. The main problem is heat removal.

Another popular concept using induced current to generate repulsion levitation forces is “Inductrack”[75] (see Figure 3.11) where the use of a Halbach array is used to intensify the magnetic field on one side of the array while having a periodic magnetic field along the same side as well [129] [130]. A more sophisticated design for the track using the same concept is described in [131]. Another instance in which a Permanent Magnet Halbach array is used for levitation involves the use of an Air-cored Halbach array for guiding the levitated carriage [132].

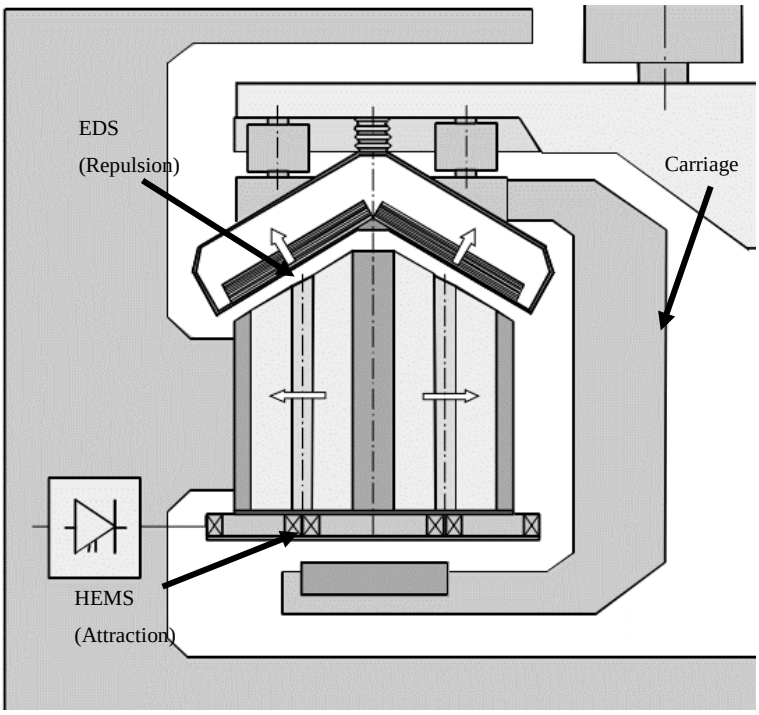

Fig. 3.29. HTSC-EM-PM configurations

Concepts where EMS and EDS are combined can be seen in Figure 3.29 [133]; a combination of HTSC-EM generates repulsion while an EM-PM generates attraction. A roof shaped top HTS interacting stabilises the carriage, whilst an HEMS system is in charge of any extra levitation force needed. Another example [134] uses a PM Halbach array-conductor to generate repulsion and EM to generate attraction (see Figure 3.30).

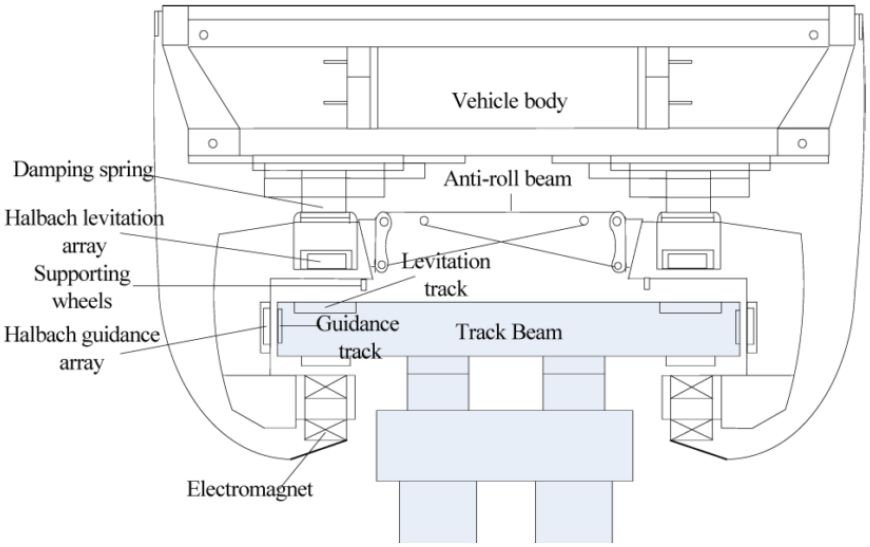

Fig. 3.30. Halbach array PM-Conductor and EM-Ferromagnetic Material configurations

3.3 Modelling & Control

As stated before distinct materials interact differently depending on the configuration of the magnetic bearings. A classic example of an AMB is shown in Figure 3.5, where a current circulating through an electromagnet is controlled in order to maintain a constant gap between the actuator and a ferromagnetic body. However it has been shown previously in section 3.4 that there are several configurations depending upon the application. The following section is aimed at classifying and clarifying the modelling and control of the cases presented.

Modelling

Materials can be modelled in various combinations: PM-PM[73] [74] [81] [135] [136], [137], PM-EM-Ferromagnetic materials[77] [121] [128], PM-Conductor Material [75], PM-Air-cored coil [122], Iron-cored coil-EM-conductor material [126], [138], and PM-HTS [91] [97] [139].

Each one of the configurations performs differently and must be modelled according to their constraints and characteristics. In the same sense, for AMB, control strategies will suit a configuration depending on the degrees of freedom, and the relationship between the floating body and the stator.

Control

On the *Control-Magnetic configuration* Figures 3.31 and 3.32, rotary and linear topologies show a tendency where Passive Magnetic bearings use EDS while EMS and HMS is used by Active Magnetic Bearings. One particular case that might seem odd is the use of electromagnet-conductor material combination using passive control on figure 3.28. This is not entirely passive but since the configuration of the system allows it to self-centre itself there is no need for position control of the translator. However there is a control system for the velocity of the moving part in the system [99].

From the same figures it can be noted that the majority of documents reviewed in this work use PID control. It is thought that this is due to its simplicity, although this control might not fulfil the practical implementation requirements.

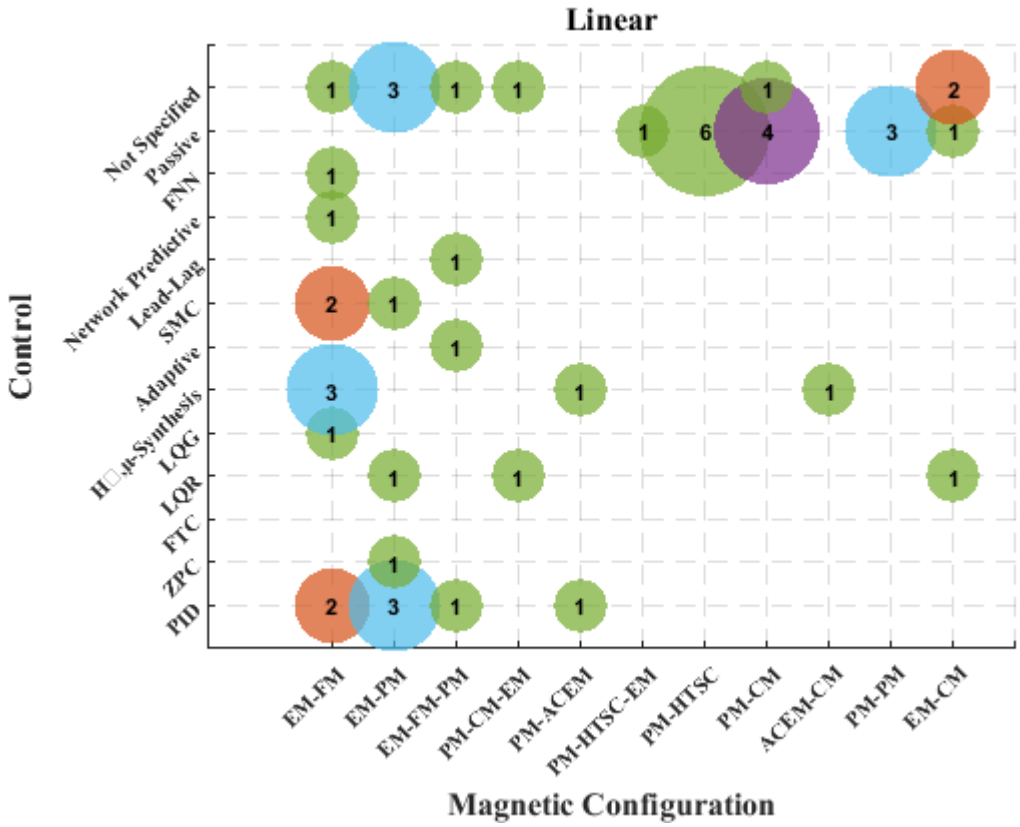

Fig. 3.31. Linear Magnetic Bearings classification: Control-magnetic configuration

In magnetic levitation systems most of the suspension controls are non-linear Multi Input Multi Output (MIMO) systems which require robust control strategies. SMC[140][141][142][143][144][119][122], H∞,μ-Synthesis[145][146], Fuzzy Neural Networks[147], Network predictive control[118], LQG[100],LQR[117], Adaptive control, Zero Power control [96], Fault Tolerant Control[90], are control strategies found in the literature that are suitable for AMB.

For linear maglev applications, SMC and H∞, μ-Synthesis appear to be the two most popular options, because of their robust characteristics. In [148] an experimental device performance is compared using PID, SMC and H∞,μ-Synthesis. The result indicates that even if SMC is robust and superior to PID, H∞ is the best controller to deal with disturbance.

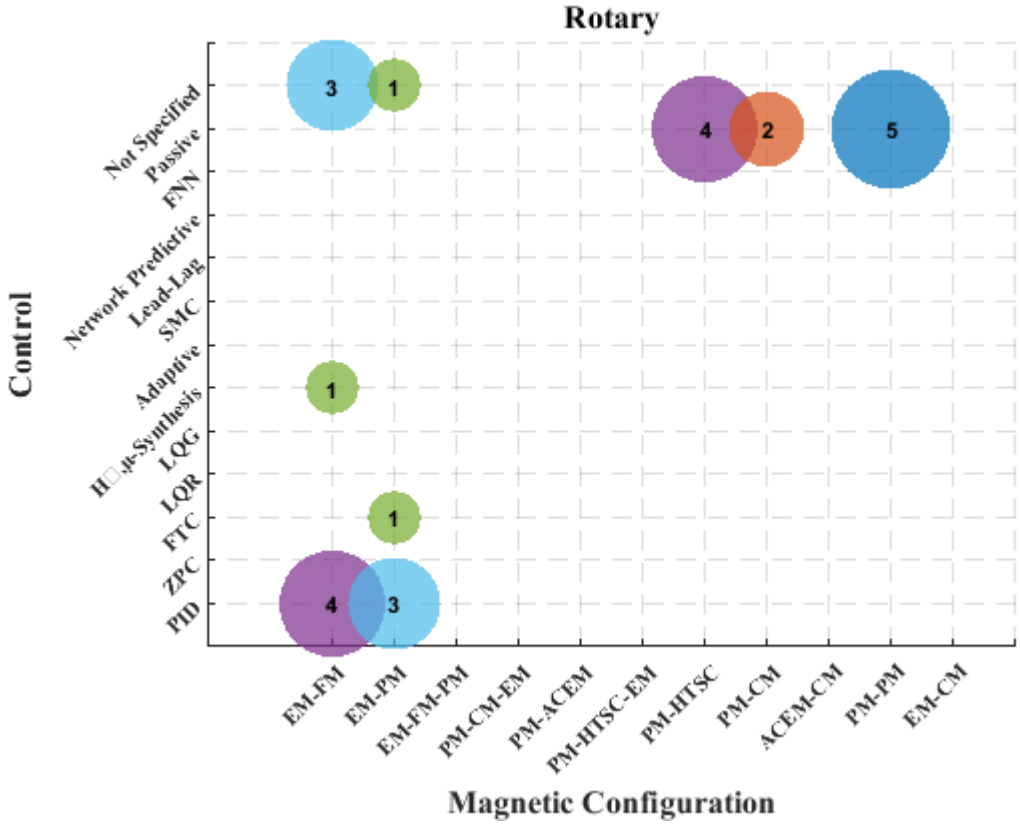

Fig. 3.32. Rotary Magnetic Bearings classification: Control-magnetic configuration

SMC and H∞ and μ-Synthesis have been tested in other applications such as autonomous underwater vehicles and industrial boiler [149], [150]. It can be

highlighted that H_∞, μ-Synthesis is more adept at dealing with uncertainties and faster than SMC, but at the same time less precise.

Some of these configurations combine different control strategies like neural networks-SMC-PID[144], PID-SMC[115], or adaptive SMC[151] in order to have better performance. In addition, improvements such as sensor-less systems [152] and sensor optimization[153], in theory will result in a more robust and reliable system resulting in a more compact, simple AMB mechatronic device according to [50], although bear in mind that in [154] the author mentions that the performance limitations are still being proved.

3.4 Conclusion

An overview of different material combinations, as well as applications, modelling and control of magnetic bearings has been covered in this section.

The most widespread application for rotary magnetic bearings is in flywheels and high speed machining, whilst transportation and ultra-fine positioning are the most common for linear magnetic bearings.

Applications like high speed machining and ultra-fine positioning need robust control strategies to avoid collisions and required high stiffness over a wide range of operation conditions such as velocity, acceleration, position, etc.

On the other hand passive magnetic levitation systems might be used whenever the operational conditions of the materials involved, such as velocity or temperature, generate high stiffness and stability. As well, although this can be argued, many authors highlight advantages of PMB over AMB, such as low consumption of energy, and high reliability.

Designers must bear in mind that the selection of materials will affect the behaviour of the entire system, not just the application, but the control, reliability and overall price of the device will be affected by the optimal design and selection of the mechatronic device. Hopefully the future market and manufacture of both NdFeB magnets and HTSC will develop to an appropriate level in order to compete with more common kind of materials found in electromagnetic bearings.

It can be concluded that there is currently no general optimal design or configuration for magnetic bearings, therefore studies into costs and reliability in addition to future control systems must be carried as a specific process for each case and application.

The next chapter shows different concepts and simulations in order to come up with a design suitable for linear C-GEN wave energy converters.

4 Alternative concepts explored during research work

During the first phase of the research a number of bearing concepts were investigated and compared. The bearing concepts studied were restricted to active magnetic bearings.

4.1 New Concepts for AMB in Linear WEC's

Three concepts were presented at the EWTEC 2013 conference[40], with the intention of finding a solution for the linear bearings problem stated in chapter 3. The requirements for the concepts were based on the previous work of Sarah Caraher on novel polymer bearings applied on linear generators[155]. The concept must overcome the forces at a range of velocities from 0.5-2.2 m/s, without adding excessive dragging forces affecting the operation of the wave energy converter.

4.1.1 Eddy Current Levitation

The first concept tries to make the most from the principle of eddy currents generated when a magnetic field is changed over an electrical conductor material. This phenomenon can be observed when a permanent magnet moves close to a conducting material (Aluminium plate, copper pipe, etc.). By Lenz's law the induced eddy currents will generate a magnetic field oppose to the permanent magnet field.

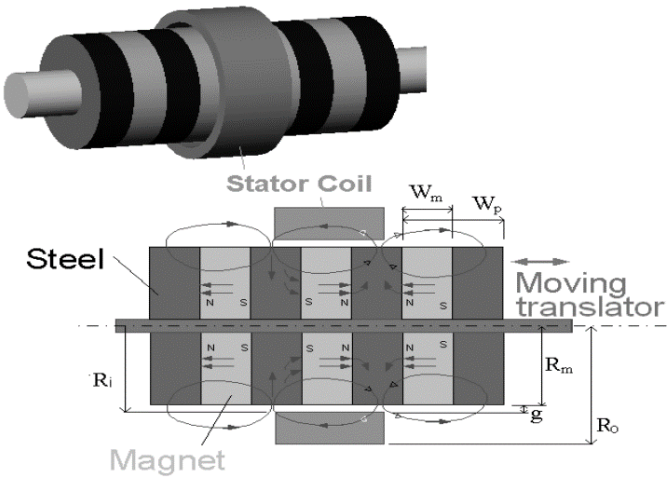

Fig. 4.1. Air-cored Permanent magnet tubular machine.

The concept is presented in Figure 4.2 which is based on the tubular linear generator presented in [38](see figure 4.1). The details of the concept can be seen in Figure 4.3. A conductor material layer was added between the permanent magnet and the air-cored coils.

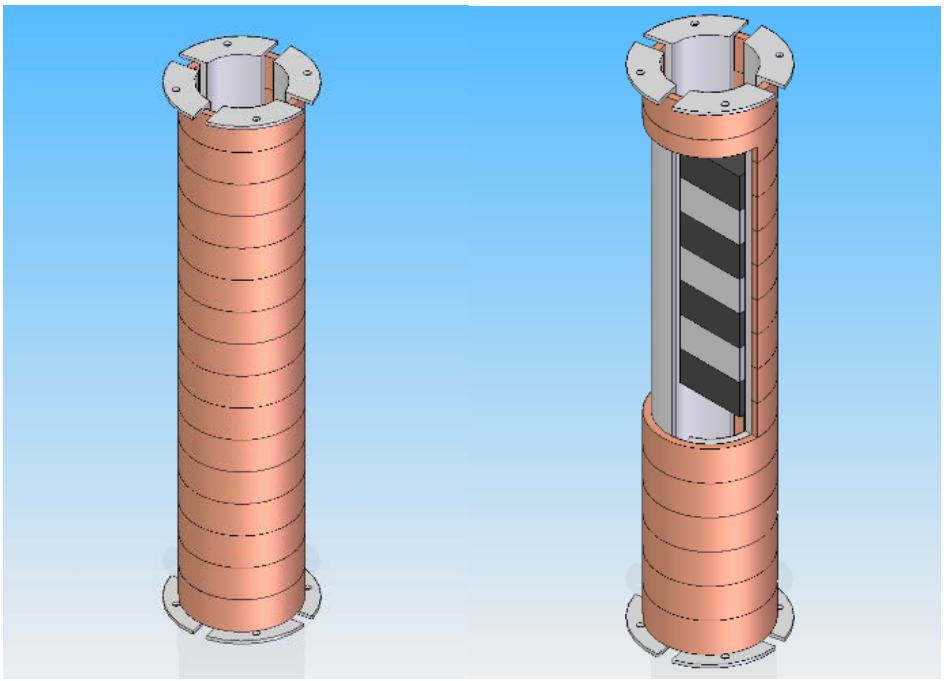

Fig. 4.2. Isometric view of the concept ““Eddy Current Levitation System for tubular PM Generator”

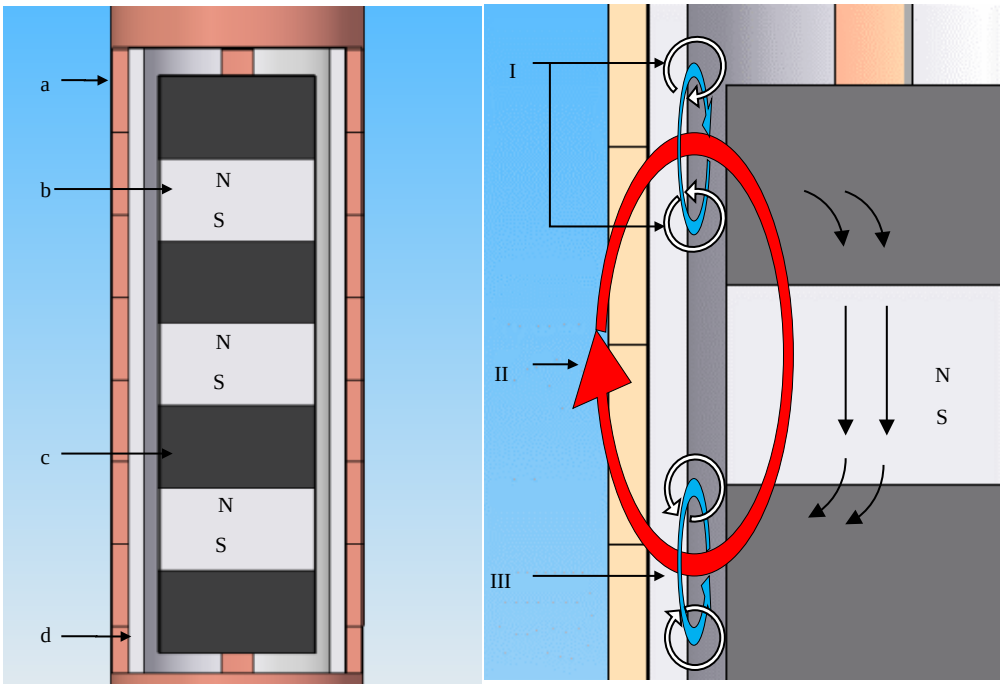

Fig. 4.3. Detail of the "Eddy Current Levitation System for tubular PM Generator". Left hand side: a) Coils; b) magnets; c) Steel; d) conductive material plate (Aluminium). Right hand side: I) Secondary magnetic field; II) Primary Magnetic field; III) Eddy Currents.

In any concept inducing a current on a conductor produces lift and dragging forces dependent on the velocity of the translator or more precisely the frequency of alternating magnetic field [156][126][157]. Examples of this behaviour are presented in figure 4.4. Thus the design must supply enough lifting forcess for the speed of operation without adding excessive amount of dragging force.

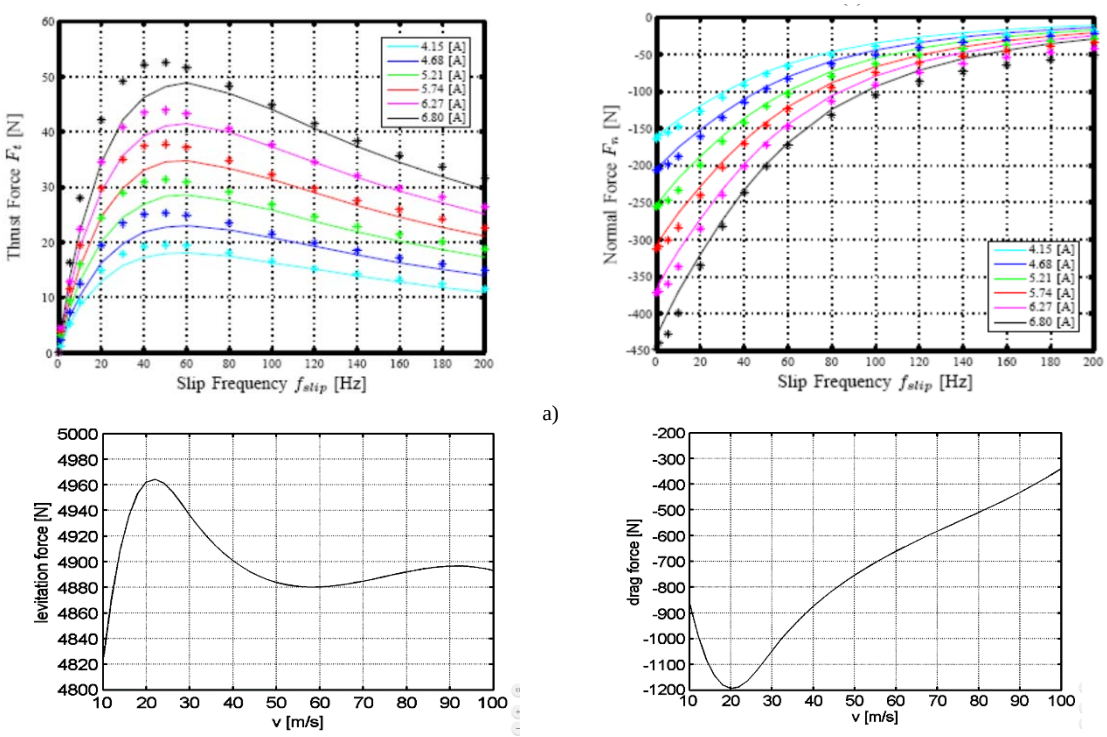

Fig. 4.4. a)linear induction motor lifting(normal) and dragging force from a linear induction motor[126]; b) lifting and dragging forces from a new passive maglev system[157].

4.1.2 Opposite Halbach array for a tubular PM generator

Another design presented at the EWTEC 2013 conference is shown in Figure 4.5 and 4.6. In this design two Halbach arrays are assembled together. An enhanced magnetic field part of a large array is faced towards air-cored coils in order to have the same energy production as the design proposed in [75]. An inner Halbach array in combination with short-circuited rings in the centre of the device is proposed. This inner array generates self-centring forces mimicking the concept from “Inductrack” [130], replacing the flat track by the previously mentioned rings. The arrays would be held together if the diminished magnetic field in both groups link as can be seen in Figure 4.6.

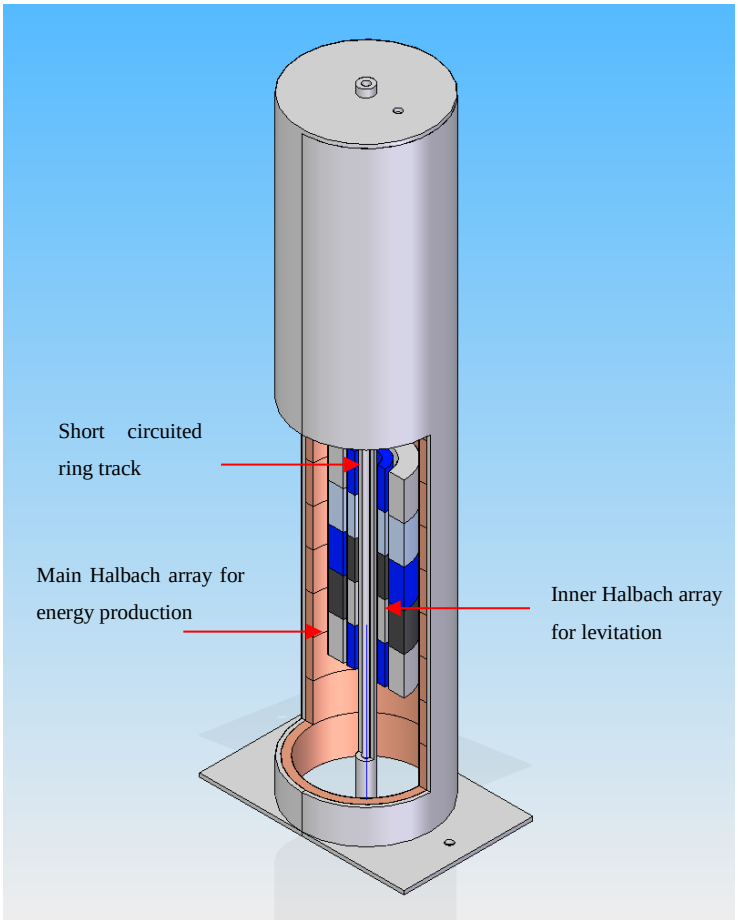

Fig. 4.5. Isometric view of the concept "Opposite Halbach arrays for tubular PM generator".

Figure 4.6 shows the detail of the concept where the enhanced magnetic field is highlighted in red whilst the diminished magnetic field is coloured in yellow. The direction of the magnets in the Halbach array is shown as red arrows.

Similar to the previous concept this design presents a transition speed (Lift/Drag Forces =1) dependant on the design of the permanent magnet array and the track. Although this concept would generate higher lifting forces from lower speeds than the previous concept, the manufacturing and assembly process increases in complexity and cost, due to the difficulty in manufacturing the centre rings and assembling the Halbach array.

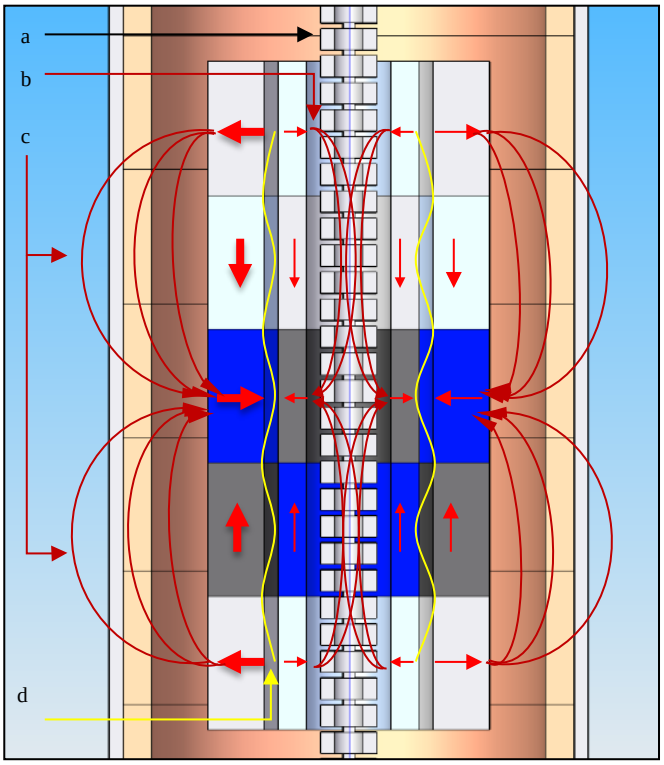

Fig. 4.6 Details of the concept “Opposite Halbach arrays for tubular PM generator”. a) Guide bar: consecutive short-circuited rings; b) Levitation main magnetic field; c) Main Magnetic field; d) Opposite secondary magnetic field

4.1.3 MB for C-GEN linear generator

Finally an active magnetic bearing system for an air-cored C-Gen linear generator is proposed due to complex loads in various directions present in wave energy converters. Hence an actuator that can react in two directions is desirable. The device must change the magnetization in the electromagnets by varying the current in the coils. The first attempt to have a design of an active magnetic bearing is shown in figure 4.7. The 1kW C-Gen generator based in Sarah Caraher prototype[155].

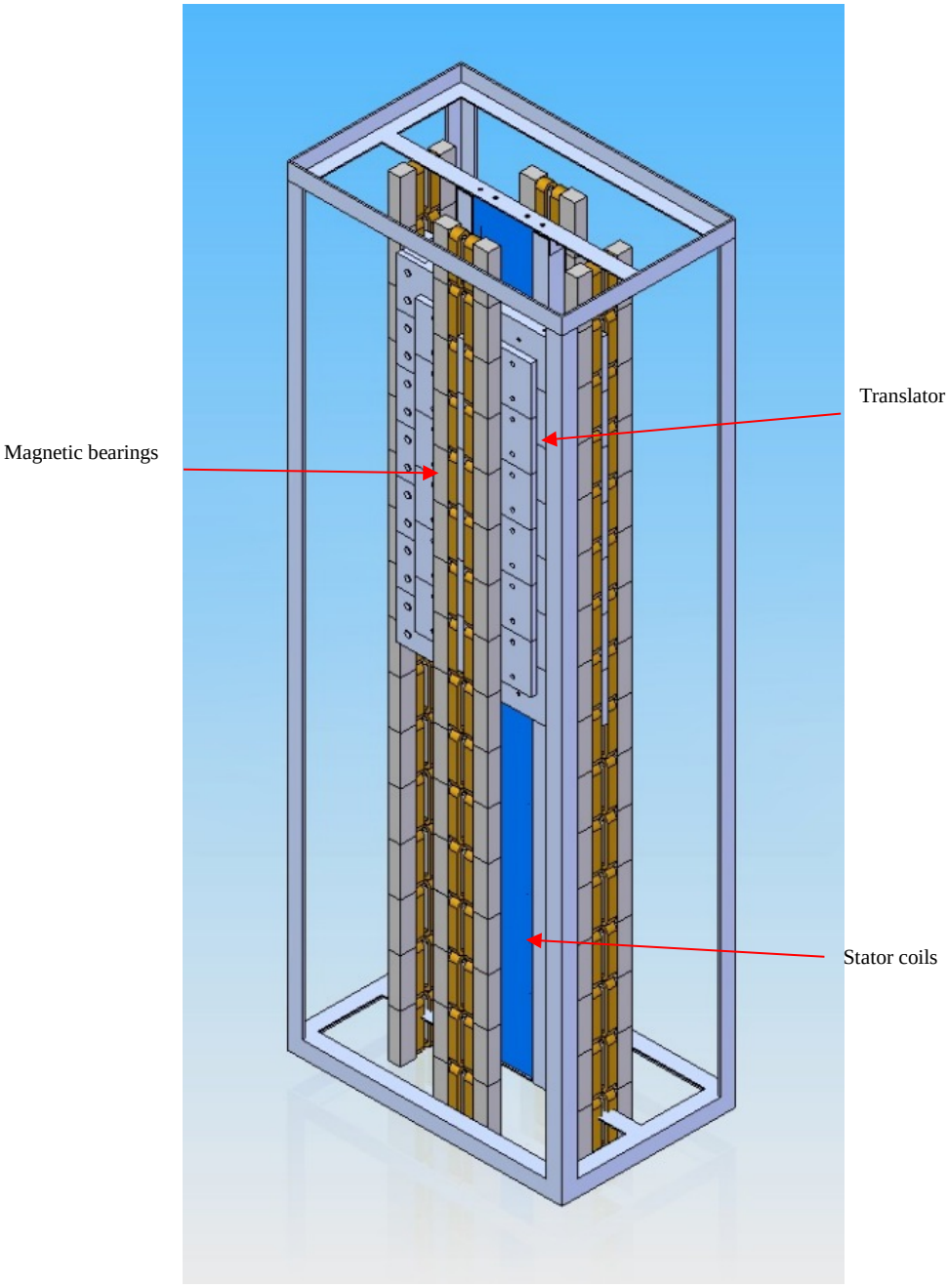

Fig. 4.7 Isometric view of the C-GEN AMB concept: a) Translator; b) Stator (Air-cored coils)

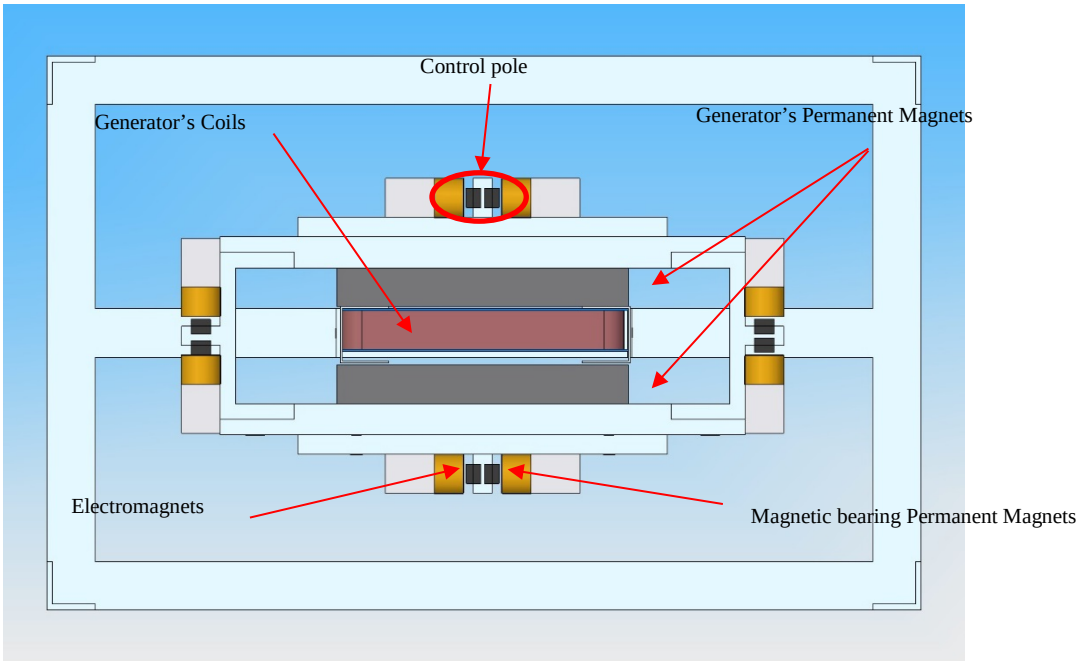

Fig. 4.8 Top view. C-Gen with HMS magnetic bearings.

Figure 4.8 shows the top view of the generator and magnetic bearings. In this proposal the magnetic bearings are a combination of electromagnets and permanent magnets (hybrid electromagnetic suspension). The permanent magnets are added to the translator in order to increase the lifting forces generated between the translator and stator. The area of the device where the magnetic levitation is taking place is called the "control pole" in this document.

This magnetic configuration can generate repulsion or attraction forces by varying the current in the electromagnets. Also the forces generated in this design are not dependant on the velocity of the translator.

4.2 Concepts Comparison

As previously mentioned the generator would be located within the marine environment and would operate at velocities ranging from 0.5-2.2 m/s [155]. Concepts where velocity are crucial for the operation of the device must be eliminated. A summary of the characteristics and limitations of the three concepts explained in the previous section is presented in TABLE 4- I.

TABLE 4-I
GENERAL COMPARISON OF CONCEPTS

Design	Pros	Cons
Eddy Current	-Low consumption of energy. -Easy and cheap solution.	-Not certain about stability and drag forces between parts. -Depends on velocity.
Opposite Halbach	-Low consumption of energy. -Low transitional speed.	-Intensive manufacturing process. -Depends on velocity.
Active Magnetic Bearings	-Active control of different aspect of the system (air gap, stiffness, damping and vibrations). -Non-dependable on velocity. -Condition monitoring, at entire range of velocity.	-Higher initial investment. -More complex hardware and software elements.

From here it is decided to develop the active magnetic bearing option due to the advantages noted in the previous table but mainly because its operation is independent of velocity. It must be kept in mind that initial cost and energy consumption is one of the biggest challenges to overcome, thus optimization tools will be used in the design process of this system.

4.3 AMB for C-GEN Development

After deciding to use active magnetic bearings some experimentation in a 2D open source software named FEMM was done. In order to have a better idea of the magnetic bearing arrangement a simple isometric view of the magnetic bearing CAD model is presented in figure 4.9 and its cutaway view in 4.10.

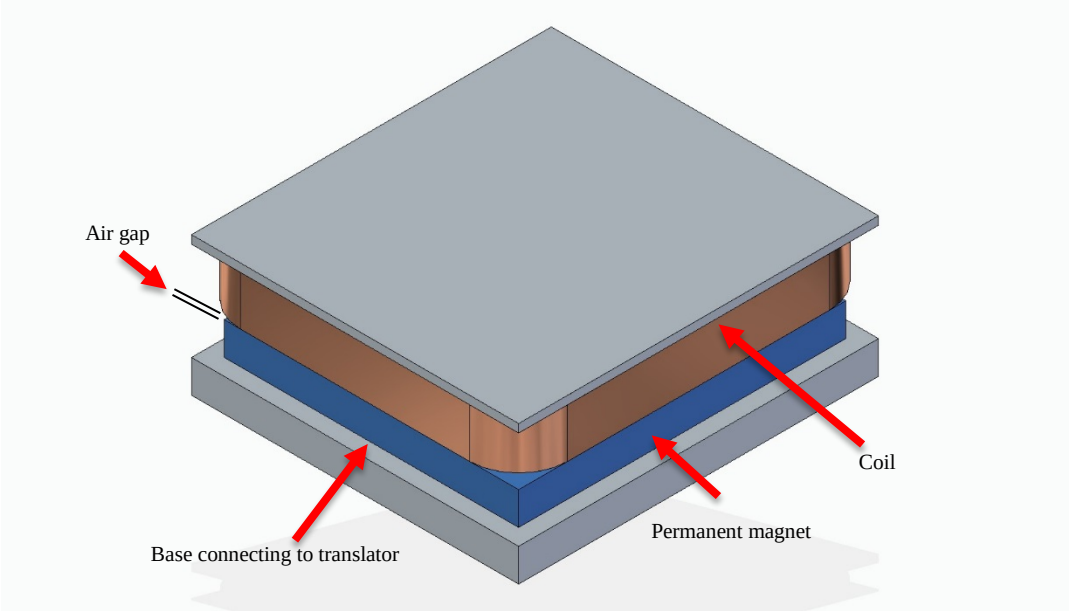

Fig. 4.9 Control Pole simulation CAD

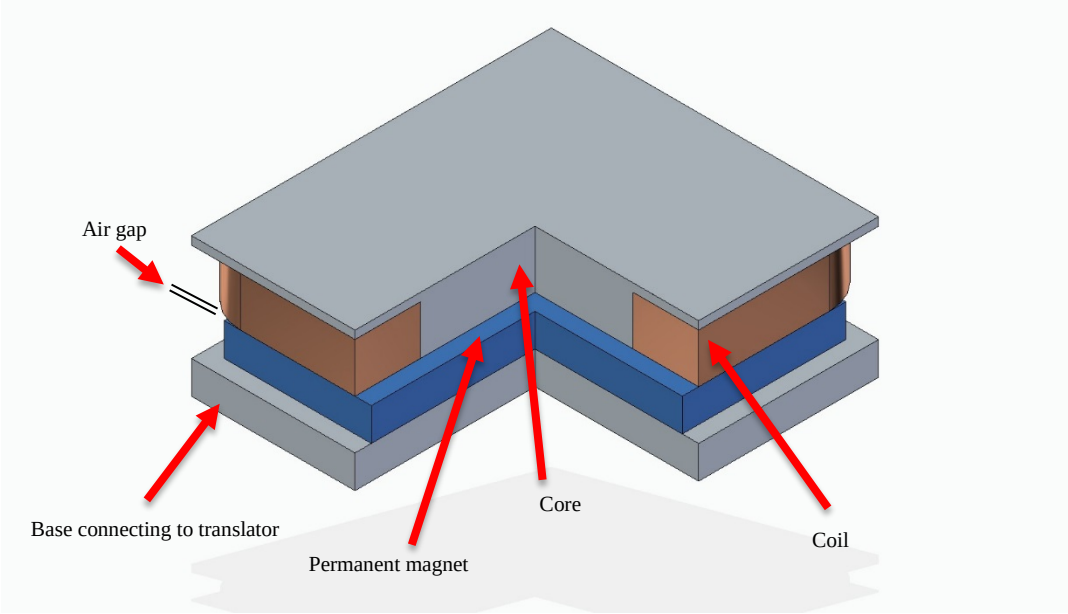

Fig. 4.10 Control pole cutaway view

The electromagnet was changed from iron-cored to coreless (air-cored) in order to study the effect on the force production. A screenshot from these simulations is presented in 4.11 and 4.12.

The active area in the simulations is 0.1m x 0.09m and the thickness of the electromagnets and magnets are shown in figure 4.11. The electromagnet has 190 turns and the configuration was simulated at 0, 30 and -30 amperes. The current was chosen so the 10 AWG calibre wire can operate at around half of its rating.

During testing two main points are being considered, the effect of air cored coils in electromagnets and the use of Halbach array to enhance the magnetic field and its effects on the forces generated.

The distribution of the field produced by the iron cored coil and the magnets and Halbach array are presented in Figure 4.11and Figure 4.12 shows the flux plot for an air-cored coil.

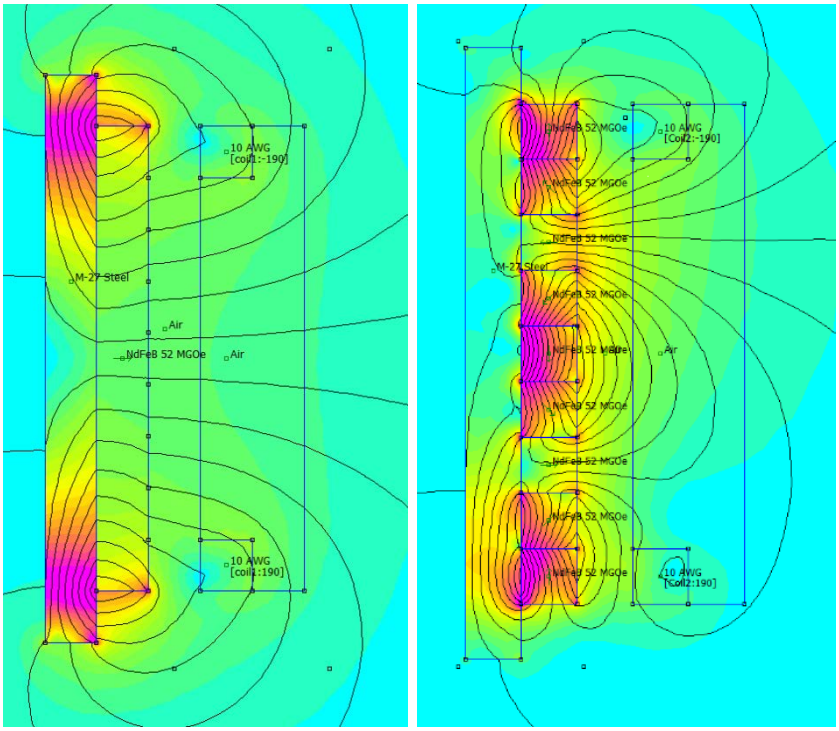

a) b)

Fig. 4.11 FEMM Results: Air-cored a) Permanent Magnet-Electromagnet; b) Halbach Array-Electromagnet

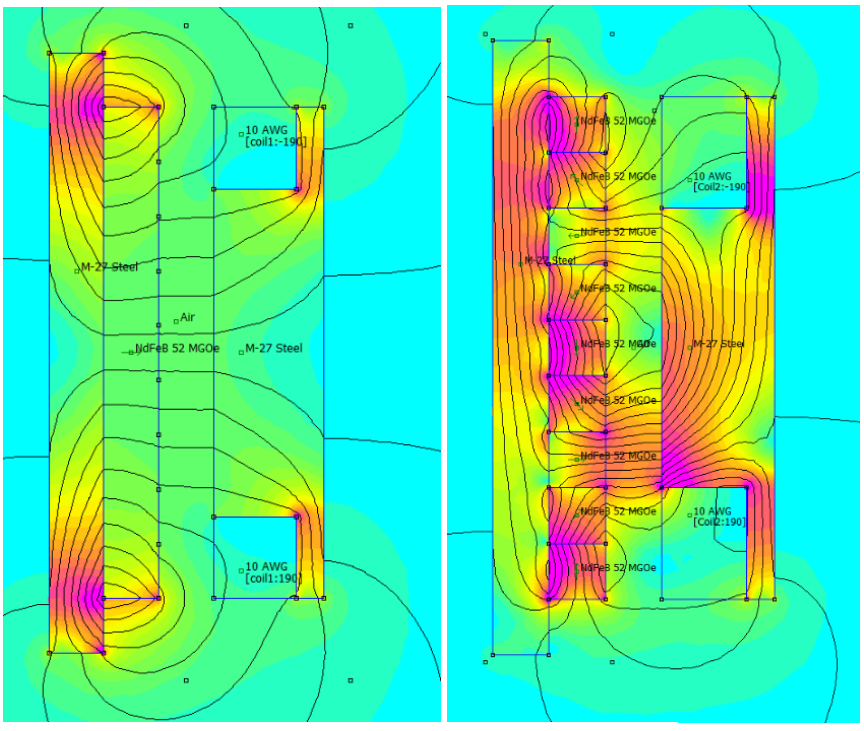

b) b)

Fig. 4.12 FEMM Results: Air-cored a) Permanent Magnet-Electromagnet; b) Halbach Array-Electromagnet

The resulting forces are shown in Figure.4.13. Attraction forces are negative while repulsion forces are represented as positive numbers.

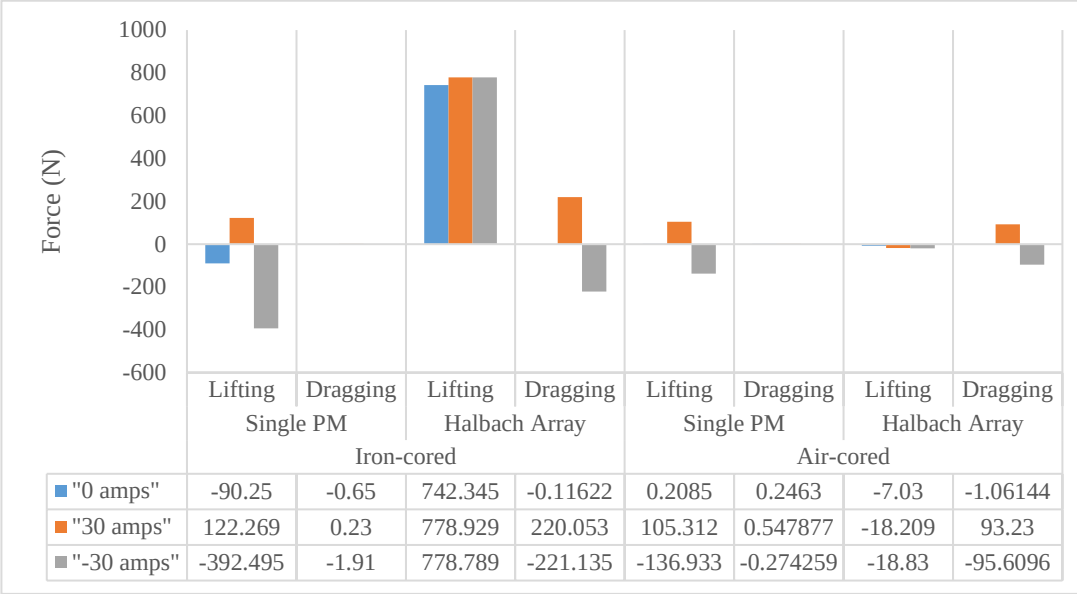

"0 amps"	-90.25	-0.65	742.345	-0.11622	0.2085	0.2463	-7.03	-1.06144
"30 amps"	122.269	0.23	778.929	220.053	105.312	0.547877	-18.209	93.23
"-30 amps"	-392.495	-1.91	778.789	-221.135	-136.933	-0.274259	-18.83	-95.6096

Fig. 4.13 Comparison of Forces with Iron and Air-cored Coils

For the first case of a permanent magnet in combination with Iron-cored electromagnet, the low dragging force is due to the magnetic field lines alignment of the two acting pieces. This doesn't happen with the simulation of a permanent magnet Halbach array facing an iron-cored electromagnet. In this case the magnetic field from the array is not constant along the array, hence the device generates forces on the "y" axis.

On the other hand a single piece of permanent magnet facing an air-cored coil seems to be capable to generate forces in two directions (attraction/repulsion) with small dragging forces. However in the case of the Halbach array-air-cored coil the direction of the force in the "x" axis (lifting) doesn't change when the current changes from 30 to -30 amperes. This is because in this configurations there will be always a part of the Halbach array magnetic field aligned to the magnetic field generated by the electromagnet (or the ferromagnetic material) as soon as both interacting parts are aligned in their geometrical centre.

Thus more experimentation to see how the forces react to the change of position is pursued.

Figure 4.14 describes how the part containing the permanent magnets is moving over a couple of electromagnets (either air-cored of iron-cored). This is with the intention to observe the transition between one magnetic actuator and the next one. The image is rotated 90˚ to illustrate the simulation in a clearer way. Note "*y*" on the horizontal axis and "*x*" on the negative vertical axis.

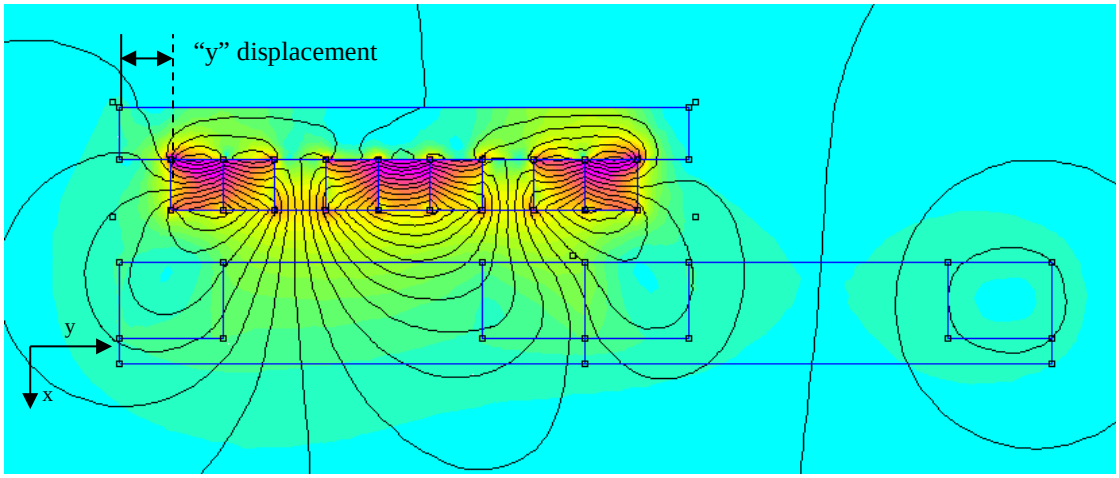

Fig. 4.14 FEMM Results: Iron cored a) Permanent Magnet-Electromagnet; b) Halbach Array-Electromagnet

The same process was made for all the 4 cases mentioned before and the results are shown below in figures 4.15 to 4.18.

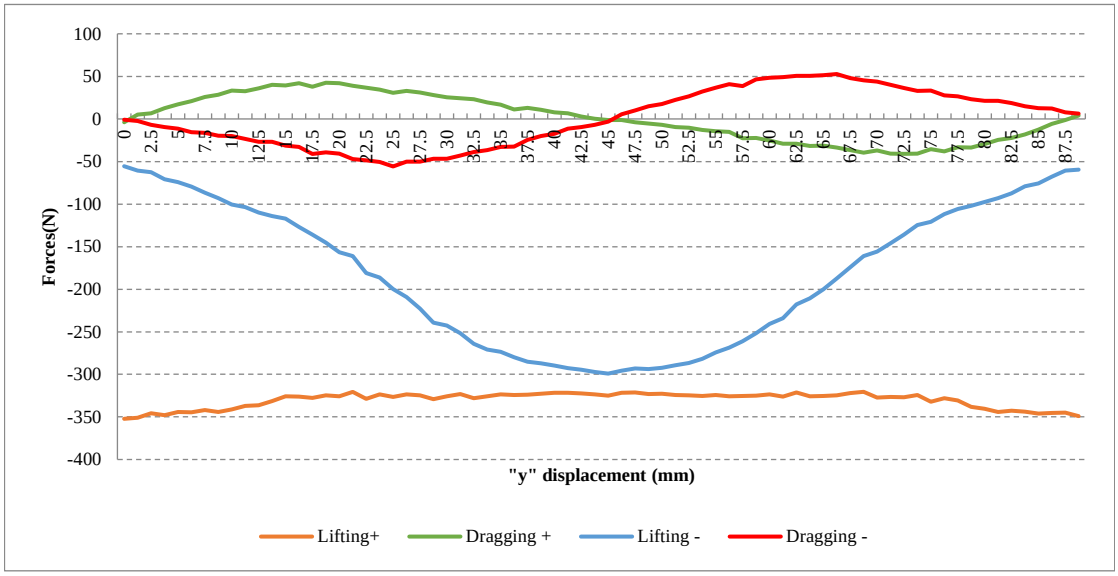

Fig. 4.15 Displacement FEMM Results: Single Permanent magnet facing Iron-cored electromagnet

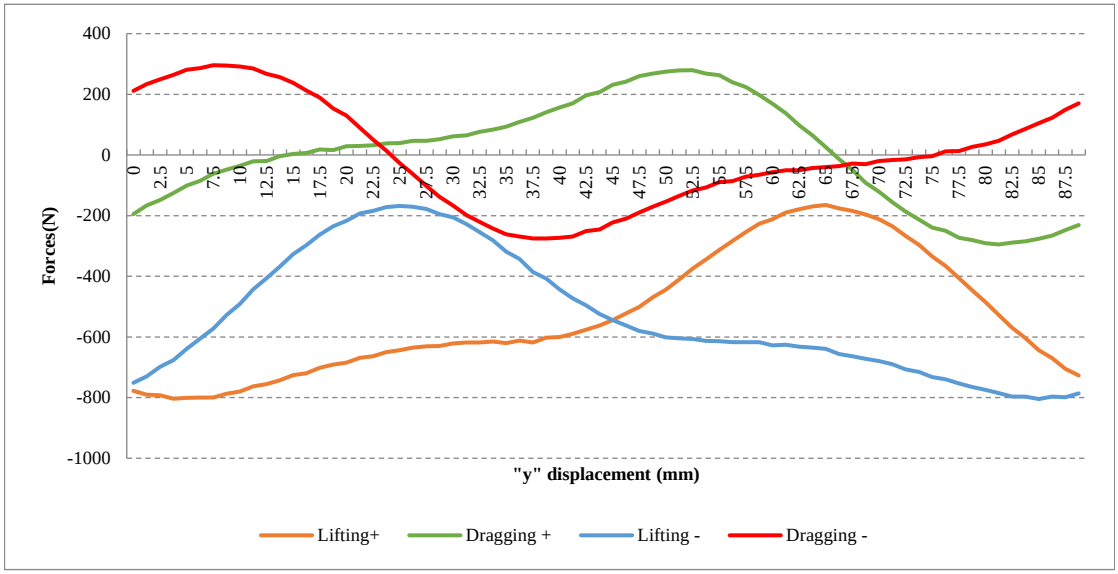

Fig. 4.16 Displacement FEMM Results: Halbach Array facing Iron-cored electromagnet

From the graphs it can be noted that the control poles that contain iron at their core don't change the sense of the forces generated in "x" axis, when the current is changed from 30 amps to -30 amps at any position.

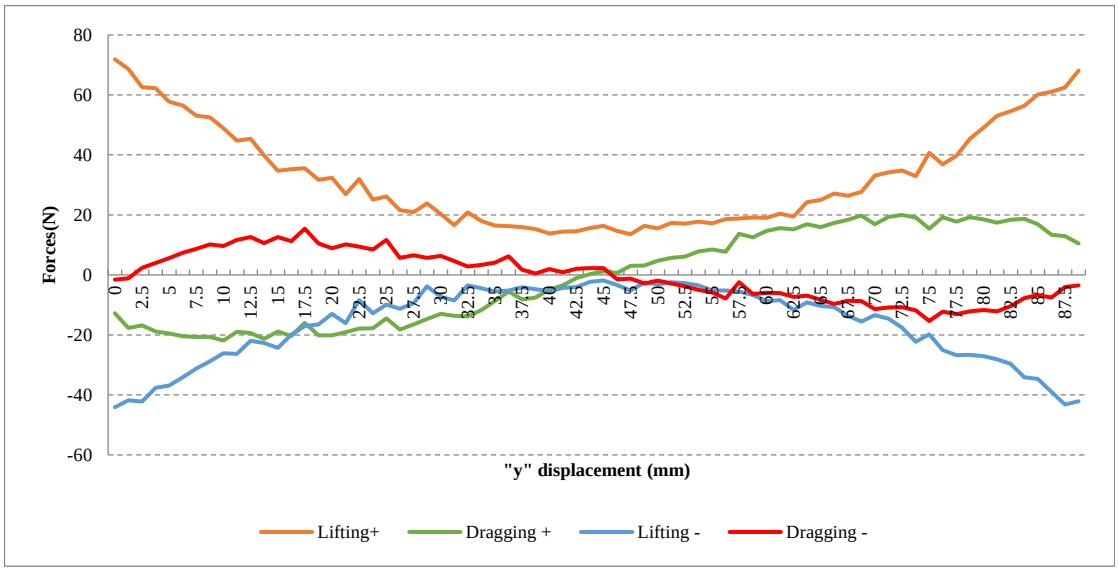

Fig. 4.17 Displacement FEMM Results: Single Permanent magnet facing Air-cored electromagnet

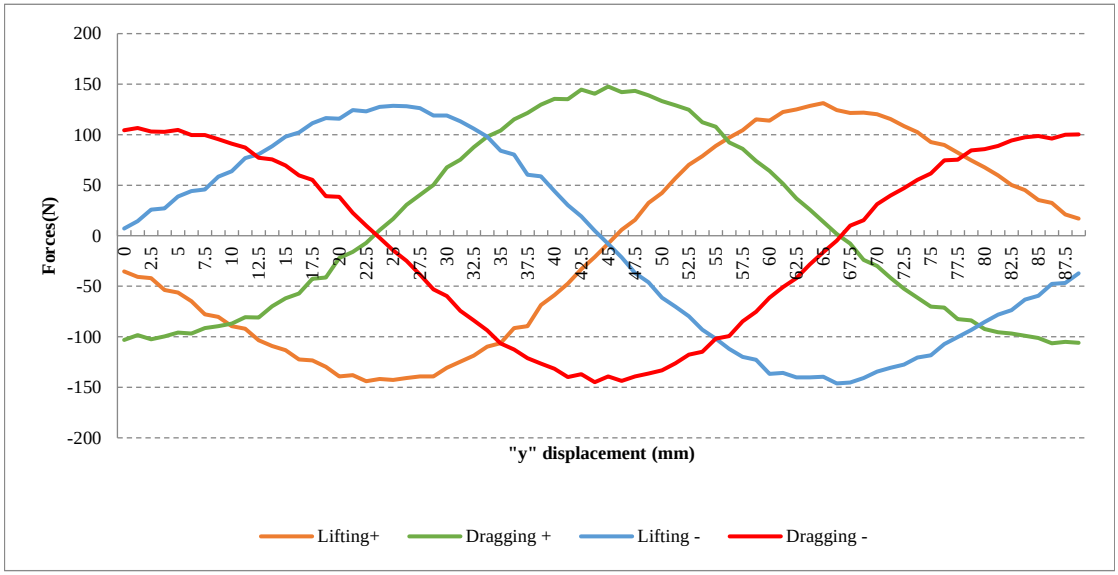

Fig. 4.18 Displacement FEMM Results: Halbach Array facing Air-cored electromagnet

Contrary to the previous two cases, the air-cored options can change the sense of the lifting force, the magnitude is related to the relative position between the permanent magnets and the electromagnet (see figure 4.17 and 4.18).

Additionally another design was tried, a 4-element permanent magnet Halbach array placed in front of a 4-element air-cored coil Halbach array. The turns and current at the coils was kept at 190 and ±30 amperes. The layout is presented in figure 4.19 (from FEMM).

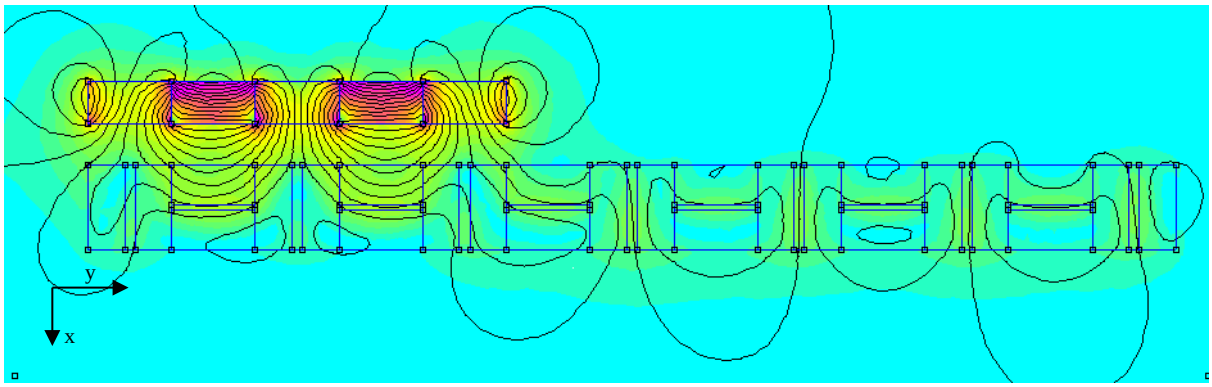

Fig. 4.19 FEMM Results: Permanent magnet Halbach array facing an air-cored coil Halbach array

The results of the displacement simulations are presented in the figure below.

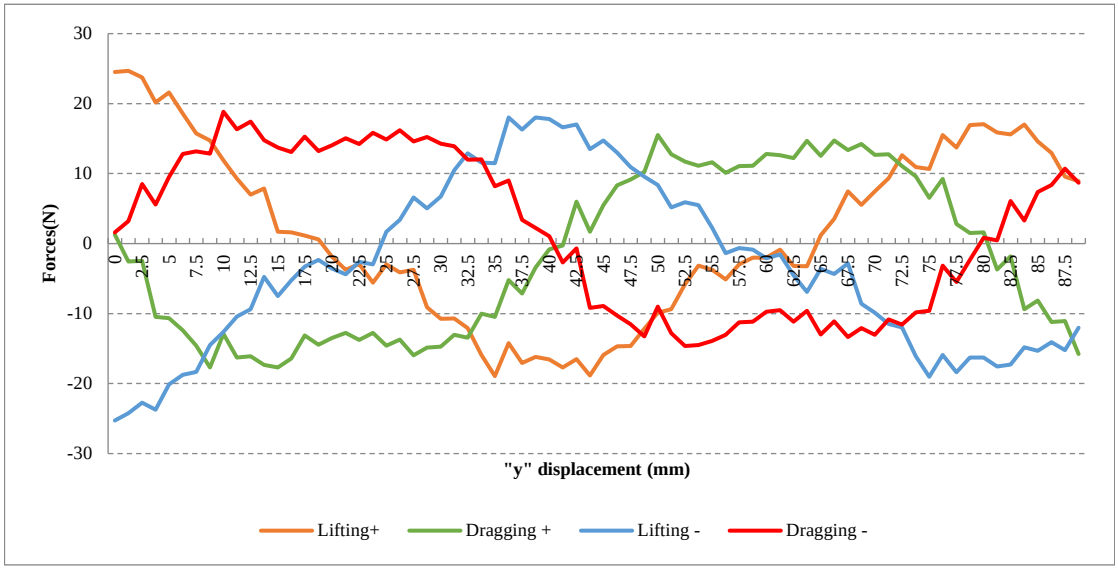

Fig. 4.20 Displacement FEMM Results: Single Permanent magnet-Air-cored electromagnet

4.4 Chapter remarks

A few points can be concluded from these simulations:

- Magnetic bearings using ferromagnetic materials are not suitable for uniform bi-directional force generation. Air cored coils would be an option for this but the magnitude of forces generated are low.
- The use of a Halbach array leads to an increase in the forces' magnitude, but the relationship between lifting and dragging forces is dependent upon the magnetic field alignment.
- All the cases present variation in the magnitude of the forces while translating to the next controlled electromagnet.

After exploring different configurations for an active magnetic bearing design it has been decided to explore a concept where the forces exhibit a better transition between one pole control and the next one, meaning that the force generated is not dependant on the magnetic bearing position. Additionally bi-directional force generation is still being pursued.

Since the Halbach array enhances the magnetic field on one of its sides the concept of Inductrack covered in section 3.3.2 is being considered. The downside for this design is the speed dependency for the generation of the forces. However the use of controlled alternating current electromagnets substituting the permanent magnets in the Halbach array eliminate the velocity constraint.

Additionally, it has been observed that the enhanced side in the Halbach array can be switched if a proper switching arrangement is used. The operation and modelling of the concept is discussed in the next chapter.

5 Modelling the Air-Cored Coil Halbach Array

Based on the concept of Inductrack a new design is proposed. This new design eliminates the velocity dependency of the concept proposed by Post [76] by replacing permanent magnets with air-cored coil electromagnets. As a result, the lifting force and its ratio with the dragging force depend on the frequency and current but not on the velocity.

An array of five air cored coils sequentially oriented at 90 degrees to each other in reference to a plane located over a Litz track is presented in Figure 5.1. The magnetic field concentrates on one side of the array and is generated by alternating current. Therefore, due to Faraday's law when the enhanced side is facing the track an electromagnetic force (emf) is induced in the short circuited Litz track. The principle of operation is similar to the one observed in a squirrel cage.

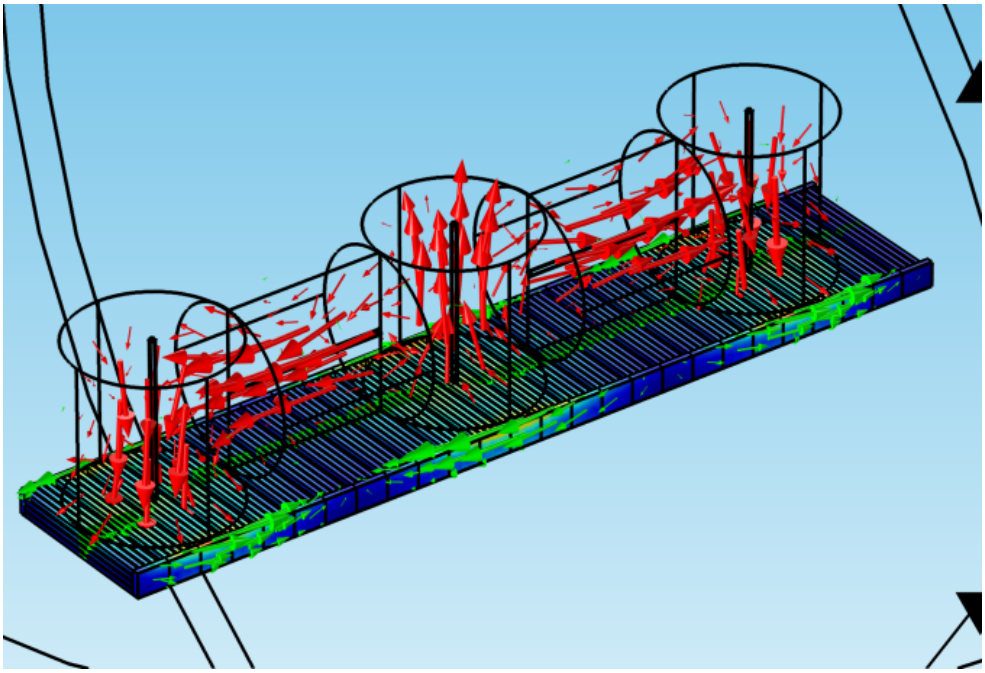

Fig. 5.1 Electromagnetic field of an Air-cored Coil Halbach Array over a Litz wire track

By varying the current frequency the Force/Drag ratio can be controlled. Correspondingly, the amplitude of forces can be controlled by varying the current.

Also with the proper switching configuration bi-directional force generation can be achieved.

The connection of a 5–coil array is depicted in Figure 5.2. The same image also shows the connection using a Double Pole Double Throw (DPDT) switch in order to reverse current direction concentrating the magnetic field on the other side of the electromagnets array. It is worth mentioning that due to the winding inductance a capacitor element to correct the power factor is required. In the following figure this capacitor is in series with the source and the coils. This is with the intention of not dividing the current.

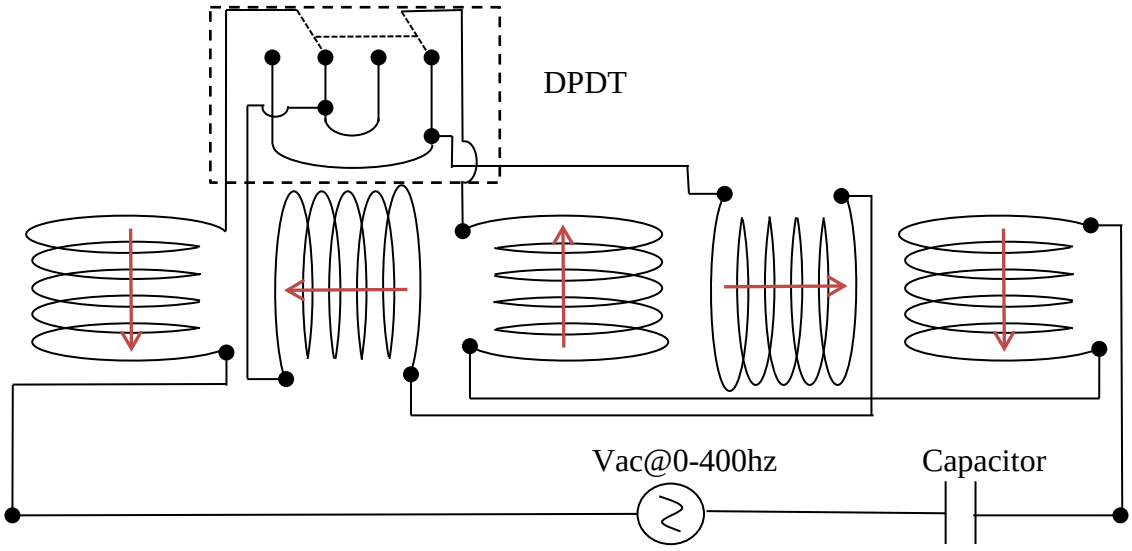

Fig. 5.2 Switching diagram

Figure 5.3 depicts how with changing the second and fourth coils' current direction the enhanced magnetic field side changes. The changing on the DPDT switch is shown of the left-hand side of the figure whilst the effect on the array is presented on the right hand side.

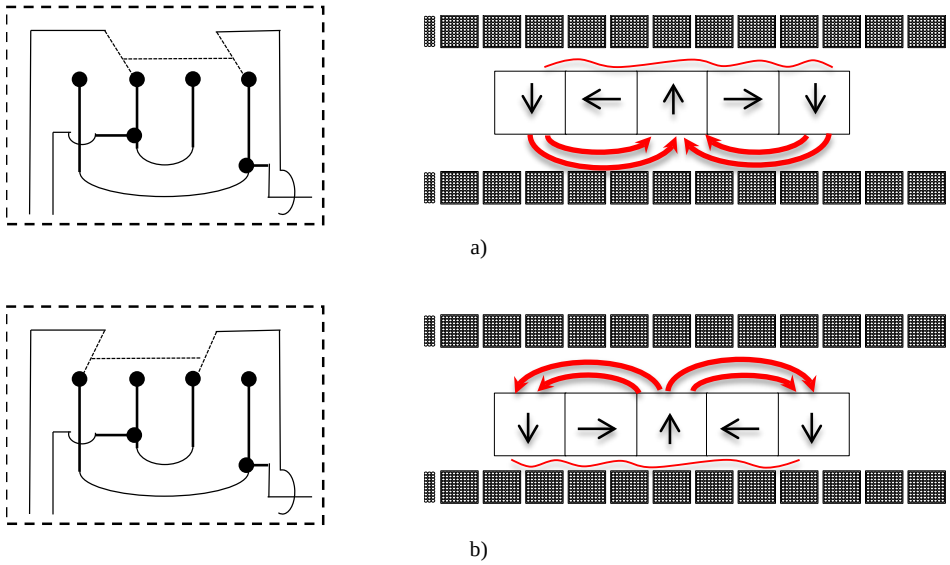

a)

b)

Fig. 5.3 Switching states

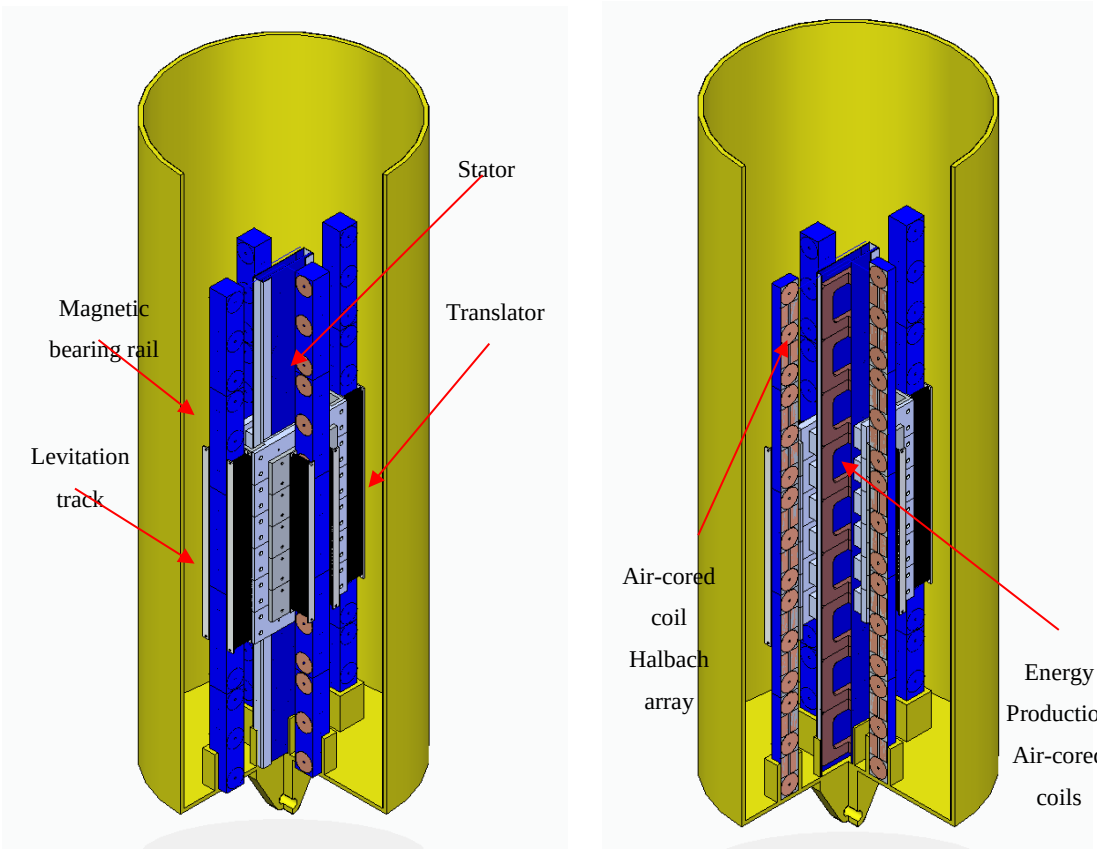

Fig. 5.4 1kW C-Gen Preliminary Design

A preliminary design of the 1kW machine rig is shown in Figure 5.4. The energy production coils can be seen in the centre of the device, while the magnetic bearing system is surrounding the translator with 4 tracks allocated in front of each side of the C-Core.

The dimensions for the Halbach array were determined as follows. The height of the coil's array was chosen to fit the narrowest dimension on the translator whilst leaving enough space for the levitation track. This levitation track was considered to have a maximum height of 16 mm for the 1kW Machine, leaving a gap of 2 mm between the array and the levitation track. This was considered a reasonable starting point for the design since linear machines of this size have a typical airgap of 1 mm.

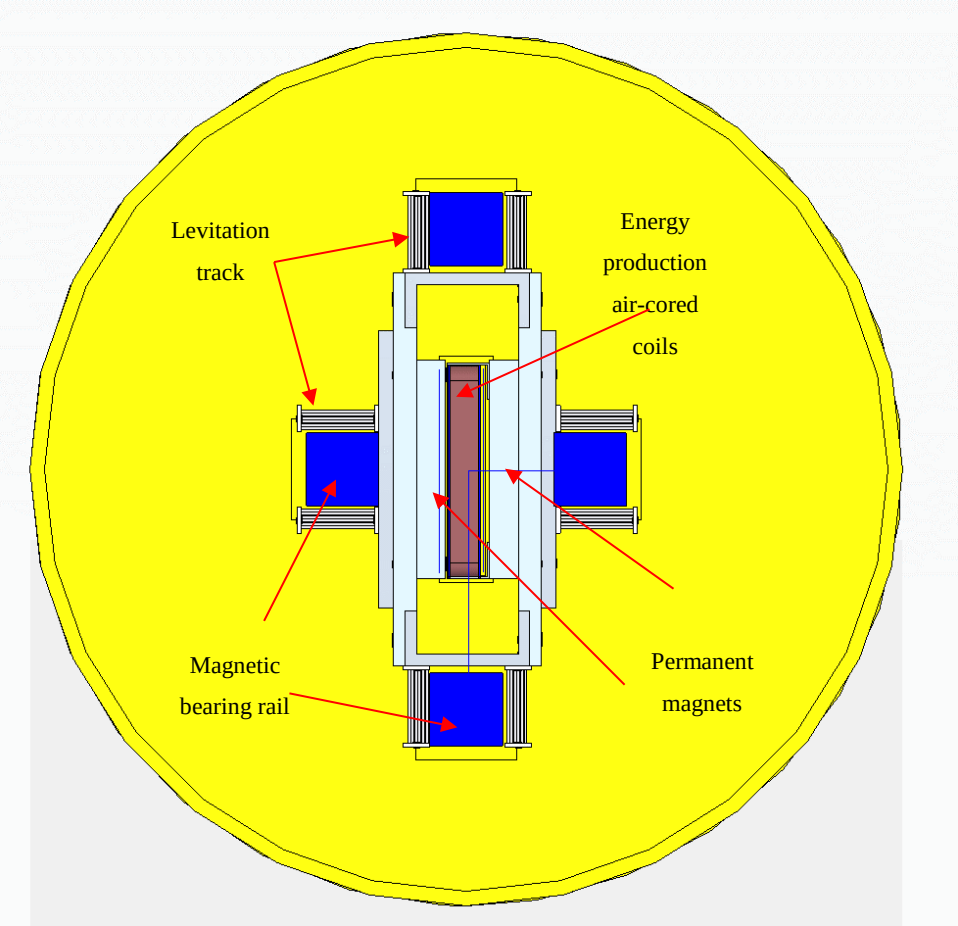

Fig. 5.5 Preliminary Design top view

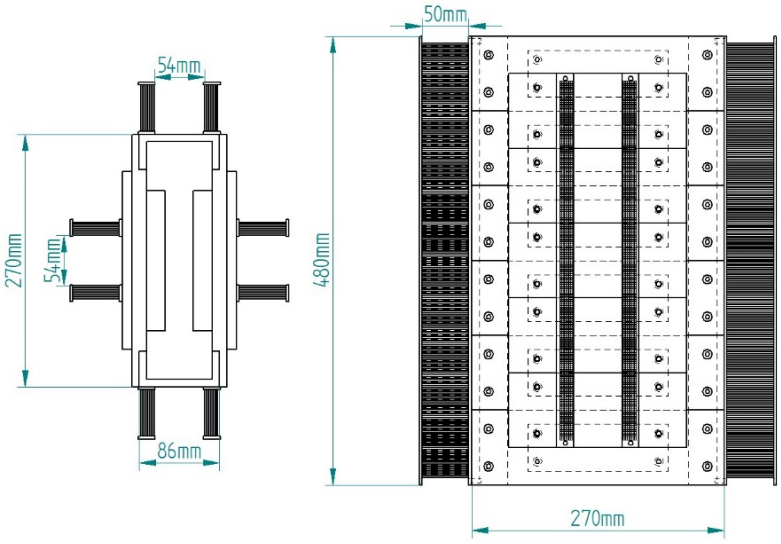

Fig. 5.6 Preliminary Design translator dimensions

The dimensions for the air cored Halbach array in the prototype design were chosen to have dimensions that can fit the preliminary design of the translator shown in figure 5.6, giving dimensions: 50 mm in diameter (D_{co}) and 50 mm in height (h_c) per coil (Figure 5.7).

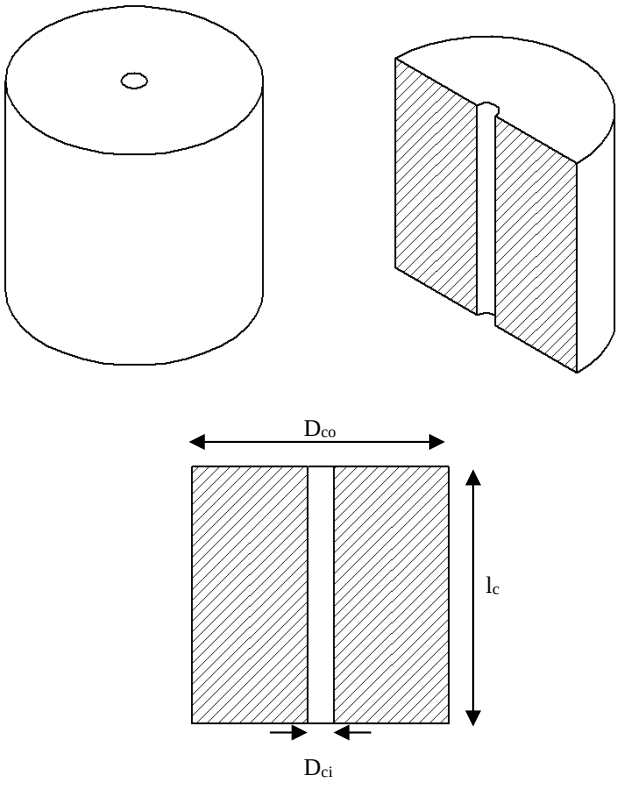

Fig. 5.7 Single air-cored coil

The wire was selected by looking at the maximum generation of magnetic field per volume using equation 5.1. From the cross sectional area shown in the previous figure the number of turns per coil was calculated for each AWG calibre taking into account the maximum chassis current recommended [158]. The result is presented in figure 5.8, from which it is clear that the maximum magnetic field is produced with wire between calibre 19 and 22 for this geometry. For this work calibre 19 has been selected.

$$B = \frac{\mu_0 NI}{l_c} \qquad \textit{Eq. 5.1}$$

In Figure 5.8 it can be noted that after the calibre 22 the trend is no longer incremental when the wire diameter keep reducing. This is because even if the fill factor is higher the AWG standard recommend to limit the current to lower limits due to heat dissipation.

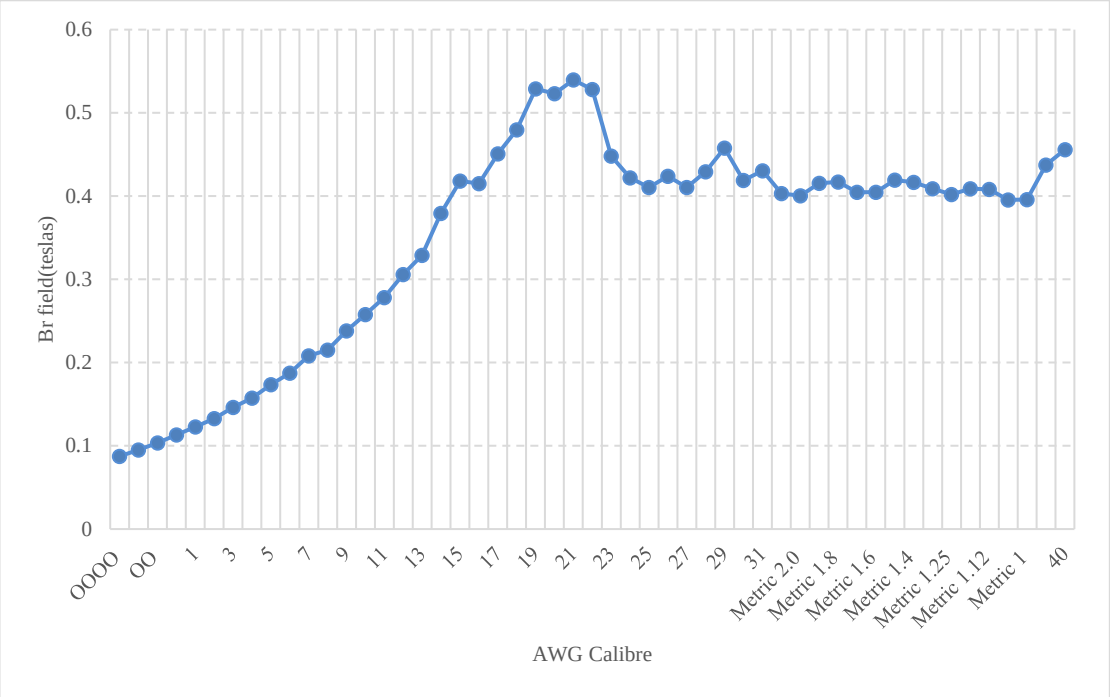

Fig. 5.8 Maximum magnetic field generated by the air-cored coil

5.1 Mathematical model

In order to have the tools to design an optimal active magnetic bearing system the calculation of the magnetic field, the effect of the track inductance and resistance in the forces generated are studied in this section.

5.1.1 Post Inductrack Mathematical model

Inductrack concept has been presented by Post in different documents [75][159][160]. The concept is used as a medium to generate levitation forces in a MagLev train. This device uses a Halbach array made of permanent magnets traveling over a Litz wire track.

The equations depicting the lifting and dragging forces according to Post are presented here in equations 5.2 to 5.4.

$$B_0 = B[1 - e^{-kd_m}]\frac{\sin \pi/M}{\pi/M} \qquad \textit{Eq. 5.2}$$

$$F_z = \frac{{B_0}^2 w_t^2}{2kL_{loop}}\left[\frac{1}{1+\left(\frac{R_{loop}}{\omega_f L_{loop}}\right)^2 e^{-kd_m}}\right]e^{-2kz_g} \qquad \textit{Eq. 5.3}$$

$$F_y = \frac{{B_0}^2 w_t^2}{2kL_{loop}} \left[\frac{\frac{R_{loop}}{\omega_f L_{loop}}}{1 + \left(\frac{R_{loop}}{\omega_f L_{loop}}\right)^2 e^{-kd_m}} \right] e^{-2kz_g} \qquad \textit{Eq. 5.4}$$

Where $k = {2\pi}/{\lambda}$, λ is the wavelength. The term w_t refers to the track width, and z_g is the gap between the array and the levitation track. Note that k is a conversion factor that allows to obtain the electric frequency (ω) considering the velocity of the "floating" body and the change of magnetic field along the Halbach array. Thus, in order to add the effect of the current frequency, the definition of ω is changed to ω_f as noted in equation 5.5.

$$\omega = kv \rightarrow \omega_f = kv + 2\pi f_c \qquad \textit{Eq. 5.5}$$

Where f_c is the current frequency flowing through the windings, and v is the velocity of the translator. The force is calculated as Newtons per loop of the track, and so the result must be multiplied by the number of loops under the active array area.

In the air-cored coil Halbach array concept the magnetic flux density B is derived in accordance to equation 5.1 [161] where μ_0 is the permeability of free space, N is number of turns, I the current in the coils and and l_c is the length of the coil.

As part of the literature review it was noted that although the Post Mathematical model [75] is useful to have a broad idea of the concept, a model that considers the array's element dimensions is needed in order to pursue optimization. Additionally the accuracy of this mathematical model is discussed later in this chapter.

5.1.2 Air Cored Coil Halbach Array Magnetic Field Calculations:

This section aims to explore different methods to model the magnetic field produced by the array, in order to have a model that includes the individual dimensions of each array element. Thus the peak magnetic field B_0 is approached differently. The supposition of this model is that once B is obtained (equation 5.1) for an air-cored coil, B_0 of a Halbach array is calculated over a plane based on [74] and [162]. The orientation of the coils is shown in Figure 5.9.

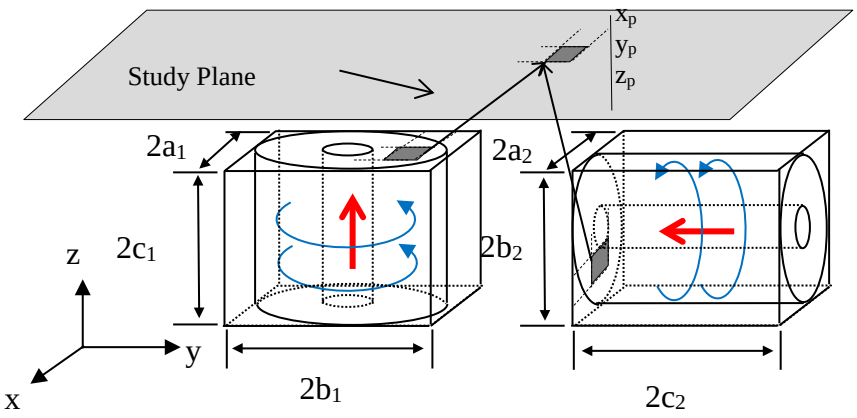

Fig. 5.9 Electromagnetic field of an Air-cored Coil Halbach Array over a Litz wire track. Blue arrows represent the current direction whilst red arrows represent the magnetic field direction.

The magnetic field is calculated in two ways:

1. Note that in figure 5.9 the coils are enclosed in cubes. Each element of the array is considered as a permanent magnet but the remanent magnetic field *B* is calculated as an air cored coil. This mathematical model of the array is simple which makes the calculations less resource intensive and time consuming (Section 5.1.2.1).
2. In the second method the geometry is taken simply as an air-cored coil. This method considers the geometry of the coils as hollow cylinders (Section 5.1.2.2).

A more detailed explanation of the models is provided in the following sections.

5.1.2.1 Magnetic field Calculation: Cube

According to [74] the equations describing the magnetic flux of the cube-shaped Halbach array are the following (see figure 5.9):

$$U_i = x_p - (-1)^i a; V_j = y_p - (-1)^j b; W_k = z_p - (-1)^k c;$$

$$r = \sqrt{U_i^2 + V_j^2 + W_k^2} \qquad \textit{Eq. 5.6}$$

$$\varepsilon_x = ln(r - V); \varepsilon_y = ln(r - U); \varepsilon_x = ln \tan^{-1}\left(\frac{UV}{Wr}\right) \qquad \textit{Eq. 5.7}$$

$$B(x,y,z) = \frac{B}{4\pi}\sum_{k=0}^{1}\sum_{i=0}^{1}\sum_{j=0}^{1}(-1)^{i+j+k}\varepsilon\left(U_i, V_j, W_k\right) \qquad \textit{Eq. 5.8}$$

$$B_0 = \max_{0 \le x \le \lambda} |B| \qquad \textit{Eq. 5.9}$$

Note that x_p,y_p,and z_p are the coordinates at the study plane and a,b, and c are the dimensions of each element of the array in Figure 5.9.

Using equations 5.6 -5.9 a mathematical model was coded in MatLab® .The magnetic field of an array of five elements was compared against models from FEMM and COMSOL (2D and 3D finite element software).

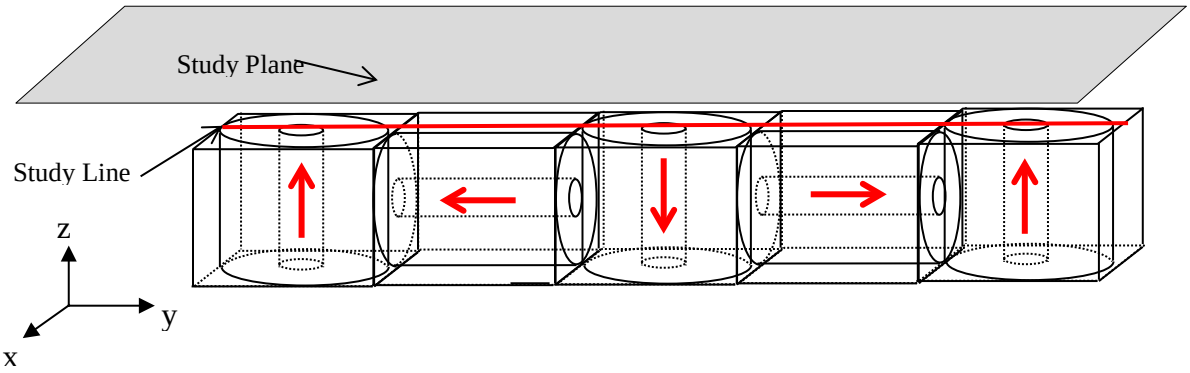

Fig. 5.10 Study placement

The simulation was run at the centre of the array in the x direction (red line in Figure 5.10), and along the y axis, from 25 mm before the position of the first magnet to 25 mm after the last magnet for a total length of 300 mm. Details of the Halbach array are summarized in the following table.

TABLE 5-I
ARRAY CHARACTERISTICS

variable	Quantity(units)
$a_1=a_2=b_1=b_2=c_1=c_2$	25(mm)
Number of turns	922(n/a)
I(current)	9(amps)
B	0.2086(T)

Figure 5.11 shows the results from the different software. In this image it can be appreciated how the magnetic field peak varies among the different models. Although the magnitude is close in each one of the graphs, it is worth remembering

that a slight change in the magnetic field might signify a large change in the force calculation.

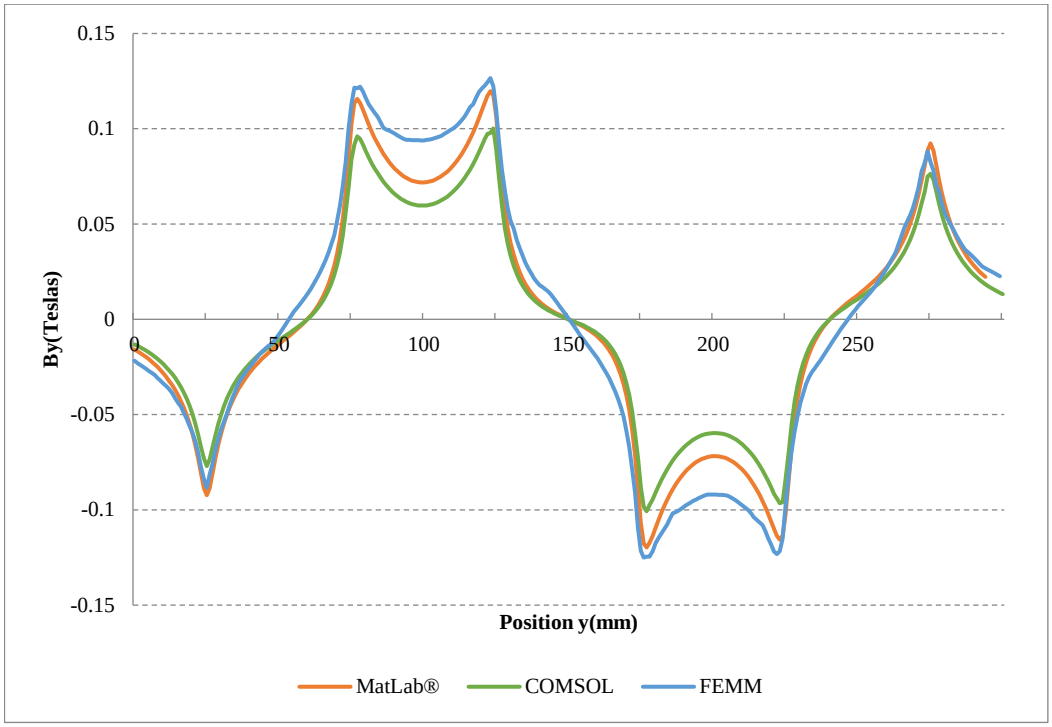

a)

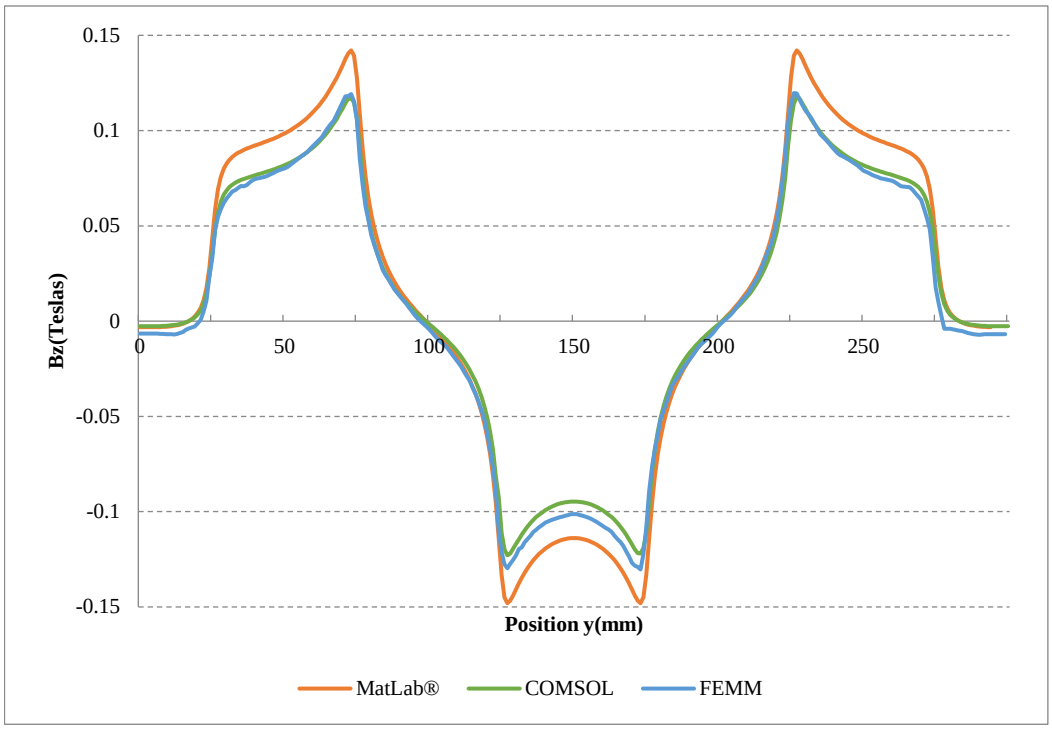

b)

Fig. 5.11 Magnetic field calculated at the centre of the track from a cubic-shape array: a) B_y ; b) B_z

Bearing in mind that the device is basically a linear induction machine, calculation of the forces depends on how the magnetic field acts over the track (squirrel cage). Thus

the next step involves determining how the magnetic field behaves over the *x-y* plane at 2 mm from the Halbach array surface. The results of the simulation made over said plane (see figure 5.9 and 5.10) are presented in Figures 5.12 and 5.13. It can be noted in those figures how the magnetic field starts diminishing around 25 mm from the centre of the array in *x* which is where the coil, represented by a cube in this model, ends.

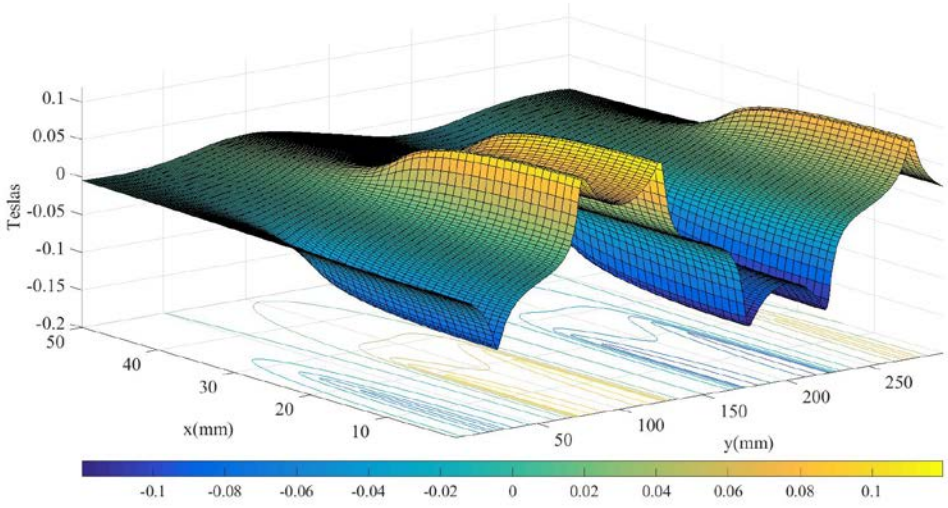

a)

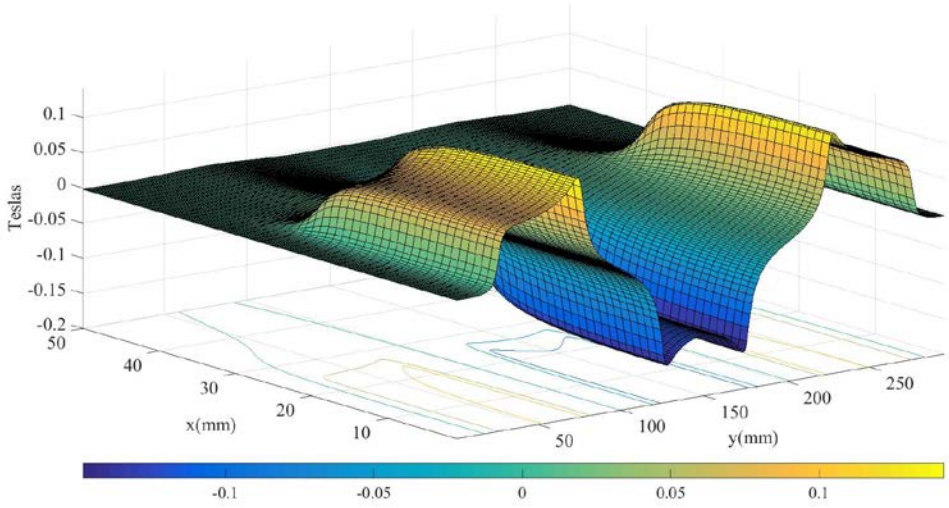

b)

Fig. 5.12 Cubic-shaped. Magnetic field result in 3-D: a)B_y b)B_z

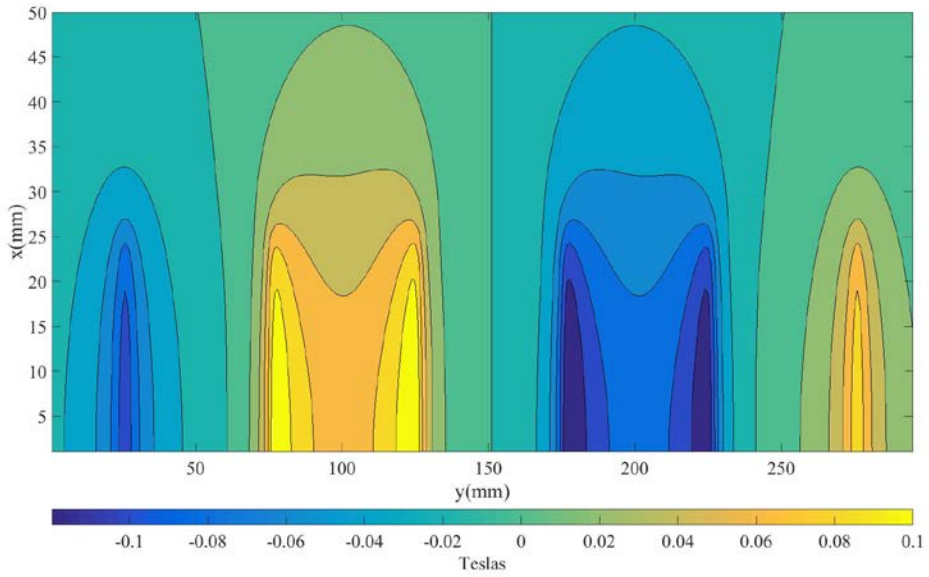

a)

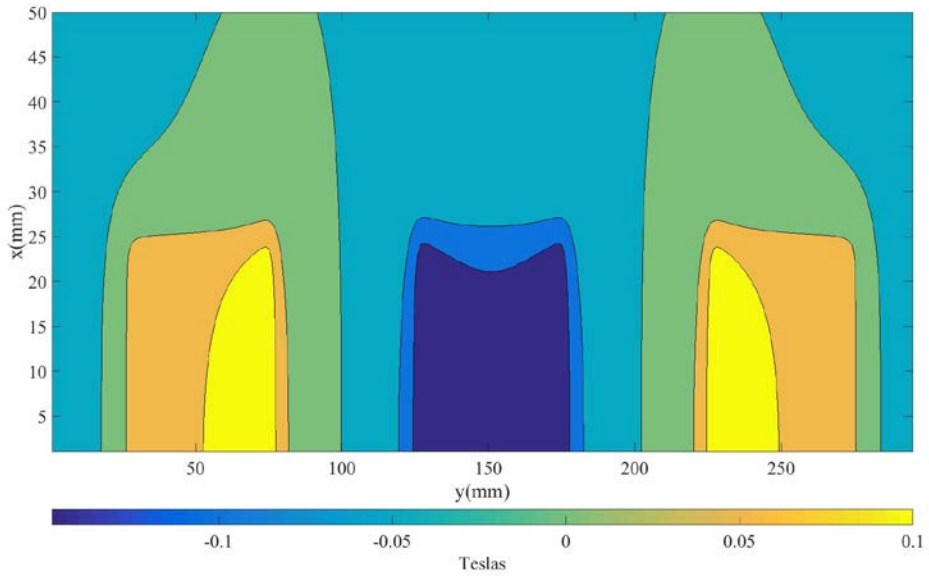

b)

Fig. 5.13 Cubic-shaped. Magnetic field plane projection a)B_y b)B_z

The calculations on the plane *x-y* are now compared with the 3-D model in COMSOL shown in Figure 5.14 and 5.15 for an equivalent PM Halbach array. A high correspondence can be noted between the results from the mathematical "*cubic-*

shaped" model in figure 5.13 and the magnetic field projected on the track from the COMSOL results shown in Figure 5.15.

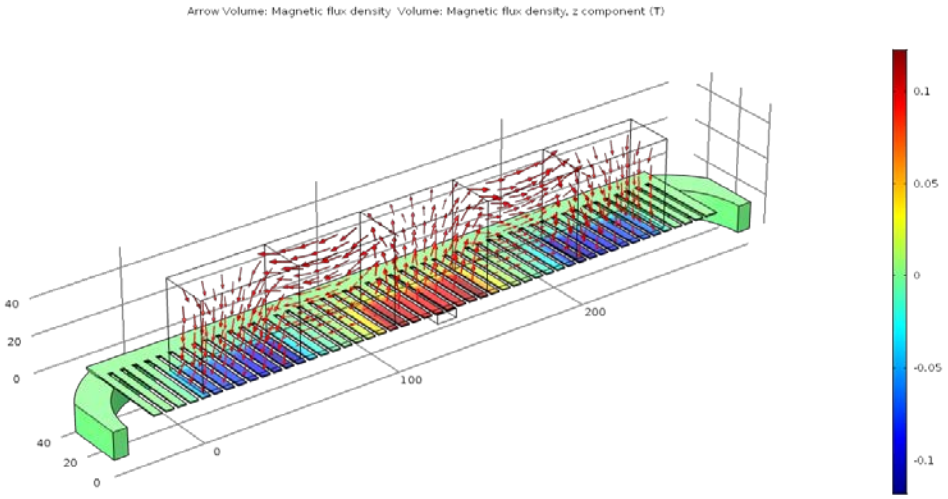

Fig. 5.14: Cubic-shaped COMSOL. B_z.from a Permanent magnet Halbach array over a copper slotted plate.

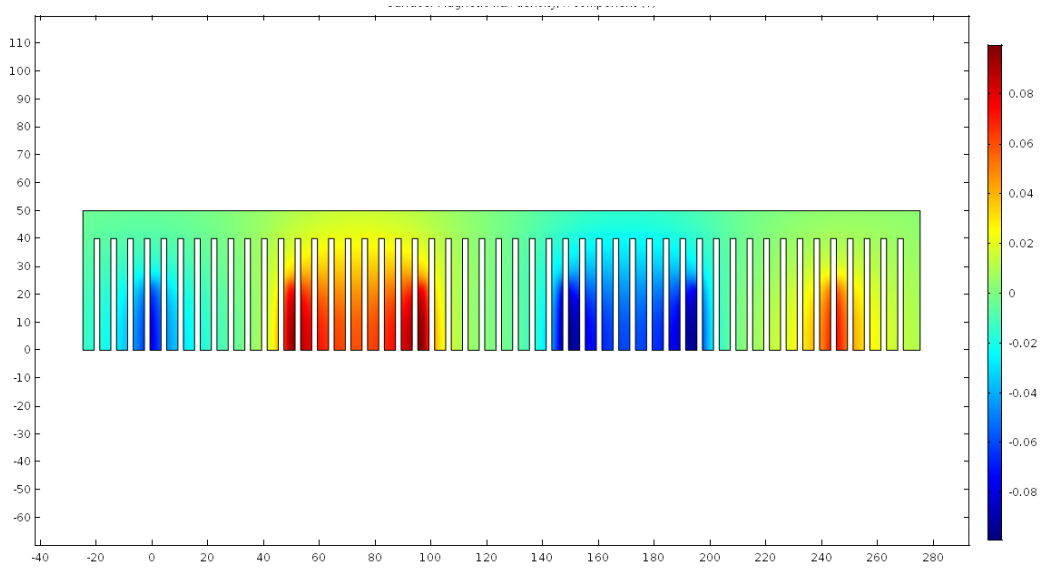

a)

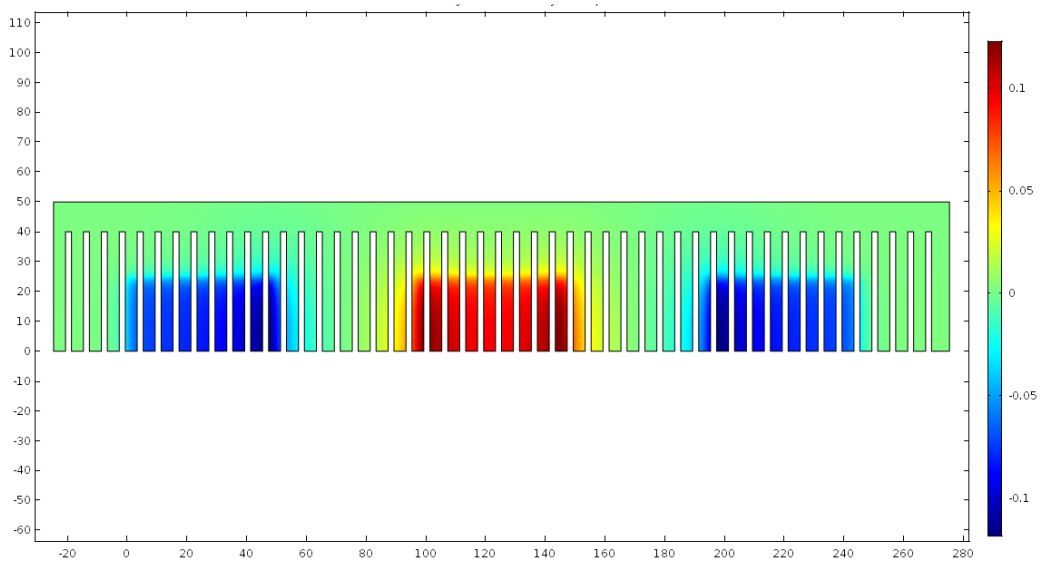

b)

Fig. 5.15 Cubic-Shaped COMSOL. Magnetic field projection over the levitation track: a) B_y b) B_z

5.1.2.2 Magnetic field Calculation: Coil

As mentioned before at the beginning of section 5.1.2 a second way to calculate the magnetic field considering hollow cylinder geometry has been studied. Basu [162] highlights the equations to obtain the magnetic field from cylindrical coils to a point in space, equations 5.10 to 5.12:

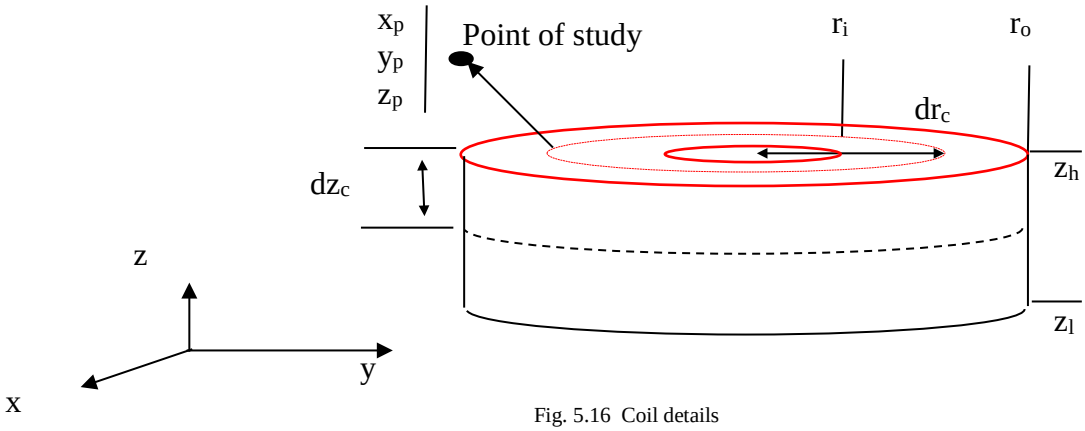

Fig. 5.16 Coil details

Where, r_o and r_i are the outside and inside radius and l_c is the length of the coils -in this case the distance between z_h and z_l from Figure 5.16.:

$$B_x(x_p, y_p, z_p) = \frac{\mu_0 J}{4\pi} \times \int_{z_l}^{z_h} \int_{r_i}^{r_o} \int_{0}^{2\pi} \frac{r_c(z_p - z_c)\cos\varphi}{\left[(x_p - r_c\cos\varphi)^2 + (y_p - r_c\sin\varphi)^2 + (z_p - z_c)^2\right]^{3/2}} d\varphi\, dr_c\, dz_c \qquad \textit{Eq. 5.10}$$

$$B_y(x_p, y_p, z_p) = \frac{\mu_0 J}{4\pi} \times \int_{z_l}^{z_h} \int_{r_i}^{r_o} \int_{0}^{2\pi} \frac{r_c(z_p - z_c)\sin\varphi}{\left[(x_p - r_c\cos\varphi)^2 + (y_p - r_c\sin\varphi)^2 + (z_p - z_c)^2\right]^{3/2}} d\varphi\, dr_c\, dz_c \qquad \textit{Eq. 5.11}$$

$$B_z(x_p, y_p, z_p) = \frac{\mu_0 J}{4\pi} \times \int_{z_l}^{z_h} \int_{r_i}^{r_o} \int_{0}^{2\pi} \frac{r_c(r_c - y_p \sin\varphi - x_p \cos\varphi)}{\left[(x_p - r_c\cos\varphi)^2 + (y_p - r_c\sin\varphi)^2 + (z_p - z_c)^2\right]^{3/2}} d\varphi\, dr_c\, dz_c \qquad \textit{Eq. 5.12}$$

The solution of these integrals proved extremely difficult. For this reason, a mathematical numeric approximation such as Simpson's rule was tried to obtain the magnetic field. However, even using this numeric approximation the simulation takes around an hour to compute the results. Therefore another approach using elliptic integrals was also studied [163]. The equations are listed below. To have a better understanding of these equations see figure 5.16.

$$B_x(x_p, y_p, z_p) = \int_{z_l}^{z_h} \int_{r_i}^{r_o} \frac{C x_p z_p}{2\alpha^2\beta\rho^2}[(r_c^2 + r^2)E(k^2) - \alpha K(k^2)]\, dr_c\, dz_c \qquad \textit{Eq. 5.13}$$

$$B_y(x_p, y_p, z_p) = \int_{z_l}^{z_h} \int_{r_i}^{r_o} \frac{C y_p z_p}{2\alpha^2\beta\rho^2}[(r_c^2 + r^2)E(k^2) - \alpha K(k^2)]\, dr_c\, dz_c \qquad \textit{Eq. 5.14}$$

$$B_z(x_p, y_p, z_p) = \int_{z_l}^{z_h} \int_{r_i}^{r_o} \frac{C}{2\alpha^2\beta}[(r_c^2 - r^2)E(k^2) - \alpha K(k^2)]\, dr_c\, dz_c \qquad \textit{Eq. 5.15}$$

Where:

$$C = \mu_0 \frac{I}{\pi};\ \rho_c^2 = x_p^2 + y_p^2;\ r^2 = x_p^2 + y_p^2 + z_p^2;\ \alpha^2 = r_c^2 + r^2 - 2r_c\rho_c;$$
$$\beta^2 = r_c^2 + r^2 + 2r_c\rho_c;\ k^2 = 1 - {\alpha^2}/{\beta^2} \qquad \textit{Eq. 5.16}$$

Equations 5.13-5.16 describe the magnetic field in a point in space generated by a close circular loop. Therefore integration over the geometry shown in figure 5.16(from r_i to r_o and from z_h to h_l) must be computed. In order to calculate the magnetic field over the array the equations must be applied according to the orientation of the coil according to figure 5.9 and 5.10.

The results of the analytical equations are compared to FEMM and COMSOL simulations in Figure 5.17. The difference between the results presented here with the legend *MatLab*® and *MatLab*® *Elliptic* is that the first one was calculated using equation 5.10 to 5.12 and the last one was obtained using equation 5.13 to 5.16.

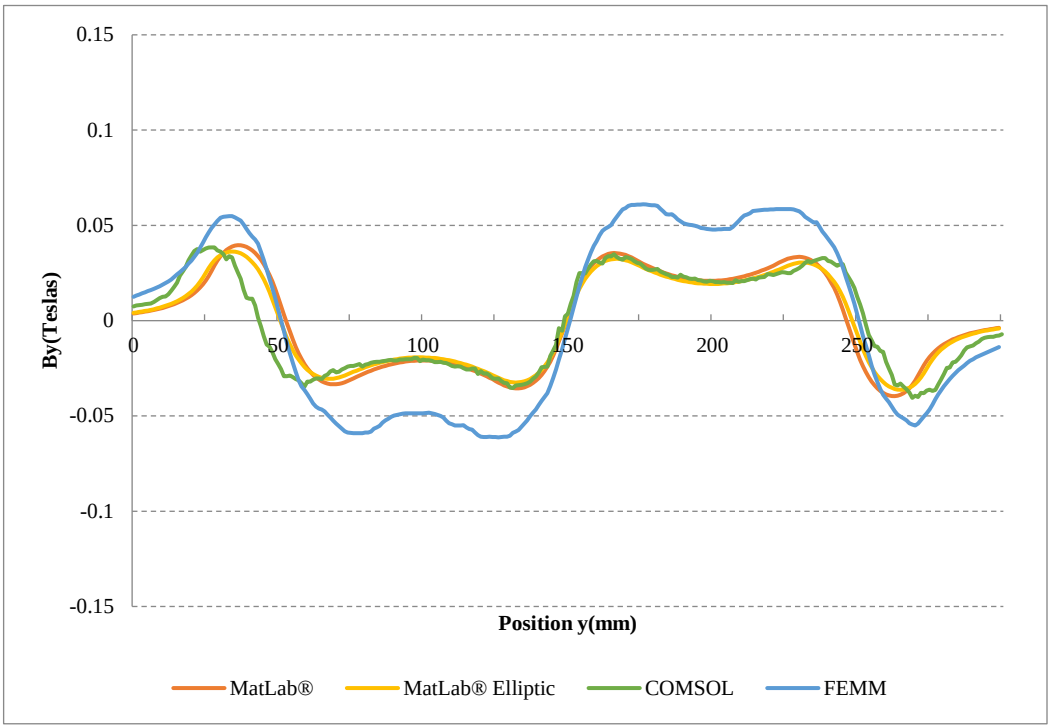

a)

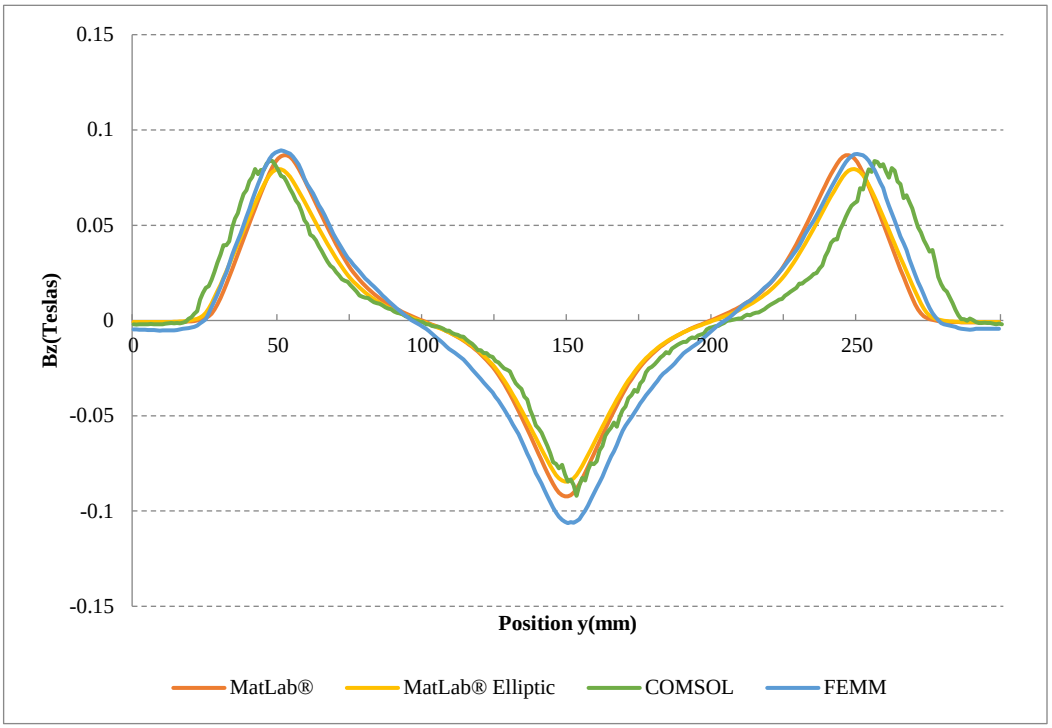

b)

Fig. 5.17 Magnetic field calculated at the centre of the track from a Coil-shape array: a) B_y ; b) B_z

The small difference between the MatLab® calculations and the COMSOL results is caused by a slight difference in the dimensions from the COMSOL 3-D model in order to build the mesh in the finite element software. It can also be noted that the FEMM model result is higher than the result calculations from the other methods. This is believed to be caused by the limitations of the 2D environment the software presents.

Similar to the previous section, results over the plane *x-y* were obtained over a plane at 2 mm from the Halbach array surface using the elliptic integral method (equations 5.13-5.16). The results are presented in Figures 5.18 and 5.19.

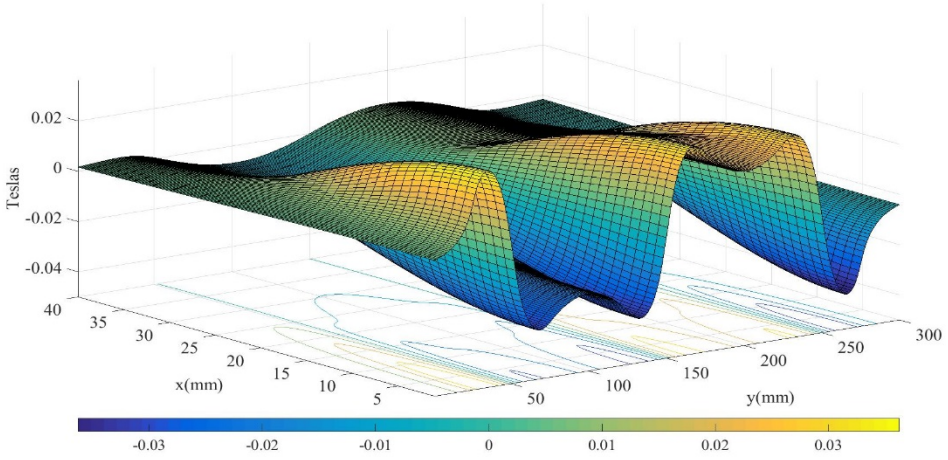

a)

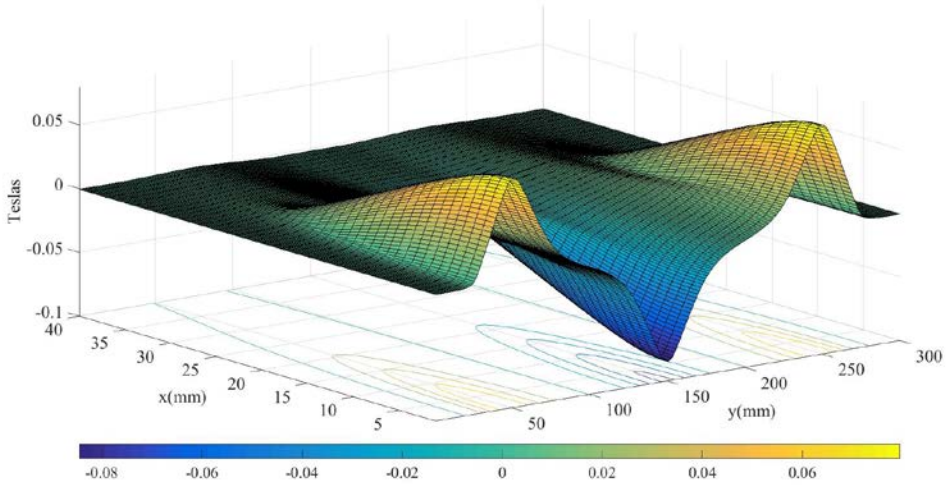

b)

Fig. 5.18 Coil-Shaped MatLab. Magnetic field result in 3-D: a)B_y b)B_z

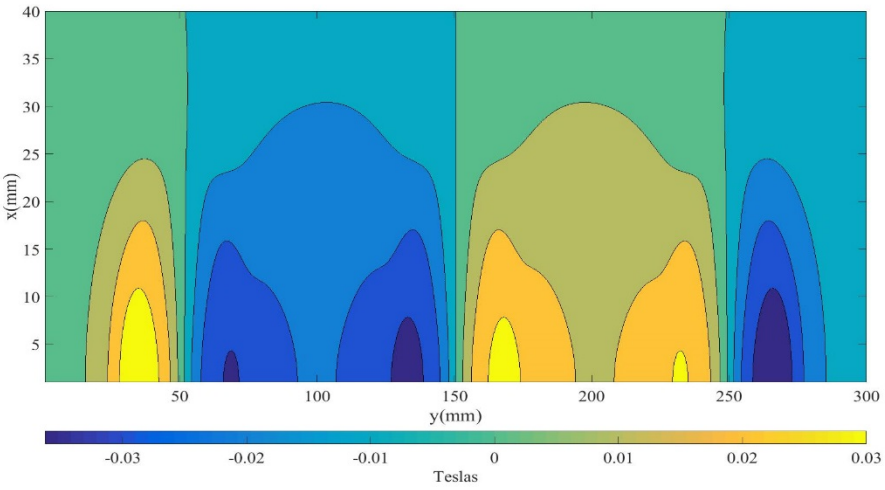

a)

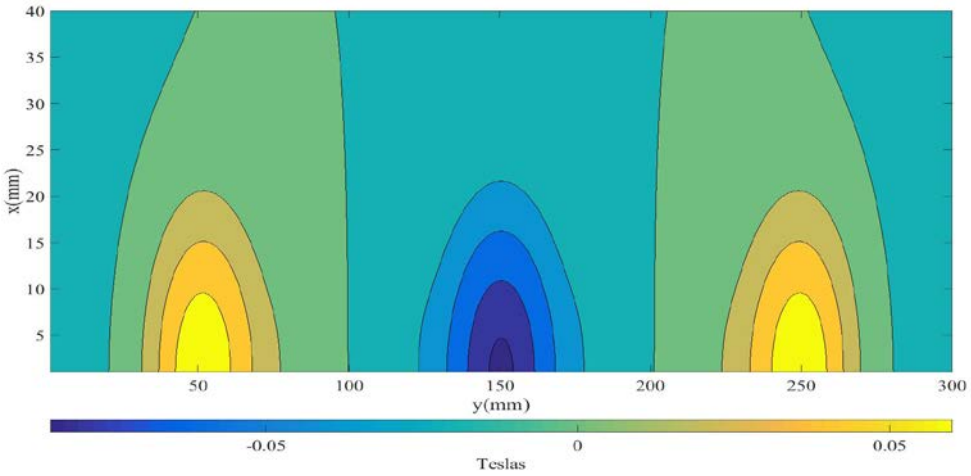

b)

Fig. 5.19 Coil-Shaped MatLab. Magnetic field plane projection a)B_y b)B_z

In Figure 5.20 the COMSOL model is presented. The coils are placed over a 1-layer slotted plate track made of copper. Again, it can be seen that the analytical model and the COMSOL model are extremely similar when compared to figures 5.18 and 5.19. In Figure 5.21 the effect of the Magnetic field in B_t and B_n (or B_y and B_z) can be seen over the plate. As stated before, when these COMSOL results are compared against the mathematical model results over a plane, a high similarity can be noted. The error is around 6% if COMSOL results are taken as a base. This instils confidence in our mathematical model, which might result in a better process for the calculation of forces and at the same time to improvements in the design.

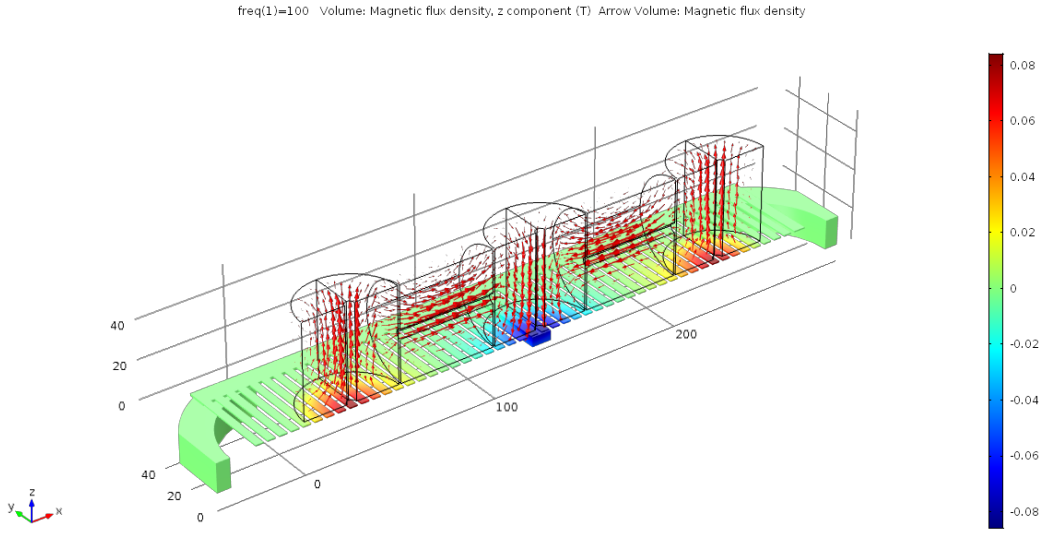

Fig. 5.20 Coil-Shaped COMSOL. B_z.from an Air-cored coil Halbach array over a copper slotted plate

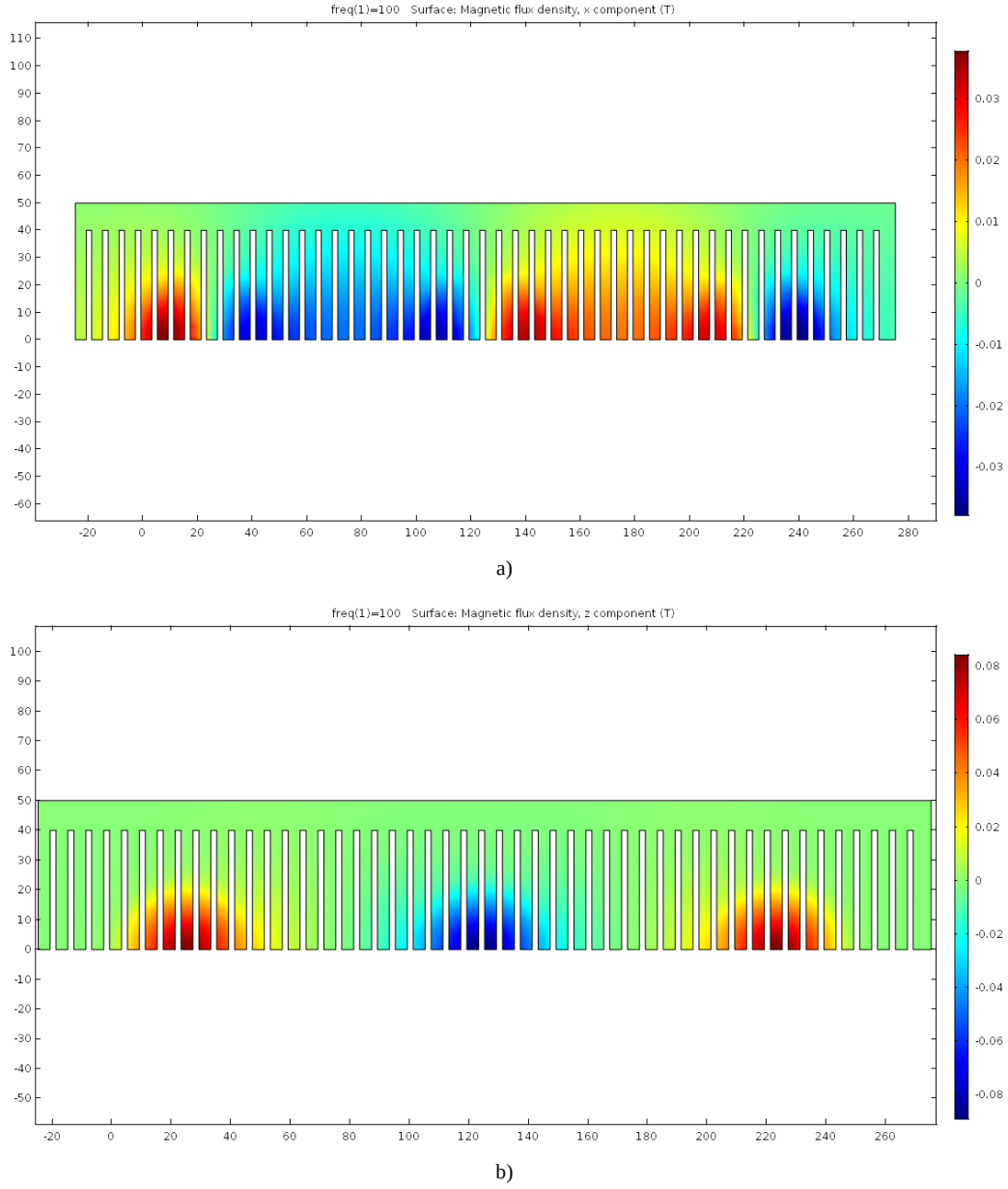

a)

b)

Fig. 5.21 Coil-Shaped COMSOL. Magnetic field projection over the levitation track :a) B_y b) B_z

5.1.2.3 Magnetic Field Measurements

In order to verify the accuracy of the magnetic field mathematical model, measurements from the prototype were taken. The coils were activated with a current of 31.8 amperes (reason for this current is explained in section 6.2.2). Field measurements were taken every 10 mm along the *y* axis of the array at around 3-5 mm from the array surface. It is worth mentioning that these measurements were taken by hand with a fluxometer without any fixing device due to high temperatures

at the coils. Therefore the measurements should be subjected to a certain tolerance. The results of the prototype measurements against the results of the mathematical calculations are shown in Figure 5.22.

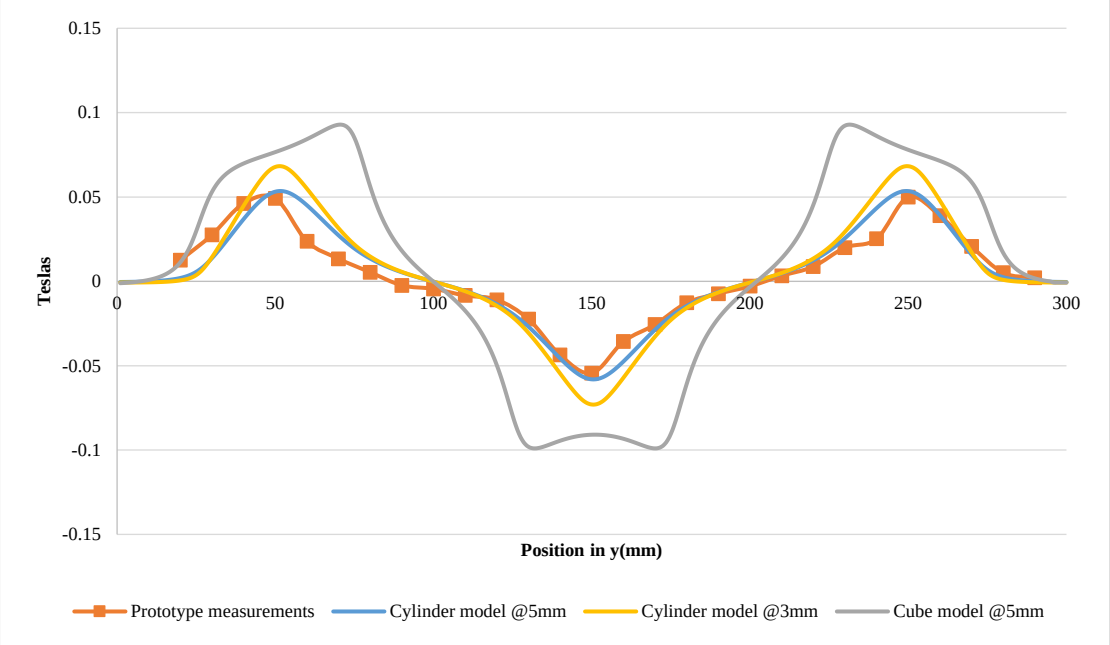

Fig. 5.22 B_n field comparison

As can be seen from Figure 5.22, there is a close correlation between the mathematical and experimental results apart from the cube model. However, the cube shape calculation seems to be far from the actual magnitude of the magnetic field. This is caused by the difference of magnetic field distribution between a permanent magnet and an air-cored- coil. In figure 5.14, one can see that the magnetic field lines, represented as arrows, are distributed over the permanent magnet face normal to the magnetic orientation of the permanent magnet. On the other hand figure 5.20 shows that the magnetic field in the coils concentrate in the centre of the cylinder as expected. Also permanent magnets keep their magnetic field uniform along the normal face to the magnetisation orientation while cylindrical coils tend to have a peak located at the centre of the core.

5.1.3 Inductance and resistance effect of The “Inductrack” concept

It is not only the characteristics and dimensions of the electromagnet array that will affect the forces generated in the system, but the track itself plays an essential role in the way the bearing will behave. In order to observe this a couple of simulations were run in accordance with the Post “Lumped” model from equations 5.2-5.4. Here the lift/drag forces ratio can be derived as:

$$\frac{Lift(F_z)}{Drag(F_y)} = \frac{\omega_f L_{loop}}{R_{loop}} \qquad \textit{Eq. 5.17}$$

It is clear that the relation between loop inductance and resistance as well as the frequency affects the force generation. Three kinds of tracks were studied, one consisting of Litz rungs, another formed of slotted plates and the last one called window shape as can be seen in Figures 5.23-5.25.

Thus, in order to calculate the inductance and resistance of rungs consisting of Litz wire calculations were made according to [164] and [165], and the window track inductance was obtained according to [166].

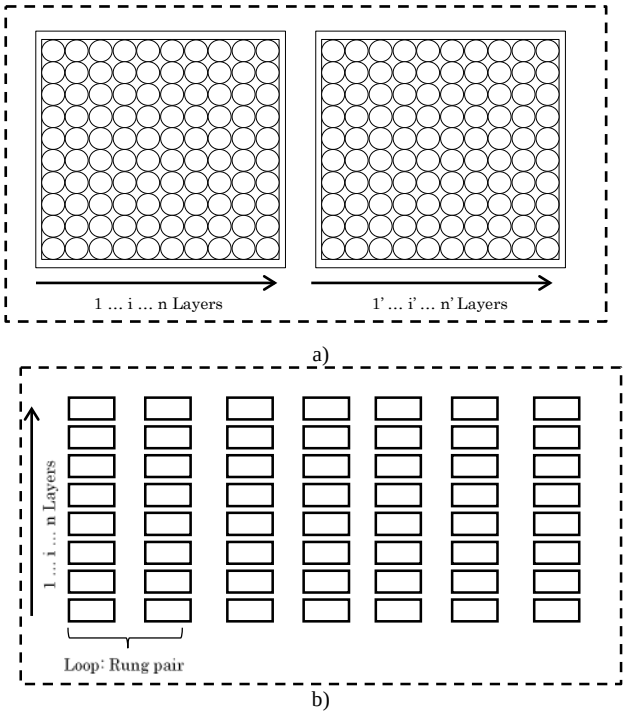

Fig. 5.23 a)Litz Rung cross section area; b) Slotted track cross section area

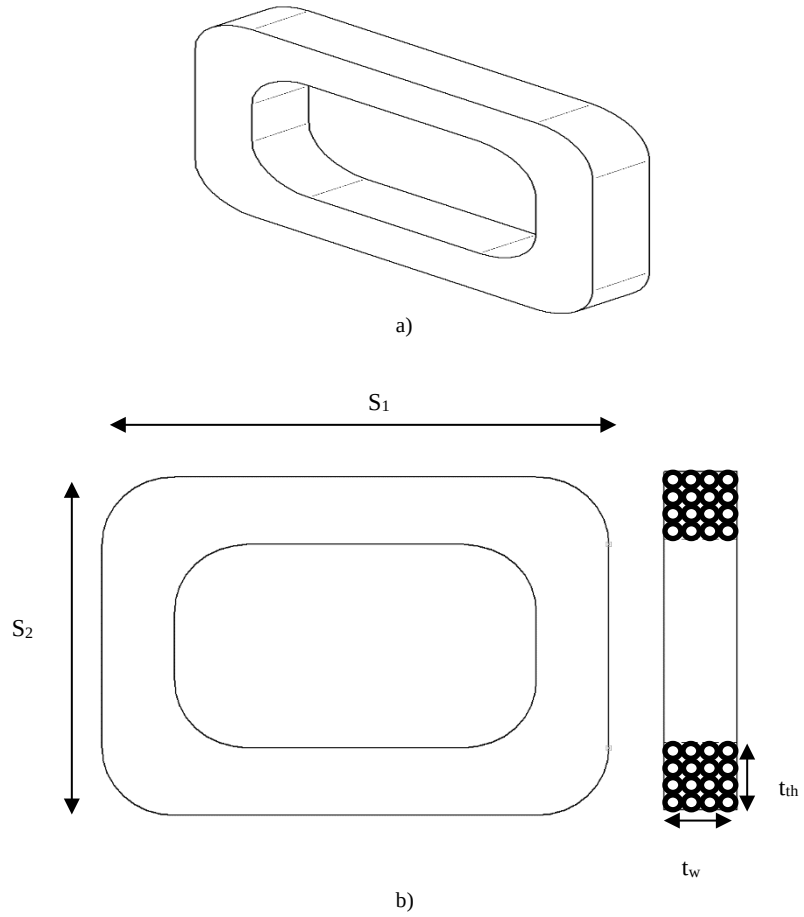

Fig. 5.24 window track coil: a) Isometric view; b) Dimensions detail

The resistance of a straight Litz R_{loop} composed by "*n*" wires is calculated as follows:

$$R_{dc} = \frac{4\rho_{cu} l_{tot}}{\pi n d_s^2} \qquad \textit{Eq. 5.18}$$

$$y_s = \frac{x_s^4}{(192 + x_s^4)} \qquad \textit{Eq. 5.19}$$

$$x_s^2 = \frac{8\pi f_c k_s \times 10^{-7}}{R_{dc}} \qquad \textit{Eq. 5.20}$$

$$R_{loop} = R_{dc}(1 + y_s) \qquad \textit{Eq. 5.21}$$

Where ρ_s , l_{tot} and d_s denote the resistivity of the material, the total length and the diameter of the wire; k_s is a factor that depends on the construction of conductor and frequency is denoted again by f_c.

Additionally the mutual and self-inductance of one straight Litz wire is calculated as follows:

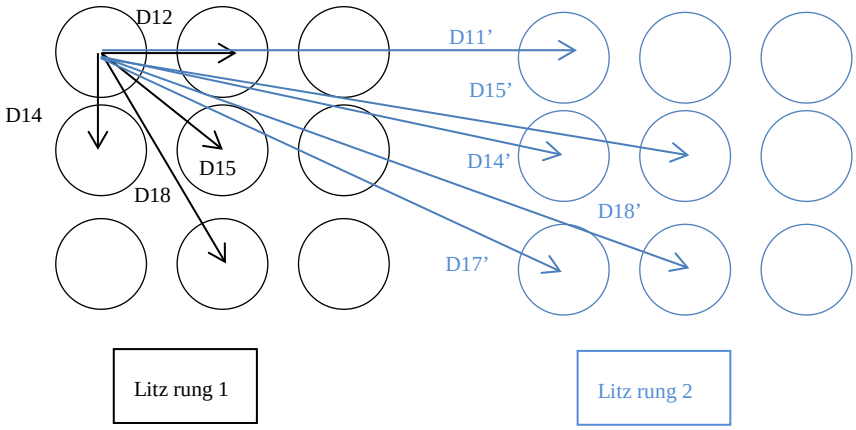

Fig. 5.25 Detail inductance calculation in litz wire

$$D_m = \left(D_{1l'} \dots D_{1j'} \dots D_{1m'}\right) \dots \left(D_{nl'} \dots D_{nj'} \dots D_{nm'}\right) \quad \textit{Eq. 5.22}$$

$$D_s = \left(D_{1l} \dots D_{1j} \dots D_{1n}\right) \dots \left(D_{nl} \dots D_{ni} \dots D_{nn}\right) \quad \textit{Eq. 5.23}$$

$$L_{litz} = 2 \times 10^{-7} ln \frac{D_m}{D_s} \quad \textit{Eq. 5.24}$$

In these equations *D* is the distance between the centres of one wire thread of the Litz compound to the next one, and L_{litz} is calculated in Henrys per metre. The slotted track inductance is calculated in the same manner from one group of bars to the next one.

In the case of the window shape track the Inductance was calculated as follows:

$$L_{wt} = 0.02339(s_1 + s_2)n^2 \left[log_{10}\left(\frac{2s_1 s_2}{t_{th} + t_w}\right) - \frac{s_1}{s_1 + s_2} log_{10}(s_1 + g) - \frac{s_2}{s_1 + s_2} log_{10}(s_2 + g) \right] + 0.01016(s_1 + s_2)n^2 \left[2\left(\frac{g}{s_1 + s_2}\right) - \frac{1}{2} + 0.447\frac{(t_{th} + t_w)}{(s_1 + s_1)} \right] \quad \textit{Eq. 5.25}$$

Where s_1 and s_2 are the length and height of the window shaped coil $g=s_1^2+s_2^2$ and t_{th} and w_{th} are the thickness and width of the cross sectional area of the coil (see figure 5.25). The resistance in this case was calculated according to equation 5.18.

5.1.3.1 Simulation Results

In order to observe the effect of the track design on the force magnitude and ratio between lift and drag a number of simulations were carried out where the model proposed by Post [75] was used due to its simplicity. The magnetic field was calculated according to equations 5.1-5.4. Also details of the coil can be seen in Table 5-I and additionally, with the intention of seeing the effect maximized, the frequency was kept to 500 Hz.

The first simulation was considering the Litz track. Layers of the square matrix presented in Figure 5.23 and 5.26, were varied from 1 to 9. In the same manner AWG calibres of the wire at the track were tried from OOOO -40 (see AWG nomenclature). Figure 5.19 shows the desired area for the design.

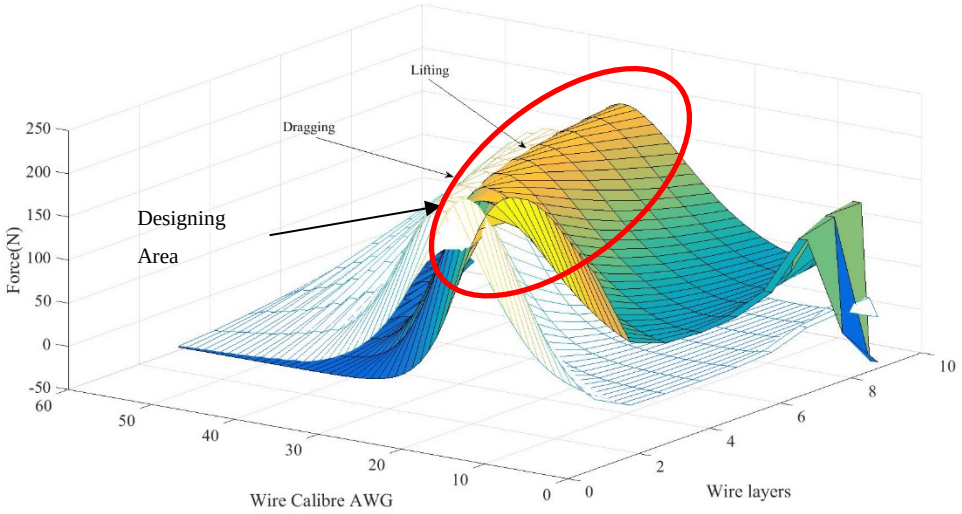

Fig. 5.26 MatLab Simulation AWG calibre vs Layers at "Litz" track

In the slotted plate track case, the number of layers (see figure 5.24) were also changed from 1 to 9. In this case, the width "x", and thickness "z", of the rung were increased gradually from 0.5mm-10mm. The results are shown in Figures 5.28. It is noted that increasing the rung width decreases the maximum force generated and the ratio lifting/dragging doesn't improve, while increasing the layer number and their thickness causes an increase on forces generated and improves the ratio up to 4.8.

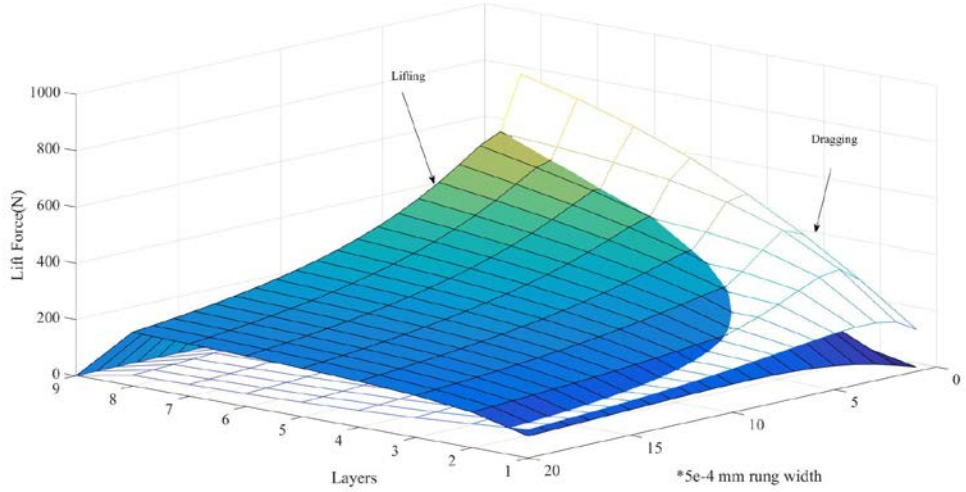

a)

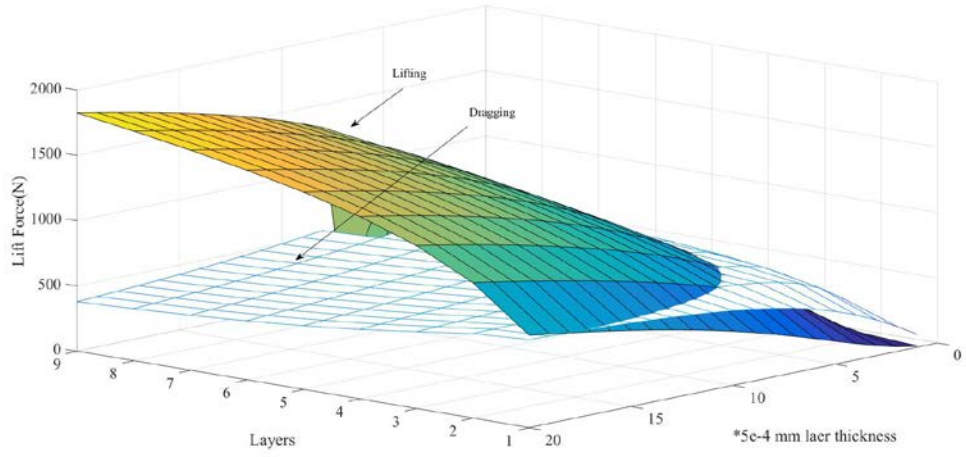

b)

Fig. 5.27 Lifting and Dragging forces: a) results varying the width; b) results varying the thickness

On the third case for the window shaped track s_1 and s_2 and t_w were set as 80mm, 50 mm and 10mm. Subsequently t_{th} was varied from 10 mm to 23mm, changing the AWG wire size in each iteration from calibre 9 to 40. The result of this simulation is presented on figure 5.29. For this design It seems that the optimal design is to keep a low calibre in combination with a thin window coil.

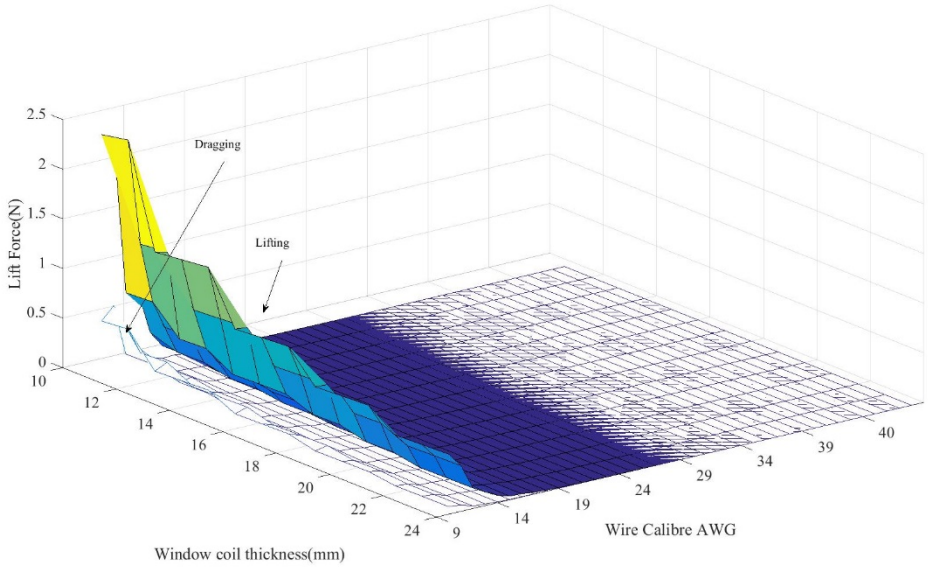

Fig. 5.28 a) Dragging and lifting Forces per loop; b) Dragging and lifting Forces under active area

These simulations show the effect that the track design can have. The variation on thickness, width, number of layers and type of track (Litz rung track or slotted) affect the lift/drag ratio and forces magnitude. Thus this is a multi-objective optimisation problem and the mathematical model should take in account not only the Halbach array dimensions but the levitation track in order to have the best design of it.

Nevertheless the design won't be entirely subjected to the force optimisation process but also to constraints of material volume and space availability.

It is important to note that this model uses "Lumped" inductance and its accuracy is still to be proven. However these graphs can give us a starting point to start our design.

5.1.4 Post Force Calculations

In order to determine how accurate the Post mathematical model[75] (see equation 5.1-5.4) is for the air-cored coil Halbach array, the lifting and dragging forces for each peak magnetic field obtained in section 5.1.2, is calculated as follows.

Due to its simplicity the track chosen for this experimentation is the slotted track discussed on section 5.3.1. This will reduce the time and computing resources required by COMSOL and MatLab to solve the models.

The details from the track are listed in table 5-II.

TABLE 5-II
GENERAL PARAMETERS FOR POST'S MODEL SIMULATION

Symbol	Quantity(units)	Description	Symbol	Quantity (units)	Description
w_t	100(mm)	Width of the track	z_g	2(mm)	Gap between track and Halbach aray
l_a	300(mm)	Length of the array(active area)	L_t	0.185 (μH)	Inductance per loop
n_l	1	Number of layers at each Litz rung	R_t	0.937(mΩ)	Resistance per loop
g_r	2(mm)	Gap between track rungs	f_c	0-500(Hz)	Frequency

The peak magnetic field for each model are summarised in table 5-III. And the results are presented in figure 5.24.

TABLE 5-III
PEAK MAGNETIC FIELD FROM DIFFERENT MODELS

Cube		Coil	
B_0	Teslas	B_0	Teslas
MatLab	0.14802	Matlab	0.092
FEMM	0.130	FEMM	0.106
COMSOL	0.122	COMSOL	0.0837
Post calculation(equation 5.2)	0.1487		

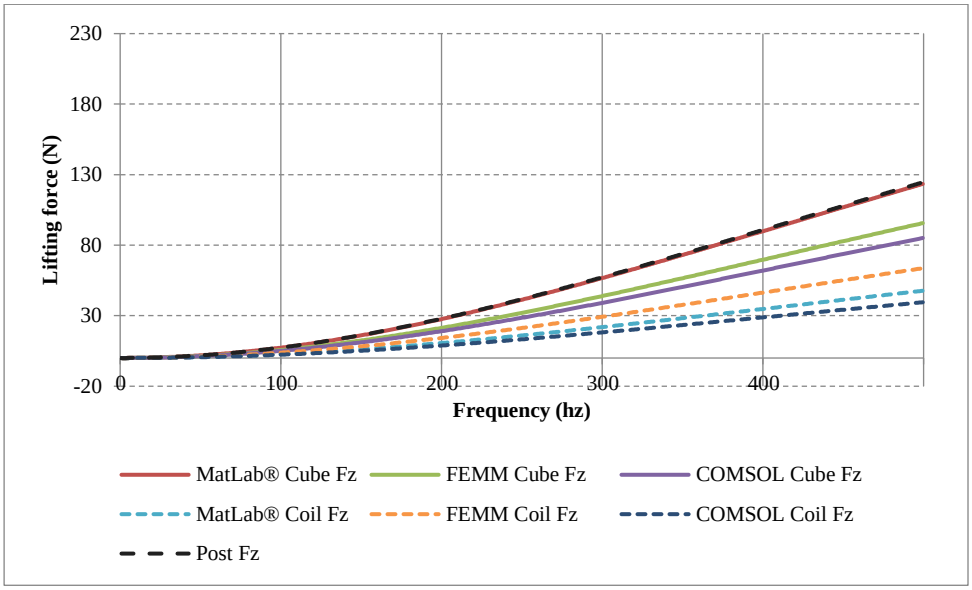

a)

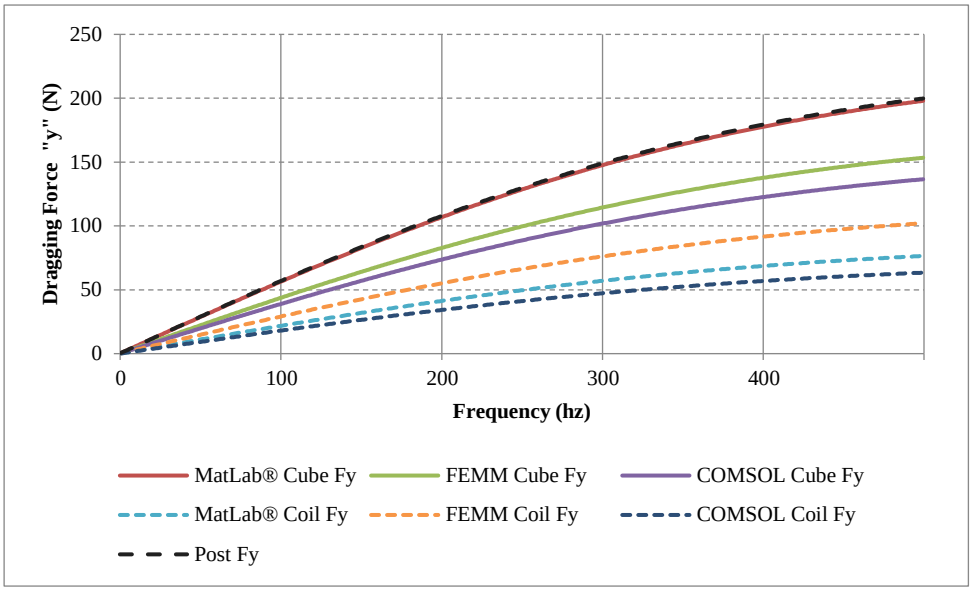

b)

Fig. 5.29 a) Lifting Forces; b) Dragging Forces

As can be seen in the previous figure 5.29, the peaks from the different models result in a difference in the force magnitude. Also, it can be noted that a relative small change in the magnetic field peak can have a large impact on the model. The red dotted line is showing the results obtained when the entire group of equations from Post model [75] is used. It can be seen as well that using the peak magnetic field from the cubic and cylindrical model results in large differences between models.

With the intention of having a reference a 3D model in COMSOL with the same characteristics was run (see figure 5.31). The only difference was that the simulation was run from 100-400 hertz in steps of 50 hertz in order to shorten the processing time.

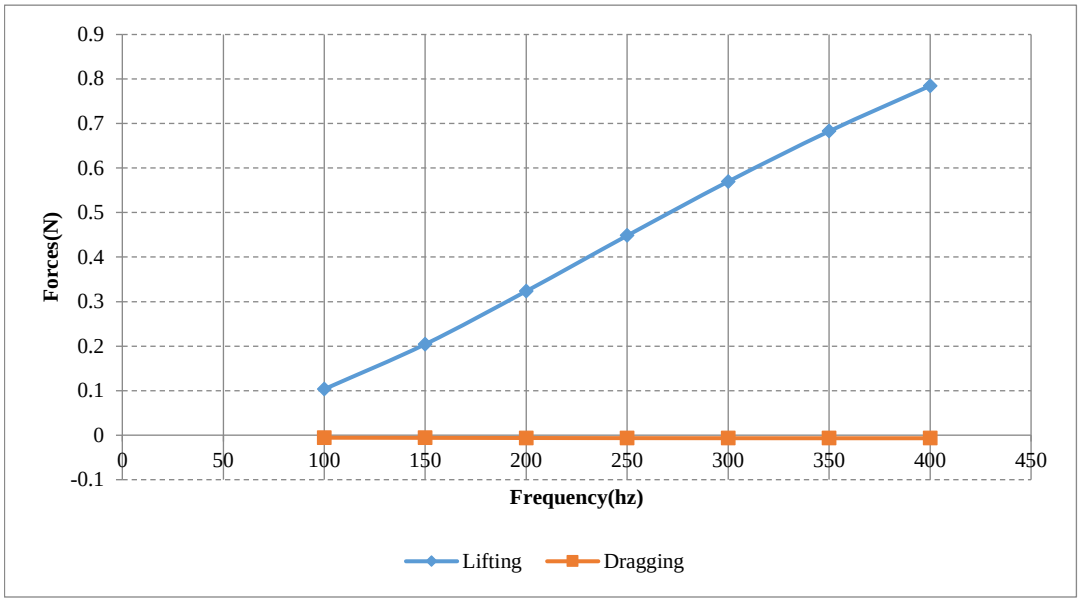

Fig. 5.30 COMSOL Results.

From the results in figure 5.30, it can be seen that even using the lowest magnetic field peak, the forces are under estimated by at least 100 times compared to the results in figure 5.29.

Storset has mentioned the difficulty of selecting the correct magnetic field peak in the Lumped(Post) model for an accurate calculation [167]. He also pointed out that it can lead to large inaccuracies. It is believed that the reason for this inaccuracy is that Post makes certain considerations related to the dimensions of the device that do not apply to all designs (see details at [168]). These considerations are listed as follow:

- Each individual loop is decoupled electrically from their neighbours.
- Self-inductance should be substantially larger than mutual inductance in the circuit.
- For a window shape track the dimension between one leg of the loop in the track and the next is larger than the wavelength.

This is why Storset calculates the forces as an Infinite Track model. In the following sections the force will be derived based on Storset's documents. Storset considers the Halbach array movement over the levitation track, although since the Air-Cored Coil Halbach Array concept is stationary, at this point, this part of the mathematical model will be obviated.

5.1.5 Storset Force Calculations

The model presented by Storset [167],[169] is similar to the process used to obtain the induced emf in a squirrel cage. In this model the changing magnetic field crossing a conductor loop will generate a current resulting in a repulsion force opposing the source of the magnetic field. Figure 5.31 illustrates the effect of the magnetic field on the track whilst figure 5.32 presents a diagram of the induced currents due to the magnetic field crossing the plane of each loop.

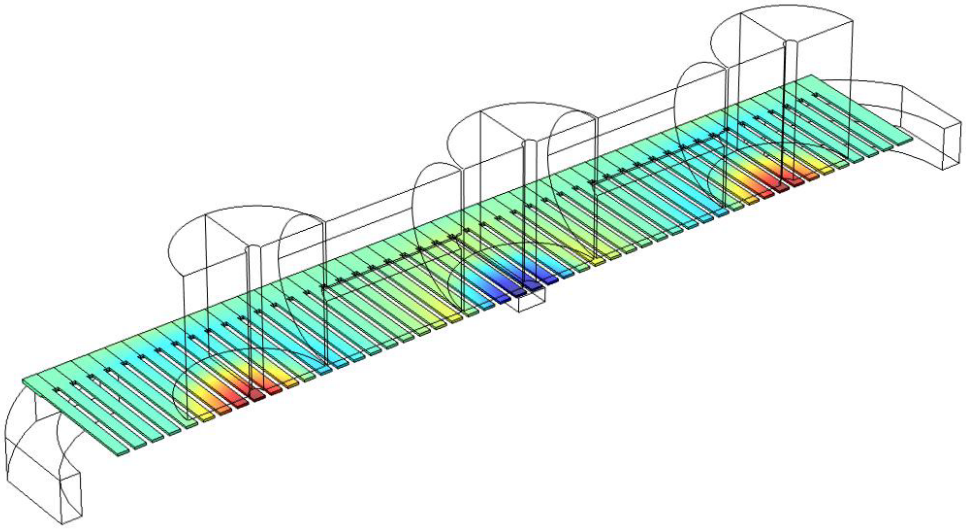

Fig. 5.31 Magnetic field crossing a ladder track.

The differential equation system shown below (equation 5.26) represents the relationship between the magnetic field crossing the track and its resistance, inductance and induced current.

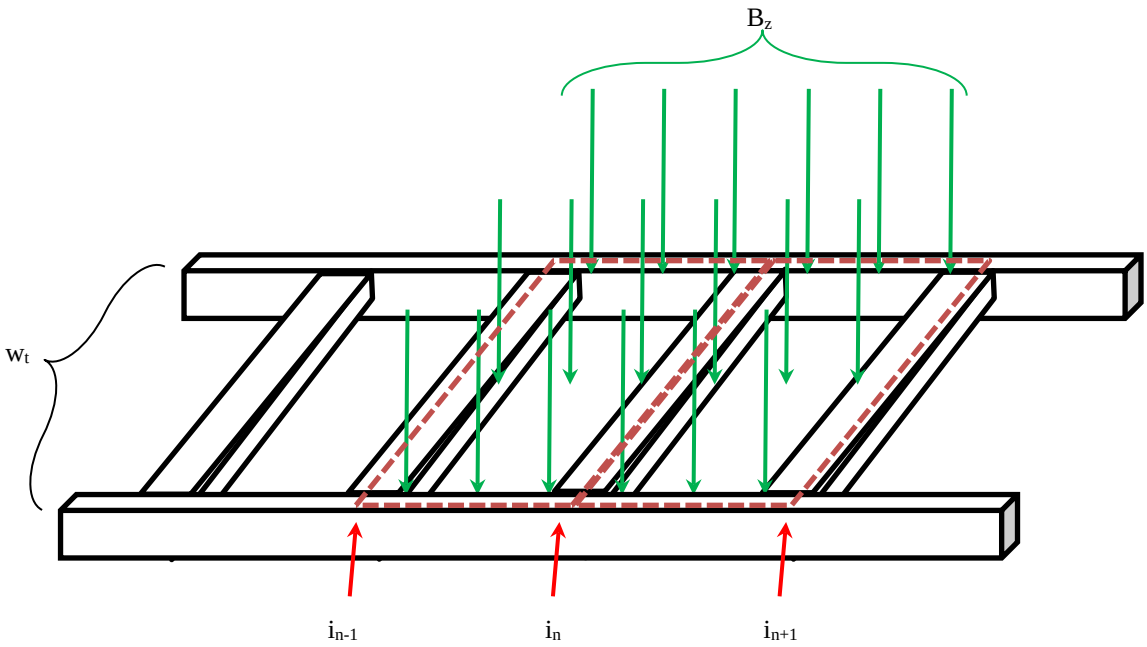

Fig. 5.32 Magnetic field crossing a ladder track.

$$\frac{d}{dt}i\{n\} = -\mathcal{R}\mathcal{L}^{-1}i\{n\} - \mathcal{L}^{-1}\{E_n\} \qquad \textit{Eq. 5.26}$$

In here i is a current vector of n elements. Similarly E is the result of the magnetic field time derivative crossing a loop area of the *nth* loop while $\mathcal{R}$ and $\mathcal{L}$ are the resistance and inductance matrix of the levitation track shown in equation 5.28 and 5.29.

$$E_n = -\frac{d}{dt}\int_{y_n}^{y_{n+1}}\int_{-w_t}^{w_t} B_z\, dx\, dy \qquad \textit{Eq. 5.27}$$

To calculate E the magnetic field from the coil mathematical model is used (figure 5.18 and 5.19).

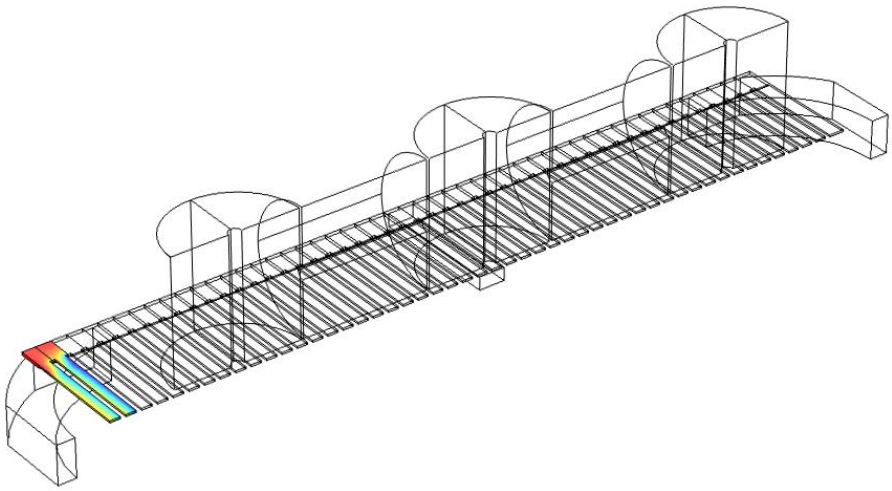

Fig. 5.33 COMSOL Results.

A double integral using Simpson's approximation over the *xy* plane is done covering each loop of the track (see figure 5.33). The parameters of the track and other details are taken from table 5-II. The results are shown in figure 5.34

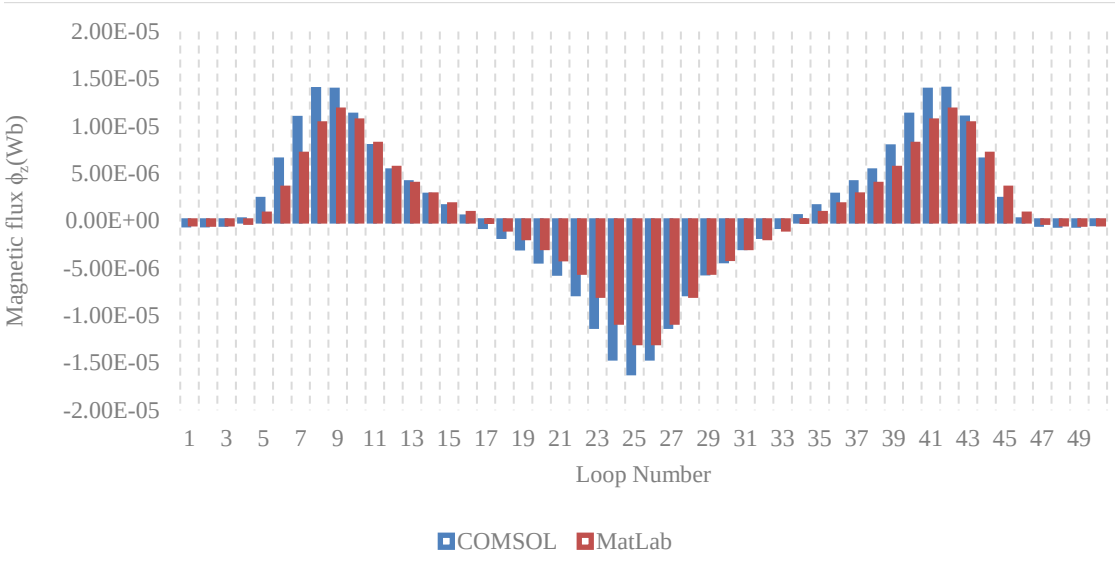

Fig. 5.34 COMSOL vs Storset MatLab code. Magnetic field per loop.

Furthermore $\mathcal{R}$ and $\mathcal{L}$ are matrices in accordance to the schematic presented in Figure 5.35.

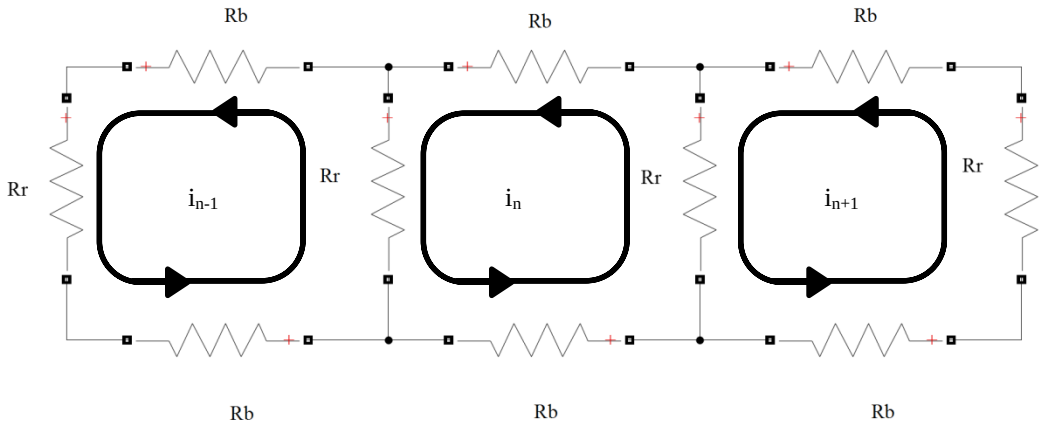

Fig. 5.35 Resistance-Current schematic

The matrices are obtained as shown in equations 5.28 and 5.29, using equation 5.18 - 5.24 to define the self-inductance, mutual inductance and resistance of the rungs and bars at the slotted track.

$$\mathcal{L} = \begin{bmatrix} \ddots & \vdots & \vdots & \vdots & \\ \cdots & L & M_1 & M_2 & \cdots \\ \cdots & M_1 & L & M_1 & \cdots \\ \cdots & M_2 & M_1 & L & \cdots \\ & \vdots & \vdots & \vdots & \ddots \end{bmatrix} \qquad \textit{Eq. 5.28}$$

$$\mathcal{R} = \begin{bmatrix} \ddots & \vdots & \vdots & \vdots & \\ \cdots & 2(R_r + R_b) & -R_r & 0 & \cdots \\ \cdots & -R_r & 2(R_r + R_b) & -R_r & \cdots \\ \cdots & 0 & -R_r & 2(R_r + R_b) & \cdots \\ & \vdots & \vdots & \vdots & \ddots \end{bmatrix} \qquad \textit{Eq. 5.29}$$

A Simulink model to solve the ordinary differential equation system was created in Simulink(figure 5.36). The current in each one of the rungs is calculated as $i_{rung} = i_n - i_{n-1}$.

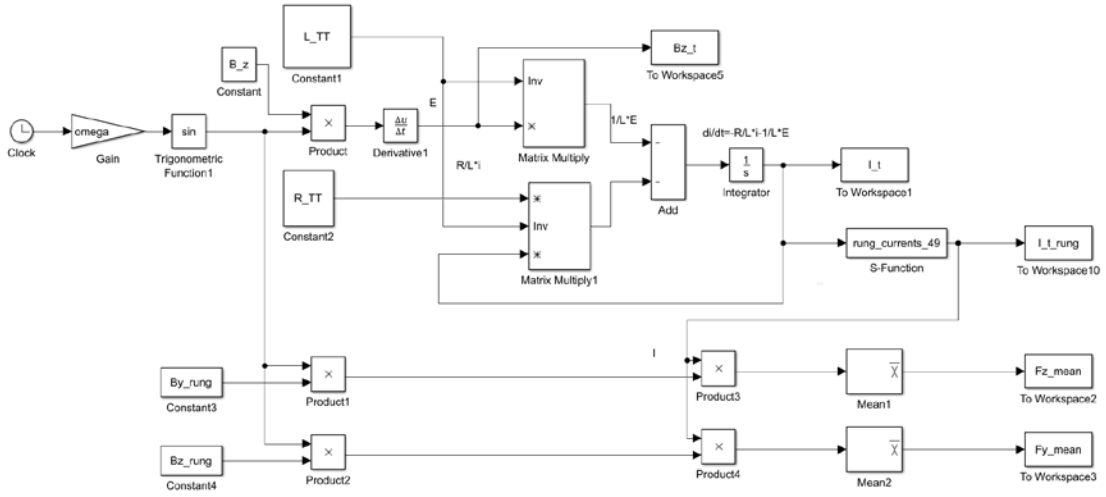

Fig. 5.36 Simulink schematic for the Differential equation system.

The currents were obtained from the Storset MatLab model from 100 Hz to 400 Hz. The currents obtained here and currents obtained from COMSOL are compared in figures 5.37-5.38.

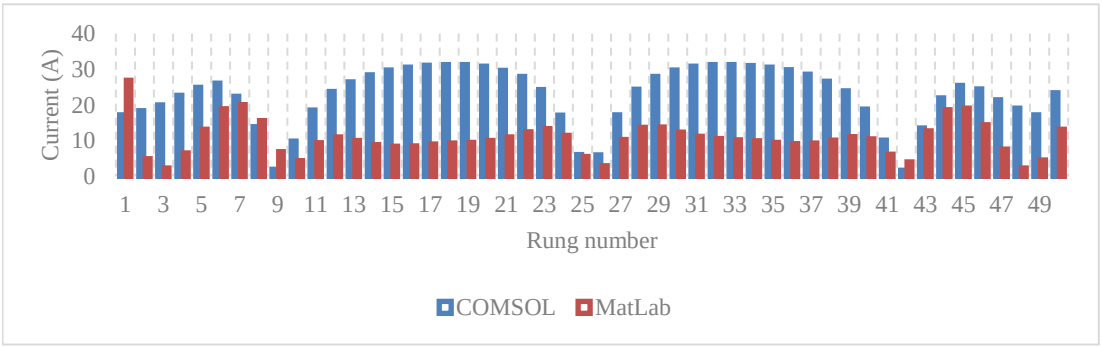

100 Hz

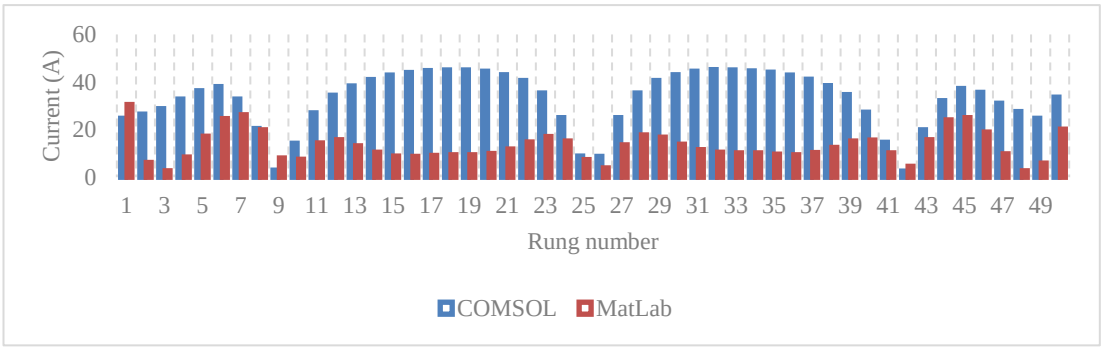

150 Hz

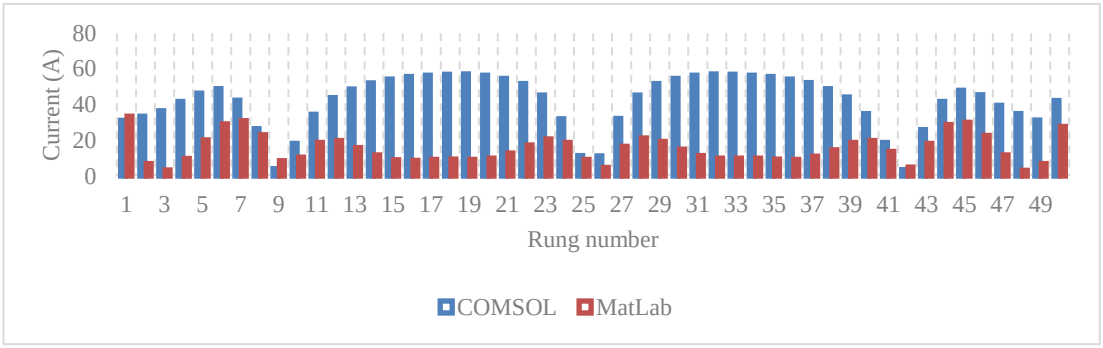

200 Hz

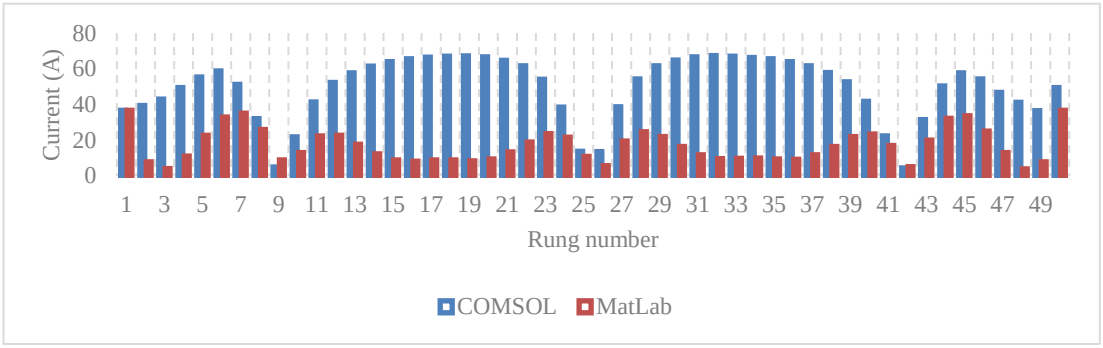

250 Hz

Fig. 5.37 COMSOL vs MatLab comparison: Current calculation results 100-250 Hz

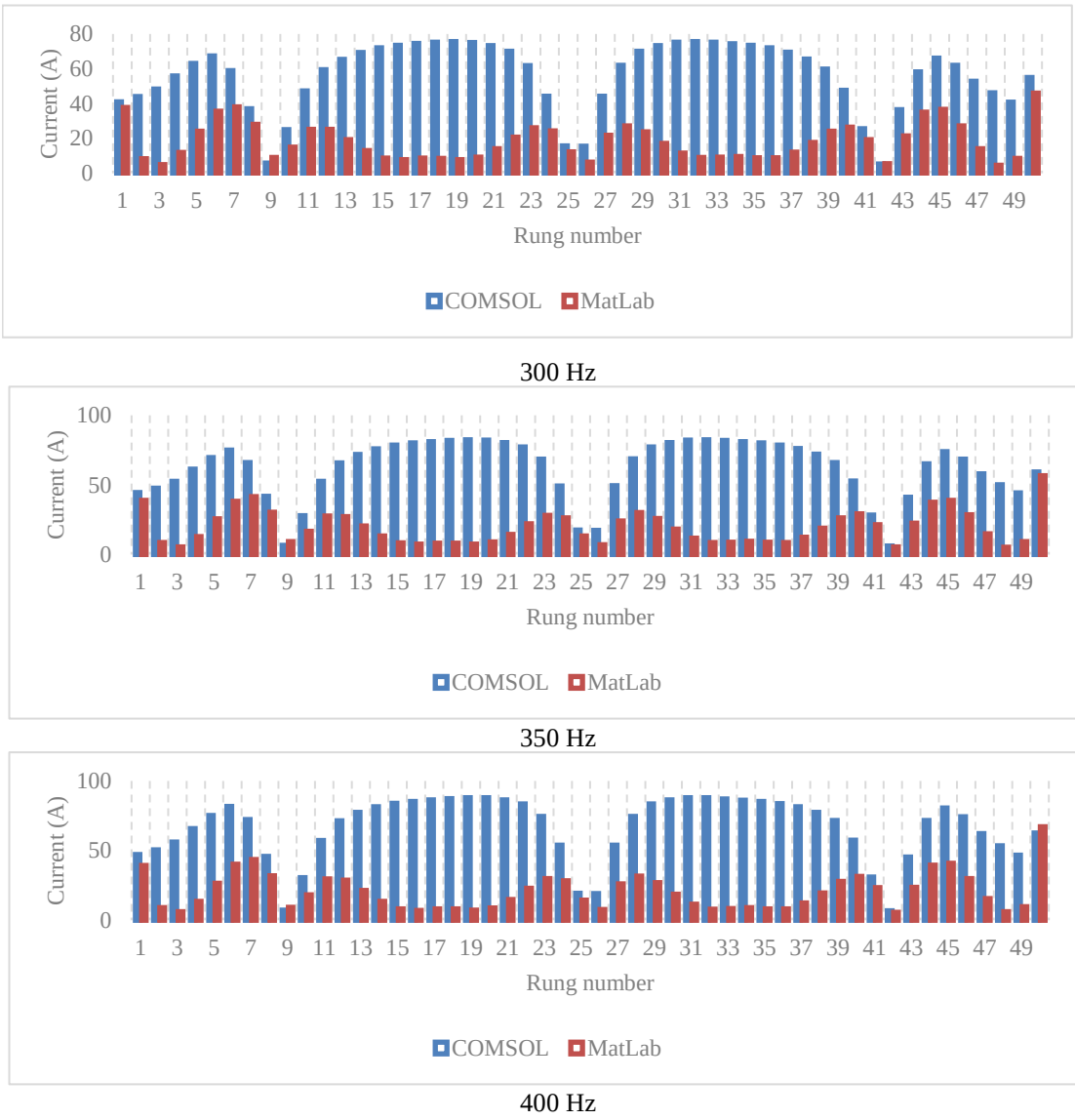

Fig. 5.38 COMSOL vs MatLab comparison: Current calculation results 300-400 Hz

Then the magnetic field was calculated over a line in the middle of each rung as shown in figure 5.39, with the results presented in figure 5.40.

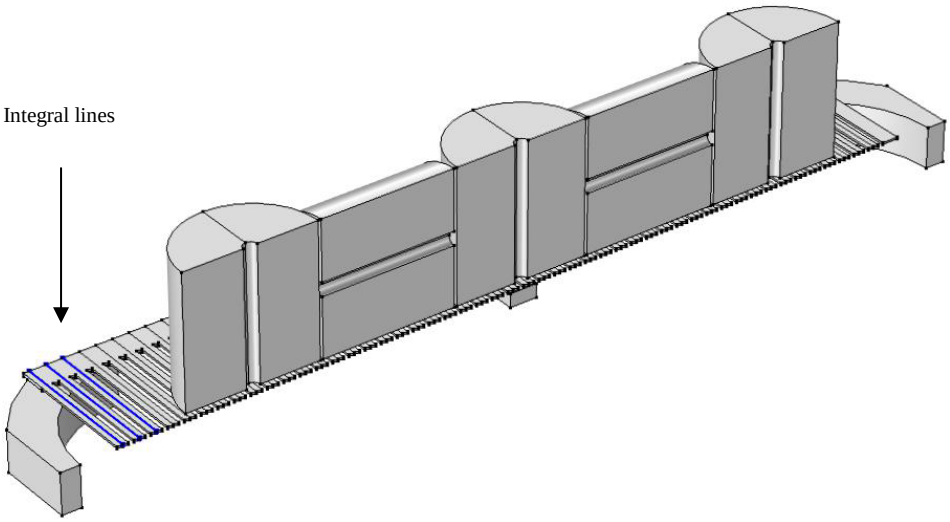

Fig. 5.39 Integral over the rungs at the track illustration

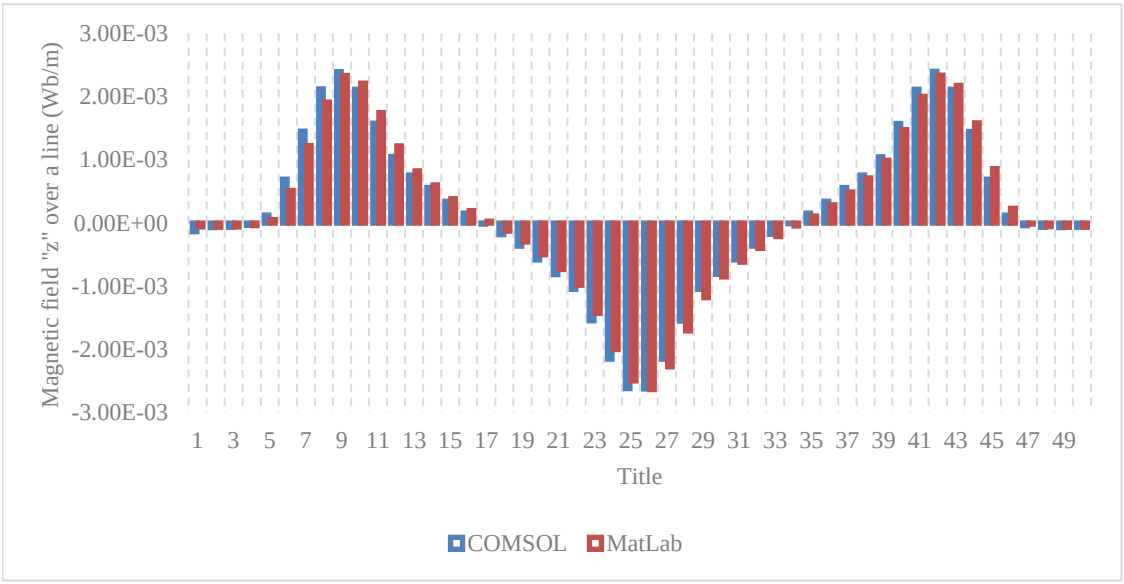

a)

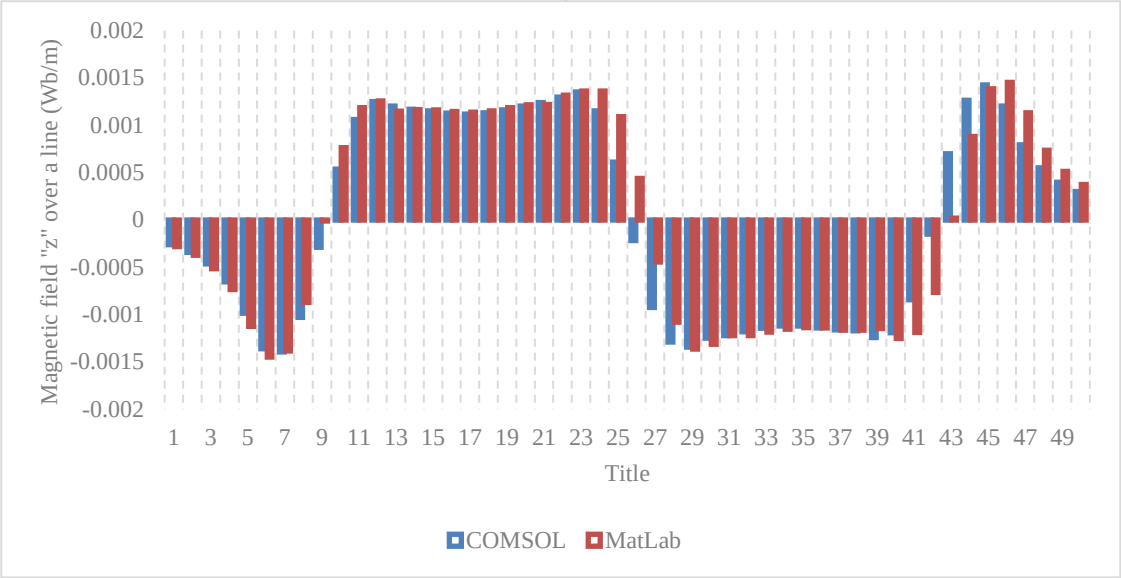

b)

Fig. 5.40 COMSOL vs MatLab comparison: a)Bz integral over each rung; b) By integral over each rung

The Lorentz force is calculated for each rung *n* as:

$$F_{yn} = \int_{-w_t}^{w_t} i_{xn} . B_{zn}^{s} \, dx \qquad \textit{Eq. 5.30}$$

$$F_{zn} = \int_{-w_t}^{w_t} i_{xn} . B_{yn}^{s} \, dx \qquad \textit{Eq. 5.31}$$

Finally the forces on the entire track are summed as presented in equation 5.32.

$$F_T = \sum_{n=1}^{N} F_n \qquad \textit{Eq. 5.32}$$

The time average force from COMSOL and MatLab using Storset method[167][169] are presented in figure 5.41.

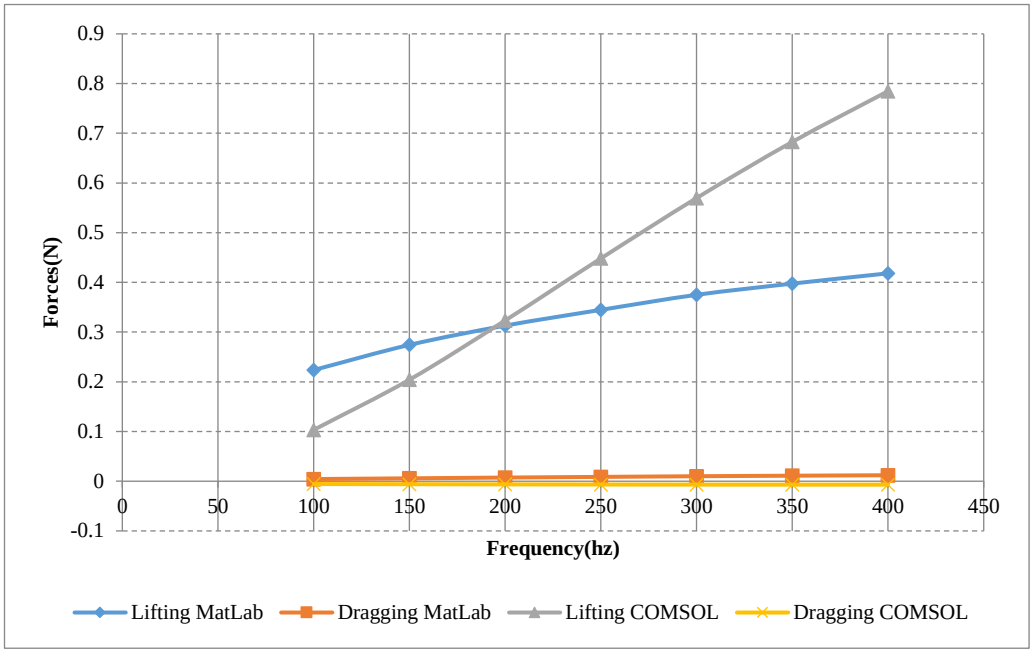

Fig. 5.41 COMSOL Results.

It can be seen that using the Storset Mathematical model result in more accurate magnitudes compared with COMSOL simulations than any of the results obtained with the “Post” mathematical model. However Storset also mentioned that the model presented in [167], [169] doesn’t take in account the forces generated by the sidebars of the track.

Figure 5.42 shows the detail of the track, and the following figure 5.43 shows how the width of the side bar affects the lifting force generated.

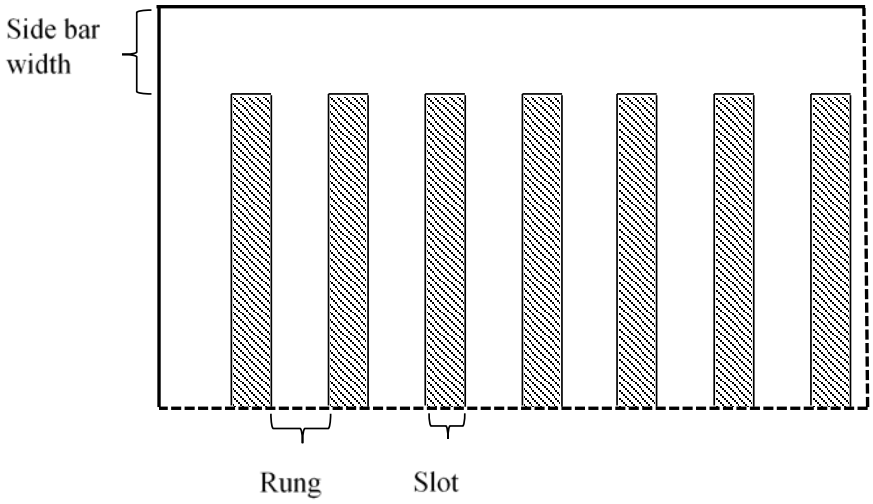

Fig. 5.42 Track detail. Top view

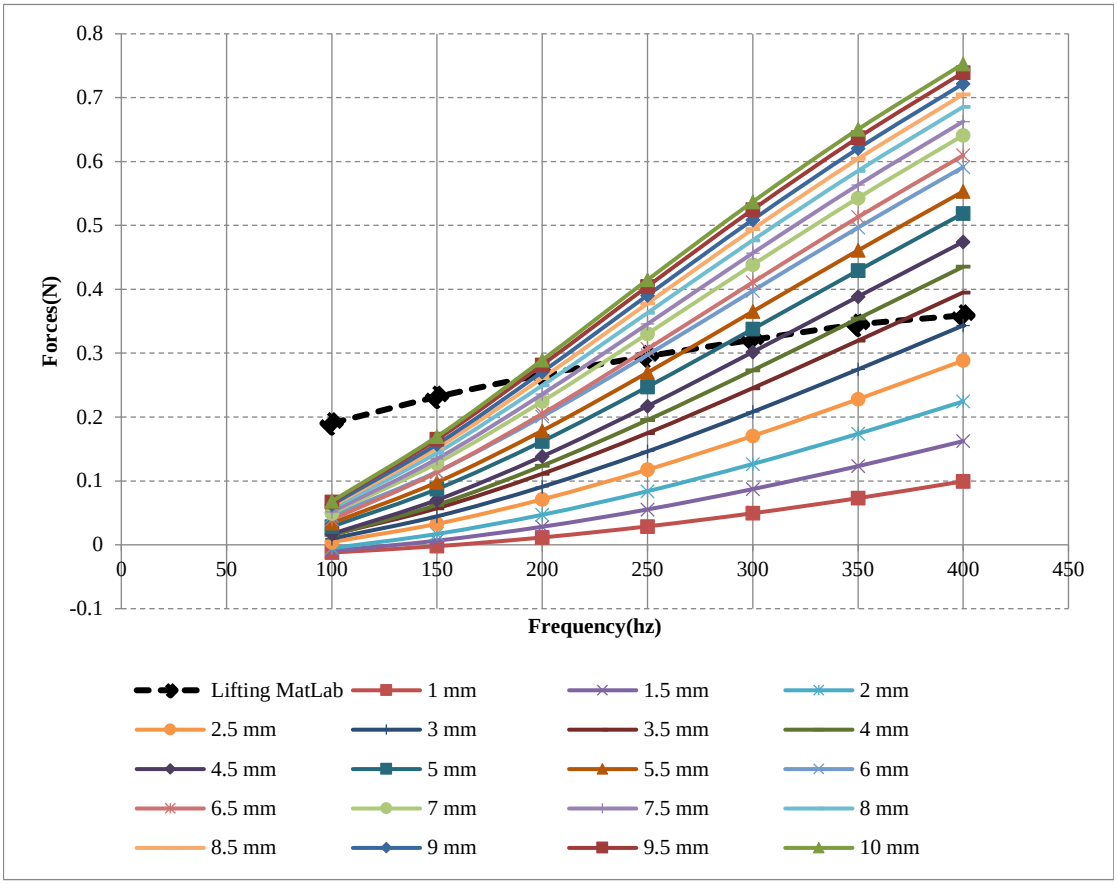

Fig. 5.43 Side bar variation effect

As can be seen in figure 5.43 varying the side bar width does affect the lifting force generation of the device. It also can be seen that not only the magnitude of the force

is different from the Storset mathematical model but the slope of it in relationship with the frequency. This might be related to the side bar induction omission in the mathematical model, since the lifting/dragging ratio at a certain frequency will be related to the inductance/resistance relationship as mentioned by Post[75], [170].

Hence for this project further iterations on the design calculations will be realised in COMSOL.

5.2 Control strategies

As stated before the goal of this project is to design an active magnetic bearing system. In order to accomplish this, a control strategy must be implemented. A strategy called sliding mode control is being studied using the concept proposed in previous chapters.

A mathematical model is essential for understanding the system from a control strategy implementation point of view [102],[121]. A common way to represent a model is in state space as shown in equation 5.33.

$$\ddot{\rho} = f(\dot{\rho}) + G(\rho)u$$
$$y = h(\rho) \qquad \textit{Eq. 5.33}$$

Where ρ is the state vector, u is the input vector and y is the ouput vector.The floating translator is presented in the following figure highlighting the dimensions as well as the axis x,y,z and angle θ orientation.

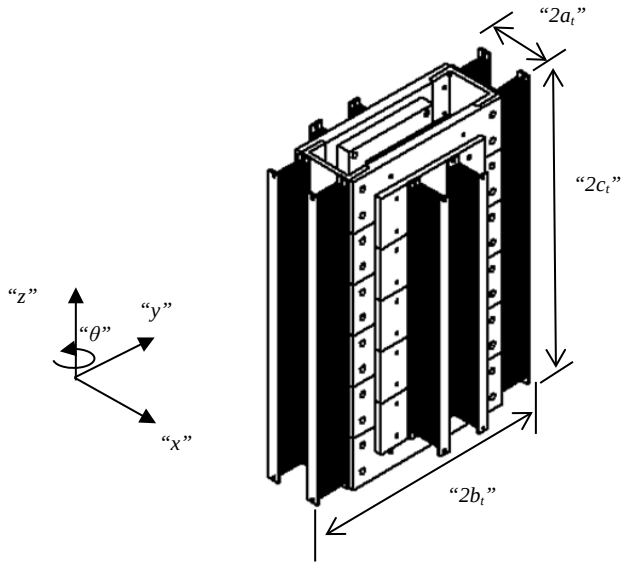

Fig. 5.44 Isometric view description of the translator C

One of the goals of this design is to leave the translator free to travel over the "*z*" axis, thus the plan is to constrain the movement on the plane "*xy*" but allow free translation along the "*z*" axis. Figures 5.44 and 5.45 presents the force locations and more detail of the translator dimensions.

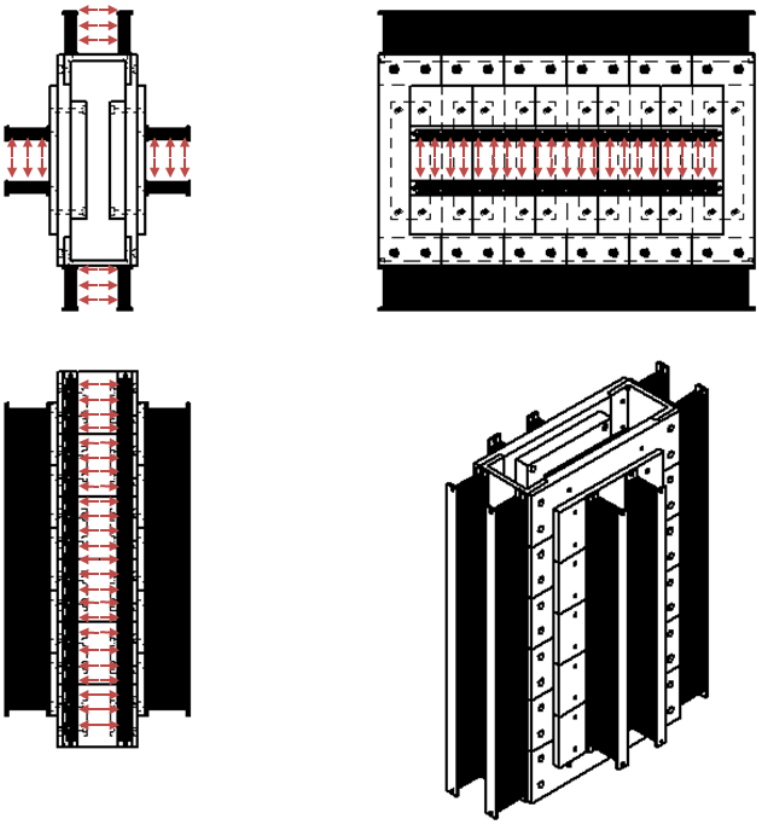

Fig. 5.45 Forces acting over an area (on the levitation track) are represented as red arrows.

Figure 5.44 shows the translator for the 1kW machine (presented previously in figure 5.4). Note that the levitation tracks are installed on the four sides of the translator. The red arrows in figure 5.45 represents the forces acting in two directions, this is achieved by switching two of the coils as explained at the beginning of this chapter (see figure 5.2).

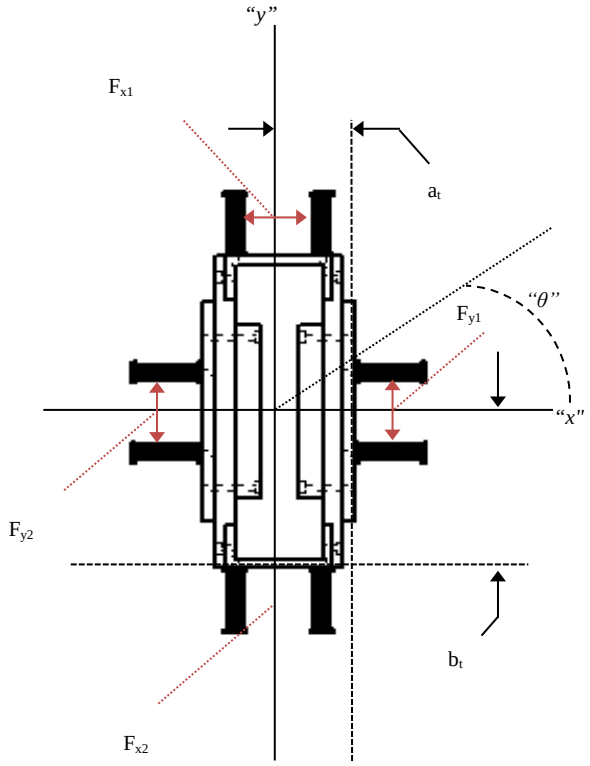

Fig. 5.46 Top view description of the translator

From figure 5.46 it can be seen that the magnetic bearing device centre positions are defined as follows:

$$p_{x1} = [a_t, 0, 0]$$
$$p_{x2} = [-a_t, 0, 0]$$
$$p_{y1} = [0, b_t, 0]$$
$$p_{y1} = [0, -b_t, 0] \qquad \textit{Eq. 5.34}$$

If Euler angular description is applied, the result is [171] :

$$R = \begin{bmatrix} \cos\theta & \sin\theta & 0 \\ -\sin\theta & \cos\theta & 0 \\ 0 & 0 & 1 \end{bmatrix} \qquad \textit{Eq. 5.35}$$

Note that for small angles $\sin\theta \approx \theta$ and $\cos\theta \approx 1$, therefore we have that equation 5.35 becomes:

$$R = \begin{bmatrix} \theta & 0 & 0 \\ 0 & \theta & 0 \\ 0 & 0 & 1 \end{bmatrix} \qquad \textit{Eq. 5.36}$$

Then according to [121] the system XYZ position is:

$$P_{mx1} = R * p_{+x} + \begin{bmatrix} x \\ y \\ 0 \end{bmatrix} = \begin{bmatrix} a_t * \theta + x \\ y \\ 0 \end{bmatrix}$$

$$P_{mx2} = R * p_{-x} + \begin{bmatrix} x \\ y \\ 0 \end{bmatrix} = \begin{bmatrix} -a_t * \theta + x \\ y \\ 0 \end{bmatrix} \qquad \textit{Eq. 5.37}$$

$$P_{my1} = R * p_{+y} + \begin{bmatrix} x \\ y \\ 0 \end{bmatrix} = \begin{bmatrix} x \\ y + b_t * \theta \\ 0 \end{bmatrix}$$

$$P_{my2} = R * p_{-y} + \begin{bmatrix} x \\ y \\ 0 \end{bmatrix} = \begin{bmatrix} x \\ y - b_t * \theta \\ 0 \end{bmatrix}$$

In order to obtain a state of states model, linearization is needed at every degree of freedom according to the following equation

$$f(x,y) \approx f(x_0,y_0) + \frac{\partial f}{\partial x}(x_0,y_0)(x - x_0) + \frac{\partial f}{\partial y}(x_0,y_0)(y - y_0) \qquad \textit{Eq. 5.38}$$

Giving figure 5.46 description, the sum of forces in the “x” and “y” axis are:

$$\sum Fx = m\ddot{x} = F_{x1} + F_{x2} \qquad \textit{Eq. 5.39}$$

$$\sum Fy = m\ddot{y} = F_{y1} + F_{y2} \qquad \textit{Eq. 5.40}$$

Whilst the momentum sum is:

$$\sum M_z = J_z\ddot{\theta} = b_t F_{x1} - b_t F_{x2} - a_t F_{y1} - a_t F_{y2} \qquad \textit{Eq. 5.41}$$

If all the initial conditions (I_{0x1},I_{0x2},I_{0x3},I_{0x4},x_0,y_0) are taken as 0, then the state space representation simplified as:

$$\begin{bmatrix}\dot{x}\\ \ddot{x}\\ \dot{y}\\ \ddot{y}\\ \dot{\theta}\\ \ddot{\theta}\end{bmatrix}=\begin{bmatrix}1&0&0&0&0&0\\0&0&0&0&0&0\\0&0&1&0&0&0\\0&0&0&0&0&0\\0&0&0&0&1&0\\0&0&0&0&0&0\end{bmatrix}\begin{bmatrix}x\\ \dot{x}\\ y\\ \dot{y}\\ \theta\\ \dot{\theta}\end{bmatrix}$$
$$+\begin{bmatrix}0&0&0&0\\ \frac{F_{x1}}{m}&\frac{F_{x2}}{m}&0&0\\ 0&0&0&0\\ 0&0&\frac{F_{y1}}{m}&\frac{F_{y2}}{m}\\ 0&0&0&0\\ \frac{F_{x1}b_1}{J_\theta}&-\frac{F_{x2}b_1}{J_\theta}&\frac{F_{y1}a_1}{J_\theta}&-\frac{F_{y2}a_1}{J_\theta}\end{bmatrix}\begin{bmatrix}I_{x1}\\ I_{x2}\\ I_{y1}\\ I_{y2}\end{bmatrix} \qquad \textit{Eq. 5.42}$$

$$y=\begin{bmatrix}x\\ \dot{x}\\ y\\ \dot{y}\\ \theta\\ \dot{\theta}\end{bmatrix} \qquad \textit{Eq. 5.43}$$

For the 1kW machine the mass of the translator was calculated as 984 kg and the moment of Inertia has been calculated as a simplified rectangular parallelepiped.

$$J_\theta=\frac{((2*a_t)^2+(2*c_t)^2)*m_t}{12} \qquad \textit{Eq. 5.44}$$

Following the documents [143] and [172], in order to calculate the sliding mode control system we first define the switching function “s” as shown below, where the error is $e_j=\rho-\rho_d$

$$s_j=\dot{e}_j+c_{j1}e_j+c_{j0}\int e_j \qquad \textit{Eq. 5.45}$$

$$\Sigma_{0j}=\dot{s}_j+Z_{0j}s_j \qquad \textit{Eq. 5.46}$$

$$\dot{\Sigma}_j=-K_j sgn(\Sigma_j) \qquad \textit{Eq. 5.47}$$

In order to take into account discontinuity the function sign was replaced by the saturation function as follows

$$\mathrm{sat}(\Sigma_j) = \begin{pmatrix} 1 & \dot{\Sigma}_j > \epsilon \\ \frac{\dot{\Sigma}_j}{\epsilon} & -\epsilon \leq \dot{\Sigma}_j \geq \epsilon \\ -1 & \dot{\Sigma}_j < \epsilon \end{pmatrix} \qquad \textit{Eq. 5.48}$$

$$\dot{u} = G(\rho)^{-1}\left[-K\mathrm{sat}(\Sigma_j) - \dot{F}(\rho) - G(\rho)u - (C_1 + Z_0)\ddot{\rho} - (C_1 + Z_0C_1)\dot{\rho} - Z_0C_2(\rho - \rho_d)\right] \qquad \textit{Eq. 5.49}$$

Having the entire model a code was implemented in MatLab and Simulink. The diagram is shown in Figure 5.47

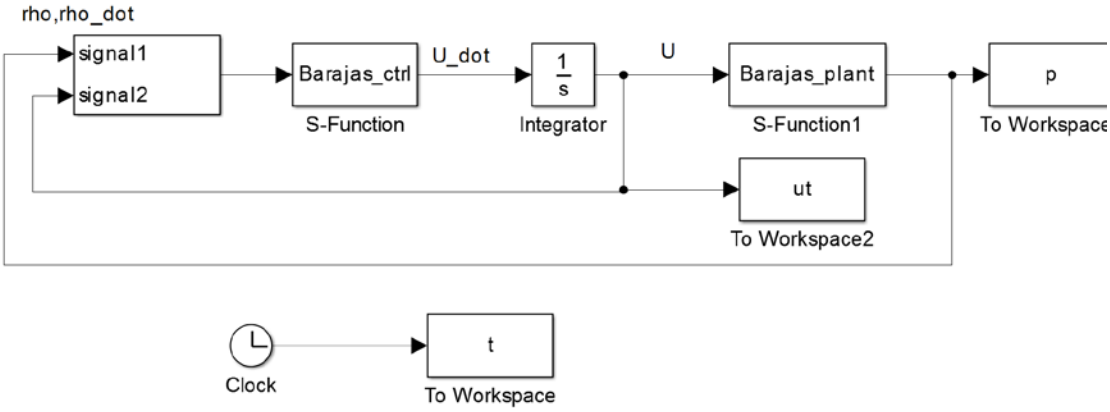

Fig. 5.47 Linear state space description with output matrix C and feed through matrix C

The control signal "U" is obtained integrating "$\dot{U}$" as seen in figure 5.47. The constants matrices C1 and C2 are chosen such that $\pi^2 + C_2\pi + C_1 = 0$ is Hurwitz. A Hurwitz polynomial is one in which the coefficients are positive real numbers and the roots are in the left half plane of the complex plane. Also $Z_0$is a real coefficient matrix. The coefficients are shown in TABLE 5-IV.

TABLE 5-IV
CONTROL COEFFICIENTS

symbol	coefficient	symbol	coefficient	symbol	coefficient	symbol	coefficient
C11	90	C21	100	Z01	100	k1	370
C12	90	C22	100	Z02	100	k2	370
C13	90	C23	100	Z03	100	k3	370

The results for a non-perturbation scenario are presented in figure 5.48-5.51. Figure 5.48 shows the control signals response whilst figure 5.49-5.51 show the controlled variables, x,y and θ.

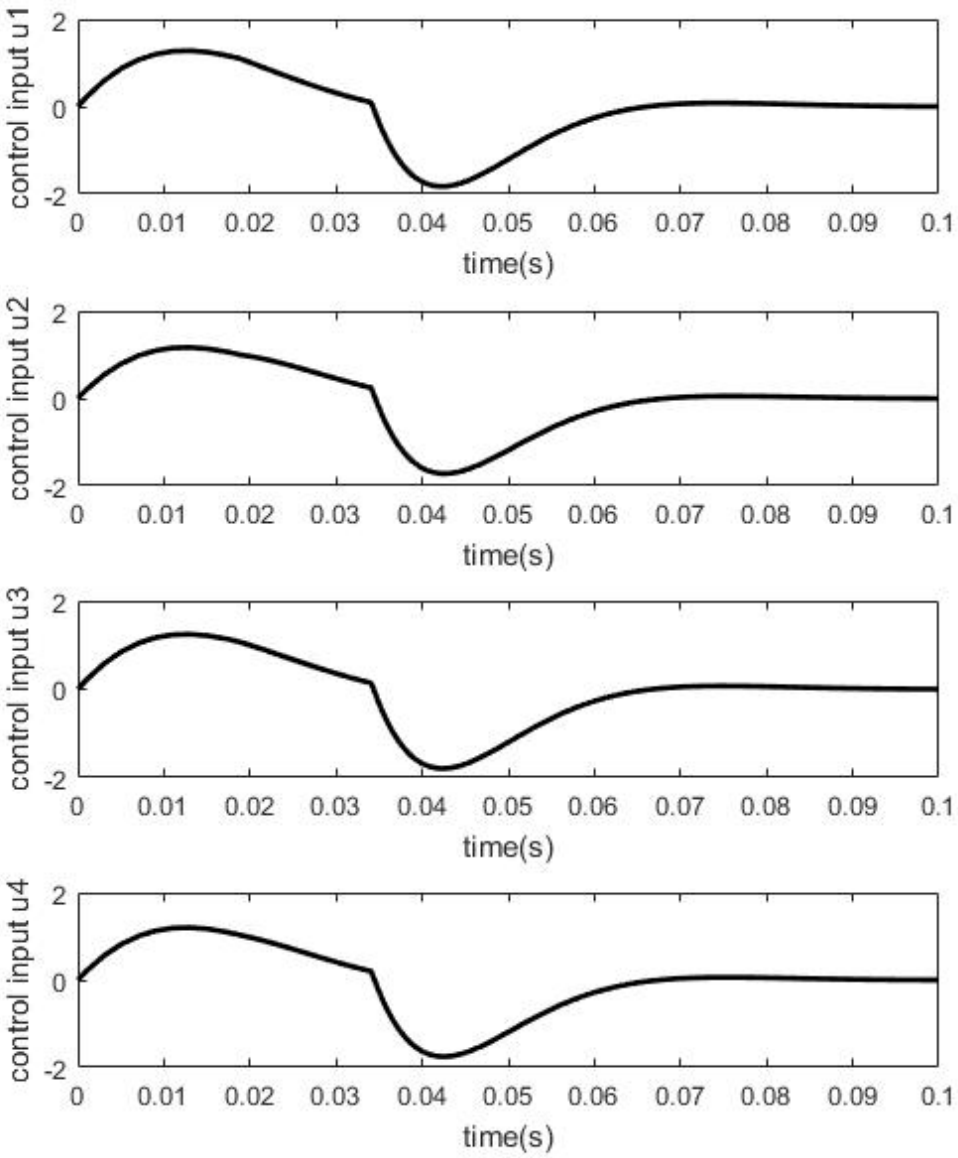

Fig. 5.48 Current control signals

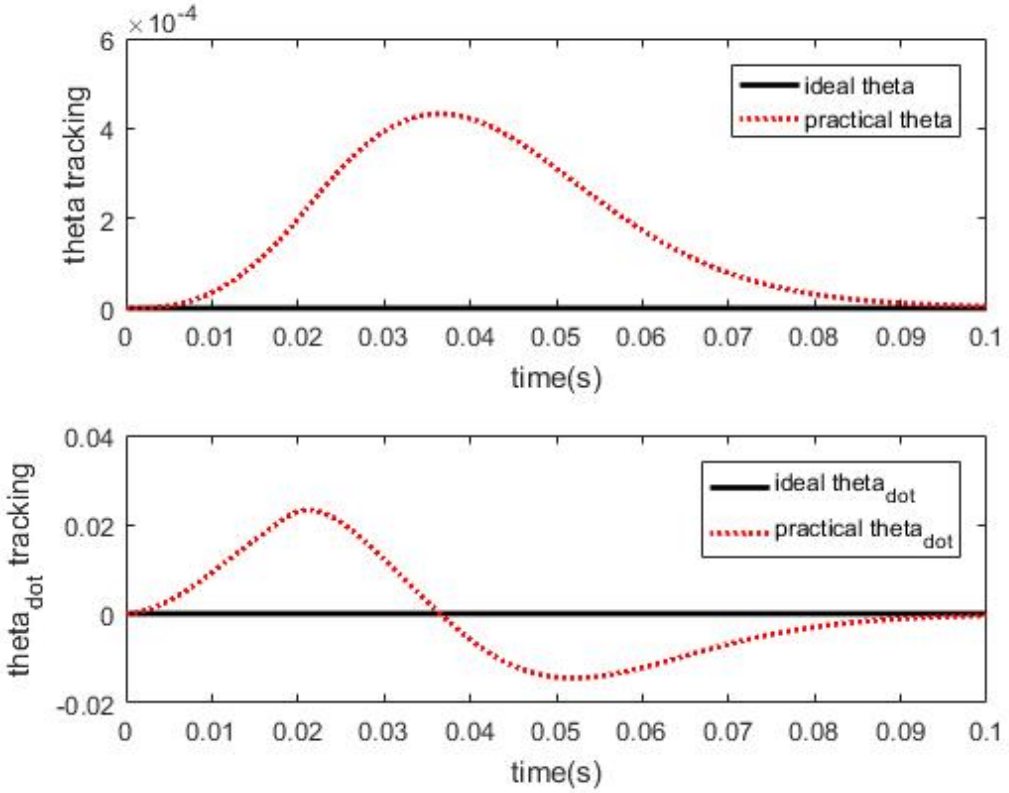

Fig. 5.49 Angle position and angular velocity θ

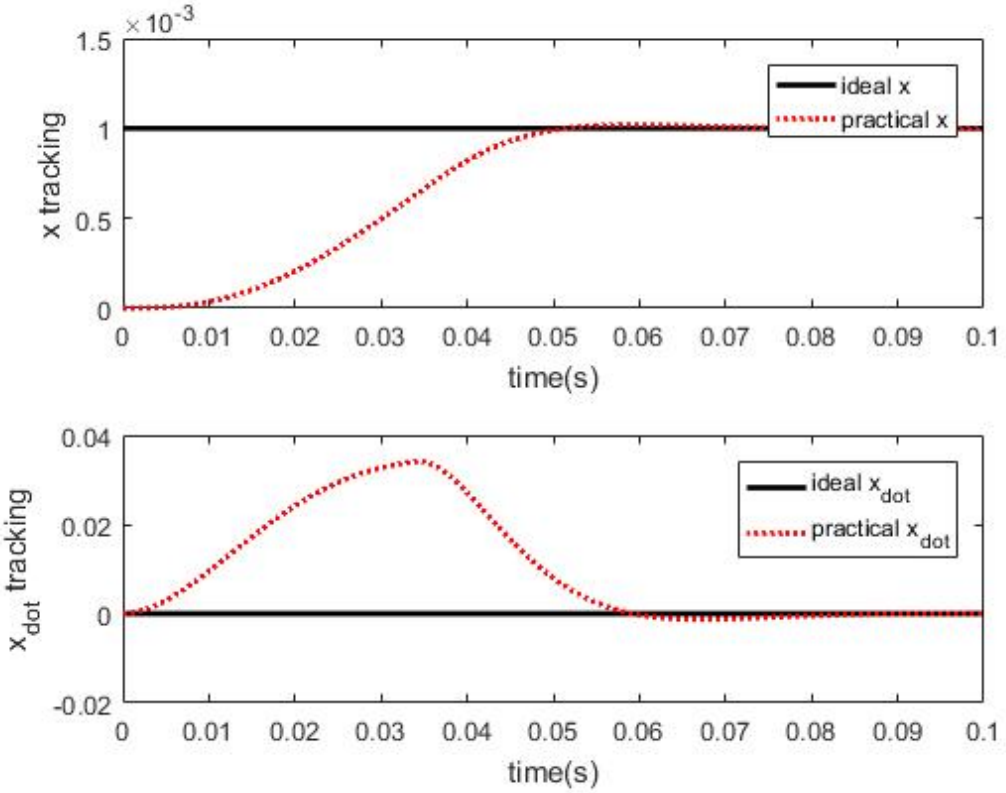

Fig. 5.50 Linear position and velocity “x”

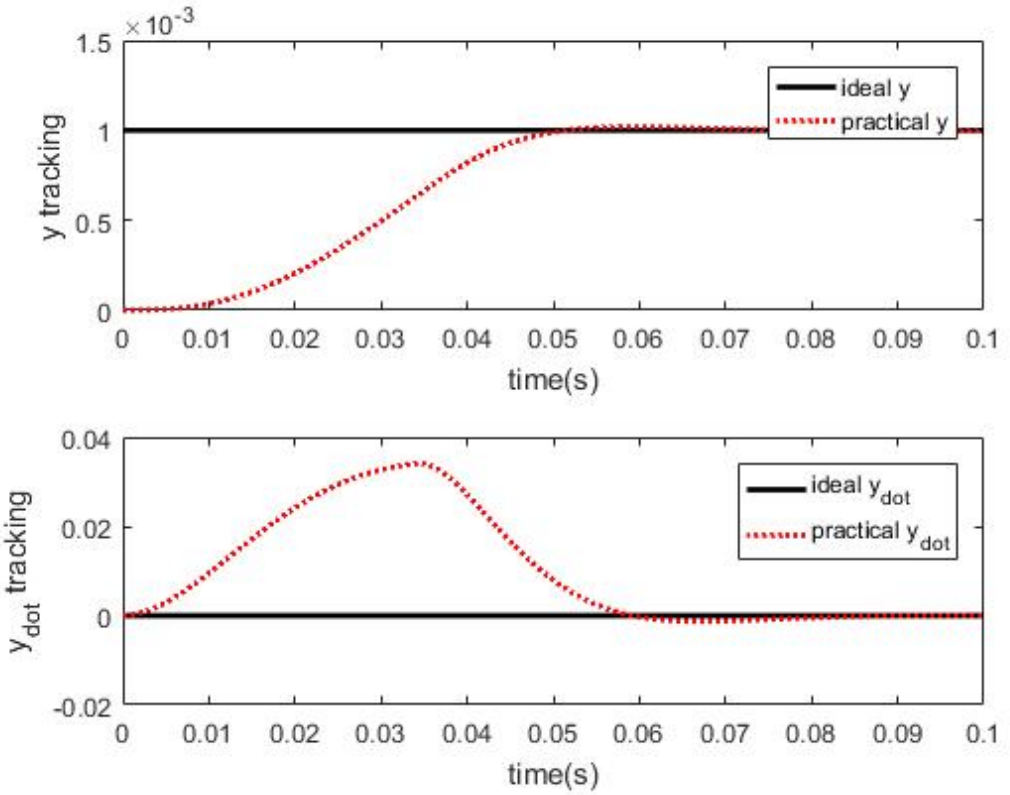

Fig. 5.51 Linear position and velocity "y"

The set point in the "*x*" and "*y*" axis is reached within 0.05s with virtually no overshoot whilst the angle position "θ" takes a little longer to stabilised.

A sign of a highly ideal model with no disturbances is the fact that the control currents remain below 2 amperes. This is expected to change in more realistic scenarios where external elements affecting the system are taken in account.

A model including disturbances is considered for future work. Thi will result in a closer representation of the system response in order to evaluate robustness of the control system and its real world applicability.

5.3 Experiments: Matching the concept to the theory

With the intention of probing the concepts and calculations presented in the previous chapter, a prototype rig was manufactured by Fountain Design Ltd. In order to corroborate the proposed concept the rig needed to cover the following points:

- The array of coils and levitation track must be static and facing each other.
- Load cells are located to measure lifting and dragging forces. Additionally data acquisition equipment is needed to record the results.
- The coils leads are accessible in order to change the electric configuration. Since different frequencies will change the impedance of the circuit, capacitors are added to correct the power factor.

It is important to mention that at the time of the rig design, the forces calculation were based on Post model [168]. This led to overestimation that meant changes to the original design.

The design of the rig was setup for static testing using the dimensions mentioned in section 5.1 for the coils and wire used. Also because of its easy manufacture a window-shaped track was considered. These dimensions are summarised in the following tables: 5-V and 5-VI. The number of turns "*N*" was determined by using a 1mm diameter wire for the windings (see Figures 5.7 and 5.23).

Dimensions for the rig (see Figure 5.52) were chosen to fit the 1kW linear prototype mentioned at the beginning of this section (see Figures 5.6 and 5.7). This was with the intention of not only prove the concept but to work as a starting point for an optimisation process which will lead to an ideal design for larger C-Gen linear generators.

This section will describe the experiments carried out, challenges and results whilst chapter 6 will address the limitations and scalability of the device.

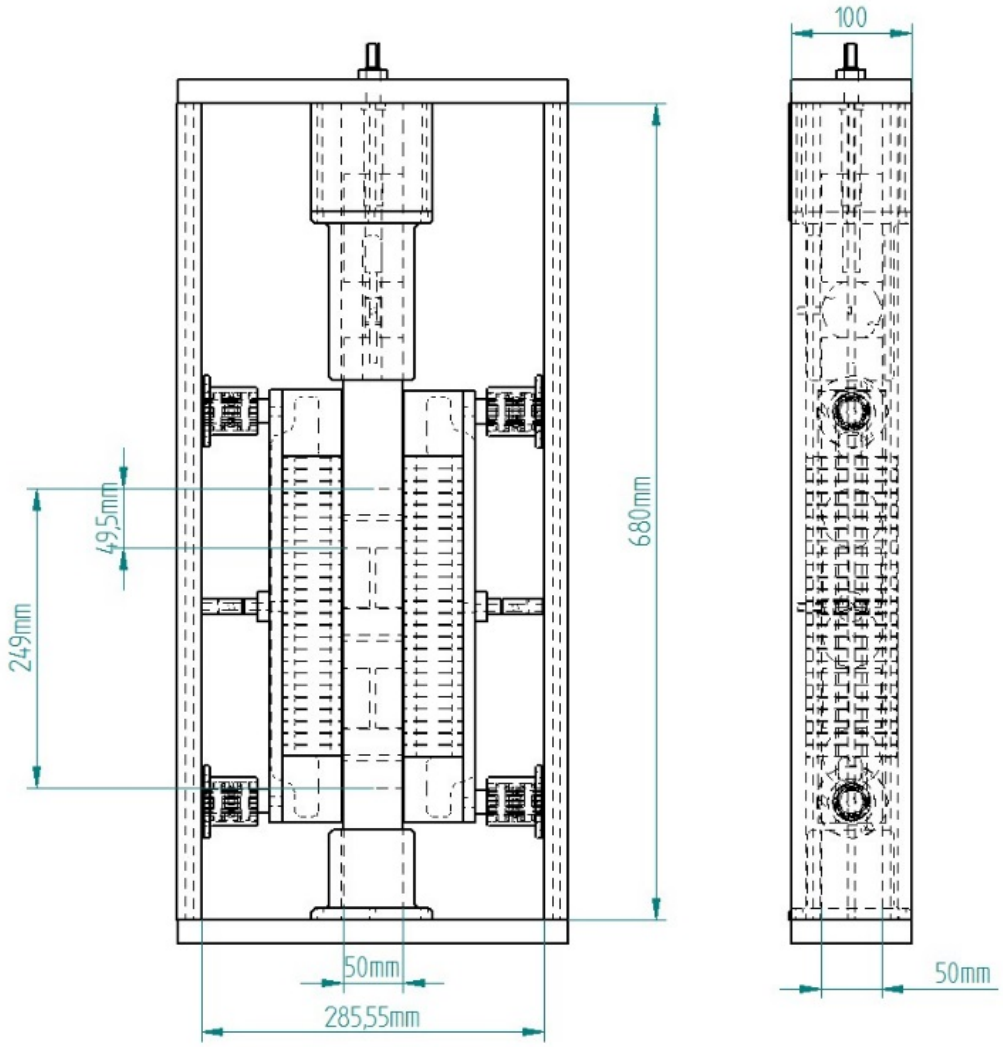

Fig. 5.52 Prototype dimensions overview

TABLE 5-V
INDIVIDUAL COIL INFORMATION HALBACH ARRAY

Symbol	Quantity(units)	Symbol	Quantity(units)
D_{co}	50(mm)	l_c	50(mm)
D_{ci}	5(mm)	N	922

TABLE 5-VI
INDIVIDUAL COIL WINDOW-SHAPE TRACK

Symbol	Quantity(units)	Symbol	Quantity(units)
S_1	67(mm)	t_{th}	9.8(mm)
S_2	40(mm)	N_t	23
t_w	9.8(mm)		

Figure 5.53 shows a CAD drawing and the actual test rig itself. The air-core coil Halbach array is located in the middle of two window-shaped tracks, which are supported by linear guides. The coils are attached to a vertical 25kg load cell on the top, but this part can slide along the vertical axis. The window shaped tracks are each attached to a 50 kg load cell as well as two linear guides which connect the tracks to the side of the rig frame while enabling freedom of movement in the horizontal axis. Both the Halbach array and levitation track are held together by a combination of fiberglass and epoxy material in order to avoid the use of ferromagnetic material.

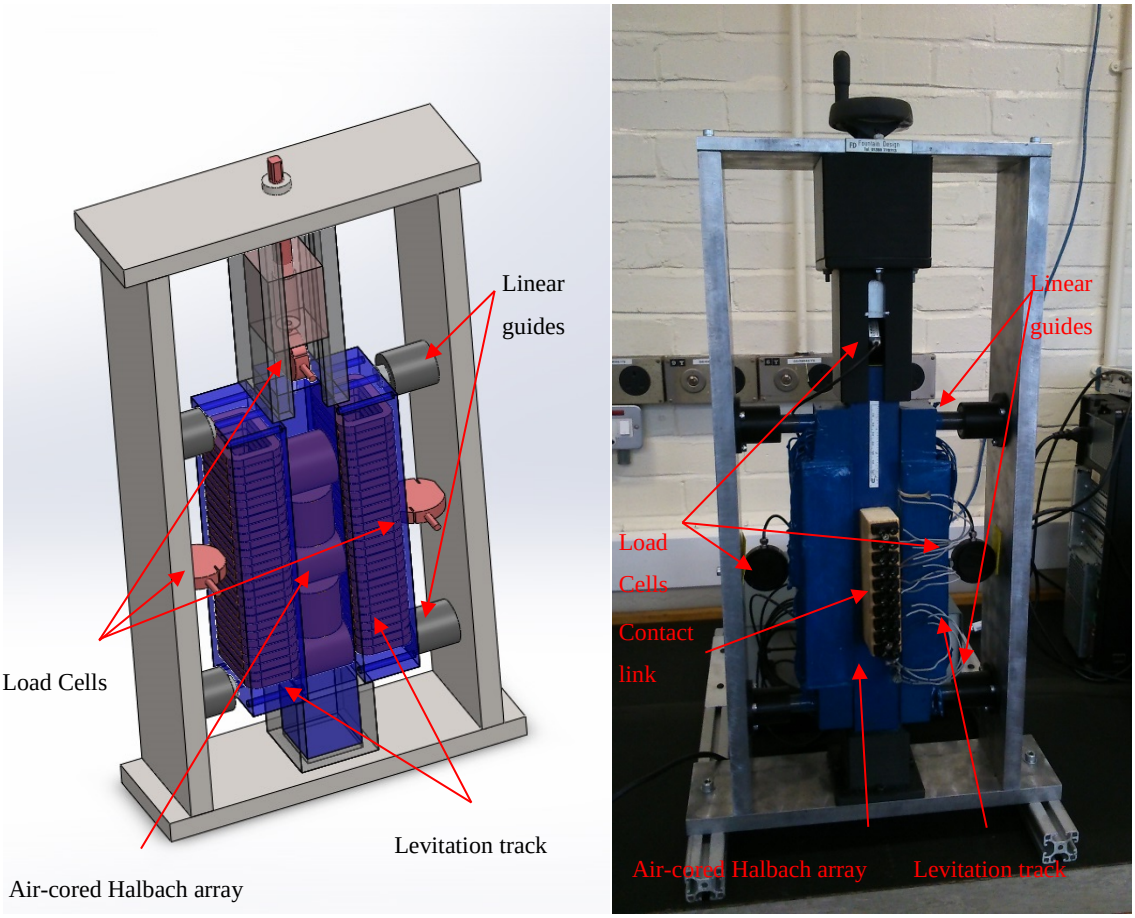

Fig. 5.53 Prototype Rig with window shaped track

5.3.1 Experimental set up

5.3.1.1 Coil magnetic field orientation.

In order to determine the orientation of the coil magnetic fields, each coil was connected to a DC power source and the magnetic field measured with a magnetic field tester. The coil terminal can be seen in figure 5.52 connected to a black contact link in the middle attached to the packed coils.

5.3.1.2 Electric circuit parameters

As mentioned before at the beginning of this chapter the current for the experiments was selected so the wire (19 AWG) in the coils had a security factor of 1.5. However, after a few trials it was found that the power source could not reach the desired current of 9 amperes. This was due to the inductance of the windings. A bank of

capacitors in series with the coils was used to compensate for the coil inductance over the range of frequencies from 90 to 420 Hz.

5.3.1.3 Power source and data acquisition equipment

The power source used to run the experiments was the "*Pacific smart source 360-amx"*. This device allows control of the voltage amplitude as well as the frequency of the wave form. The schematic in figure 5.54 represents the connection between the power source, Halbach array and capacitor bank.

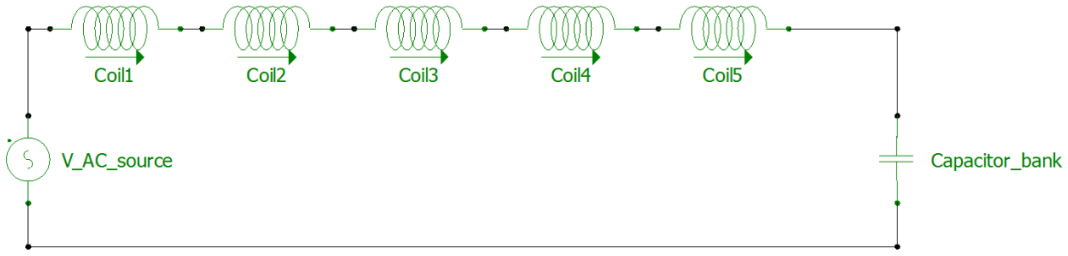

Fig. 5.54 Electric circuit of the air-cored coil Halbach array prototype.

The values of the electric circuit without the capacitors are presented below.

TABLE 5-VII
INDIVIDUAL COIL INFORMATION

Symbol	Value	Units	Description
R	8.51	Ω	Total resistance 5 coils.
L	28.6	mH	Total inductance 5 coils

Compensation for the coil inductance was achieved using 4 capacitors of 20 µF each connected in various combinations depending upon frequency. The various values are shown in Table 5-VIII.The capacitor bank connection details are presented in appendix A.2.

TABLE 5-VIII
CAPACITANCE CORRESPONDENCE TO EACH FREQUENCY

Frequency (hz)	Capacitor (F)	Capacitor Reactance ($X_C=1/2\pi fL$)	Coil Reactance ($X_L=2\pi fL$)	Frequency (hz)	Capacitor (F)	Capacitor Reactance ($X_C=1/2\pi fL$)	Coil Reactance ($X_L=2\pi fL$)
104.4564	8.00E-05	18.76416	18.77072	243.0342	1.50E-05	43.65776	43.67303
121.5171	6.00E-05	21.82888	21.83652	257.8089	1.33E-05	46.31184	46.32804
133.1153	5.00E-05	23.91234	23.9207	271.7205	1.20E-05	48.81086	48.82793
148.8275	4.00E-05	26.73481	26.74416	297.6549	1.00E-05	53.46962	53.48832
171.8511	3.00E-05	30.8707	30.8815	332.7883	8.00E-06	59.78085	59.80176
182.2745	2.67E-05	32.74312	32.75457	364.5504	6.67E-06	65.48648	65.50938
210.4738	2.00E-05	37.80873	37.82195	420.9476	5.00E-06	75.61746	75.64391

Additionally a data acquisition board "*mccDAQ 2523*" was used to record measurements from the ±10V amplifier interface outputs supplying the load cells [173]. A schematic of the reading devices connection is presented in figure 5.55.

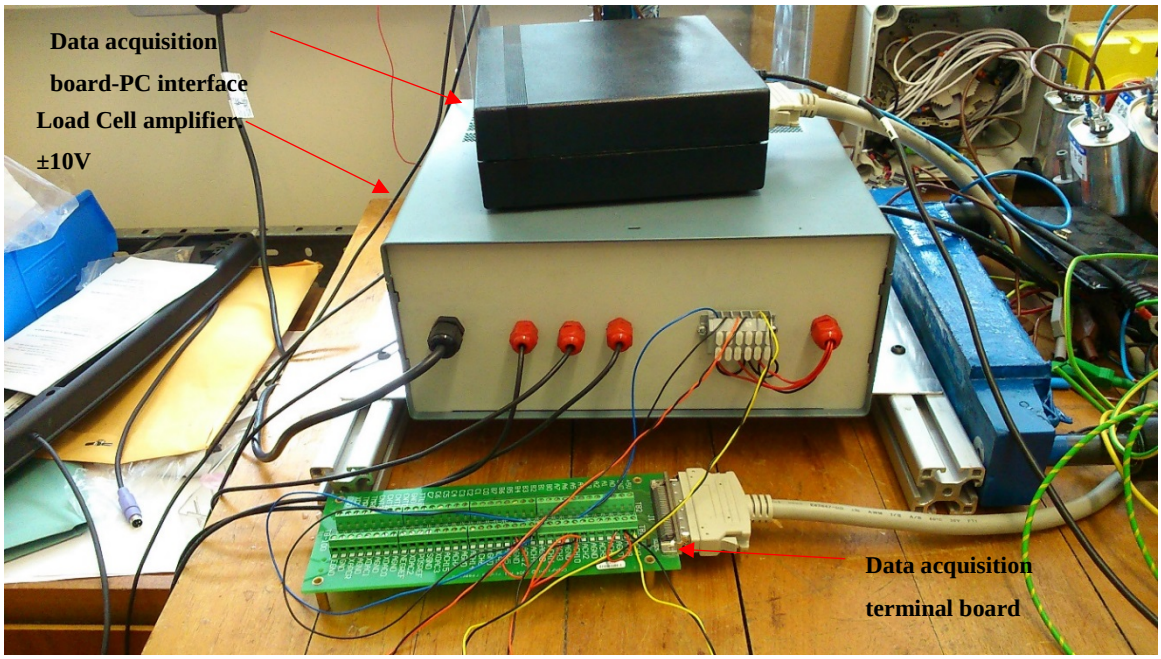

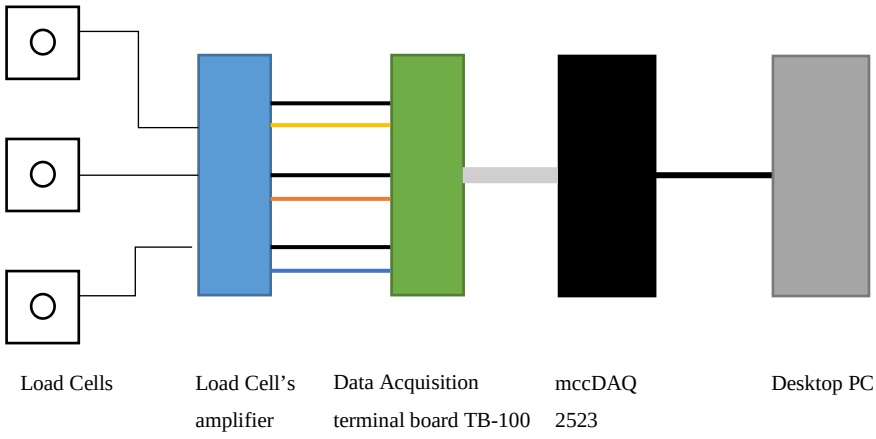

Fig. 5.55 Data Acquisition's equipment and ±10Vinterface connection

The load cell signals were connected to channel 0-2 of the TB- 100 terminal shown in figure 5.56.

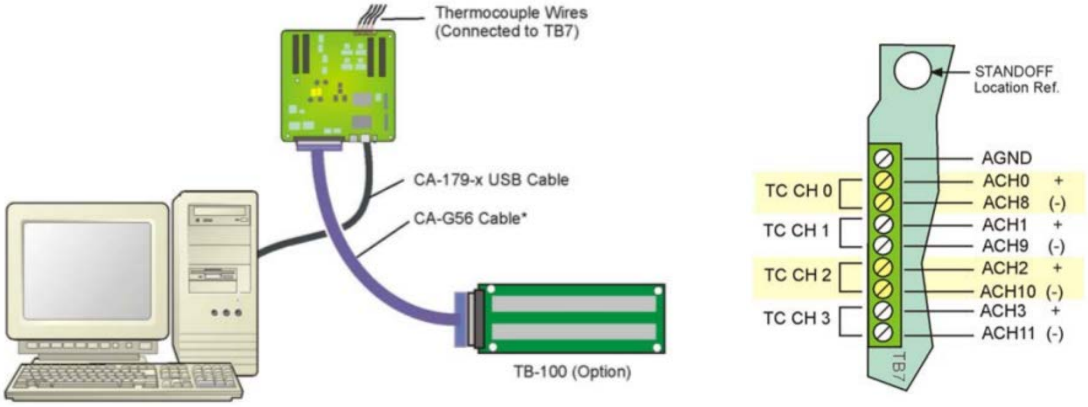

Fig. 5.56 Connection detail of the data acquisition equipment

5.3.2 Challenges

As with any experimental work a number of challenges were encountered, in particular manufacturing, instrumentation, and design issues of the track.

One of the first challenges to overcome is the difficulty to manufacture a Litz track similar to that used by Post in [168],[3],[4]. Soldering the track to ensure good connection and electrical current conduction as described by Post [174], required special equipment. A paper describing the manufacturing process of a Litz ladder track is described in [174] by Holko. In this document a 21 step process is explained, including mechanical, chemical and electrical, procedures.

Then a window shape track was chosen to probe the concept. Unfortunately after a few runs it was noticed that no significant forces were generated at the window shape track. This is the point when it was realised that Post's simplified model was not accurate for this application. This is believed to be the cause of the miscalculations in the design that led to overestimating the forces generated by the device.

5.3.2.1 New track

As mentioned previously the window track design was adopted in the beginning due to the simpler manufacturing process. The forces calculate with Post's [170] model resulted in forces of magnitude of around the 300 Newtons. However, in the experiments no readings were detected by the load cells. Initially it was thought that the problem might have originated from false contact between the loops at the track.

Nevertheless, by conducting a number of experimental runs with single home-made loop samples, it was demonstrated that in fact the forces were overestimated.

In an attempt to improve the design a new track was manufactured. Instead of using a Litz wire track, a slotted plate track was used following the example shown in [175]. The objective of the design was to keep the track rungs as small as possible in order to reduce eddy current losses. Thus plates of 0.7 mm were slotted every 4 mm with a 2mm diameter end-mill cutting tool. The thickness of the plates was defined by the supplier availability, and the distance and size of the slots was recommended by the staff in charge of machining the pieces. They recommended a change in dimensions that accounted for the thinner material physical characteristics. It was for this reason that rung and slot width had to be constrained to a lower limit.

a)

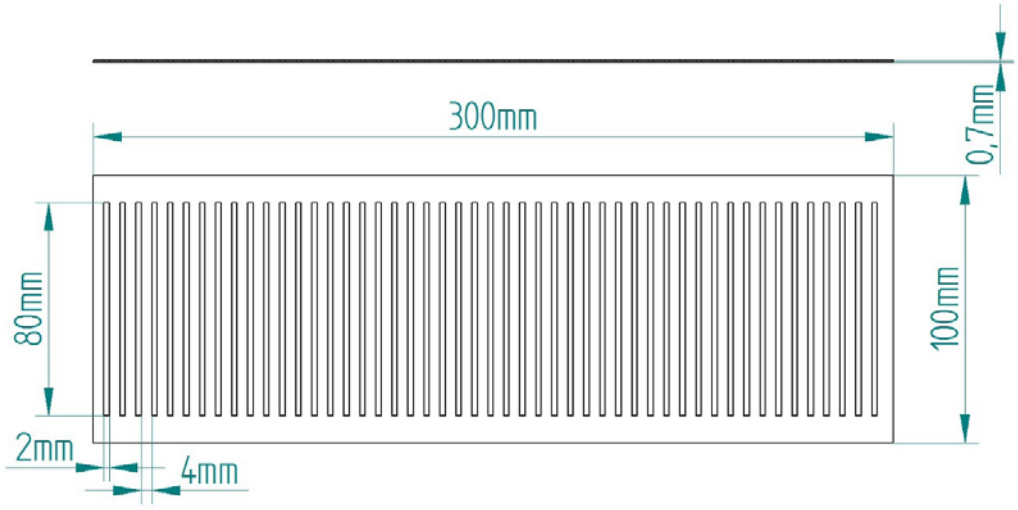

b)

Fig. 5.57 CAD model and dimension details of the levitation slotted track.

For the experiments the track was assembled by adding 1 layer at the time in order to see the effects on the forces generated. The plates are electrically insulated by electric tape between layers. Also, all the layers share shorting strips on the sides made of conductive copper spacers of 0.5 mm along the plates (see Figure 5.58).

a)

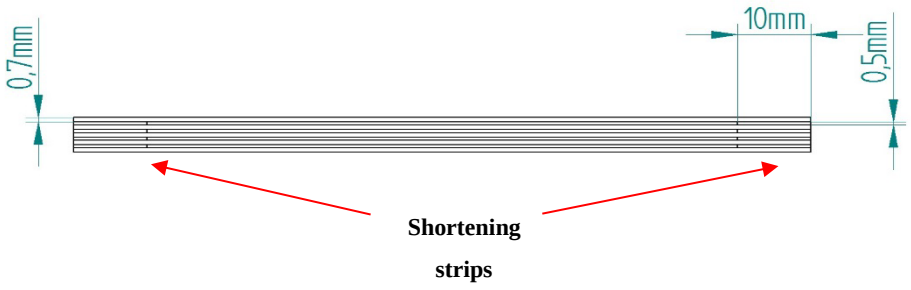

b)

Fig. 5.58 CAD MODEL of a 5-Layer slotted track assembled

Details of the slotted plates insulations and assembly can be seen in Figure 5.57 and 5.58.The new track installed in the rig is shown in Figure 5.59.

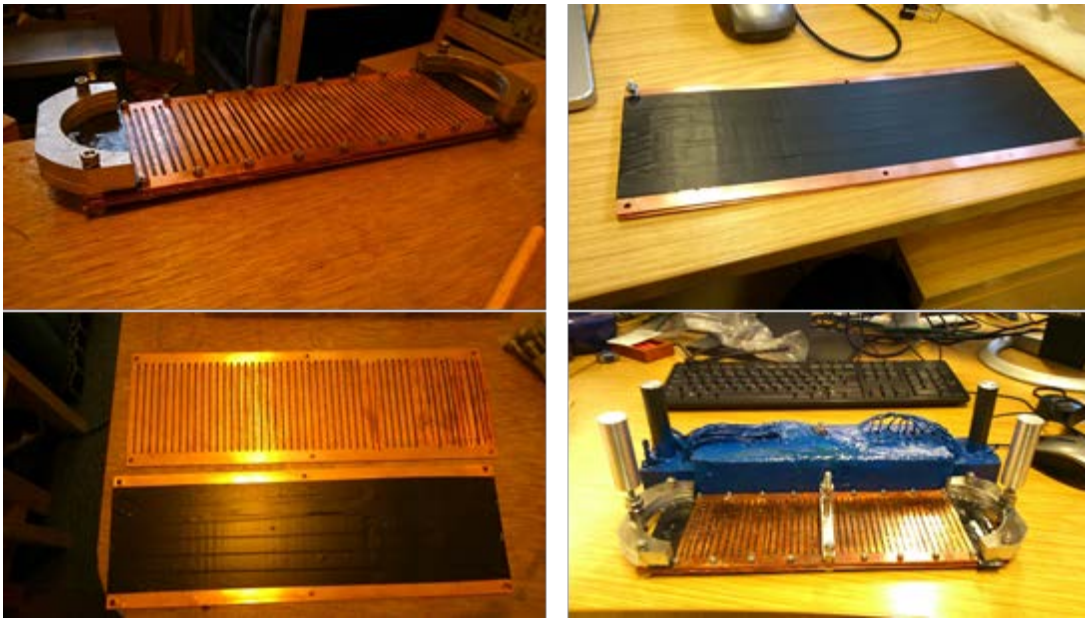

Fig. 5.59 Slotted plate track construction

The plates were assemble by bolting them on the sides and adding conductive paste between layers. An image of the slotted levitation track installed is presented in figure 5.60.

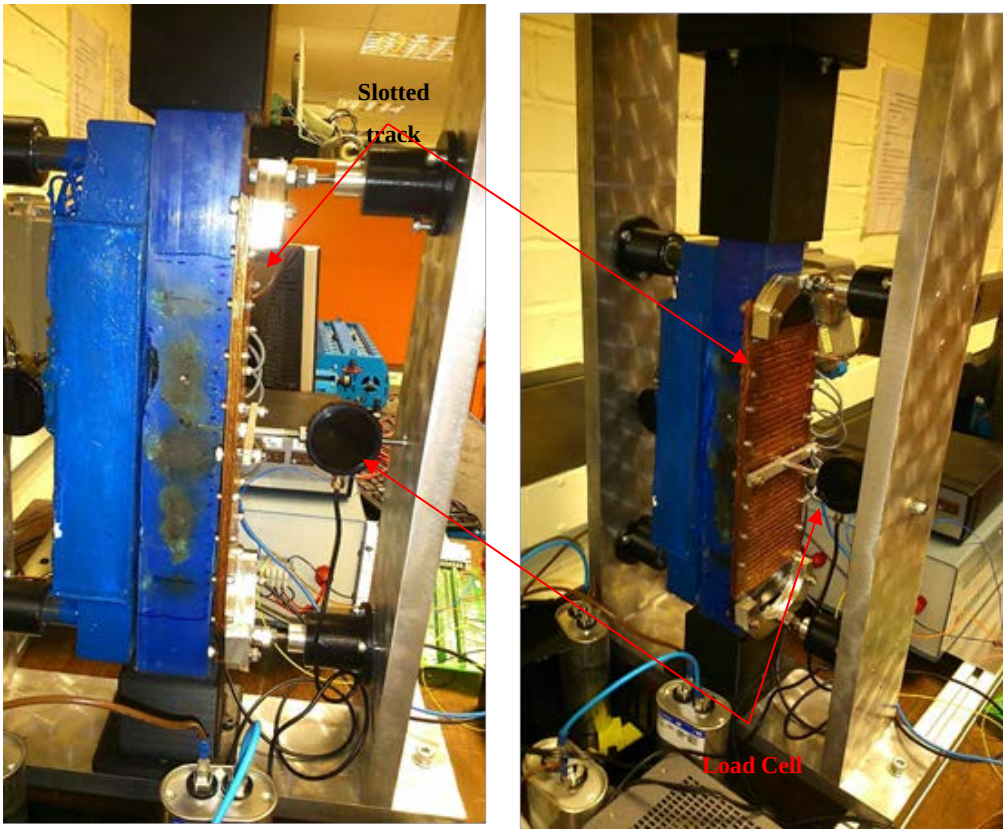

Fig. 5.60 Slotted track installed

5.3.2.2 Power source

The new track was put in place and experiments commenced, covering the frequencies mentioned before. After some experimentation it was noticed however that the power source was not behaving normally as the current displayed by the power source software “UPC Studio” did not match the actual current measured on a scope using a current probe. It is worth clarifying that this was taken in account when the magnetic field was measured in chapter 5.

Thus, measurements to determine the correspondence between current display and current supplied were taken. In order to determine a point of comparison between the experiments and simulations. The results are presented in Figure 5.61.

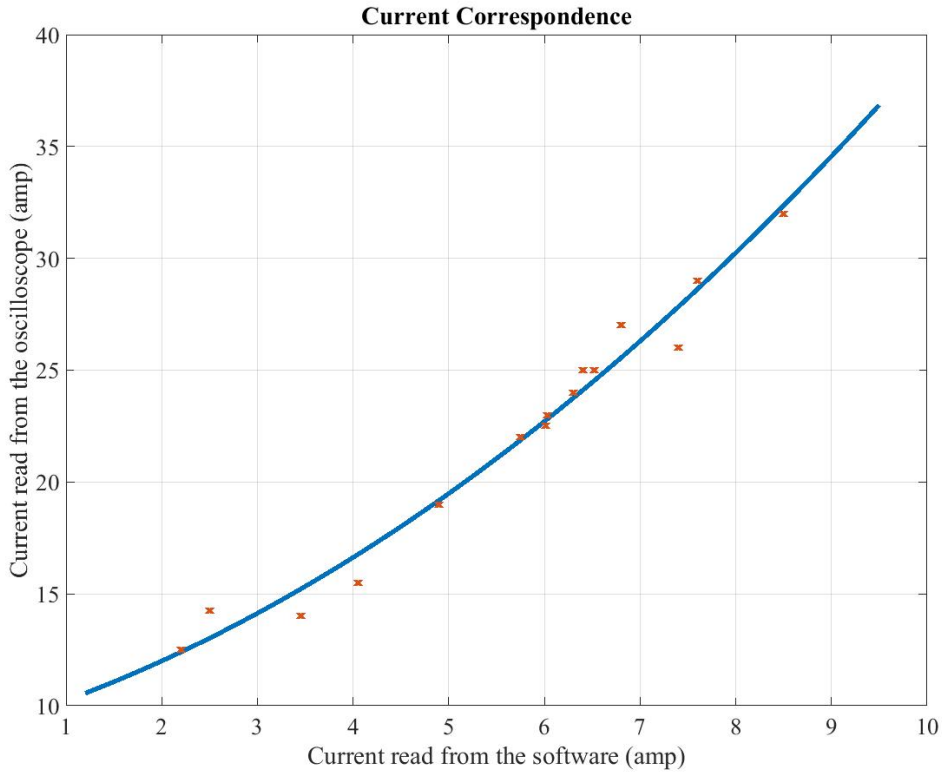

Fig. 5.61 Coils Current correction

Heat dissipation represented another challenge. Temperature rapidly rose, changing the electric characteristics of the coil array. Consequently, tests could only be conducted for a few seconds before the epoxy surrounding the coil array started to change colour due to the rise in temperature, as shown in Figure 5.62. In addition the glue holding the contact clamp to the centre coil array failed.

Fig. 5.62 Coils high temperature effects on rig

5.3.3 Results

Finally the tests were ran at a current of 31.8 A from 100 to 420 hertz. Each run was measured and recorded for few seconds. The rise in temperature cause the coil characteristics to change, therefore obtaining the measurement from a specific current was difficult. Therefore several measurements were taken at each frequency around the desired current. These measurements are presented in figure 5.65- figure 5-74 at the end of this chapter and the results are condensed as follow.

Figures 5.63-5.-67 show the comparison of results between the readings from the rig and the COMSOL model. The lifting forces are shown on the left and dragging forces on the right in each one of the figures. Additionally a trending line from these measurements is highlighted in each illustration.

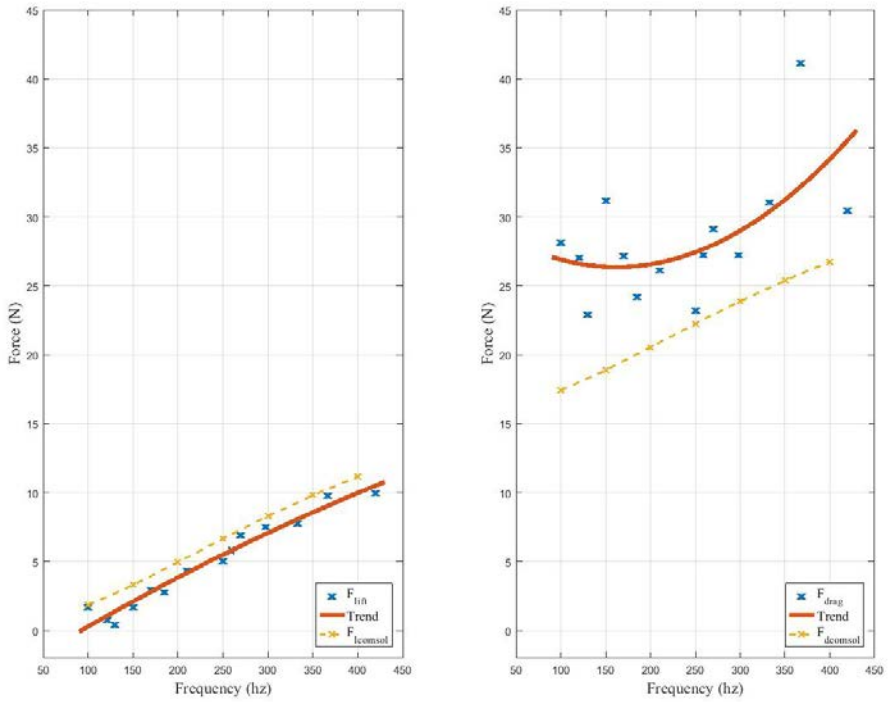

a) b)

Fig. 5.63 1-Layer track results: a) Lifting force; b) Dragging force.

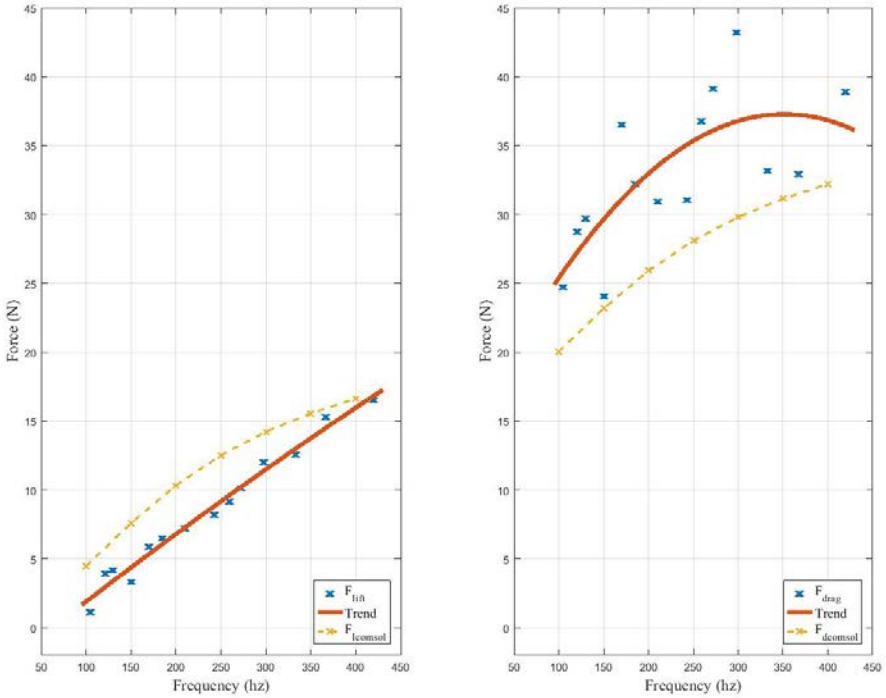

a) b)

Fig. 5.64 2-Layer track results: a) Lifting force; b) Dragging force.

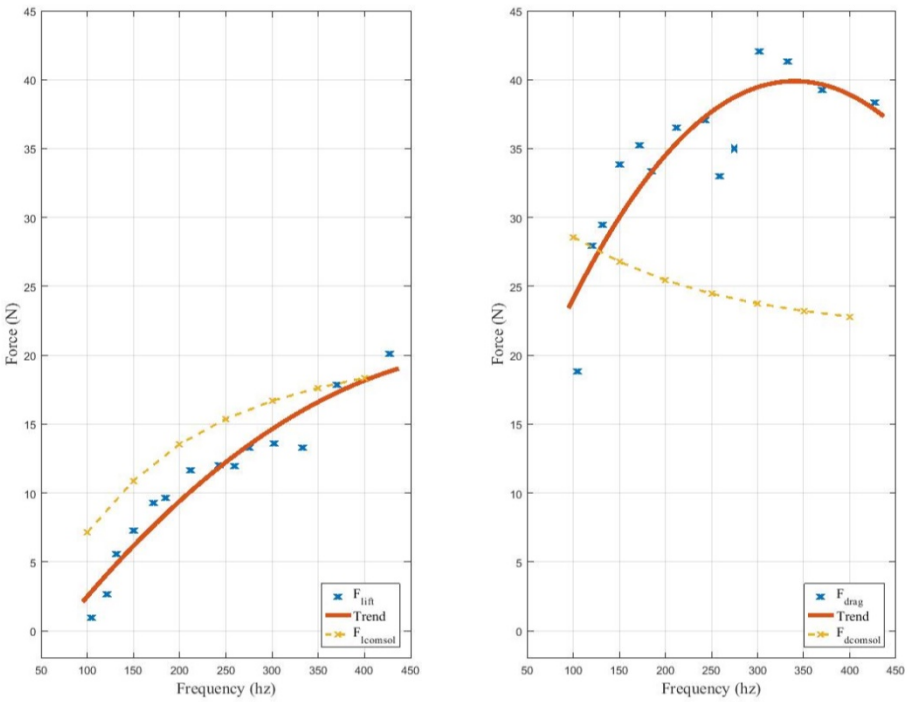

a) b)

Fig. 5.65 3-Layer track results: a) Lifting force; b) Dragging force.

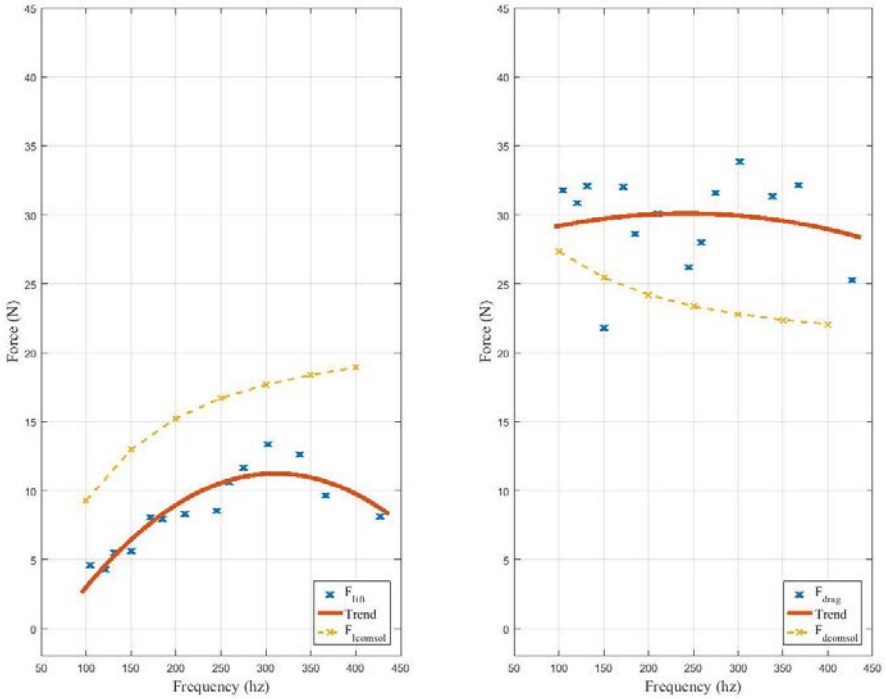

a) b)

Fig. 5.66 4-Layer track results: a) Lifting force; b) Dragging force.

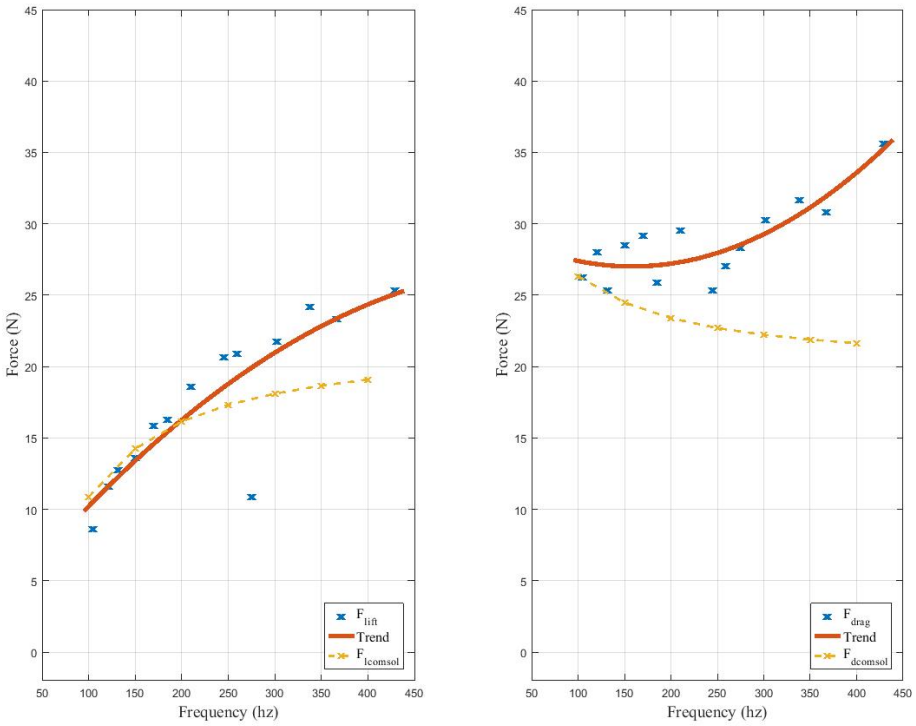

a) b)

Fig. 5.67 5-Layer track results: a) Lifting force; b) Dragging force.

5.4 Conclusions

The mathematical model proposed by Post was analysed for this application. Two different ways to calculate the magnetic field from the Halbach array adding the dimensions of each individual element were considered. The first one contemplates each element as a cube while the second approach calculated the magnetic field of each element of the Halbach array as a cylindrical coil. The result was that the second method was closer to the measurements from the prototype rig.

Also the description of how the levitation track design can affect the forces generated has been covered in section 5.1.3. However, the Post model was proven to be not suitable for this application. Instead a mathematical model based on Storset papers was implemented resulting in a more accurate model. An ideal sliding mode control system was also implemented and the results for a non-perturbed model were shown at the end on section 5.2.

Additionally experimental tests on a prototype were undertaken with the results shown in figure 5.63 to figure 5.67. The images show a correspondence between the forces obtained from COMSOL and the measurements from the rig. The dragging forces seemed to be not as close as the lift forces. These differences are believed to be caused by a range of diverse issues listed below.

- The frame providing structural support to the rig could be affected by the magnetic field from the Halbach array. This was corroborated by detaching the slotted track (see Figure 5.60) and running a few tests where the vertical load cell showed force readings. Also a different model simulation in COMSOL was created where the slotted track was omitted. The result was that up to 50% of the dragging forces were generated by frame-array interaction. This issue was taken in account in the results presented in section 5.3.3.
- Track manufacturing imperfections might create undesirable effects in the track. False contact, poor electric insulation or asymmetric geometry of the track and the attachment elements to the load cells can also affect the readings.
- After some observation it is believed that lifting and dragging forces readings are not completely isolated from one another. This means that part of the lifting forces might be read by the dragging force load cell and vice versa.
- Over-estimation of load cell result in a low resolution measurement for the forces that are presented. As mentioned before using Post's Model the forces expected were around 10 times larger than the equipment actually generates.

Despite these issues the readings from the prototype seem to match the finite element model results. Thus the model can be used to optimise the concept for real applications.

In previous cases such as AWS the loads were handled by a protective structure, but in these designs the device's translator guide bearings were designed to endure the loads applied onto the generator by the movement of the waves. Thus an

optimisation process might reduce the material as well as the amount of energy spent by the active magnetic bearings. The optimisation process along with reliability analysis is covered in the next chapter.

6 Design Requirements for a Linear C-Gen Topology

Bearings are an essential part of any electrical machine, so the proper design and sizing of these elements is extremely important. Consequently any maintenance and operation is preferably avoided since access to underwater energy devices is a complex process that involves high cost and special skills. The work presented in this chapter uses work by Caraher as a starting point, who investigated the bearing requirements for iron-cored generators[176]. Caraher proposed that the wave device itself would react to the wave induced loads, and thus protect the generator bearings, which in turn would only have to react to the internal magnetic attraction and shear forces of the generator. The C-GEN generator technology enables a single bearing solution for the generator and wave device since magnetic attraction forces within the generator are eliminated through the use of air-cored windings. In this chapter the Halbach Array Magnetic Bearing is therefore applied to the C-GEN technology, to investigate appropriate designs and control strategies while taking into account both wave induced loads, and internal generator loads. The Archimedes Wave Swing is used as an example, and follows on from Caraher's work as well as previous design work for a linear C-GEN for AWS[48] .

6.1 Wave Loads

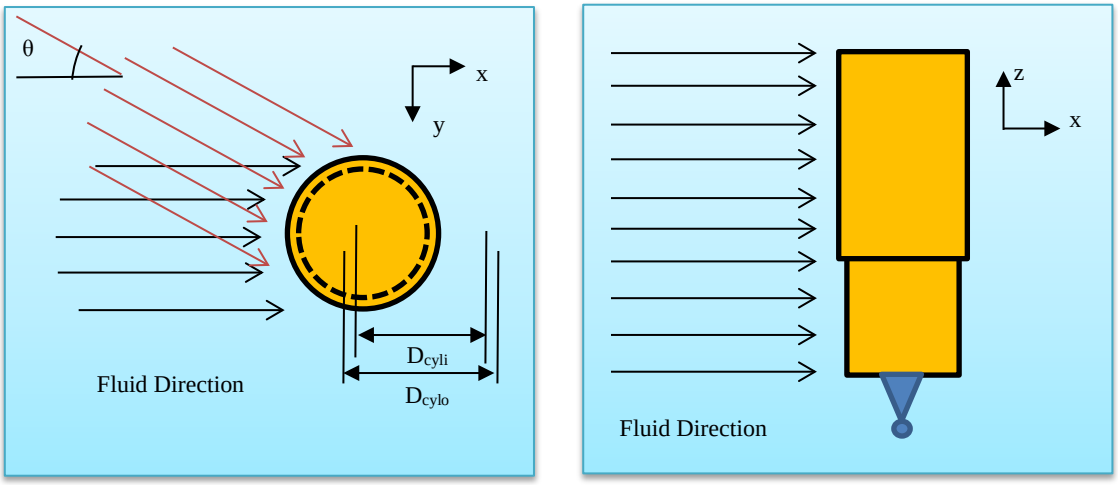

a) b)

Fig. 6.1.AWS simplified: a)Top view; b)Side view

A simplified diagram of the AWS is presented in Figure 6.1. This device works under the principle of submerged pressure differential explained briefly in section 2.1. Although fluid flow is three dimensional, Figure 6.1 shows a simplified view of the vertical and horizontal fluid loading on the AWS structure, highlighting the varied direction of flow and loading along the entire structure of the body enclosing the power take-off.

A more detailed diagram is presented in figure 6.2. In order to design the magnetic bearings, a case where the device is fully extended and the fluid acts perpendicular to the structure is studied. In this case the load acting over the bearings is at its maximum point.

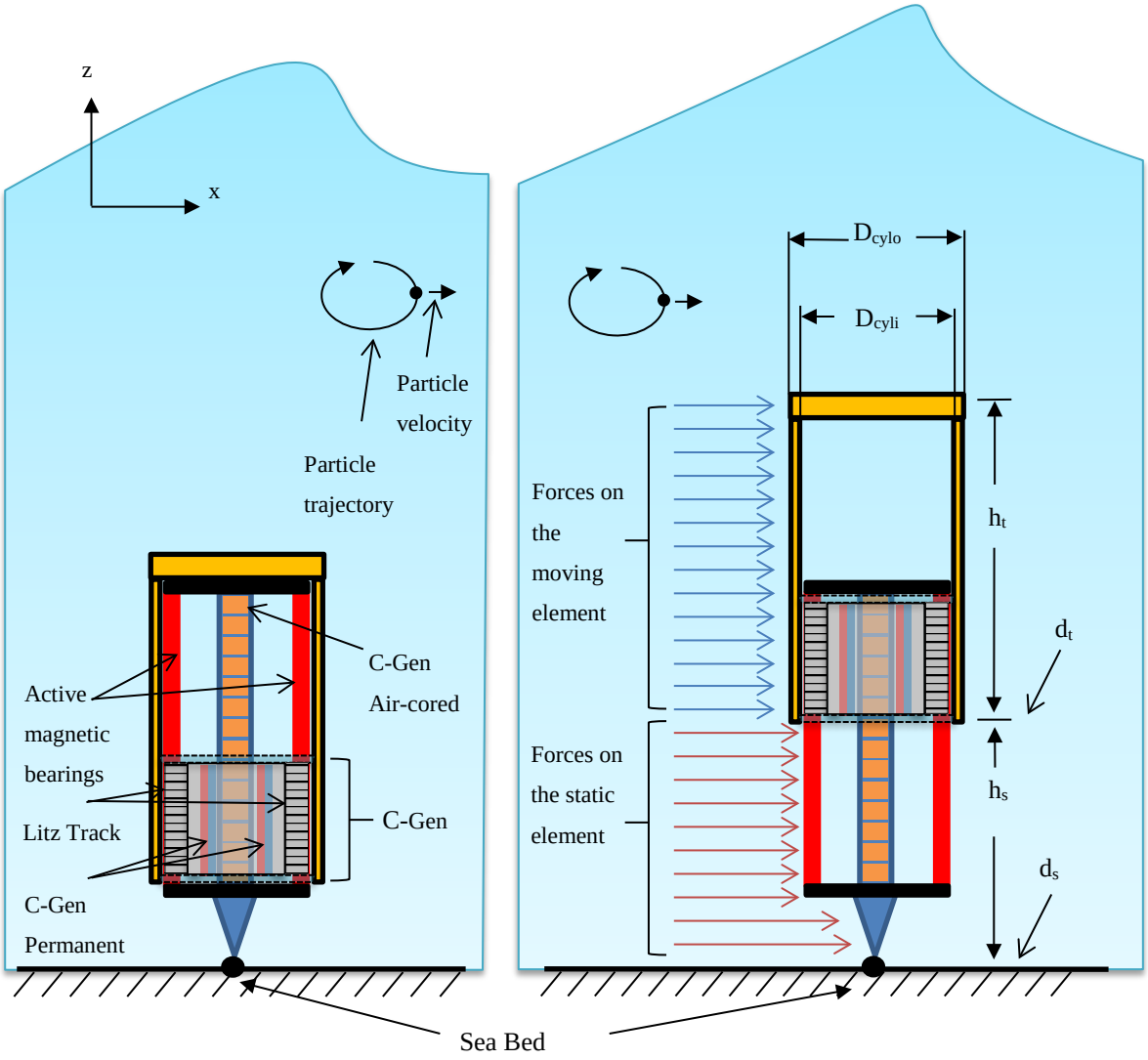

Fig. 6.2. Descriptive image of an air cored permanent magnet C-Gen linear generator.

In order to determine the forces acting on the linear generator bearings, the following two steps are followed:

3. Calculate the diameter of the enclosing cylinder to generate enough buoyant force to accelerate the translator to reach the desired maximum velocity.
4. Calculate the peak forces for a totally extended body in an extreme wave condition.

6.1.1 Cylinder Diameter Calculation

To calculate the loads tolerated by the floating bodies in the "*z*" axis some considerations have been made. It is assumed that submerged cylinders are perpendicular to the sea bed and in 90° reference to the fluid's traveling direction. These conditions represent the scenario where the forces are at their peak.

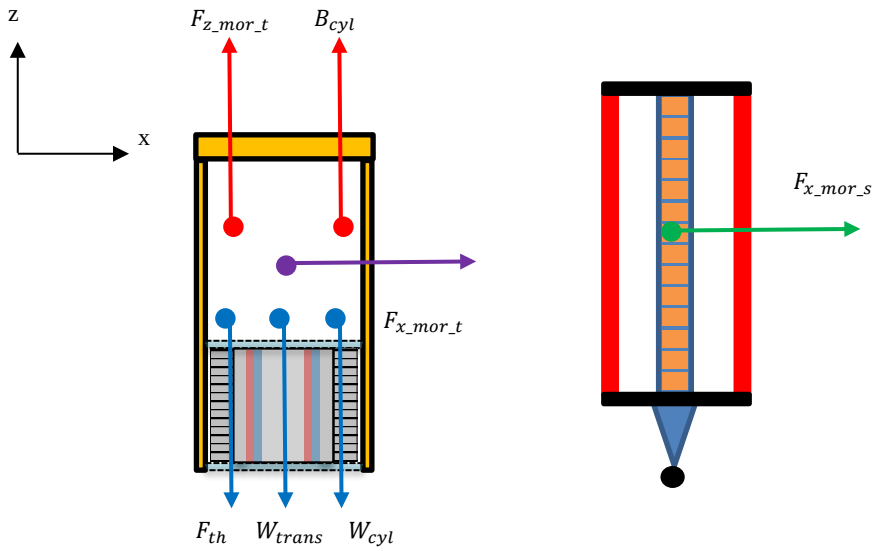

Fig. 6.3. Descriptive image of an air cored permanent magnet C-Gen linear generator.

The forces acting on the buoyant cylinder in the z-direction are represented in equation 6.1 and presented on figure 6.3, where B_{cyl}, $F_{z\_mor\_t}$,F_{th} ,W_{trans} ,W_{cyl} are the cylinder buoyant force, force from the movement of the wave in "*z*" direction, thrust force of the machine, weight of the translator core and weight of the cylinder respectively. In addition, m_{wec} and a_{wec} are the mass and acceleration of the moving part (Cylinder and translator).

$$\sum F_z = m_{wec} a_{wec} \qquad \textit{Eq. 6.1}$$

$$B_{cyl} + F_{z\_mor\_t} - F_{th} - W_{trans} - W_{cyl} = m_{wec} a_{wec}$$

The equations used are listed below, where the subscript "*cylo*" and "*cyli*" relate to the outer and inner diameter of the hollow cylinder (See Figure 6.1):

$$W_{trans} = g(\rho_s V_{core} + \rho_{pm} V_{pm}) \qquad \textit{Eq. 6.2}$$

$$W_{cyl} = g\rho_{pol}(V_{cylo} - V_{cyli}) \qquad Eq.\ 6.3$$

The buoyancy force over the cylinder is presented as follow:

$$B_{cyl} = g\rho_{sw}V_{cylo} \qquad Eq.\ 6.4$$

Where ρ_s is the mild steel density, ρ_{pm} represents the permanent magnet density, ρ_{pol} is the cylinder's polyethylene density and ρ_{sw} is the sea water density . Additionally the volume of the core, permanent magnets and cylinder, are represented as $V_{core}, V_{pm}, V_{cyli}$, and V_{cylo} respectively.

The calculation of the thrust force is simplified so that it assumes the efficiency of conversion from mechanical energy to electrical energy is 100%. Therefore Power can be shown as $P = F_{th} \times v$ where *v* is the velocity of the body.

$$F_{th} = \frac{P}{v} \qquad Eq.\ 6.5$$

Also the force generated by the particle of water traveling perpendicular to the device, acting along the length is derived as:

$$F_{z\_mor\_t} = \int_{d}^{d+h} f\, dz \qquad Eq.\ 6.6$$

Where *d* is the lower point of the column and *h* the length of the device (sub index *s* and *t* for stator and translator) as shown in figure 6.2. This calculation is based on Airy's Theory using the Morrison equation for a monopole [155][177]:

$$f = C_m\rho_{sw}\frac{\pi}{4}D^2\dot{u} + C_d\frac{1}{2}\rho_{sw}Du|u| \qquad Eq.\ 6.7$$

Here *w* relates to the vertical flow velocity and $\dot{w}$ relates to the vertical flow acceleration expressed as follows [178]:

$$w(x,z,t) = \frac{\pi H}{T}\frac{\sinh[k(d+z)]}{\sinh(kd)}\sin(kx - \omega t) \qquad Eq.\ 6.8$$

$$\dot{w}(x,z,t) = \frac{2\pi^2 H}{T^2}\frac{sinh[k(d+z)]}{sinh(kd)}\cos(kx - \omega t) \qquad Eq.\ 6.9$$

While "k" is defined as:

$$k = \frac{gT^2}{2\pi} \qquad \textit{Eq. 6.10}$$

The characteristics of the waves as well as other information are presented in the following table 6-I. As mentioned before the design of the magnetic bearings must aim to successfully overcome the forces applied on the device by an extreme wave when the device is fully extended. The period and height of a normal and extreme wave are listed as follow:

TABLE 6-I
INFORMATION FOR MORRISON'S EQUATION

Symbol	Value	Units	Description
ρ_{sw}	1025	kg^3/m	Density of sea water
ρ_{pm}	7700	kg^3/m	Density of permanent magnets
ρ_s	7850	kg^3/m	Density of mild steel
ρ_{pol}	970	kg^3/m	Density of cylinder's polyurethane
g	9.81	kg^3/m	Gravity
C_d	1	n/a	Drag coefficient
C_m	2	n/a	Inertia coefficient
		Normal Waves	
H	2.5	m	Wave height normal wave
T	7	s	Wave period normal wave
		Extreme Waves	
H	10	m	Wave height extreme wave
T	10	s	Wave period extreme wave

Finally the mass of the moving parts (excluding the water displaced) can be obtained from the following equation:

$$m_{wec} = (\rho_s V_{core} + \rho_{pm} V_{pm}) + \rho_{cyl}(V_{cylo} - V_{cyli}) \qquad \textit{Eq. 6.11}$$

Once the sum of vertical forces has been defined the acceleration for a maximum velocity operation needs to be calculated. It is stated in Hodgins [179] a maximum translator velocity "v_f" of 2.2 m/s and total traveling distance equal to 4 m are

required for a full scale design to achieve an output of 0.25-2MW. The dimensions for a 1MW generator are shown in figure 6.4.

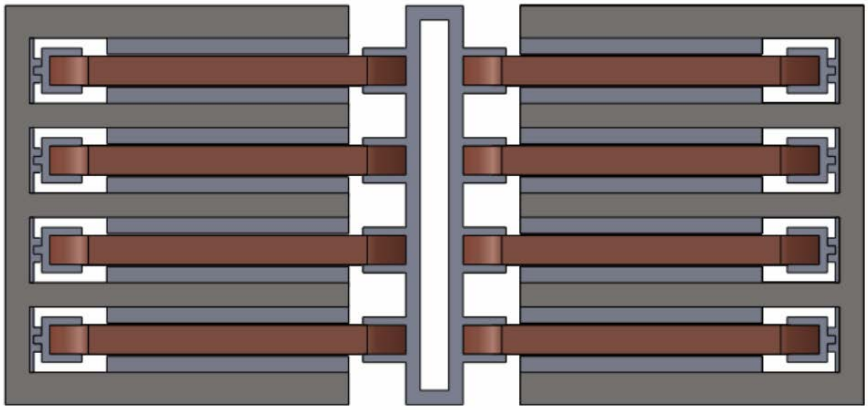

a)

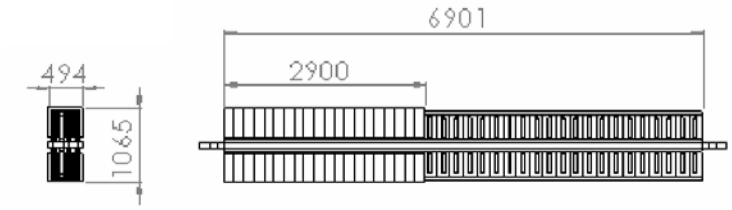

b)

Fig. 6.4.a) Top view: Double sided stacked generator b) 2 MW device dimensions

To obtain the acceleration of the translator it is assumed that the velocity peak is reached at the middle of the stroke length (l_s =2 m) and the translator starts moving from idle speed. Thus from equation 6.12 the acceleration of the traveling body results in 1.21 m/s^2.

$$v_f^2 = v_i^2 + 2a_{wec}l_s \qquad \textit{Eq. 6.12}$$

Subsequently in order to obtain the cylinder's diameter that will result in the desired acceleration mentioned above, calculations on the size of the machine were made from 0.125 MW to 1MW. This takes advantage of the modularity of this machine presented in Figure 6.5.The results are presented in Figure 6.6 and details of the device in Table 6-II.

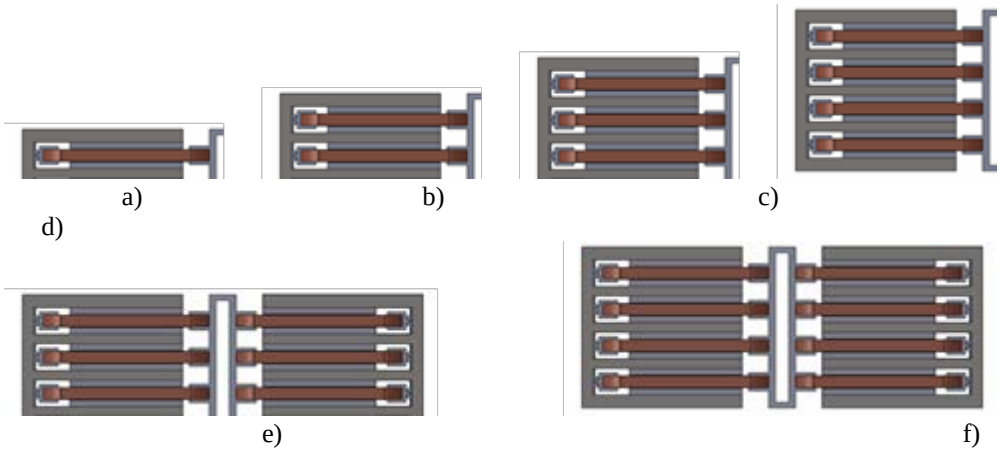

Fig. 6.5 Modular increments: a) 0.125MW b) 0.25MW c) 0.375MW d) 0.5MW e) 0.75MW f) 1MW

Figure 6.6 shows the minimum required diameter for buoyancy for the double sided stacked generator. Also in the same image the minimum size required to locate the apparatuses inside the cylinder is presented. From here it can be seen that the buoyancy diameter required is larger than the space needed to allocate the device. Therefore the buoyancy diameter obtained will be taken to calculate the loads acting horizontally in the next subsection.

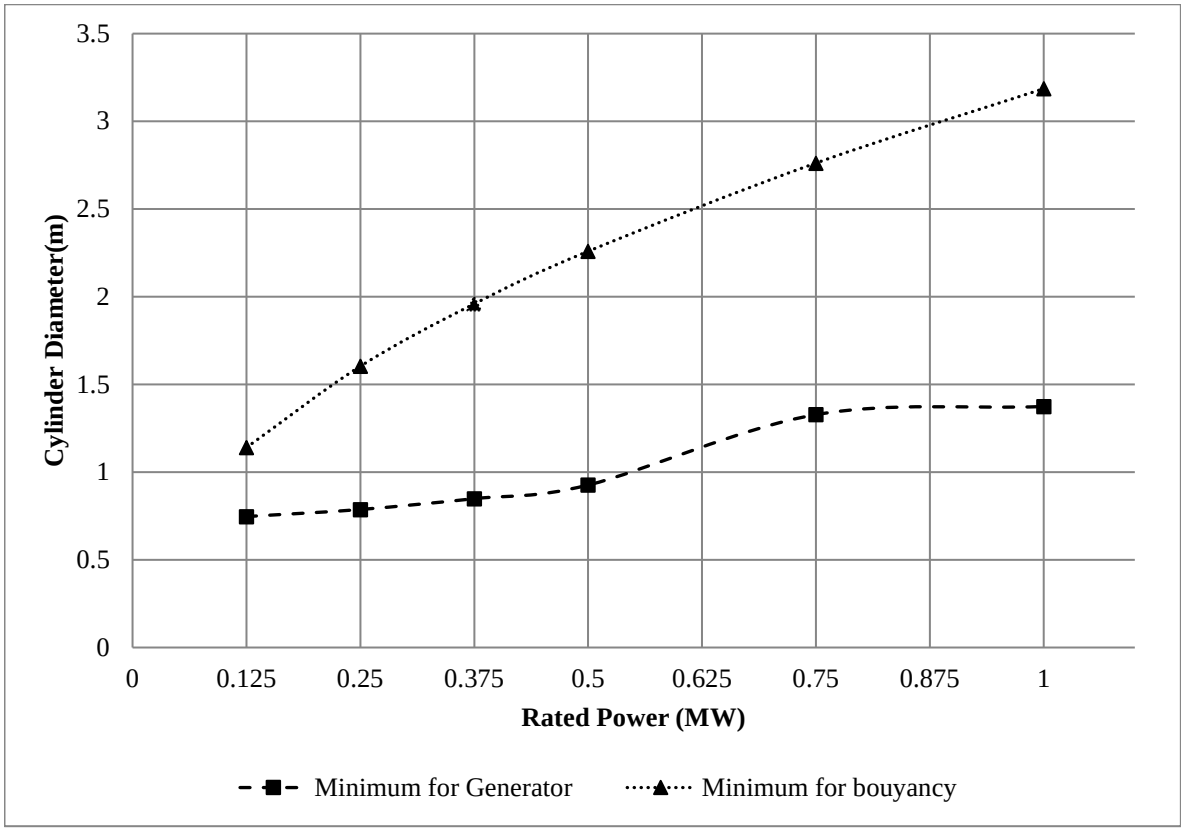

Fig. 6.6. Cylinder Diameter comparison

TABLE 6-II
GENERAL COMPARISON

Symbol	Description	0.125MW	0.25MW	0.325MW	0.5MW	0.75MW	1 MW
D_{st}	Stator diameter (m)	1.14	1.6	1.9	2.26	2.76	3.19
m_{trans}	Translator mass (kg)	1031.25	2062.5	3093.75	4125	6187.5	8250
m_{cyl}	Cylinder mass (kg)	237.74	335.23	410.03	473.09	578.88	668.07
F_{th}	Thrust force (kN)	56.818	113.636	170.454	227.272	340.909	454.545
l_t	Total Length of travel (m)	4	4	4	4	4	4
h_t	Translator height (m)	6.9	6.9	6.9	6.9	6.9	6.9
h_s	Stator height (m)	2.9	2.9	2.9	2.9	2.9	2.9
d	Sea bed depth (m)	40	40	40	40	40	40

6.1.2 Forces due to wave action.

According to the assumptions mentioned previously, the forces due to wave action act perpendicular to the device, namely in the x-direction (Figure 6.2). The magnetic

bearings react to the total force acting due to the waves leading to equation 6.13 (Figure 6.3).

$$\sum F_x = 0$$

$$F_{x\_mor\_t} - F_{x\_mor\_s} - F_{x\_MB} = 0 \qquad \textit{Eq. 6.13}$$

Where $F_{x\_mor\_t}$, $F_{x\_mor\_s}$ and F_{x_MB} are the loads on the translator, stator and forces generated by the magnetic bearings, respectively. In this document the peak difference between the translator and stator once the stator is fully extended is the maximum load the magnetic bearing system must counteract. This is calculated with the previously mentioned Morrison equation but now the particle velocity equation corresponds to the horizontal direction "x" shown in equation 6.14 and 6.15:

$$u(x,z,t) = \frac{\pi H}{T}\frac{cosh[k(d+z)]}{sinh(kd)}cos(kx-\omega t) \qquad \textit{Eq. 6.14}$$

$$\dot{u}(x,z,t) = \frac{2\pi^2 H}{T^2}\frac{cosh[k(d+z)]}{sinh(kd)}sin(kx-\omega t) \qquad \textit{Eq. 6.15}$$

Following the same process, calculations to show the effect of the size of the device are depicted in figure 6.7.

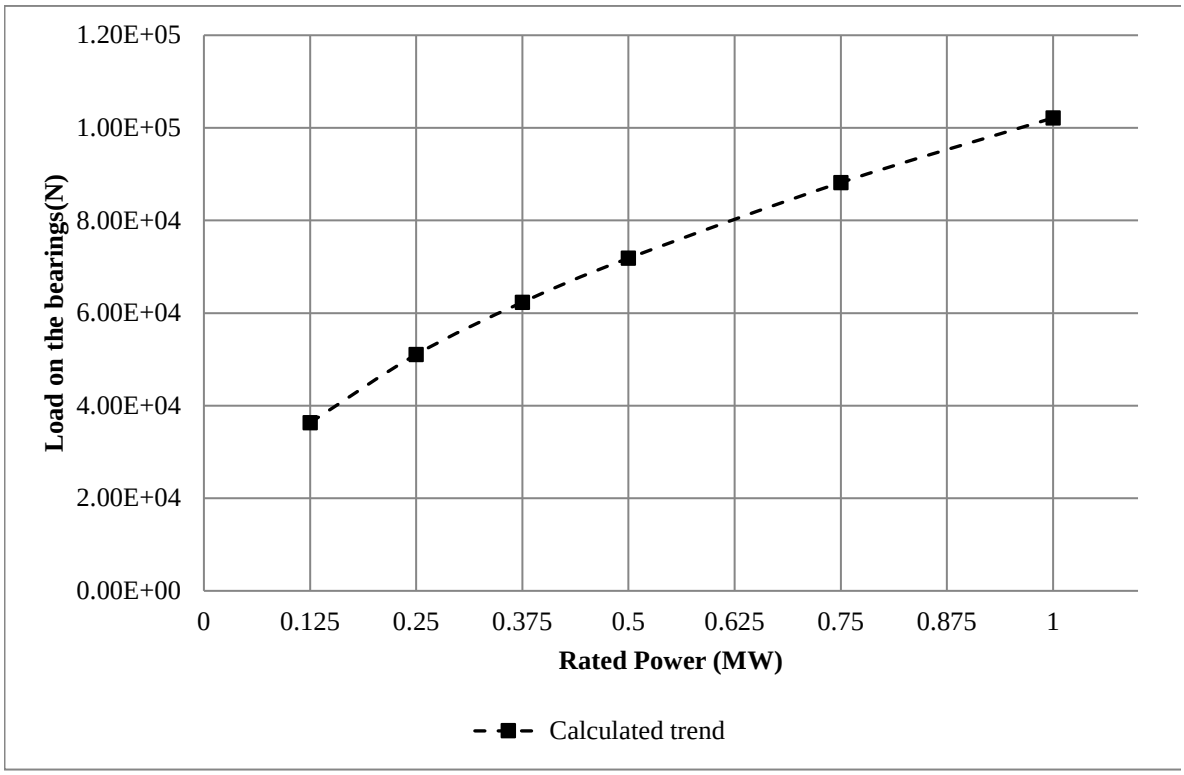

Fig. 6.7. Peak load on the bearings

With the load calculations it is now possible to establish the bearing design. The size of the buoyant body and generator sets the dimension constraints for the magnetic levitation device.

6.2 Optimisation of the device

In chapter 5, it was demonstrated how the dimension of the coils and track affect the capabilities of this device. In order to design a device capable of dealing with the forces highlighted in the previous section, the active magnetic bearing design needs to be improved.

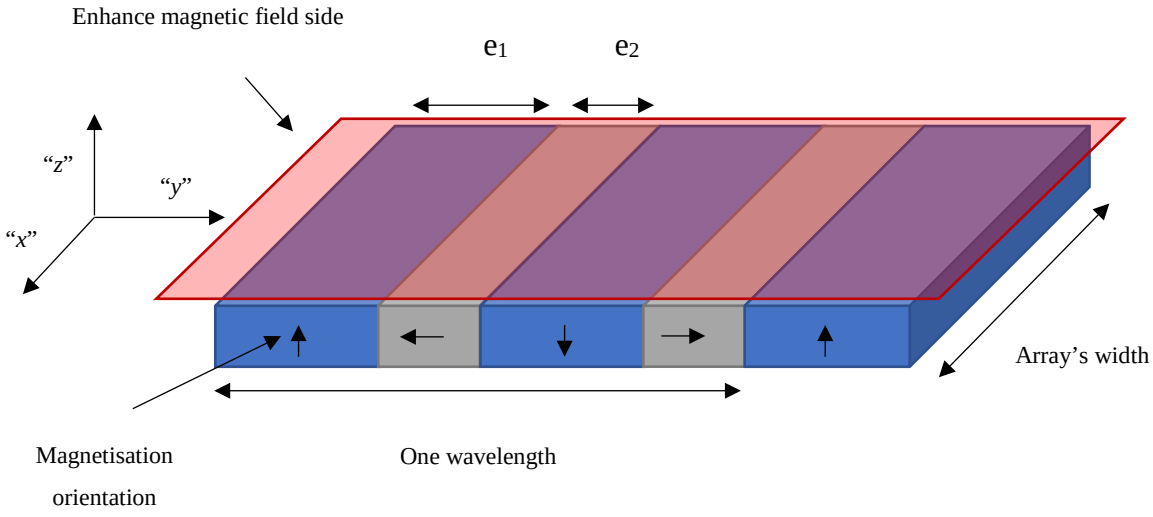

Fig. 6.8 Halbach array of different element sizes

Robertson's work has been used in chapter 5 to calculate the magnetic field from a cube shaped Halbach array composed of permanent magnets. In this section Robertson's paper [180] is been reviewed for the optimisation process. In this document he studied the interaction between Halbach arrays, specifically the relationship between element sizes (in figure 6.8 appears as e_1 and e_2) and their impact on the forces generated in an array with various numbers of wavelengths in it. From here a relationship of 4:1 from the first (e_1) to the second (e_2) element of the Halbach array is chosen.

A paper by Jiangbo shows how the ratio between length of element and width of the array affects the force generation of an Inductrack system[76]. The author showed how changing the element length to the array width ratio affects the relation between the magnetic field on the "z" axis and the magnetic field on the "*y*" axis. From figure 6.8 a ratio of 1:6 seems to be the best option.

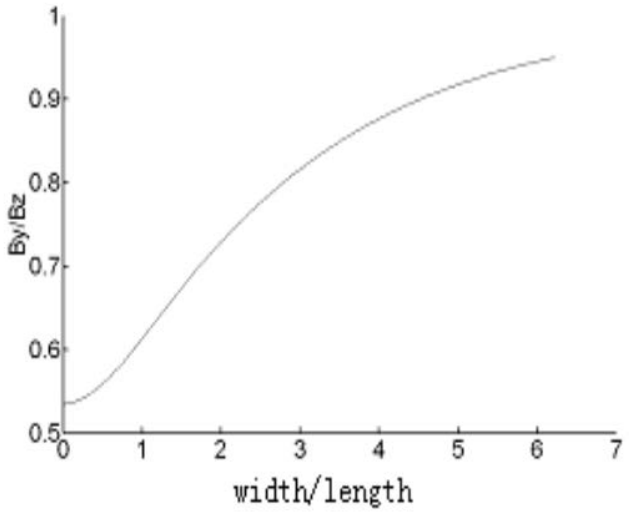

Fig. 6.9 Halbach array of different element sizes[76]

Although Robertson and Jianbo are considering permanent magnets, these documents can act as a guide to improve the performance of the Air-cored coil Halbach array.

Hence a number of changes from the design studied in section 5 are proposed:

1. The width of the array will cover the entire track.
2. The size of the Halbach array's first element (e_1) will be one sixth of the array's width.
3. The ratio between the first (e_1) and second element (e_2) will be of 4:1.

The dimensions resulting from this steps are shown in figure 6.10 and summarised in table 6-III.

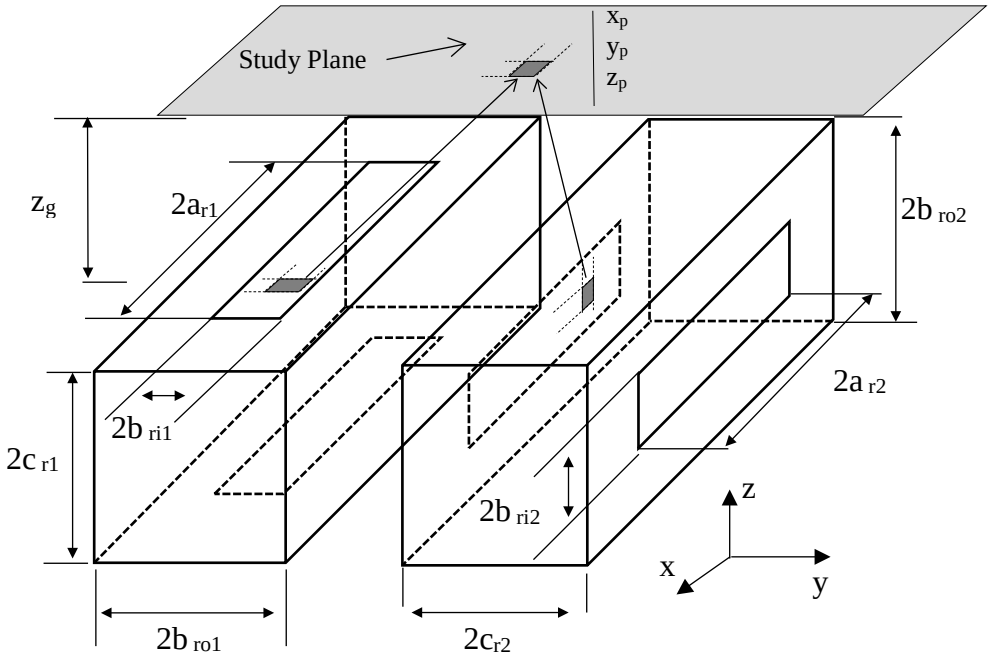

Fig. 6.10 Rectangular coils for Halbach array; dimension details.

TABLE 6-III
HALBACH ARRAY OPTIMISED DIMENSIONS

Symbol	Quantity(units)	description	Symbol	quantity	description
$2*a_{r1}$	100(mm)	Air core length. "*x*" axis	$2*a_{r2}$	100(mm)	Air core length. "*x*" axis
$2*b_{ri1}$	5(mm)	Air core length. "*y*" axis	$2*b_{ri2}$	5(mm)	Air core length. "*y*" axis
$2*b_{ro1}$	16.7 (mm)	Coil thickness. "*y*" axis	$2*b_{ro2}$	50(mm)	Coil thickness. "*y*" axis
$2*c_{r1}$	50(mm)	Coil height "*z*" axis	$2*c_{r2}$	16.7/4(mm)	Coil height "*z*" axis
n_1	290	Number turns in coil 1	n_2	90	Number of turns in coil 2

Symbol	Quantity(units)	description	Symbol	Quantity(units)	description	Symbol	quantity	description
I	31.8(A)	current	f_c	100-400(Hz)	frequency	z_g	2(mm)	Gap from levitation track

A simulation using the optimised dimensions shown in table 6-III was run. The array of coils is acting over the same track used in the array presented in chapter 5 (see

figure 6.11 a)), with the intention of comparing the original design with the one presented in this section.

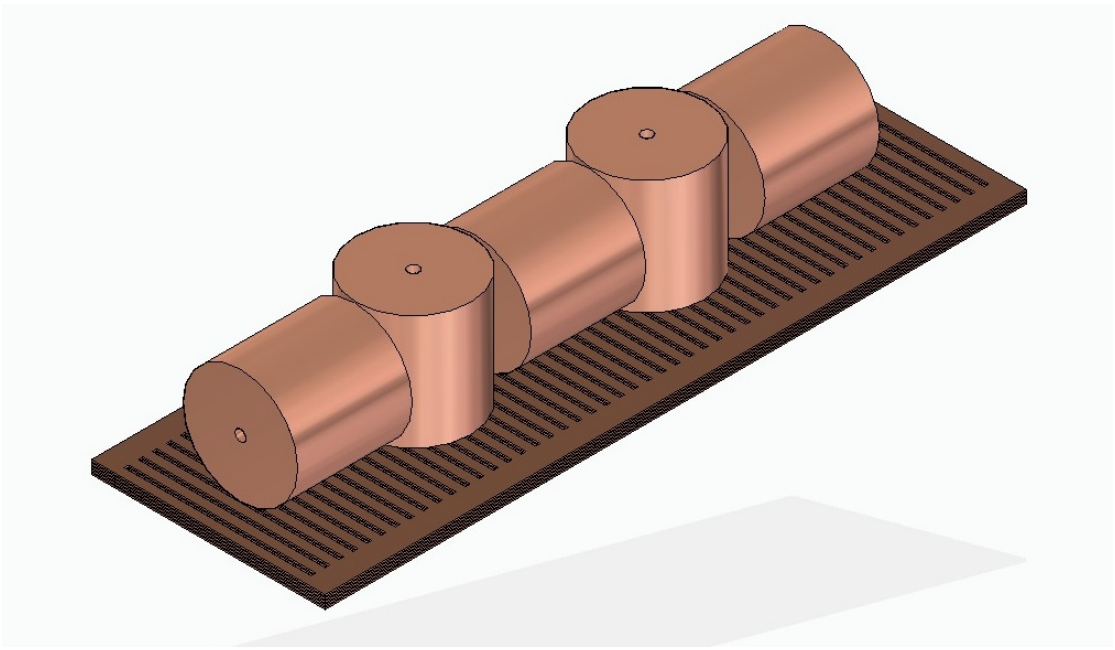

a)

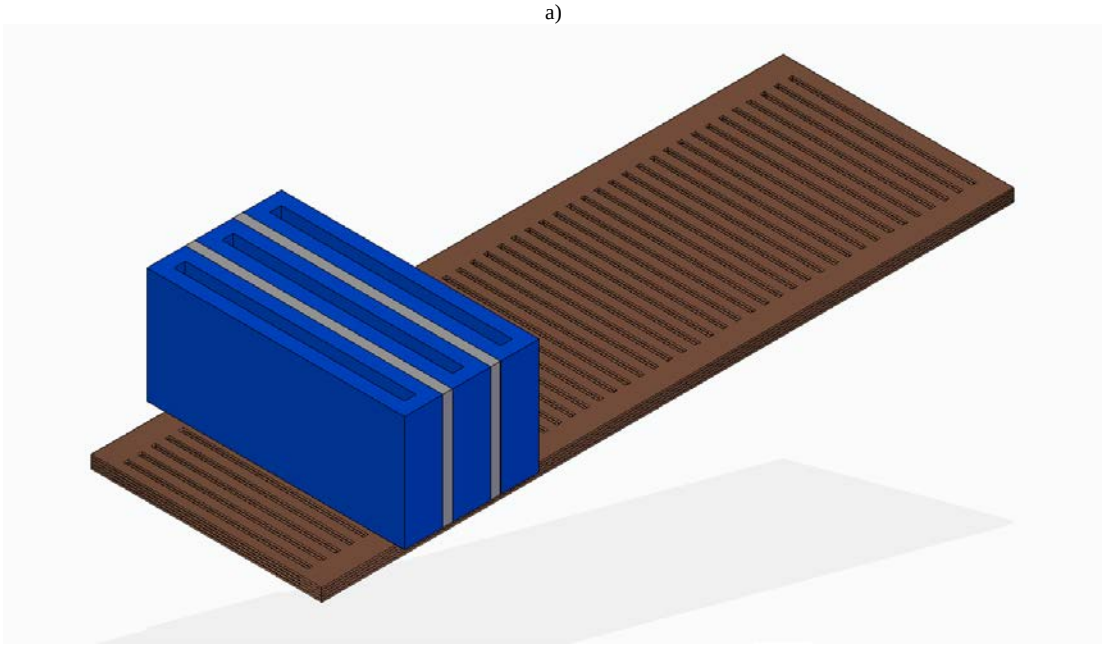

b)

Fig. 6.11 CAD model illustration: a) original design; b) optimized rectangular coils Halbach array

A 3-D graphic representation of the magnetic field acting on the array and the track from COMSOL is shown in Figures 6.12-6.13.

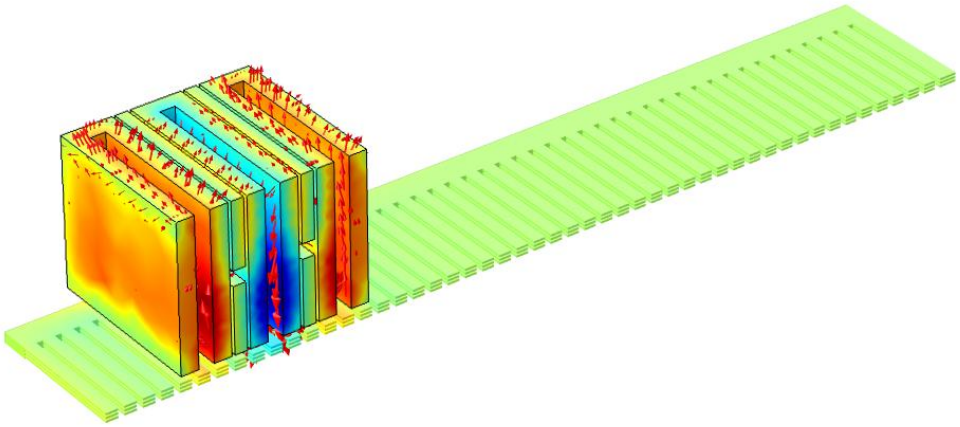

a)

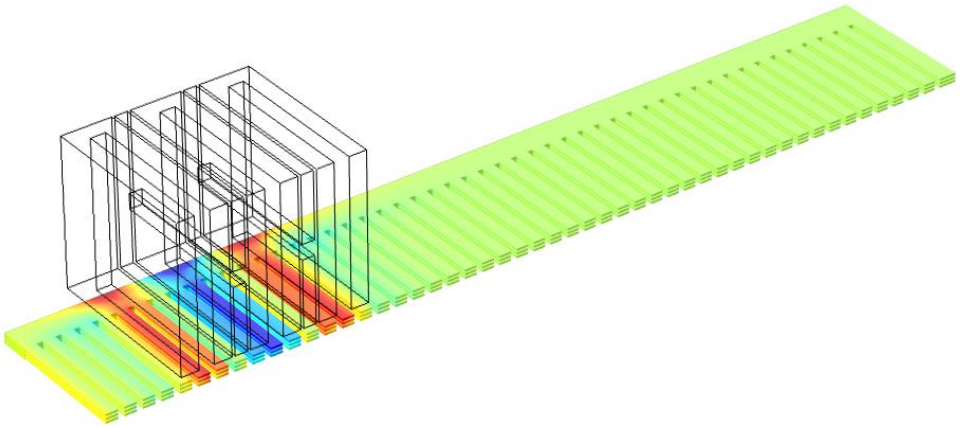

b)

Fig. 6.12 Optimized dimensions COMSOL results: a) Volume representation magnetic field; b) effect of the magnetic field on the track

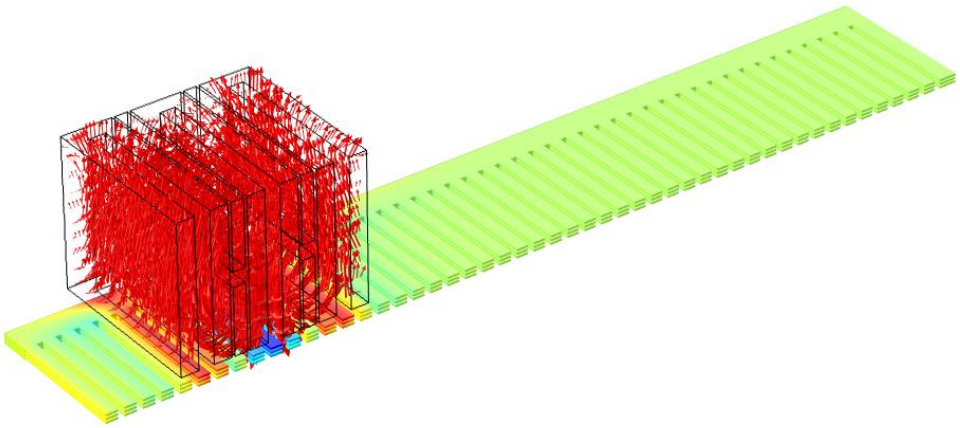

a)

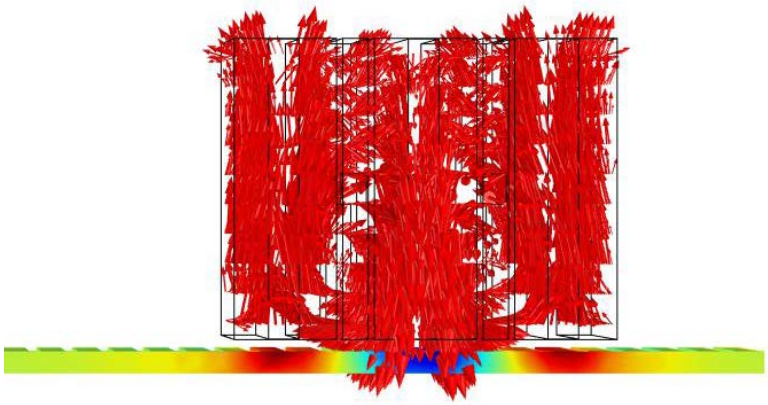

b)

Fig. 6.13 Optimized dimensions COMSOL results: Magnetic field arrow representation. a) Isometric view; b) Front view

A comparison of the forces generated over an active area by each design is presented in figures 6.14-6.15.

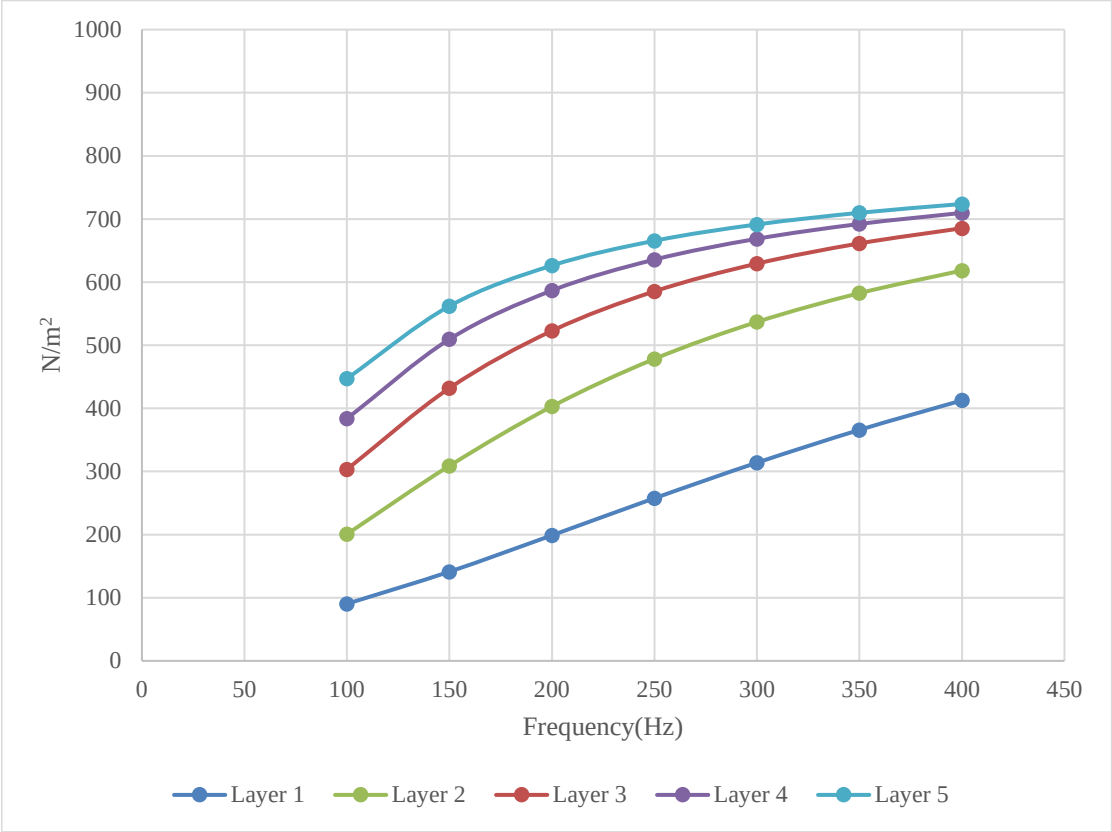

a)

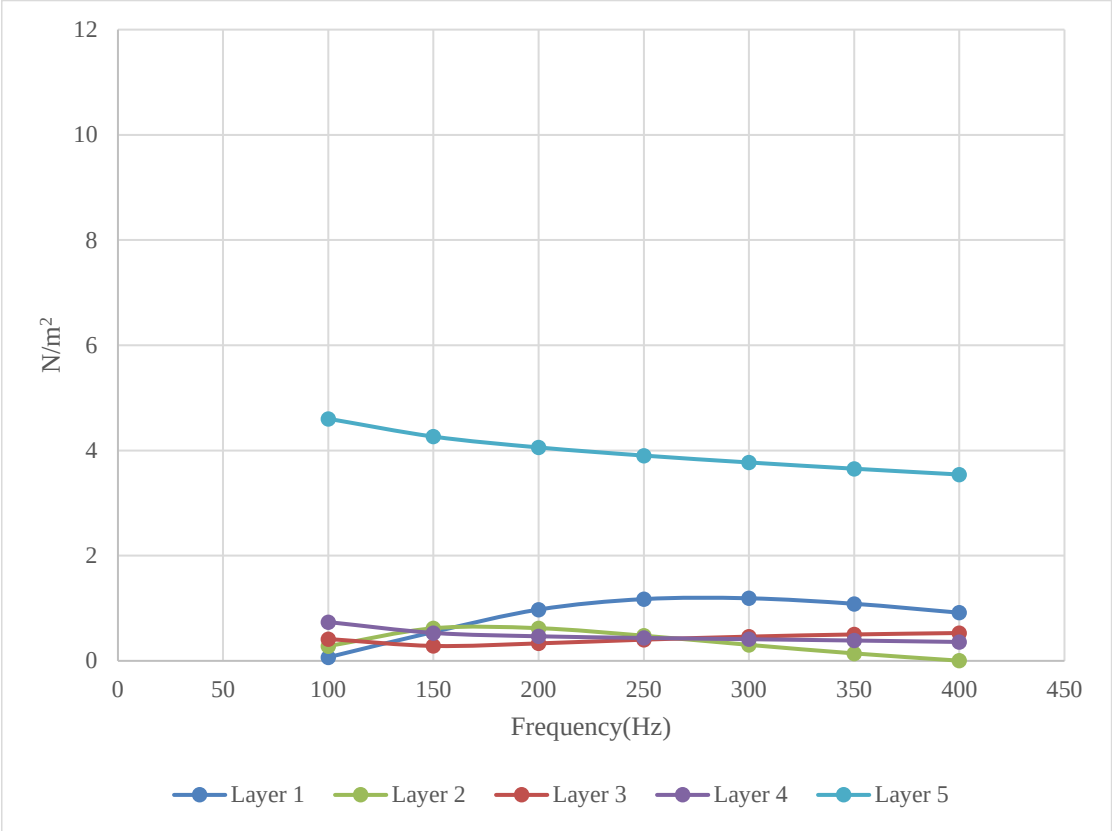

b)

Fig. 6.14 Original design forces per square meter from 100Hz to 400 Hz: a) Lifting; b) Dragging.

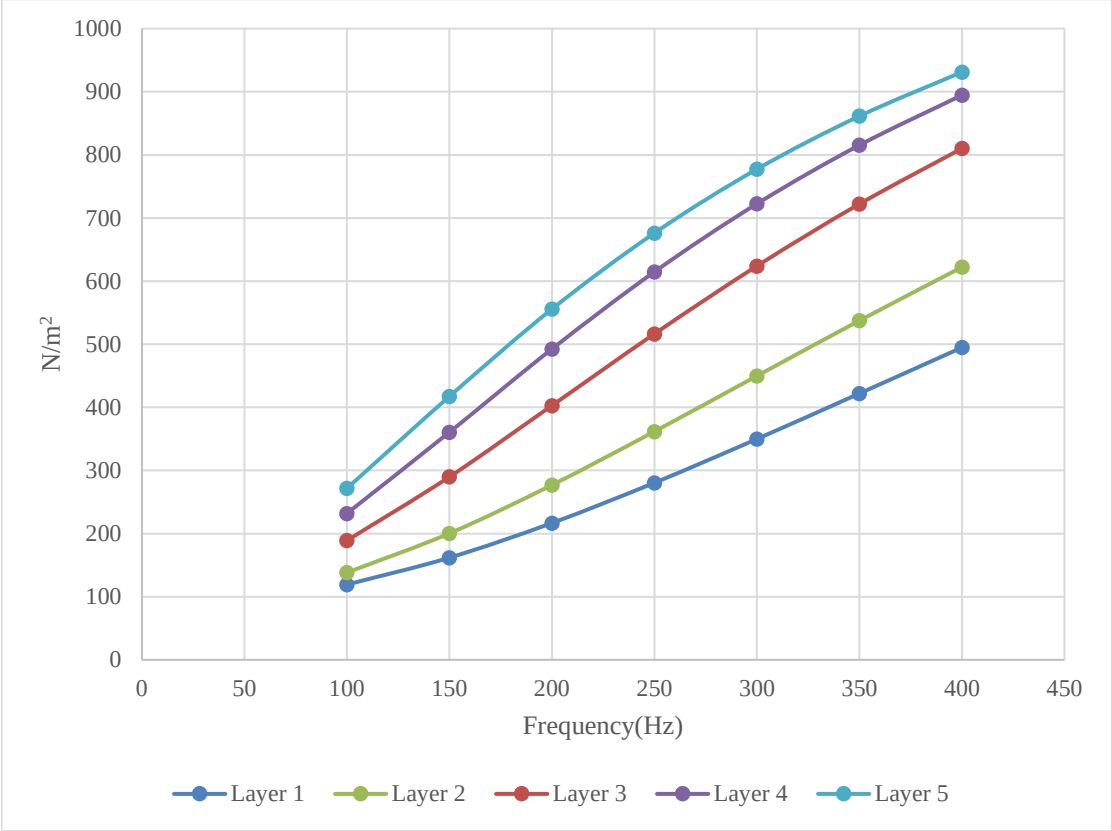

a)

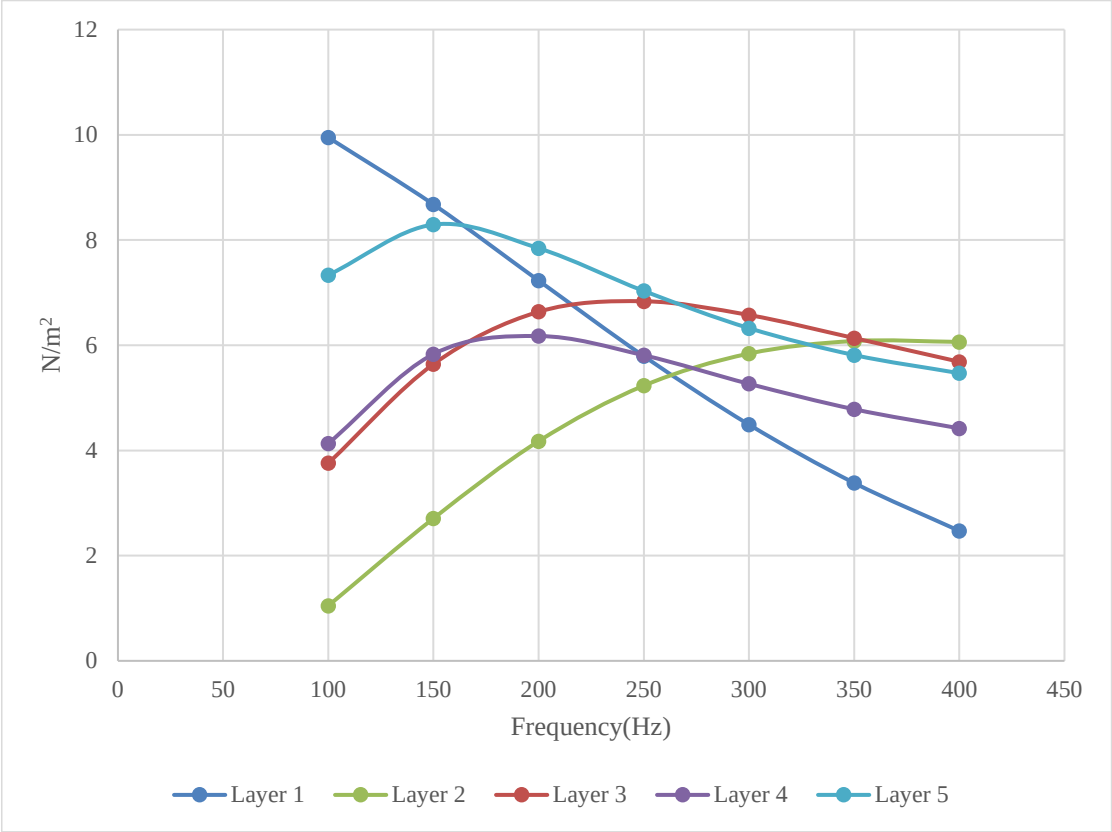

b)

Fig. 6.15 Optimised design forces per square meter from 100Hz to 400 Hz: a) Lifting; b) Dragging.

It can be noted that with a 5-layer track at 400 Hz the lifting forces have been improved by around 30% from the original design. Additionally it can be seen that the original designs lifting forces reached their steady state limit at 400 Hz, while the optimised design appears to be able to increase its lifting forces with an increase in frequency. However it should also be noted that the drag forces are higher in the optimised design. Finally the total mass per unit area used in the improved design is 54% the mass used in the original design, meaning a significant reduction in the magnetic bearing total mass.

6.3 1MW linear generator

It has been observed in section 6.1.1 that the higher the generator rating, the more efficient the device becomes in terms of size/installed capacity. Therefore it was decided to design a magnetic bearing using the dimensions of the 1MW machine shown in figure 6.4.

It has been decided that a sensible limitation to put in the design is that the amount of copper used in the magnetic bearings should not surpass 25% of the copper used in the generator (7200kg). Thus a topology of 6 active rails surrounding the translator divided into sections of 5-coil Halbach arrays was considered. Each rail must cover a length of 6.9 m (length of the stator) although the active part would be covering only the translator length at any one time. A CAD model is presented in figure 6.16 in which the arrangement of the coils, translator, active rails and levitation tracks can be observed.

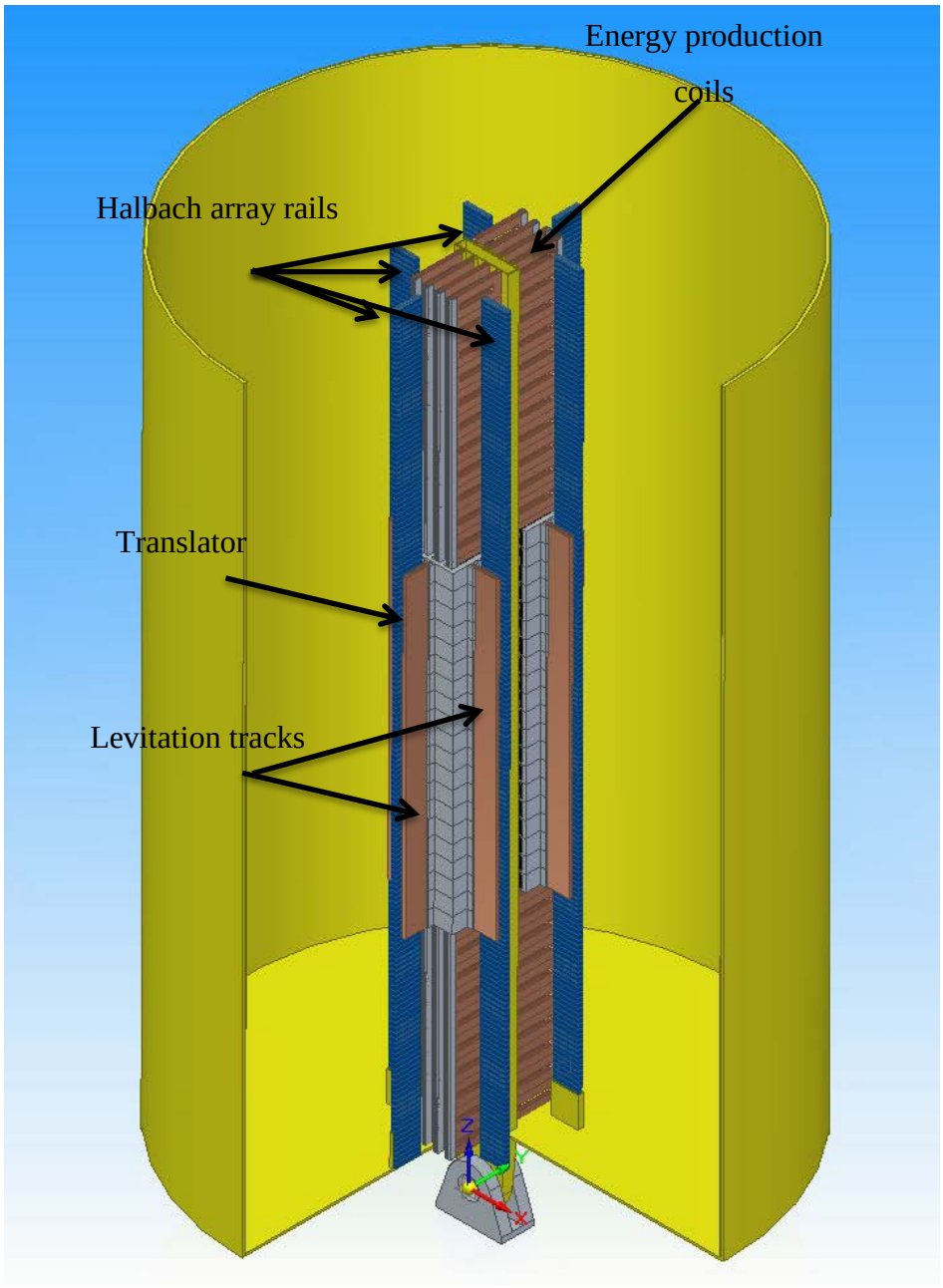

Fig. 6.16 Isometric view. Inside the 1 MW Generator.

Figure 6.17 shows the top view of the generator and the location of the parts mentioned in the last few Paragraphs, as well as generators permanent magnets facing the armature coils.

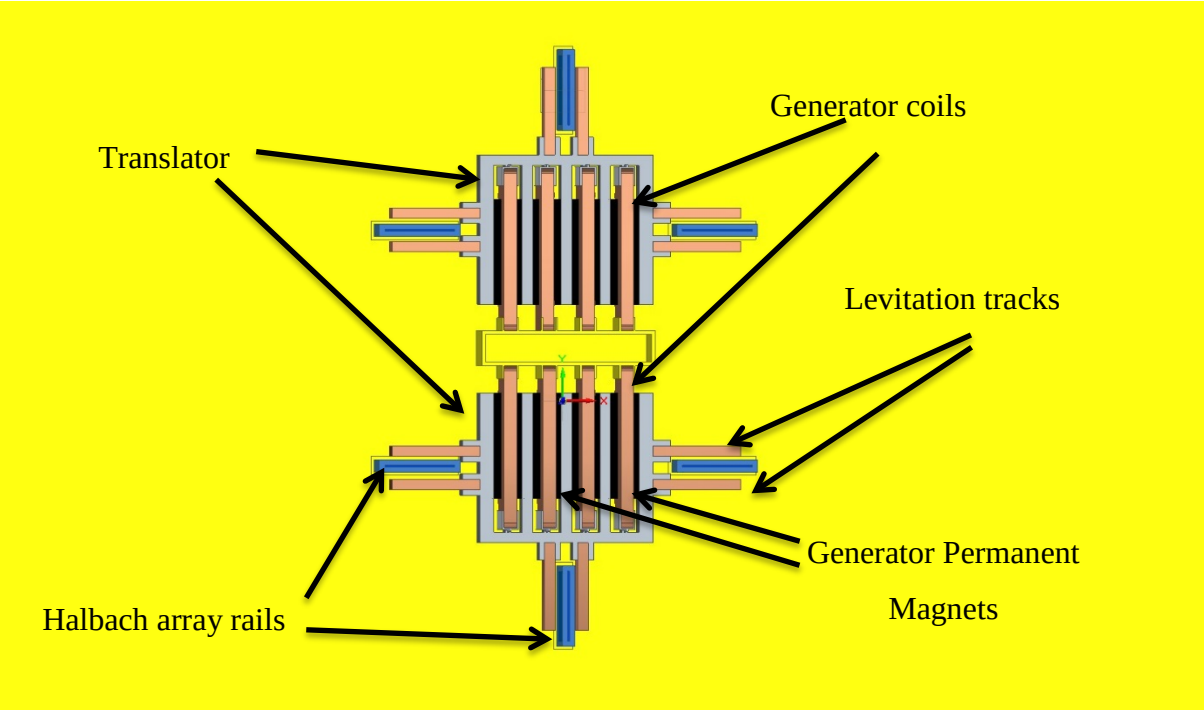

Fig. 6.17 Top view. Generator and magnetic bearings distribution.

Finally an isometric view of the generator is presented in figure 6.18 showing the translator in the generator in a clearer manner.

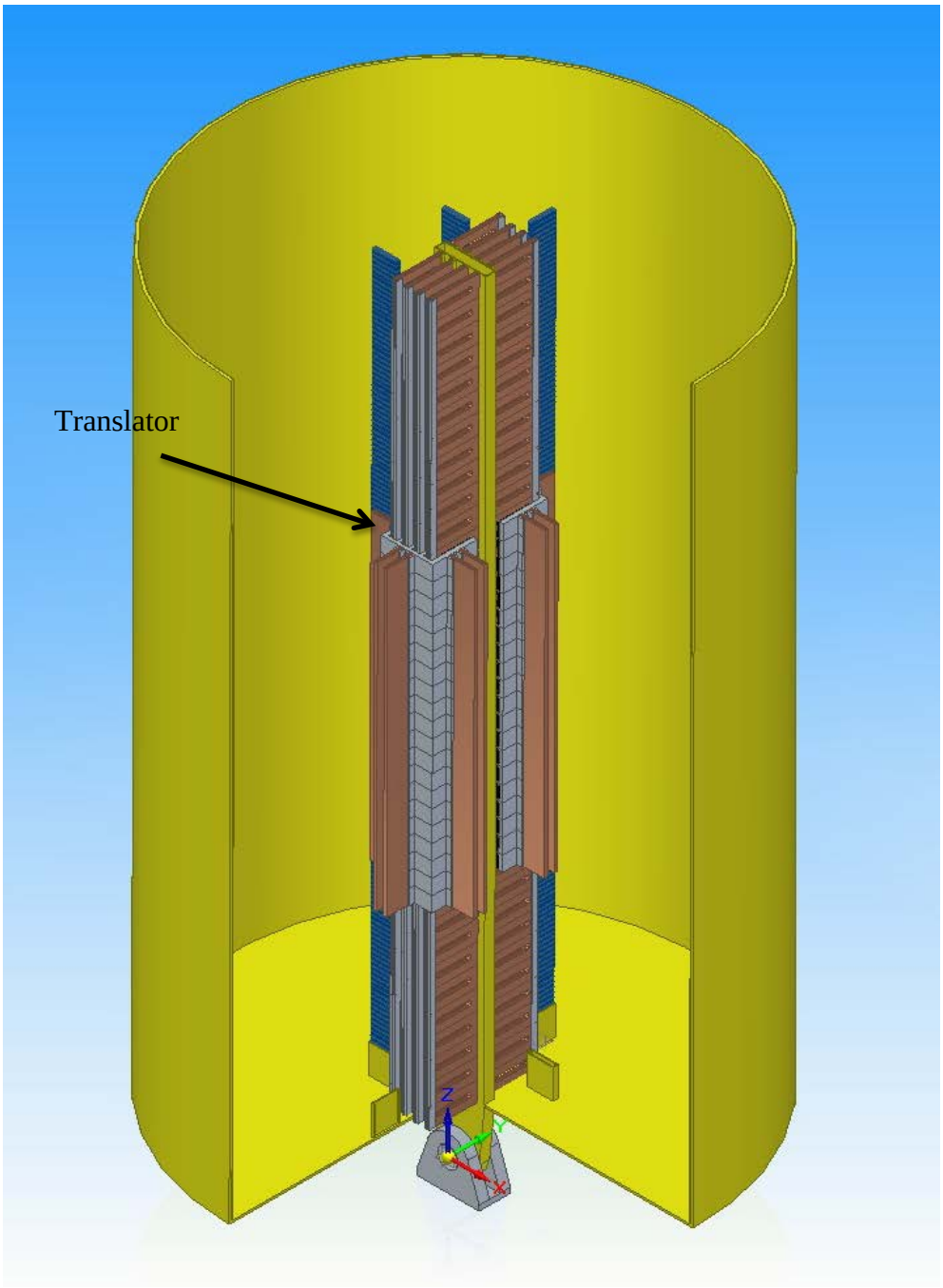

Fig. 6.18 Isometric view. Translator

According to the dimensions presented for the 1MW generator (see figure 6.4) the loads calculated will be acting on an area of 0.58m^2 (2.9mx 0.2m) if a 20 cm width on the levitation track is considered. The maximum load experienced by bearings, according to section 6.1.2, is 102.39 kN. This results in a force concentration per square meter of 253 kN/m^2.

The generators copper weight is 7200kg as stated, before the design for the magnetic bearings aims to use 25% of this mass split between 6 rails. Therefore the dimensions of the magnetic bearing for the 1MW machine is proposed to be as shown in table 6-IV.

TABLE 6-IV
OPTIMIZED DIMENSIONS 2MW GENERATOR

Symbol	Quantity(units)	description	Symbol	quantity	description
2*a1	200(mm)	Air core length. "*x*" axis	2*a2	200	Air core length. "*x*" axis
2*b1i	5(mm)	Air core length. "*y*" axis	2*b2i	5	Air core length. "*y*" axis
2*b1o	33.3334(mm)	Coil thickness. "*y*" axis	2*b2o	35.5	Coil thickness. "*y*" axis
2*c1	35.5(mm)	Coil height "*z*" axis	2*c2	33.3334/4	Coil height "*z*" axis
n_1	385	Number turns in coil 1	n_2	66	Number of turns in coil 2

Symbol	Quantity(units)	description	Symbol	Quantity(units)	description	Symbol	quantity	description
i	14.1(amp)	current	f	400(hz)	frequency	z_g	2(mm)	Gap from levitation track

The supplied current was chosen as the maximum value for a 19 AWG calibre wire. Operating Frequency was selected as the maximum frequency a commercial variable frequency drive can operate at.

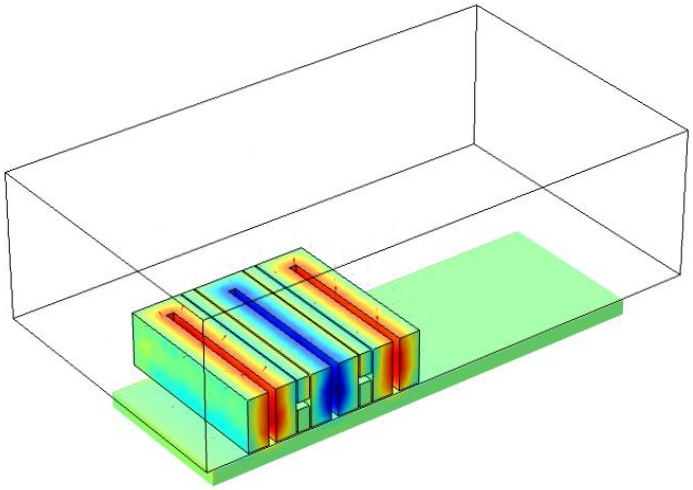

Fig. 6.19 First iteration rectangular air-cored Halbach array over a conductive plate.

The simulation results supply a force per square meter of 711.4 N/m^2, which is not enough to overcome the predicted loads.

A second iteration of the dimension was tried using a levitation track active area of 1.45m^2 (2.9mX0.5m). The dimensions for the coils in this case were designed to use the maximum area available from the translator. Therefore the dimensions are as follow.

TABLE 6-V
OPTIMIZED DIMENSIONS 1MW GENERATOR 2ND ITERATION

Symbol	Quantity(units)	description	Symbol	quantity	description
$2*a_{r1}$	500(mm)	Air core length. "*x*" axis	$2*a_{r2}$	500	Air core length. "*x*" axis
$2*b_{ri1}$	5(mm)	Air core length. "*y*" axis	$2*b_{ri2}$	5	Air core length. "*y*" axis
$2*b_{ro1}$	75(mm)	Coil thickness. "*y*" axis	$2*b_{ro2}$	235	Coil thickness. "*y*" axis
$2*c_{r1}$	235(mm)	Coil height "*z*" axis	$2*c_{r2}$	75/4	Coil height "*z*" axis
n_1	8225	Number turns in coil 1	n_2	4407	Number of turns in coil 2

This time the force result was 25.48 kN/m^2. This drastic change is due to the increase in coil turns and active levitation area. The forces generated are still not

enough to overcome the load applied onto the generator. The size of the bearing and hence the amount of copper used seem to be excessive compared to the size of the generator coils (see Figure 6.23).

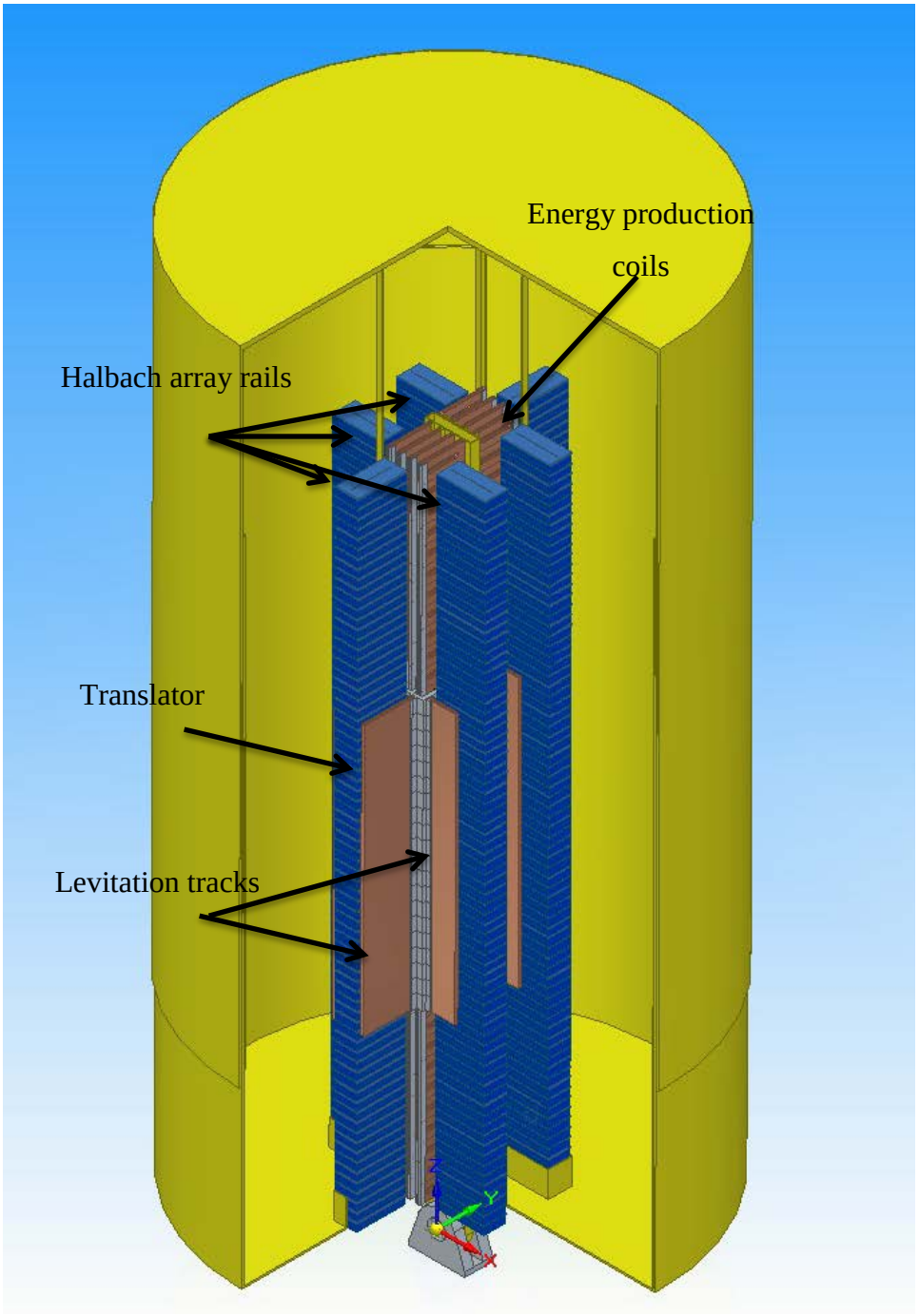

Fig. 6.20 Isometric view of the 1 MW generator with the second iteration design of Active magnetic bearings.

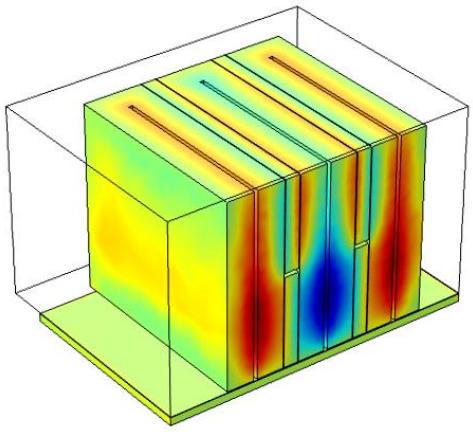

Fig. 6.21 Second iteration air-cored Halbach array over a conductive plate.

However a study on the reliability of the design, considering the scenario where the active magnetic bearing is able to overcome the forces is covered in the following section. The number of Halbach arrays is defined by the first station case dimensions.

6.4 Reliability

The importance of reliability in wave energy converters has been detailed in previous chapters. In fact, the main reason for exploring active magnetic bearings was to avoid the use of bearings, which have been proven to have a short life span[176].

At this point the size and equipment needed for the magnetic bearing has been established. Thus a study on reliability of Active Magnetic bearings as a mechatronic device was completed in this section.

It has been noted that Passive magnetic bearing (PMB) are more reliable than Active magnetic bearings (AMB) due to the simplicity of the system and the stability of levitation generated by repulsion effects [88],[181]. However it must also be considered that PMB depends on special operational conditions to achieve acceptable levels of levitation, stiffness and damping.

Basic terms of safety and reliability for AMB are covered in [182]. One of the most crucial aspects to improve reliability in AMB is redundancy. A redundant element is the one that can act partially or entirely in case of a main element failure. Failure detection and strategies need to act promptly in case of malfunctions and must be planned for as part of the control system. Therefore redundancy in mechatronic devices has been moving from hardware to software, with the implementation of robust and fault tolerant control systems [182].

In order for AMB to compete with PMB in reliability, the use of control robustness and the correct management of information and analytical redundancy must be applied to these systems[183],[98].

Unfortunately, although many magnetic bearing documents guarantee high reliability for different applications such as, altitude control for a satellite[80], precise linear positioning[100], energy storage flywheels for spacecraft [89], and Maglev trains[184], there is no mention of quantified data, a future comparison or study on this matter would therefore be useful.

6.4.1 Fuzzy reliability

Although there are processes to define the reliability of conventional systems formed from standardized parts, it should be noted that active magnetic levitation systems

are relatively new and these mechatronic systems with their mechanical, electrical, electronics and information process subsystems compound difficulties. Therefore the reliability analysis for devices like these has to be refined to cover each area of the mechatronic system [185]. Due to the differing levels of reliability uncertainties presented in these devices, statistical tools must be used to define the global reliability of the system, such as the ones presented in [186],[187]. Thus the main steps to follow are:

1. Identify possible failures.
2. Set the kind of membership function for each failure.
3. Divide the causes of the main failure into a logical diagram fault tree. Each node in this diagram could then represent individual subsystem malfunctions.
4. Calculate the probability for each membership at each failure.
5. Solve the logical diagram with the result probabilities.

Following these steps an AMB system can be separated into different subsystems where faults can originate.

- Control system(Digital signal processor or DSP)
- Power electronics(reliable switching amplifier or RSA)
- Electromagnetics (Coils)
- Back up bearings (Ball bearings for mechanical redundancy).
- Direction and energizing relays
- Displacement sensor

Most of the subsystems from the list have a failure rate with a negative exponential distribution (equation 6.16). The exception here is the backup bearings which follow the Weibull distribution shown in equation 6.17 where β=1.3.

$$F_{ne} = e^{-\lambda t} \qquad \textit{Eq. 6.16}$$

$$F_{w} = e^{-\left(\frac{t}{\lambda}\right)^{\beta}} \qquad \textit{Eq. 6.17}$$

According to [188] for a 90% of confidence level the failure rate must be considered between 0.08 and 11.9 the failure rate obtained, hence in this document we have a

lower, medium and high failure rate. Failure rates were found for each subsection of the device and are presented in table 6-III. Note that since the backup bearing has a Weibull distribution, an inverse of failure rate is presented on the table.

It is worth mentioning that the controller and switching system is a combination of digital signal processor (DSP) and a reliable switching amplifier (RSA) using a two-quadrant industrial switching digital controller concept. These amplifiers are generally formed by 2 amplifiers half bridges working in hot redundancy, thus increasing reliability.

TABLE 6-VI
FAILURE RATES

Subsystem	λ_l	λ_m	λ_h	Reference
Halbach array windings	2.5955e-6	3.3925e-6	4.5678e-6	[195]
Energizing Relay SPST	3.8184e-6	47.7296e-6	567.9819e-6	[195]
Direction Relay DPDT	7.6367e-6	95.4591e-6	1.1360e-3	[195]
Displacement sensor	600e-9	7.5e-6	89.25e-6	[196]
Power supply	288e-9	3.6e-6	42.84e-6	[197]
Back Up Bearings	1/378.5e3	1/30.2800e3	1/2.5445e3	[188]
Control system (DSP)	136.8e-9	1.71e-6	20.349e-6	[198]
Reliable Switching Amplifier 2Q-ISd	543.5964e-9	6.795e-6	80.86e-6	[185]

Following this, the next step is to draw and solve the Fault tree. The Fault tree diagram for the main failure event is shown in the following figure (figure 6.22). The following figures 6.23-6.26 present the detail of the subsystems (D1, C1, B1, and A1) that might cause a general failure. As indicated the failure of either the controller, the power source or 2 out of 4 magnetic bearing rails would cause a main failure of the system.

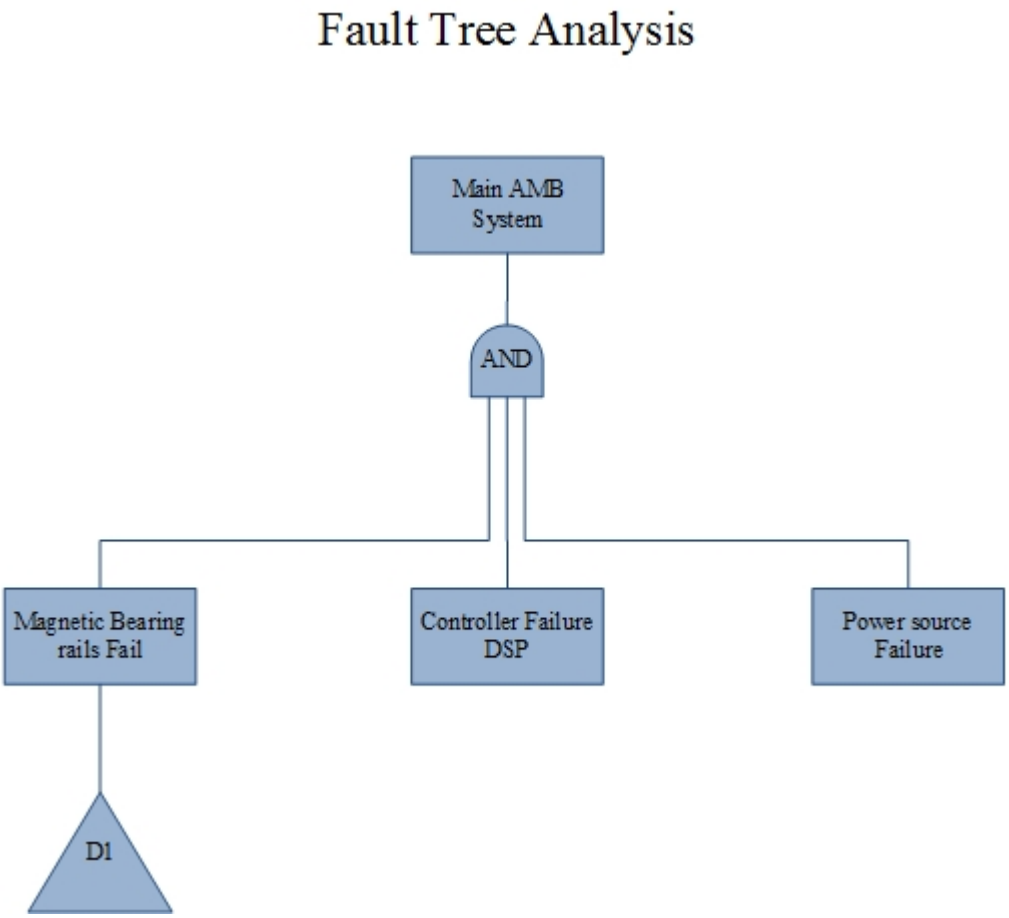

Fig. 6.22 Fault Tree Main failure

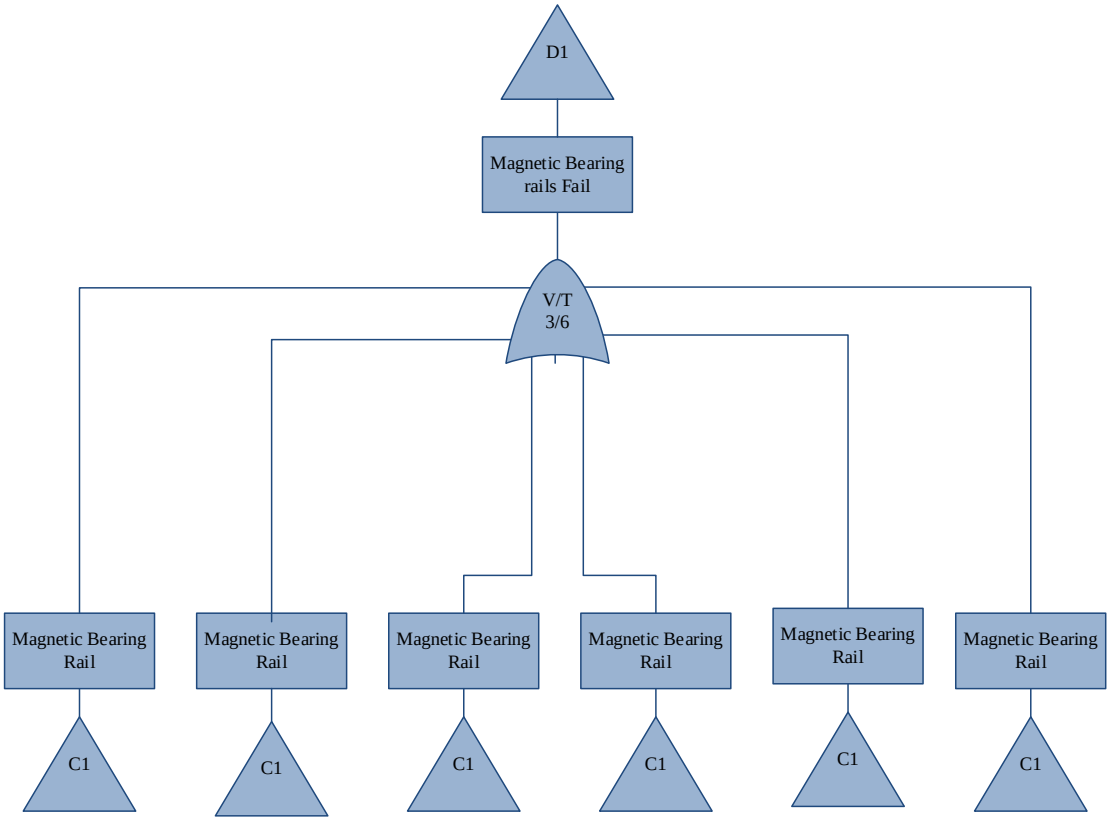

Fig. 6.23 D1 Detail

The reliability of the system can be calculated as:

$$P_m = \left(P_{3/6C1} * P_{ps} * P_{DSP}\right) \qquad \textit{Eq. 6.18}$$

Where the probability of failure of each system can be obtained with their respective failure rates and the probability of failure of *k-out-of-n*, in this case *2-out-of-4*, elements are obtained as follows:

$$P_{3/6C1} = \sum_{r=k}^{n} \binom{n}{r} P_{C1}^{r}(1 - P_{C1})^{n-r} \qquad \textit{Eq. 6.19}$$

The subsystem C1 is the magnetic bearing rail. Based on figure 6.26, C1 can be obtained from

$$P_{C1} = 1 - \left(\left(1 - \left(P_{25/50B1} * P_{RSA} * P_S\right)\right) * \left(1 - \left(P_{BUB}\right)\right)\right) \qquad \textit{Eq. 6.20}$$

Where the subsection *25-out-of-50* B1 is calculated as:

$$P_{25/50B1} = \sum_{r=k}^{n} \binom{n}{r} P_{B1}^{r}(1 - P_{B1})^{n-r} \qquad \textit{Eq. 6.21}$$

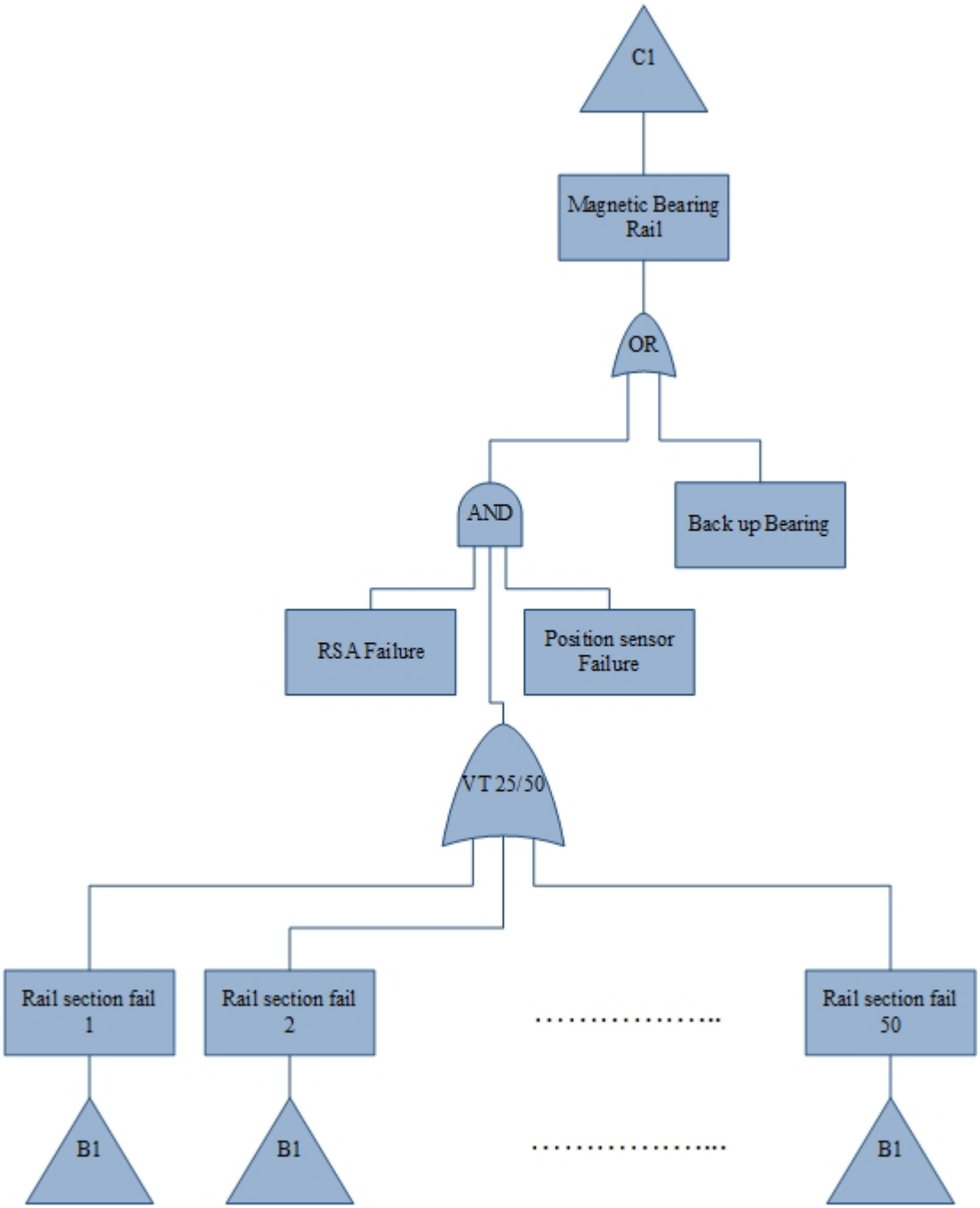

Fig. 6.24 Fault Tree section C1

Subsystem B1 is depicted in figure 6.27. It can be seen that there is a directional switch along with the energizing switch of each Halbach array section.

$$P_{B1} = P_{A1} * P_{DS} * P_{ES} \qquad \textit{Eq. 6.22}$$

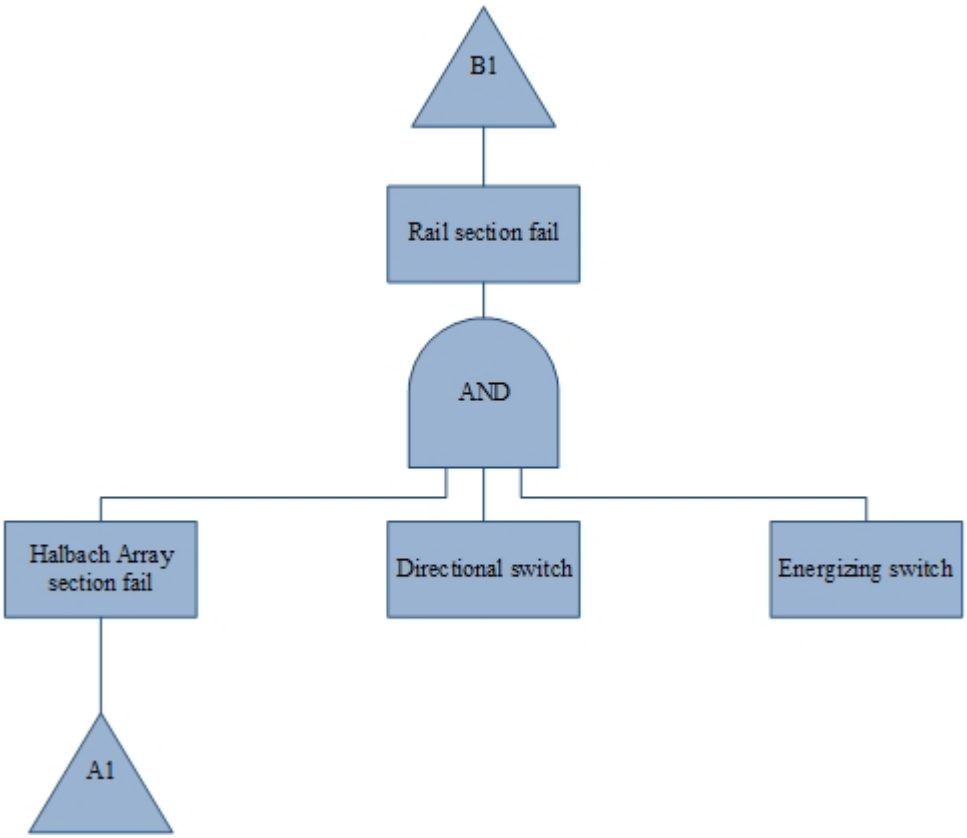

Fig. 6.25 Fault Tree section B1: Rail Section failure

The subsystem A1 (figure 6.23) is composed of the windings in the Halbach array If one these arrays fails the subsystems fails. Therefore:

$$P_{A1} = {P_w}^5 \qquad \textit{Eq. 6.23}$$

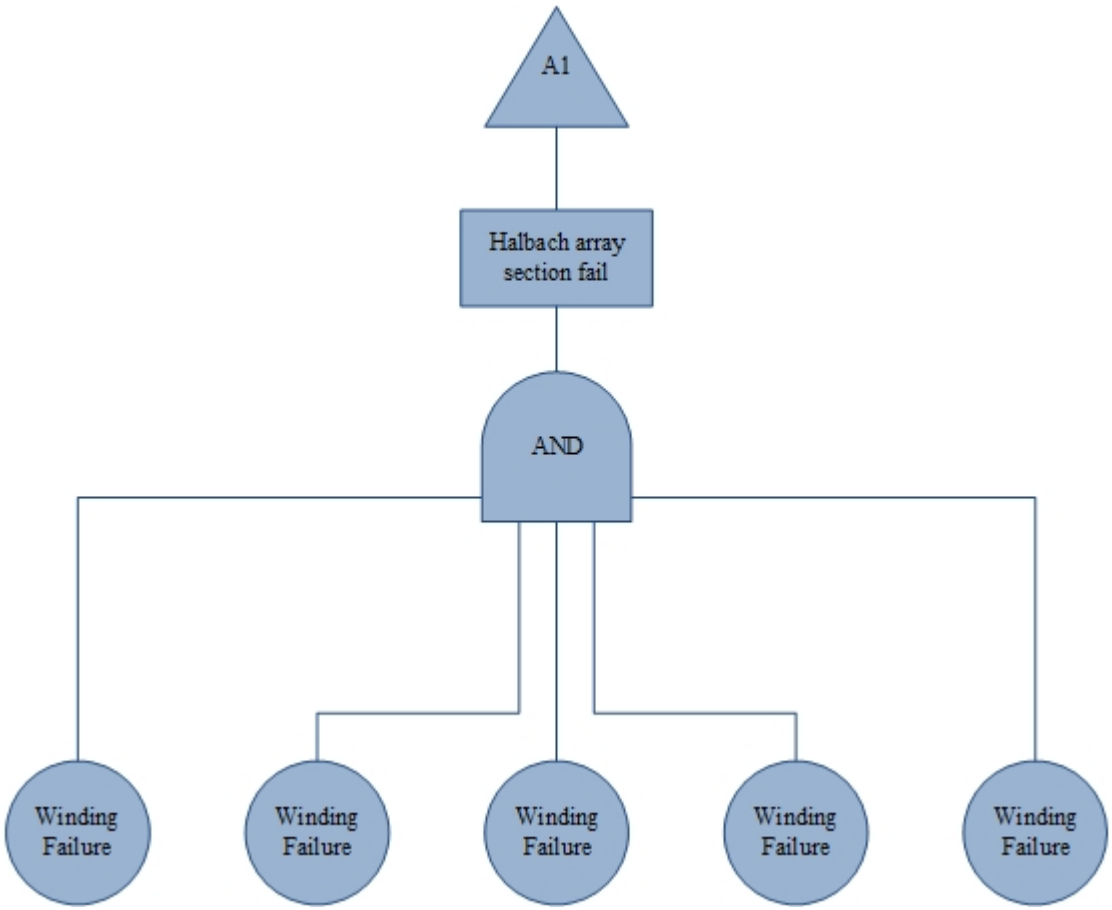

Fig. 6.26 Fault Tree section A1: Halbach array failure

The following figure 6.27 shows the comparison between a system using regular rolling element bearings and a system using active magnetic bearing with mechanical redundancy (Back Up Bearings) and software robustness (Sliding mode control).

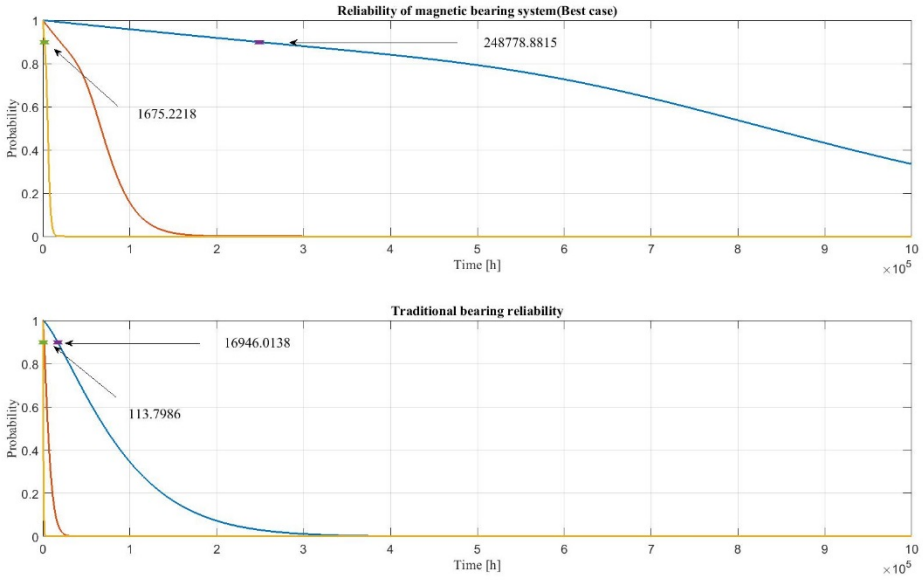

Fig. 6.27 Active magnetic bearings vs Traditional rolling element bearings reliability comparison.

TABLE 6-VII
RELIABILITY RESULTS

Subsystem	Time units	L_{10_high}	L_{10_low}	$MTTF_{high}$	$MTTF_{low}$
Best case Scenario Magnetic Bearings	Hours	248098	1666	993643.2	249087.6
	Days	10773	69	41401	10379
	Years	28.3	0.19	113	28.4
Traditional bearings	Hours	16946	113.79	88087.1	582.2
	Days	706.	4.74	3670	24.258
	Years	1.9	0.013	10.05	0.066

As can be seen from the reliability analysis, the overall reliability of the bearings has increased. The use of mechanical redundancy and control robustness have increased the Mean Time To Failure (MTTF) by almost 10 times. However it must be kept in mind that there is no hard data to compare with this study. A more detailed comparison must take place in the future.

6.5 Brief cost analysis

In the first design iteration of the C-Gen 1 MW machine, it was mentioned that the weight ratio of active copper in the bearings to the active copper in the generator

windings would be 1:4. Therefore 7200/4 kg is equal to1800kg of copper. If the price per kilogram of copper is £10[189] this result is £18k. Now if the price of manufacturing is 2.5 times[190] the price of the material, this adds up to a total of £63k. Now following [190] the price of power electronics per megawatt is £580k multiplied by 1.3 of assembly cost, then if the generator is rated to 1 MW, the coils are 1/4th of it and half of it will be active most of the time, if the power electronic cost is considered as £94.25k (580x1000x1/8). The total cost for the first iteration design is £157.25k. Hodgings calculated a price of £900k for a 1MW generator meaning that the magnetic bearing for a 1MW generator would cost around a 17% of the generator total. Additionally this design would not be able to overcome the loads applied onto the generator. Following the same process for the second iteration the result is £732,068. This is 80% of the entire generator cost and the device is still not able to cope with the loads.

6.6 Conclusions

The diameters needed for buoyancy in order to reach maximum speed of 2.2 m/s were calculated for the C-Gen linear generator (with capacities from 0.125 MW to 1 MW). Subsequently the loads acting on the bearings were calculated. The forces per square meter were 253 kN/m^2. Keeping this in mind, two design iterations for the magnetic bearings were obtained, optimizing the dimensions to have higher concentration of forces.

The first iteration was aimed at using only 25% of the total copper mass the generator uses for energy production. However this design fails to cope with the loads. Ignoring the excessive amount of copper a second iteration was done resulting in the same negative result.

Although the concept was proven to be insufficient for this application a reliability study was realised in section 6.4 showing that using magnetic bearings along with back up bearings the system can improve reliability, as measured by the MTTF, by a factor of 10.

Additionally a brief cost analysis was completed in which the second design iteration was calculated to cost 80% of the entire generator costs which make this design

unattractive. Therefore improvements in the design most be pursued or a more cost effective option must be explored.

7 Conclusions

This thesis presented a novel active magnetic bearing for a wave energy converter. The proof of concept, modelling, control and reliability analysis were carried out.

The motivation for this research is the massive potential of wave energy converters in the renewable energy scene and its challenge to become a mature technology in order to compete against renewable energy technologies such as wind energy.

In order to achieve this a more compact and reliable linear generator system must be designed. Therefore improving the life span of the bearing system is essential for these kind of devices. In section 3 it was stated that the goal for this research was to develop a design that can endure the complex loads and irregular speed present in linear wave energy converters replacing traditional rolling bearings and increasing the overall reliability of the system.

To reach to this point a literature review on the current state of Marine energy and wave energy converter as well as concepts of different magnetic bearings were presented. Active magnetic bearings vary in configuration and they are complex in operation. The optimum design requires a deep understanding of the application and also of the magnetic configuration planned for use. The material and configuration of the magnetic bearing presents advantages and disadvantages and the best option is still to be determined.

Electromagnetic suspension (EMS) bearings tend to be used in applications where the position, speed and stiffness must be controlled by the user. However they consume more energy and have higher initial investment than their counterpart electrodynamic suspension (EDS). On the other hand EDS systems are dependable of condition such as velocity or temperature to achieve acceptable level of levitation (HTSC applications or Inductrack).

Magnetic bearing concepts were reviewed in chapter 4 with different magnetic configurations. As a result, in this thesis a hybrid concept was proposed consisting of an air cored coil Halbach array facing a levitation track. This development resembles an active version of the Inductrack concept.

7.1 Concept and mathematical model

The air core cored Halbach array presents a high Lift/drag ratio, eliminates velocity dependency, and can generate bi-directional forces that increases as the gap between stator and translator decreases.

In order to understand this novel active magnetic bearing concept, simulations in MatLab and a 3D finite element software "COMSOL" were made. Different ways to calculate the magnetic field over a plane were compared to the results obtained in COMSOL showing a remarkable similarity.

Additionally two mathematical models to obtain the lifting and dragging forces were coded in MatLab based on Post[159], [168], [170], [191] and Storset [167], [169]. In chapter 5 the two different models were compared to the results from COMSOL, but it should be noted that both mathematical models assume simplifications that do not apply to this project prototype.

Specifically Post's Mathematical reasons for inaccuracy are listed below:

- This mathematical model is sensitive to the selection of the magnetic field peak B_0. Storset mentioned that the selection of the peak magnetic field is crucial for the force calculation in Post's mathematical model, and can lead to up to the 70% overestimation of the forces generated.
- Also for this research work in specific, another reason for the Post mathematical model being unsuitable is the consideration of the magnetic field being uniform across the transverse plane over the array. It has been observed that when air-cored coils are used in the Halbach array, the magnetic field concentrates at the centre of the array decreasing in magnitude along the array's sides.
- Additionally Post's considerations that were not fulfil in this device design are:
    - Each individual track loop is electrically isolated.
    - Each loop Self-inductance should be substantially larger than mutual inductance from other loops in the circuit.

- For a window shape track the dimension between the top and bottom leg of the track must be larger than the wavelength.

On the other hand the lifting and dragging forces obtained by Storset model are closer to the COMSOL results. However, the Storset model ignores the side bar effect on the model since he considers that the effect of these bars is negligible if the length of the rung is much larger than the space between rungs, although Storset never mentions a precise ratio for this. By experimenting with the COMSOL model it has been shown, in chapter 5, that the side bar dimension of the levitation track affects the forces generated.

Based on the comparison of the analytical and COMSOL model the Storset mathematical model is accurate enough to serve as a base to provide a first order design to dimension the bearing, but more detailed modelling is required to finalise a design. For this reason COMSOL was used for further investigations and comparison with experimental results.

7.2 Proof of concept and concept sizing

In order to prove and investigate the concept further a prototype was built. The magnetic bearing was tested over a range of frequencies comparing the readings with the COMSOL model results. The prototype presented a few setbacks that made the experimentation process time consuming and difficult. One can say that there were two main problematic areas: design and manufacturing mistakes, and faulty equipment. Although this is debatable since the first one, caused part of the second.

Design was based on the Post model, which resulted in an overestimation of lifting and dragging forces generated by the device. In order to overcome manufacturing difficulties, a window frame type levitation track was chosen. During the experiment it was noted that the track wasn't generating enough forces for the load cell to read, linked to the overestimation of the design using the Post model. Therefore a new slotted levitation track was manufactured.

Another design mistake was to overlook the heat transfer in the air-cored coils. The air-cored coil Halbach array is completely potted in fibre glass and epoxy. The air-cored array structure does not provide effective paths for removing heat, and there is

no circulation of air. Hence the coil temperature rises rapidly changing the resistance of the coils and, at the same time, the current circulating through them. As a result it was only possible to run each experiment for a few seconds making it difficult to have an accurate reading of the forces generated. The solution was to take many readings of different currents at each frequency. Subsequently a polynomial trend using MatLab was calculated in order to get the forces generated for any desired current (see appendix).

The second complication was the equipment malfunctioning. In order to control the current and frequency for the experiment a power source Pacific Smart Source 360-amx was used. The software installed in the computer did not give current readings, which matched with the current measured using a calibrated current transducer and scope. Thus more measurements were made comparing the current from the Pacific Smart Source with readings from the scope in order to produce an adaptation curve, to set the correct conditions of the experiments and COMSOL simulations.

Despite these setbacks the results from the experiments match the simulations carried out in COMSOL. This serves as a guide to understand the device behaviour and future improvements in the design.

After proof and further investigation of the concept, the magnetic bearing size needed for a 1MW generator was obtained. From here it was concluded that the magnitude of the lifting force is not large enough to make this device remotely apt for the application even when the design is optimised and oversized.

Even though the concept in its present form failed to achieve its goal a reliability study was completed, which showed an increase of around 10 times the MTTF compared to traditional rolling bearings. This highlights the potential advantage of such an electromagnetic bearing, but more work is required to improve the technology in terms of performance, and design. The future work section below outlines some improvements and options in order to make this happen.

7.3 Future work

After this study a few interesting points considered for future exploration are listed below.

Mathematical model

A more accurate mathematical model is needed to improve the optimization of the device. Having an analytical model would allow improvements in the design using optimization tools without the use of computational expensive 3D finite element models. The new model would also include the structural material and include calculation of the power losses within the device, the latter required for predicting the thermal performance.

Heat dissipation

The heat management of the air core Halbach array must be studied and improved. In operation the Halbach array the rate of rise of winding temperature was significant so that continuous operation was not possible. Thermal modelling and a cooling system is required to improve the bearing design and performance. Having the device flooded with water represents a cooling advantage, but operation in seawater has its own challenges, of corrosion and the capacitance effect of the coils will result in large current spikes due to high dV/dt..

Iron-cored coils

Using iron core can be a solution to increase the magnetic field generated by the array. COMSOL simulations were run, replacing the air core by soft iron core with a relative permeability of 4000 for both original an optimised design (see figure 6.11). The results over a range of frequencies are compared in figure 7.1. It can be seen that the force per square meter in the original design has been increased but the optimised design with an iron core results in an outstanding improvement.

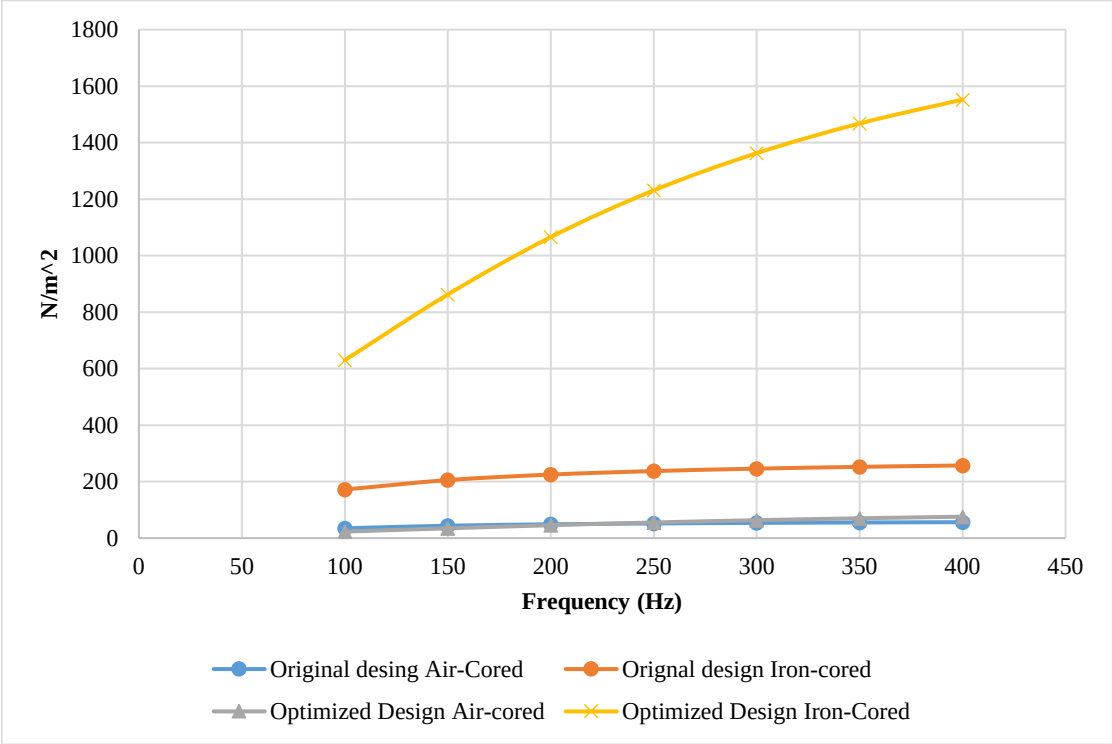

Fig. 7.1 Original and optimized deign comparison. Air-cored vs Iron-Cored

However, significant magnetic attraction forces acting within the generator requires a more stiff structure in the Halbach array and the track. A study on the structural composition of the Halbach array must be carried out. As well as providing electromagnetic function to improve the lift force, the iron can also provide structural function and. In figure 7.2 a proposed layout is shown. The disadvantage from this design is that the magnetic field enhance side cannot be changed by switching two elements as shown in chapter 5 figures 5.2 and 5.3. This is due the presence of Iron in the design (see figure 7.2).

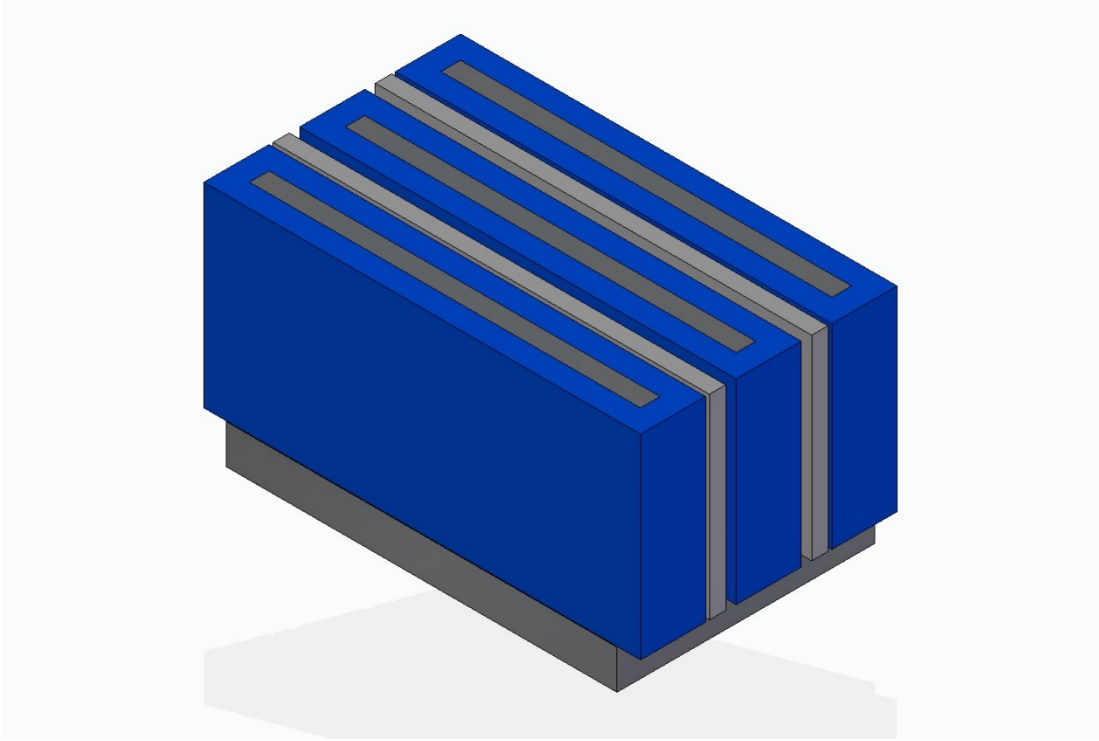

a)

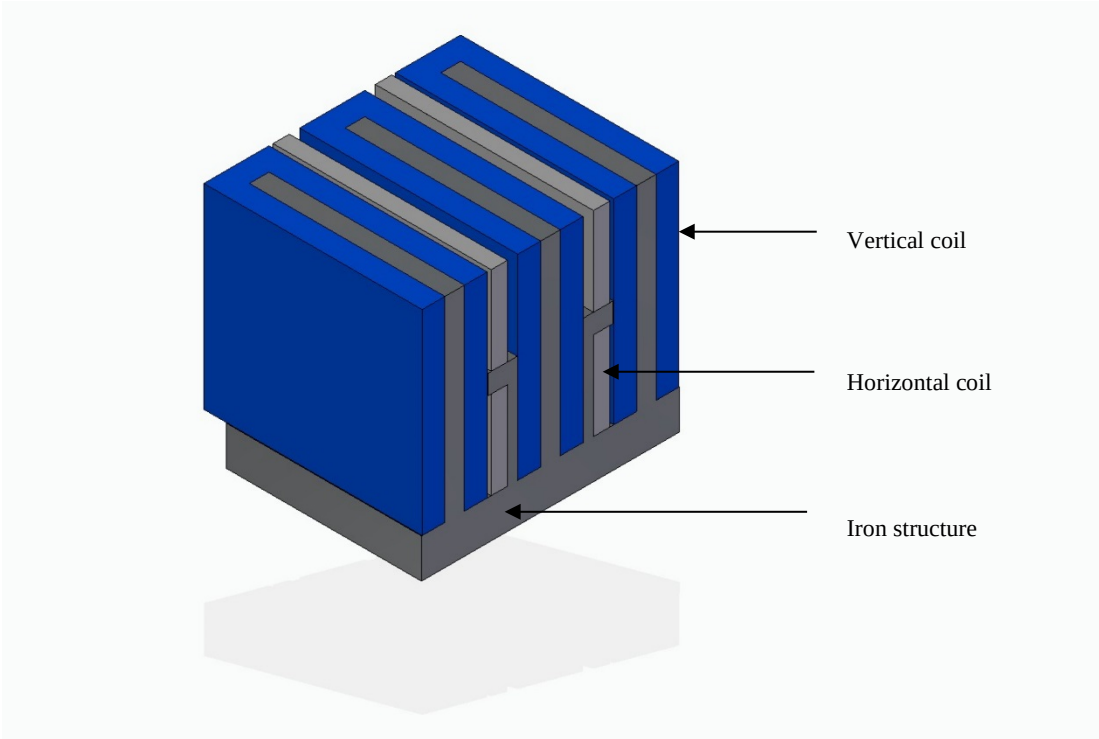

b)

Fig. 7.2 Proposed Iron structure holding the optimised Iron-Cored Halbach array. A) Isometric view; b) cutaway view and details

However the design could emulate the dual Halbach array, increasing improving the lift/drag ratio according to [191]. In the dual Halbach array two Halbach arrays face each other having the levitation track in the middle. The repelling force then augment when the track approach to either side of the dual Halbach array. This arrangement is shown in figure 7.2.

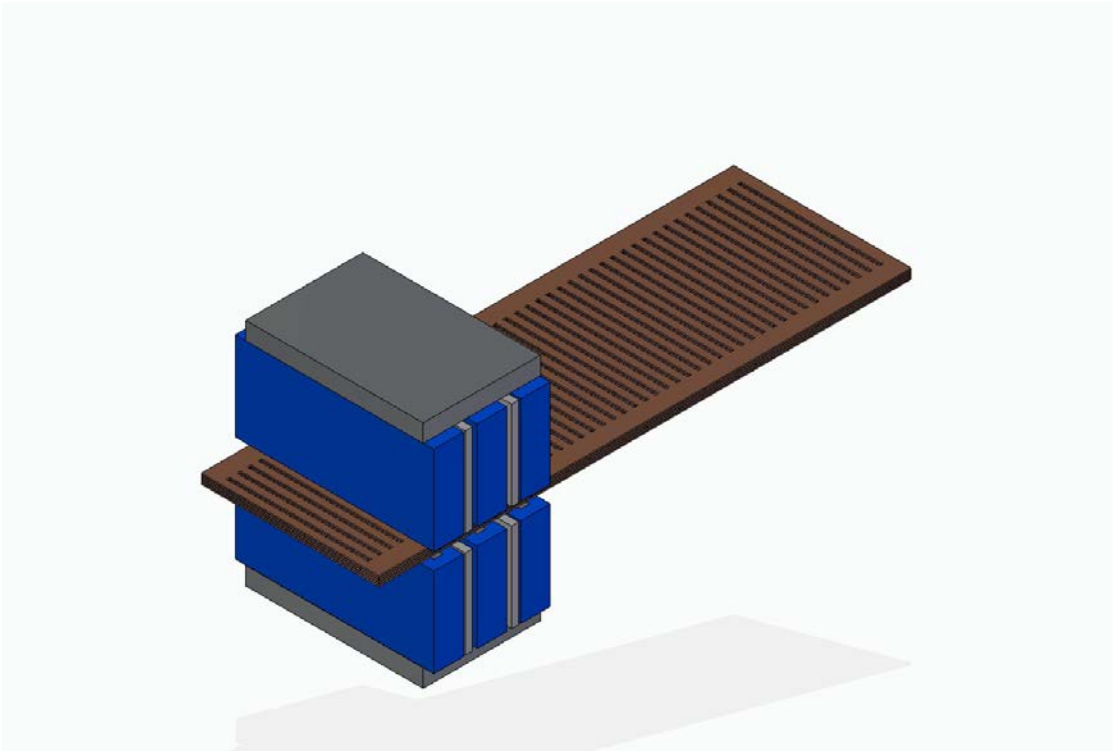

Fig. 7.3 Dual Iron-Cored Halbach array Isometric view.

Additionally a more detailed study on the slotted levitation track design will help to potentially improve the capabilities of the device without the use of Litz track making the manufacturing of easy.

Control and hardware improvement

Although this document present a control model where the conditions are highly ideal. A more realistic implementation of a robust control must be done. Besides the implementation of the control strategy itself, High frequency, switching circuits and underwater conditions affect the electrical behaviour of the concept. Including iron in the device will also affect the control.

Novel bearing for future studies

Since the design presented in this thesis was not able to overcome the loads acting on the wave energy converter, other solutions should be investigated..

Magnetic bearings using high temperature superconductors (HTSC) are common in the passive configuration. With the right design the velocity dependency can be overlooked. Also using HTSC can decrease the size of generators which make them attractive for developers. Perhaps a design that combine the superconductor coils for energy production and levitation at the same time could come as a solution for the problem.

Surface contact bearings with novel polymeric materials can also be a possible solution. In the current magnetic bearing state of the art it is highly probable that surface contact bearings will be used as a back –up in case of failure of the magnetic bearing.

Bibliography

[1] T. Barker, L. Bernstein, P. Bosch, O. Canziani, Z. Chen, R. Christ, O. Davidson, W. Hare, S. Hug, D. Karoly, V. Kattsov, Z. Kundzewicz, J. Liu, U. Lohmann, M. Manning, T. Matsuno, B. Menne, B. Metz, M. Mirza, N. Nicholls, L. Nurse, R. Pachauri, J. Palutikof, M. Parry, D. Qin, N. Ravindranath, A. Reisinger, J. Ren, K. Riahi, C. Rosenzweig, M. Rusticucci, S. Schneider, Y. Sokona, S. Solomon, P. Stott, R. Stouffer, T. Sugiyama, R. Swart, D. Tirpak, C. Vogel, and G. Yohe, "Climate Change 2007: An Assessment of the Intergovernmental Panel on Climate Change," *Change*, no. November, pp. 12–17, 2007.

[2] J.H.Mercer, "No TitleWest Antartic ice sheet and CO2 greenhouse effect: a threat of disaster," *Macmillan Journals*, vol. 271, 1978.

[3] C. David and J. C. Mackay, *Sustainable Energy — without the hot air This Cover-sheet must not appear in the printed book* . 2009.

[4] K. Onozaki, "Population Is a Critical Factor for Global Cabon dioxide Increase," vol. 55, no. 1, pp. 125–127, 2009.

[5] R. K. Pachauri, L. Meyer, J.-P. Van Ypersele, S. Brinkman, L. Van Kesteren, N. Leprince-Ringuet, and F. Van Boxmeer, *Climate Change 2014 Synthesis Report The Core Writing Team Core Writing Team Technical Support Unit for the Synthesis Report*. 2014.

[6] "Environmental Implications of Population Dynamics.pdf." .

[7] U. Bardi, "Peak oil: The four stages of a new idea," *Energy*, vol. 34, no. 3, pp. 323–326, Mar. 2009.

[8] R. W. Bentley, "Global oil & gas depletion: an overview," *Energy Policy*, vol. 30, no. 3, pp. 189–205, 2002.

[9] E. Outlook, *International Energy Outlook*, vol. 484, no. July. 2010.

[10] European Parliament, "At a Glance: Doha Amendment to the Kyoto Protocol-second commitment period," vol. 3, no. June, p. 2015, 2015.

[11] United Nations/Framework Convention on Climate Change, "Paris Agreement," *21st Conf. Parties*, p. 3, 2015.

[12] HM Government, *The UK Low Carbon Five point plan*, no. July 2009. 2009.

[13] Decc, "UK Renewable Energy Roadmap," *Carbon N. Y.*, vol. 5, no. July, pp. 293–298, 2011.

[14] M. Gunnar, S. Barstow, A. Kabuth, and M. T. Pontes, "Assessing the global wave energy potential," *Proc. 29th Int. Conf. Offshore Mech. Artic Eng.*, no. 2008, pp. 1–8, 2010.

[15] D. Krohn, M. Woods, J. Adams, B. Valpy, F. Jones, and P. Gardner, "Wave and Tidal Energy in the UK: Conquering Challenges , Generating Growth," *Issue 2*, no. February, pp. 1–32, 2013.

[16] "ocean energy race The UK ' s inside track."

[17] Carbon Trust and AMEC Environment & Infrastructure UK Limited, "UK Wave Energy Resource," p. 66, 2012.

[18] J. Falnes, "A review of wave-energy extraction," *Mar. Struct.*, vol. 20, no. 4, pp. 185–201, 2007.

[19] B. Drew, A. R. Plummer, and M. N. Sahinkaya, "A review of wave energy converter technology," *Proc. Inst. Mech. Eng. Part A J. Power Energy*, vol. 223, no. 8, pp. 887–902, Dec. 2009.

[20] M. a. Mueller, H. Polinder, and N. Baker, "Current and Novel Electrical Generator Technology for Wave Energy Converters," *2007 IEEE Int. Electr. Mach. Drives Conf.*, no. 1, pp. 1401–1406, May 2007.

[21] O. Keysan, "Superconducting Generators for Large Offshore Wind Turbines," p. 228, 2014.

[22] P. A. Measures, C. Of, S. Wave, and E. Converters, “Omae2011-40360 Power Absorption Measures and Comparisons of Selected Wave,” 2011.

[23] D. Silva, E. Rusu, and C. G. Soares, “Evaluation of various technologies for wave energy conversion in the portuguese nearshore,” *Energies*, vol. 6, no. 3, pp. 1344–1364, 2013.

[24] G. Dalton, N. Rousseau, F. Neumann, and B. Holmes, “Non-technical barriers to wave energy development, comparing progress in Ireland and Europe,” *8th Eur. Wave Tidal Energy Conf.*, pp. 1–9, 2009.

[25] J. M. Pinar Pérez, F. P. García Márquez, A. Tobias, and M. Papaelias, “Wind turbine reliability analysis,” *Renew. Sustain. Energy Rev.*, vol. 23, pp. 463–472, 2013.

[26] T. M. Delorm, Y. Lu, A. Christou, and P. McCluskey, “Comparisons of offshore wind turbine reliability,” *Proc. Inst. Mech. Eng. Part O J. Risk Reliab.*, vol. 230, no. 3, pp. 251–264, 2016.

[27] T. R. No, C. Engineering, and E. P. Engineering, *Design of Direct-driven Permanent-magnet Generators by Anders Grauers*, no. 292. 1996.

[28] D. Bang, H. Polinder, G. Shrestha, and J. A. Ferreira, “Review of Generator Systems for Direct-Drive Wind Turbines,” *Technology*, pp. 1–11.

[29] H. Polinder, B. C. Mecrow, A. G. Jack, P. Dickinson, and M. A. Mueller, “Linear generators for direct-drive wave energy conversion,” in *IEEE International Electric Machines and Drives Conference, IEMDC’03*, 2003, pp. 798–804.

[30] H. Polinder, M. E. C. Damen, and F. Gardner, “Linear PM Generator System for Wave Energy Conversion in the AWS,” *IEEE Trans. Energy Convers.*, vol. 19, no. 3, pp. 583–589, Sep. 2004.

[31] H. Polinder, M. A. Mueller, M. Scuotto, and M. G. D. S. Prado, “Linear generator systems for wave energy conversion,” *Technology*, pp. 1–8, 2007.

[32] H. Polinder, B. C. Mecrow, A. G. Jack, P. Dickinson, and M. a. Mueller, “Linear generators for direct-drive wave energy conversion,” in *IEEE International Electric Machines and Drives Conference, 2003. IEMDC’03.*, 2003, vol. 2, pp. 798–804.

[33] M. a. Mueller, H. Polinder, N. Baker, M. A. M. Member, and M. Ieee, “Current and Novel Electrical Generator Technology for Wave Energy Converters,” *2007 IEEE Int. Electr. Mach. Drives Conf.*, no. 1, pp. 1401–1406, May 2007.

[34] C. A. Oprea, C. S. Martis, F. N. Jurca, D. Fodorean, and L. Szabó, “Permanent Magnet Linear Generator for Renewable Energy Applications : Tubular vs . Four-Sided Structures,” pp. 588–592, 2013.

[35] L. Szabo, C. Oprea, J. Viorel, K. A. Biro, and E. L. Szabogmae, “Novel Permanent Magnet Tubular Linear Generator for Wave Energy Converters i .) eBybit,” pp. 983–987, 2010.

[36] R. Vermaak, M. J. Kamper, M. Ieee, and S. M. Ieee, “Construction and control of an air-cored permanent magnet linear generator for direct drive wave energy converters,” in *2011 IEEE International Electric Machines & Drives Conference (IEMDC)*, 2011, no. Section III, pp. 1076–1081.

[37] A. S. S. McDonald, M. a. M. A. Mueller, and J. G. G. Jeffrey, “Development of a novel permanent magnet linear generator topology for direct-drive wave energy converters,” *Power Electron. Mach. Drives, 2008. PEMD 2008. 4th IET Conf.*, pp. 81–85, 2008.

[38] M. Mueller, A. Mcdonald, K. Ochije, and J. Jeffrey, “A Novel Lightweight Permanent Magnet Generator for Direct Drive Power Take Off in Marine Renewable Energy Converters,” *Flux*.

[39] O. Keysan, A. S. McDonald, M. A. Mueller, R. Doherty, and M. Hamilton, “C-GEN, a lightweight direct drive generator for marine energy converters,” in *5th IET International Conference on Power Electronics, Machines and Drives (PEMD 2010)*, 2010, p. MO244-MO244.

[40] I. Barajas-solano, M. Mueller, and A. Kiprakis, “Active Magnetic Bearings for Linear Generators.”
[41] P. By, “World â€™ s largest Science , Technology & Medicine Open Access book publisher Pretreatments of Textiles Prior to Dyeing : Plasma Processing.”
[42] P. N. Barnes, M. D. Sumption, and G. L. Rhoads, “Review of high power density superconducting generators: Present state and prospects for incorporating YBCO windings,” *Cryogenics (Guildf).*, vol. 45, no. 10–11, pp. 670–686, 2005.
[43] O. Keysan and M. a. Mueller, “A homopolar HTSG topology for large direct-drive wind turbines,” *IEEE Trans. Appl. Supercond.*, vol. 21, no. 5, pp. 3523–3531, 2011.
[44] O. Keysan and M. Mueller, “A modular and cost-effective superconducting generator design for offshore wind turbines,” *Supercond. Sci. Technol.*, vol. 28, no. 3, p. 34004, 2015.
[45] N. Hodgins, A. S. Mcdonald, J. Shek, O. Keysan, and M. A. Mueller, “Current and Future Developments of the C-GEN Lightweight Direct Drive Generator for Wave & Tidal Energy,” in *Proceedings of the 8th European Wave and Tidal Energy Conference*, 2009.
[46] C. Radu, “THE MOST COMMON CAUSES OF BEARING FAILURE AND THE IMPORTANCE OF The Most Common Causes of Bearing Failure and the Importance of Bearing Lubrication,” no. February, pp. 1–7, 2010.
[47] C. Bianchini, F. Immovilli, M. Cocconcelli, R. Rubini, and A. Bellini, “Fault Detection of Linear Bearings in Brushless AC Linear Motors by Vibration Analysis,” *IEEE Trans. Ind. Electron.*, vol. 58, no. 5, pp. 1684–1694, May 2011.
[48] S. L. Caraher, J. P. Chick, and M. A. Mueller, “Investigation of Fluid Film Bearings for use in Direct Drive Linear Generators in Submerged Wave Energy Converters,” vol. 8, pp. 409–416, 2008.
[49] J. Prudell, M. Stoddard, E. Amon, S. Member, T. K. A. Brekken, and A. Von Jouanne, “A Permanent-Magnet Tubular Linear Generator for Ocean Wave Energy Conversion,” vol. 46, no. 6, pp. 2392–2400, 2010.
[50] J. R. Votano, M. Parham, L. H. Hall, L. B. Kier, and L. M. Hall, *Magnetic Bearings and bearingless Drives*, vol. 1, no. 11. Wiley Online Library, 2004.
[51] G. Schweitzer, “Introduction and survey,” *Magnetic Bearings: Theory, Design, and Application to Rotating Machinery*, pp. 1–26, 2009.
[52] R. Hellinger, P. Mnich, and B. R. Hellinger, “Linear Motor-Powered Transportation: History, Present Status, and Future Outlook,” *Proc. IEEE*, vol. 97, no. 11, pp. 1892–1900, Nov. 2009.
[53] T. J. Carbino, “A BRIEF HISTORY AND THEORY BEHIND AC , DC AND MAGLEV TRAINS AND SUBWAYS Mega Volt-Amps,” no. December 1979, pp. 165–171, 2005.
[54] M. Trains, “Maglev trains,” no. October, 2009.
[55] a Peijnenburg, J. Vermeulen, and J. Vaneijk, “Magnetic levitation systems compared to conventional bearing systems,” *Microelectron. Eng.*, vol. 83, no. 4–9, pp. 1372–1375, Apr. 2006.
[56] B. Ebihara, “A passive magnetic bearing flywheel,” *IECEC- 36 th* …, no. February, 2001.
[57] R. Larsonneur, “Principle of Active Magnetic Suspension,” in *Magnetic Bearings*, vol. 2, 2009, pp. 27–68.
[58] A. G. Clegg, P. Beckley, E. C. Snelling, and R. V Major, “Magnetic Materials.”
[59] S. R. Trout, “MATERIAL SELECTION OF PERMANENT MAGNETS, CONSIDERING THERMAL PROPERTIES CORRECTLY S. R. Trout Spontaneous Materials,” *Time*, pp. 365–370.
[60] R. Stephan, “Levitation force and stability of superconducting linear bearings using NdFeB and ferrite magnets,” *Phys. C Supercond.*, vol. 386, pp. 490–494, Apr. 2003.

[61] M. S. Review, “Review of the application of high temperature superconductors in coated conductor development and the measurement of their properties . I . Van Driessche *, B . Schoofs , G . Penneman , E . Bruneel , S . Hoste Ghent University Department of Inorganic and,” *Science (80-.).*, vol. 5, pp. 19–29, 2005.

[62] J. Wang, S. Wang, J. Zheng, F. Yen, G. Ma, L. Liu, J. Li, and W. Liu, “Recent Developments of the High Temperature Superconducting Maglev at ASCLab,” *IEEE Trans. Appl. Supercond.*, vol. 21, no. 3, pp. 1551–1555, Jun. 2011.

[63] F. N. Werfel, U. Floegel-delor, R. Rothfeld, T. Riedel, B. Goebel, D. Wippich, P. Schirrmeister, A. High, and T. Superconducting, “Recent Up-Scaling in HTS Magnetic Device Technology,” *Design*, vol. 21, no. 3, pp. 1473–1476, 2011.

[64] H. Lee, K. Kim, and J. Lee, “Review of maglev train technologies,” *IEEE Trans. Magn.*, vol. 42, no. 7, pp. 1917–1925, Jul. 2006.

[65] A. Traxler and E. Maslen, “Hardware Components,” in *Magnetic Bearings*, E. H. Maslen and G. Schweitzer, Eds. Berlin, Heidelberg: Springer Berlin Heidelberg, 2009, pp. 69–109.

[66] S. Nishijima, S. Eckroad, A. Marian, K. Choi, W. S. Kim, M. Terai, Z. Deng, J. Zheng, J. Wang, K. Umemoto, J. Du, P. Febvre, S. Keenan, O. Mukhanov, L. D. Cooley, C. P. Foley, W. V Hassenzahl, and M. Izumi, “Superconductivity and the environment: a Roadmap,” *Supercond. Sci. Technol.*, vol. 26, no. 11, p. 113001, Nov. 2013.

[67] M. Hirose, Y. Yamada, T. Masuda, K. Sato, and R. Hata, “Study on Commercialization of High-Temperature Superconductor,” no. 62, pp. 15–23, 2006.

[68] H. Nakashima, “The superconducting magnet for the Maglev transport system,” *IEEE Trans. Magn.*, vol. 30, no. 4, pp. 1572–1578, Jul. 1994.

[69] M. R. Osorio, D. E. Lahera, and H. Suderow, “Magnetic levitation on a type-I superconductor as a practical demonstration experiment for students,” *Eur. J. Phys.*, vol. 33, no. 5, pp. 1383–1395, Sep. 2012.

[70] Y. Yang, “Effects of Parameters of High-Temperature Superconductor Levitation System on the Vertical Force in Zero-Field Cooling when a Permanent Magnet Is Laterally Traversing,” *J. Supercond. Nov. Magn.*, vol. 22, no. 4, pp. 381–385, Dec. 2008.

[71] C. Diagram, “MAGNETISM : FIELDS AND FORCES.”

[72] “Janssen-Analytical calculation of interaction force between orthogonally magnetized permanent magnets.pdf.” .

[73] J.-P. Yonnet and H. Allag, “Three-Dimensional Analytical Calculation of Permanent Magnet Interactions by ‘Magnetic Node’ Representation,” *IEEE Trans. Magn.*, vol. 47, no. 8, pp. 2050–2055, Aug. 2011.

[74] H. Allag, J. Yonnet, M. E. H. Latreche, I. P. De Grenoble, S. Martin, and E. Hichamallaggelabinpgfr, “3D Analytical Calculation of Forces between Linear Halbach-Type Permanent Magnet Arrays,” pp. 1–6, 2009.

[75] R. F. Post and D. D. Ryutov, “The Inductrack: a simpler approach to magnetic levitation,” *IEEE Trans. Appiled Supercond.*, vol. 10, no. 1, pp. 901–904, Mar. 2000.

[76] W. Robertson, B. Cazzolato, and A. Zander, “Parameters for optimizing the forces between linear multipole magnet arrays,” *IEEE Magn. Lett.*, vol. 1, 2010.

[77] S. H. Ni, “Dynamic Characteristics of Hybrid Maglev Systems with Different Thickness Permanent Magnets,” *Mechatronics*, pp. 1336–1341, 2010.

[78] C. R. Knospe, “Active magnetic bearings for machining applications,” *Control Eng. Pract.*, vol. 15, no. 3, pp. 307–313, Mar. 2007.

[79] J. Van Eijk, “Design and Realization of a Miniature Spindle Test Setup with Active Magnetic Bearings,” *Engineering*, pp. 1–6.

[80] X. Yanliang, D. Yueqin, W. Xiuhe, and K. Yu, “Analysis of hybrid magnetic bearing with a permanent magnet in the rotor by FEM,” *IEEE Trans. Magn.*, vol. 42, no. 4,

pp. 1363–1366, Apr. 2006.
[81] J. L. G. Janssen, J. J. H. Paulides, J. C. Compter, and E. a. Lomonova, "Three-Dimensional Analytical Calculation of the Torque Between Permanent Magnets in Magnetic Bearings," *IEEE Trans. Magn.*, vol. 46, no. 6, pp. 1748–1751, Jun. 2010.
[82] T. . H. Sung, S. . Han, Y. . Han, J. . Lee, N. . Jeong, S. . Hwang, and S. . Choi, "Designs and analyses of flywheel energy storage systems using high-Tc superconductor bearings," *Cryogenics (Guildf).*, vol. 42, no. 6–7, pp. 357–362, Jun. 2002.
[83] T. Sung, "300 Wh class superconductor flywheel energy storage system with a horizontal axle," *Phys. C*, vol. 376, pp. 1451–1456, 2002.
[84] M. H. Kimman, H. H. Langen, and R. H. Munnig Schmidt, "A miniature milling spindle with Active Magnetic Bearings," *Mechatronics*, vol. 20, no. 2, pp. 224–235, Mar. 2010.
[85] E. H. Maslen and K. R. Bischof, "Modeling and Performance Evaluation of Machinig spindle with active magnetic bearings," *J. Mech. Sci. Technol.*, vol. 21, pp. 847–850, 2007.
[86] G. Li, Z. Lin, P. E. Allaire, and J. Luo, "Modeling of a High Speed Rotor Test Rig With Active Magnetic Bearings," *J. Vib. Acoust.*, vol. 128, no. 3, p. 269, 2006.
[87] X. Zhang, T. Shinshi, H. Endo, A. Shimokohbe, Y. Imai, H. Miyake, and T. Nakagawa, "Development of a 5-DOF Controlled, Wide-Bandwidth, High-Precision Maglev Actuator for Micro Electrical Discharge Machining," *2007 Int. Conf. Mechatronics Autom.*, pp. 2877–2882, Aug. 2007.
[88] A. V Filatov, E. H. Maslen, and A. Member, "Storage Systems," vol. 37, no. 6, pp. 3913–3924, 2001.
[89] W. Morales, R. Fusaro, and A. Kascak, "Permanent Magnetic Bearing for Spacecraft Applications," no. January, 2008.
[90] M.-H. Li, A. B. Palazzolo, A. Kenny, A. J. Provenza, R. F. Beach, and A. F. Kascak, "Fault-Tolerant Homopolar Magnetic Bearings," *IEEE Trans. Magn.*, vol. 40, no. 5, pp. 3308–3318, Sep. 2004.
[91] G. G. Sotelo, R. De Andrade, and A. C. Ferreira, "Test and Simulation of Superconducting," vol. 19, no. 3, pp. 2083–2086, 2009.
[92] D. J. Clark, M. J. Jansen, and G. T. Montague, "An Overview of Magnetic Bearing Technology for Gas Turbine Engines," no. August, 2004.
[93] W. Generators, G. Shrestha, H. Polinder, D. Bang, and J. A. Ferreira, "Structural Flexibility : A Solution for Weight Reduction of Large Direct-Drive," *Energy*, vol. 25, no. 3, pp. 732–740, 2010.
[94] I. Introduction, "linear Electric Machines-," vol. 63, no. 2, 1975.
[95] J. Duan, H. Zhou, and N. Guo, "Electromagnetic Design of a Novel Linear Maglev Transportation Platform," vol. 47, no. 1, pp. 260–263, 2011.
[96] M. Morishita, T. Azukizawa, S. Kanda, N. Tamura, T. Yokoyama, and M. Mofushita, "A new MAGLEV system for magnetically levitated carrier system," *IEEE Trans. Veh. Technol.*, vol. 38, no. 4, pp. 230–236, Nov. 1989.
[97] D. Henrique, N. Dias, E. S. Motta, G. G. Sotelo, R. De Andrade, R. M. Stephan, L. Kuehn, O. De Haas, and L. Schultz, "Simulations and Tests of Superconducting Linear Bearings for a MAGLEV Prototype," vol. 19, no. 3, pp. 2120–2123, 2009.
[98] G. Schweitzer, I. Centre, E. T. H. Zurich, and C.- Zurich, "u i n s b) A fe = A a," .
[99] U. Hasirci, A. Balikci, Z. Zabar, S. Member, and L. Birenbaum, "A Novel Magnetic-Levitation System : Design , Implementation , and Nonlinear Control," *Bioelectromagnetics*, vol. 39, no. 1, pp. 492–497, 2011.
[100] O. Kim, S. Lee, and D. Han, "Positioning performance and straightness error compensation of the magnetic levitation stage supported by the linear magnetic bearing," *IEEE Trans. Ind. Electron.*, vol. 50, no. 2, pp. 374–378, Apr. 2003.

[101] X. Shan, S. Kuo, J. Zhang, and C. Menq, “Ultra precision motion control of a multiple degrees of freedom magnetic suspension stage,” *IEEE/ASME Trans. Mechatronics*, vol. 7, no. 1, pp. 67–78, Mar. 2002.

[102] M. Chen, S. S. Member, M. Wang, and L. Fu, “Modeling and Controller Design of a Maglev Guiding System for Application in Precision Positioning,” vol. 50, no. 3, pp. 493–506, 2003.

[103] W. Kim, J. M. Lee, S. Kim, and A. Bllm, “Rolling Motion Control of a Levitated Mover in a Permanent-Magnet-Type Bearingless Linear Motor,” vol. 46, no. 6, pp. 2482–2485, 2010.

[104] J. W. Spronck, E. A. Lornonova, and B. Dag, “A LINEAR MAGNETIC BEARING WITH INTEGRATED LONG STROKE PROPULSION - DESIGN AND REALIZATION OF AN IU-MODULE,” 2004.

[105] A. V. a. V. Lebedev, E. a. E. A. Lomonova, P. G. van Leuven, J. Steinberg, D. a. H. Laro, and P. G. Van, “Analysis and initial synthesis of a novel linear actuator with active magnetic suspension,” *Conf. Rec. 2004 IEEE Ind. Appl. Conf. 2004. 39th IAS Annu. Meet.*, vol. 3, pp. 2111–2118, 2004.

[106] H. Maheshwari, “High-precision control of a maglev linear actuator with nanopositioning capability,” *Proc. 2002 Am. Control Conf. (IEEE Cat. No.CH37301)*, vol. 5, pp. 4279–4284, 2002.

[107] K. S. Jung and Y. S. Baek, “Contact-free moving-magnet type of micropositioner with optimized specification,” *IEEE Trans. Magn.*, vol. 38, no. 3, pp. 1539–1548, May 2002.

[108] E. Prof, M. Weck, and D. U. Wahner, “Linear Magnetic Bearing and Levitation System for Machine Tools,” vol. 47, 1998.

[109] Y. Choi and D. Gweon, “A High-Precision Dual-Servo Stage Using Halbach,” vol. 16, no. 5, pp. 925–931, 2011.

[110] Y.-M. Choi, M. G. Lee, D.-G. Gweon, and J. Jeong, “A new magnetic bearing using Halbach magnet arrays for a magnetic levitation stage.,” *Rev. Sci. Instrum.*, vol. 80, no. 4, p. 45106, Apr. 2009.

[111] R. Fesperman, O. Ozturk, R. Hocken, S. Ruben, T.-C. Tsao, J. Phipps, T. Lemmons, J. Brien, and G. Caskey, “Multi-scale Alignment and Positioning System – MAPS,” *Precis. Eng.*, vol. 36, no. 4, pp. 517–537, Oct. 2012.

[112] J. I. Barajas-solano and M. Mueller, “ACTIVE MAGNETIC BEARINGS USING AN AIR-CORED COIL HALBACH ARRAY IN A LINEAR GENERATOR FOR WAVE ENERGY,” vol. 30, 2013.

[113] and W. F. Tsung-Li Tang, Hsueh-An Yang, Han-tang Su, “A Magnetic Repulsive Force MEMS Actuator,” … *-State Sensors, Actuators* …, pp. 2235–2238, 2007.

[114] and E. M. H. Hayashuya, D. Iizuka, H.Ohsaki and E. Engneering, “A Novel combined Lift and propulsion system for a Steel Plate Conveyance by Electromagnets,” vol. 34, no. 4, pp. 2093–2095, 1998.

[115] Q. Hu, M. Hao, and D. Yu, “Neural sliding mode control on suspension gap for single electromagnetic guiding actuator of linear elevator,” *2012 24th Chinese Control Decis. Conf.*, pp. 2728–2732, May 2012.

[116] R. Appunn, B. Schmülling, K. Hameyer, and S. Member, “Electromagnetic Guiding of Vertical Transportation Vehicles : Experimental Evaluation,” vol. 57, no. 1, pp. 335–343, 2010.

[117] R. B. Arreola, “NONLINEAR CONTROL DESIGN FOR A MAGNETIC LEVITATION SYSTEM,” *Science (80-.).*, 2003.

[118] B. Wang, G. Liu, and D. Rees, “Networked Predictive Control of Magnetic Levitation System,” *Technology*, no. October, pp. 4100–4105, 2009.

[119] a. El Hajjaji and M. Ouladsine, “Modeling and nonlinear control of magnetic levitation systems,” *IEEE Trans. Ind. Electron.*, vol. 48, no. 4, pp. 831–838, 2001.

[120] B. Doh, Y. Park, B. C. Shin, and H. Han, “Korea’s Urban Maglev Program,” *Proc. IEEE*, vol. 97, no. 11, pp. 1886–1891, Nov. 2009.
[121] E. Alvarez-Sanchez, J. Alvarez-Gallegos, and R. Castro-Linares, “A Maglev System: Modeling and Controller Design,” *2005 Int. Conf. Ind. Electron. Control Appl.*, pp. 1–6, 2005.
[122] I.-Y. a. Wang and I. Busch-Vishniac, “A new repulsive magnetic levitation approach using permanent magnets and air-core electromagnets,” *IEEE Trans. Magn.*, vol. 30, no. 4, pp. 1422–1432, Jul. 1994.
[123] G. G. Sotelo, D. H. N. Dias, R. de Andrade, and R. M. Stephan, “Tests on a Superconductor Linear Magnetic Bearing of a Full-Scale MagLev Vehicle,” *IEEE Trans. Appl. Supercond.*, vol. 21, no. 3, pp. 1464–1468, Jun. 2011.
[124] R. M. Stephan, R. de Andrade, G. C. dos Santos, M. a. Neves, and R. Nicolsky, “Levitation force and stability of superconducting linear bearings using NdFeB and ferrite magnets,” *Phys. C Supercond.*, vol. 386, pp. 490–494, Apr. 2003.
[125] R. M. Stephan, R. Nicolsky, M. a. Neves, a. C. Ferreira, R. de Andrade, M. a. Cruz Moreira, M. a. Rosário, O. J. Machado, R. Deandradejr, M. Cruzmoreira, and M. Rosario, “A superconducting levitation vehicle prototype,” *Phys. C Supercond.*, vol. 408–410, pp. 932–934, Aug. 2004.
[126] a. a. Kuijpers, C. Nemlioglu, F. Sahin, A. Verdel, J. C. Compter, and E. a. Lomonova, “Force analysis of linear induction motor for magnetic levitation system,” *Proc. 14th Int. Power Electron. Motion Control Conf. EPE-PEMC 2010*, pp. 17–20, Sep. 2010.
[127] J. Ronald, B. N. Turman, S. L. Shope, and A. C. History, “APPLICATIONS OF COILGUN ELECTROMAGNETIC PROPULSION,” pp. 703–707.
[128] K. R. Davey, A. Maglev, and N. S. Beach, “Electrodynamic Maglev Coil Design and Analysis,” vol. 33, no. 5, pp. 4227–4229, 1997.
[129] D. L. Trumper, M. E. Williams, and T. H. Nguyen, “Magnet Arrays for Synchronous Machines Overview of Halbach arrays.”
[130] Z. Q. Zhu and D. Howe, “Halbach permanent magnet machines and applications: a review,” *IEE Proc. - Electr. Power Appl.*, vol. 148, no. 4, p. 299, 2001.
[131] N. H. Kim and L. Ge, “Dynamic modeling of electromagnetic suspension system,” *J. Vib. Control*, vol. 19, no. 5, pp. 729–741, Feb. 2012.
[132] C. Science and S. Term, “ANALYSIS AND MODELING OF THE EDS MAGLEV SYSTEM BASED ON THE HALBACH PERMANENT MAGNET ARRAY,” 2004.
[133] H. Weh, “New Maglev Concepts with Magnetically Active Rails,” pp. 3–8.
[134] Z. Long, G. He, and S. Xue, “Study of EDS & EMS Hybrid Suspension System With Permanent-Magnet Halbach Array,” *IEEE Trans. Magn.*, vol. 47, no. 12, pp. 4717–4724, Dec. 2011.
[135] J. Yonnet, I. Introduction, and U. Sommerfeld, “Permanent Magnet Bearings and Couplings,” vol. M, no. 1, pp. 1169–1173, 1981.
[136] G. Akoun, “3d analytical calculation,” vol. M, no. 5, pp. 1962–1964, 1984.
[137] J. L. G. Janssen, J. J. H. Paulides, and E. A. Lomonova, “Three-Dimensional Analytical Field Calculation of,” vol. 45, no. 10, pp. 4628–4631, 2009.
[138] S.-C. P. S.-C. Park, “Thrust and attraction force calculation of a linear induction motor with the moving cage-type secondary,” *Sixth Int. Conf. Electr. Mach. Syst. 2003. ICEMS 2003.*, vol. 1, pp. 226–229, 2003.
[139] H. Search, C. Journals, A. Contact, M. Iopscience, and I. P. Address, “Forces between arrays of magnets,” vol. 759.
[140] H.-J. Shieh, J.-H. Siao, and Y.-C. Liu, “A robust optimal sliding-mode control approach for magnetic levitation systems,” *Asian J. Control*, vol. 12, no. 4, p. n/a-n/a, 2010.
[141] M. Zribi, “Sliding Mode Control of a Magnetic Levitation System,” vol. 2, no.

October 2003, pp. 93–107, 2004.
[142] a. S. Kadalla and M. I. Onogu, “Sliding Mode Control of Magnetic Levitation Vehicles,” *Adv. Mater. Res.*, vol. 18–19, no. 2, pp. 79–86, 2007.
[143] E. Alvarez-Sanchez, J. Alvarez-Gallegos, and R. Castro-Linares, “Dynamical sliding mode control of a MagLev system with 3 DOFs: Experimental results,” *2007 4th Int. Conf. Electr. Electron. Eng. ICEEE 2007*, no. Iceee, pp. 270–273, 2007.
[144] H. Alipour, “A PID Sliding Mode Control for Ropeless Elevator Maglev Guiding System,” *Energy Power Eng.*, vol. 4, no. 3, pp. 158–164, 2012.
[145] D. Wang, “Design and performance of QFT-H-infinity controller for magnetic bearing of high-speed motors,” *2009 4th IEEE Conf. Ind. Electron. Appl.*, pp. 2624–2629, May 2009.
[146] E. M. S. Coktrol and M. V. Using, “H , DESIGS OF AS EMS COKTROL SYSTEM FOR A MAGLEV VEHICLE USING,” no. 414, pp. 226–231, 1995.
[147] R. Wai, S. Member, and J. Lee, “Robust Levitation Control for Linear Maglev Rail System Using Fuzzy Neural Network,” vol. 17, no. 1, pp. 4–14, 2009.
[148] Ji.-C. Shen, “H∞Control and Sliding mode control of magnetic levitation system,” *Asian J. Control*, vol. 4, no. 3, pp. 333–340, 2002.
[149] C. L. Logan, “A Comparison Between H-InfinityMu-Synthesis Control and Sliding-Mode Control for Robust Control of a- Small Autonomous Underwater Vehicle,” 1994.
[150] H. Moradi, F. Bakhtiari-Nejad, and M. Saffar-Avval, “Robust control of an industrial boiler system; a comparison between two approaches: Sliding mode control & technique,” *Energy Convers. Manag.*, vol. 50, no. 6, pp. 1401–1410, Jun. 2009.
[151] O. Barambones, P. Alkorta, and M. D. La Sen, “An adaptive sliding mode position control for induction motor drives,” *2011 IEEE EUROCON - Int. Conf. Comput. as a Tool*, pp. 1–4, 2011.
[152] D. Vischer and H. Bleuler, “Self-sensing active magnetic levitation,” *IEEE Trans. Magn.*, vol. 29, no. 2, pp. 1276–1281, Mar. 1993.
[153] K. Michail, A. Zolotas, R. Goodall, and J. Pearson, “Sensor Optimisation via H ∞ Applied to a MAGLEV Suspension System,” no. 2, pp. 143–149, 2009.
[154] K. S. Peterson, R. H. Middleton, and J. S. Freudenberg, “Fundamental limitations in self-sensing magnetic bearings when modeled as linear periodic systems,” *2006 Am. Control Conf.*, p. 6 pp., 2006.
[155] S. Caraher, “Bearing Options , including Design and Testing , for Direct Drive Linear Generators in Wave Energy Converters,” 2010.
[156] M. H. Partovi and E. J. Morris, “Electrodynamics of a Magnet Moving through a Conducting Pipe,” pp. 1–21, 2008.
[157] A. Musolino, R. Rizzo, M. Tucci, and V. M. Matrosov, “A new passive maglev system based on eddy current stabilization,” *IEEE Trans. Magn.*, vol. 45, no. 3, pp. 984–987, 2009.
[158] P. S. Errede, “American Wire Gauge (AWG) & Metric Gauge Wire Sizes AWG Wire Sizes (see table below) AWG : In the American Wire Gauge (AWG), diameters can be calculated by applying the -1 , -2 , -3 , which makes more sense mathematically than ‘ double nought .’ Thi,” pp. 1–3, 2015.
[159] R. F. Post, “Maglev: A New Approach,” *Sci. Am.*, vol. 282, no. 1, pp. 82–87, 2000.
[160] F. Richard and D. D. Ryutov, “Thc Inductrack : A Simpler Approach to Magnetic Levitation,” vol. i, no. I, 2000.
[161] W. Samuel and P. Robertson, “Modelling and design of magnetic levitation systems for vibration isolation,” no. August, 2013.
[162] S. Basu, S. S. Pany, P. Bannerjee, and S. Mitra, “Pulsed Magnetic Field Measurement Outside Finite Length Solenoid : Experimental Results & Mathematical Verification,” vol. 2013, no. October, pp. 371–378, 2013.

[163] J. Simpson, J. Lane, C. Immer, and R. Youngquist, “Simple Analytic Expressions for the Magnetic Field of a Circular Current Loop,” *Recon*, pp. 1–3, 1829.
[164] D. Sinha, P. K. Sadhu, N. Pal, and A. Bandyopadhyay, “Computation of inductance and AC resistance of a twisted litz-wire for high frequency induction cooker,” *2010 Int. Conf. Ind. Electron. Control Robot.*, pp. 85–90, Dec. 2010.
[165] D. P. Kothari and I. J. Nagrath, *Modern Power System Analysis*. .
[166] F. Terman, “Radio engineer’s handbook,” *Text. Res. J.*, vol. 28, no. 6, 1943.
[167] O. F. Storset and B. E. Paden, “Electrodynamic magnetic levitation with discrete track Part II : Periodic track model for numerical simulation and lumped parameter model,” 2005.
[168] R. E. Post, “The Inductrack Concept : a New Approach to Magnetic Levitation Richard E Post and D ~ nitri,” 1996.
[169] O. F. Storset and B. E. Paden, “Discrete track electrodynamic maglev Part I : Modelling,” 2005.
[170] R. F. Post, “Inductrack Demonstration Model ce re n re mo l y w r a r La ive tion rato L a o N ab,” 1998.
[171] J. Peraire and S. Widnall, “3D Rigid Body Dynamics,” pp. 1–13, 2009.
[172] H. Elmali and N. Olgac, “Robust output tracking control of nonlinear MIMO systems via sliding mode technique,” *Automatica*, vol. 28, no. 1, pp. 145–151, Jan. 1992.
[173] A. D. Canonsburg, “DesignModeler User â€™ s Guide,” vol. 15317, no. April, pp. 724–746, 2016.
[174] B. Y. K. H. Holko, “Induction Soldering Gets Maglev Vehicle on Track,” *Weld. J.*, pp. 53–57, 2009.
[175] J. F. Hoburg, “A Laminated Track for the Inductrack System : Theory and Experiment,” no. 2.
[176] S. Caraher, “Bearing options, including design and testing, for direct drive linear generators in wave energy converters,” 2011.
[177] P. Agarwal and L. Manuel, “On the Modeling of Nonlinear Waves for Prediction of Long-Term Offshore Wind Turbine Loads,” *J. Offshore Mech. Arct. Eng.*, vol. 131, no. 4, p. 41601, 2009.
[178] “Marine Energy - 5 Wave Analysis,” *Analysis*, pp. 1–23.
[179] N. Hodgins and M. Mueller, “C-Gen : A Lightweight , Robust and Low Cost Powertrain for Direct Drive Wave Energy Converters Interim Project report March 2009 Milestone 2 School of Engineering University of Edinburgh,” *Energy*, no. March, pp. 1–17, 2009.
[180] W. Jiangbo, L. Chunsheng, X. Wei, and Y. Baofeng, “Optimization design of linear Halbach array for EDS Maglev,” *2008 IEEE Veh. Power Propuls. Conf.*, vol. 0, no. 1, pp. 1–5, Sep. 2008.
[181] F. Transit, “Low Speed Maglev Technology Development Program,” no. March, 2002.
[182] G. Schweitzer, “Safety and Reliability Aspects for Active Magnetic Bearing Applications - A Survey,” *Proc. Inst. Mech. Eng. Part I J. Syst. Control Eng.*, vol. 219, no. 6, pp. 383–392, Jun. 2005.
[183] J. Wassermann, a. Schulz, and M. Schneeberger, “Active magnetic bearings of high reliability,” *IEEE Int. Conf. Ind. Technol. 2003*, pp. 194–197, 2003.
[184] I. Kim, R. Kratz, and D. Doll, “Technology Development for U . S . Urban Maglev.”
[185] A. Schulz, M. Schneeberger, and J. Wassermann, “A Reliability Analysis of Switching Amplifier Concepts for Active Magnetic Bearings,” *2006 IEEE Int. Conf. Ind. Technol.*, pp. 1460–1465, 2006.
[186] D.-L. Mon and C.-H. Cheng, “Fuzzy system reliability analysis for components with different membership functions,” *Fuzzy Sets Syst.*, vol. 64, no. 2, pp. 145–157, Jun. 1994.

[187] A. Mihalache, “Reliability Analysis of Mechatronic Systems Using Censored Data and Petri Nets : Application on an Antilock Brake System (ABS),” vol. 0, no. C, pp. 140–145, 2006.
[188] E. S. Supervisor and M. A. Mueller, “Reliability Assessment of Direct- Drive and Hydraulic PTO Systems in the Archimedes Wave Swing . Final report.”
[189] H. Polinder, B. C. Mecrow, A. G. Jack, P. G. Dickinson, and M. a. Mueller, “Conventional and TFPM linear generators for direct-drive wave energy conversion,” *IEEE Trans. Energy Convers.*, vol. 20, no. 2, pp. 260–267, 2005.
[190] M. Mueller, N. Hodgins, M. Galbraith, J. Bingham, and T. U. V Nel, “C-GEN : a lightweight , robust and low cost powertrain for direct drive wave energy,” *Design*, pp. 1–86.
[191] R. F. Post, “The Design of Halbach Arrays for Inductrack Maglev Systems.”
[192] M. Misakian, “Equations for the Magnetic Field Produced by One or More Rectangular Loops of Wire in the Same Plane,” *J. Res. Natl. Inst. Stand. Technol.*, vol. 105, no. 4, pp. 557–564, 2000.
[193] S. R. Motors, “Electrical Machines in the Power Engineering and Automatics Electrical Machines in Automatics,” pp. 1–47.
[194] MIT, “Introduction to magnetic fields,” *Lect. Massachusetts Inst. Technol.*, pp. 0–39, 2000.
[195] E. Equipment, “MILITARY HANDBOOK RELIABILITY PREDICTION OF,” 1991.
[196] L. T. Support, *Handbook of Reliability Prediction Procedures for Mechanical Equipment*, no. May. 2011.
[197] S. W. Yates and R. D. Williams, “A FaultTolerant Multiprocessor Controller for Magnetic Bearings,” vol. 80, 1988.
[198] R. S. Report, P. Number, R. Des, I. Voltage, F. Rate, and A. Name, “Standard Reliability Prediction Report,” pp. 1–13.

Appendix A

A.1 Prototype readings

A limited number of measurements were taken at each frequency ranging from 100 to 420 Hz. This was due to the short amount of time the rig could maintain active before it overheated. The same rise in temperature caused the characteristics of the coil to change. Consequently the current circulating through the coils also change rapidly.

In order to obtain the force readings from the prototype some calculations had to be done. First of all the currents noted for each experiment was corrected following the correspondence graph shown in figure 5.58, subsection 5.3.2.2. The obtained measurements can be seen in the following figures, with lift forces represented by blue crosses while purple crosses represent the dragging force measurements. The second step was to obtain a trend line, this can be seen as the dotted lines in the same figures, red for the lifting forces and green for the dragging forces. Finally converting the desired current from 9 amperes to the new value of 31.8 amperes, the force values were obtained for each frequency and presented in the figures as a yellow x for lifting forces and a cyan x for dragging forces.

This procedure was repeated from a 1-layer track to a 5-layer track shown in figures A.1-A.10. After this process the forces were concentrated in figures 5.60 to 5.64.

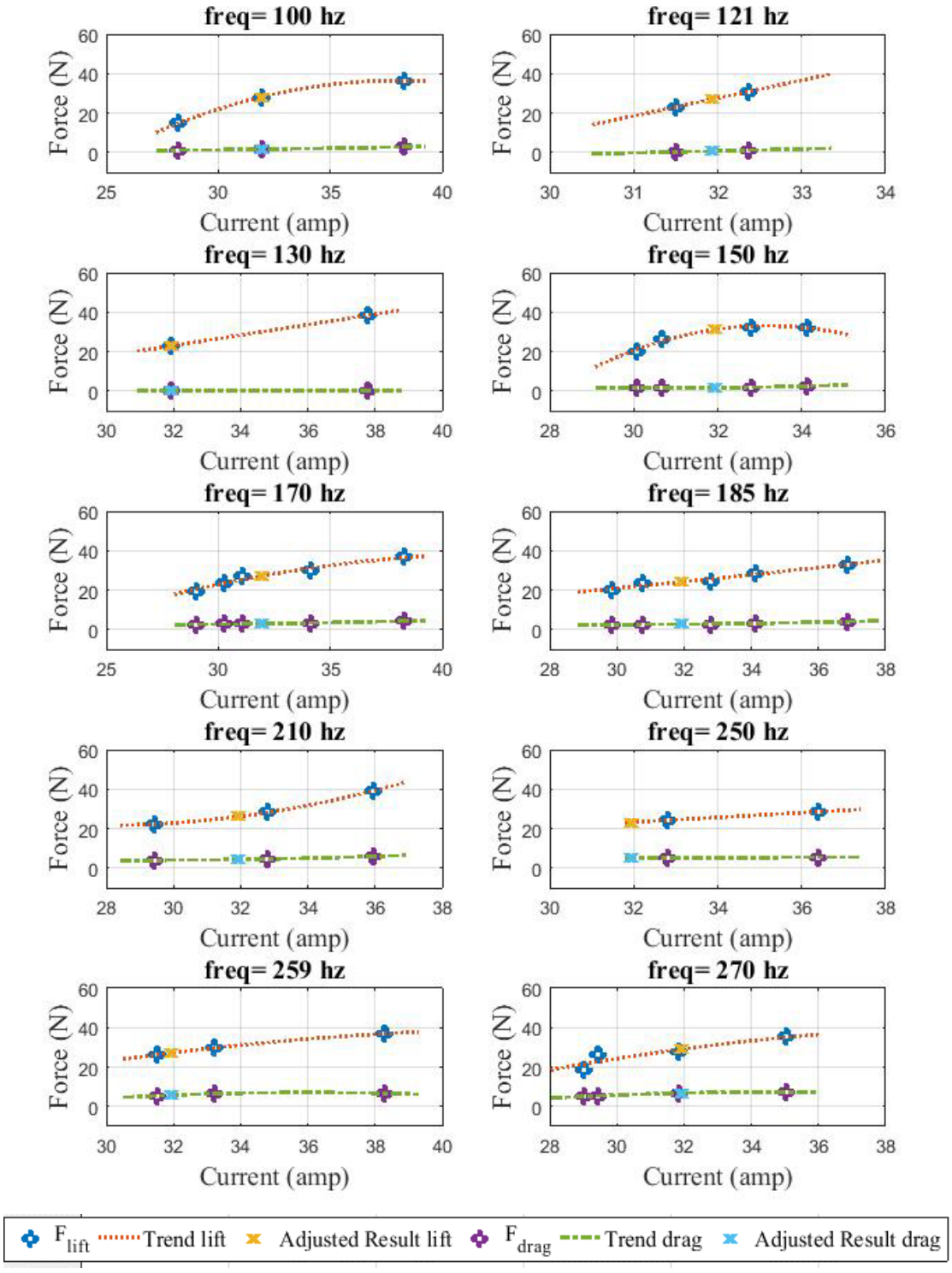

Fig. A.4 1-Layer track results: 100-270 hz

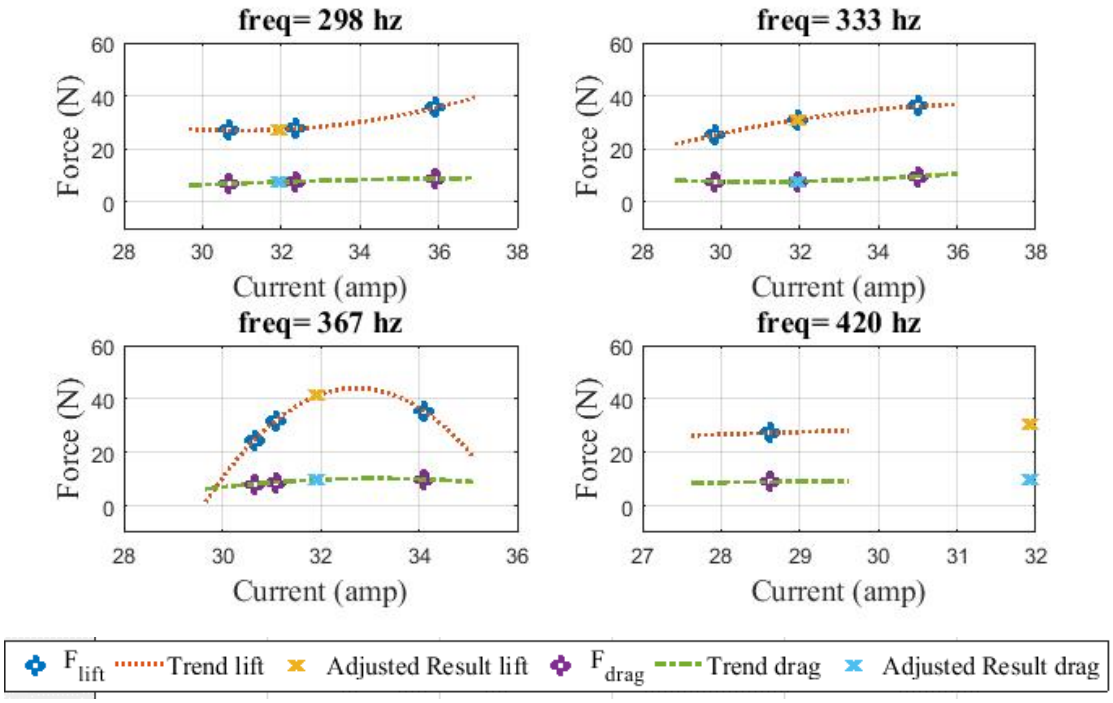

Fig. A.5 1-Layer track results: 298-420 hz

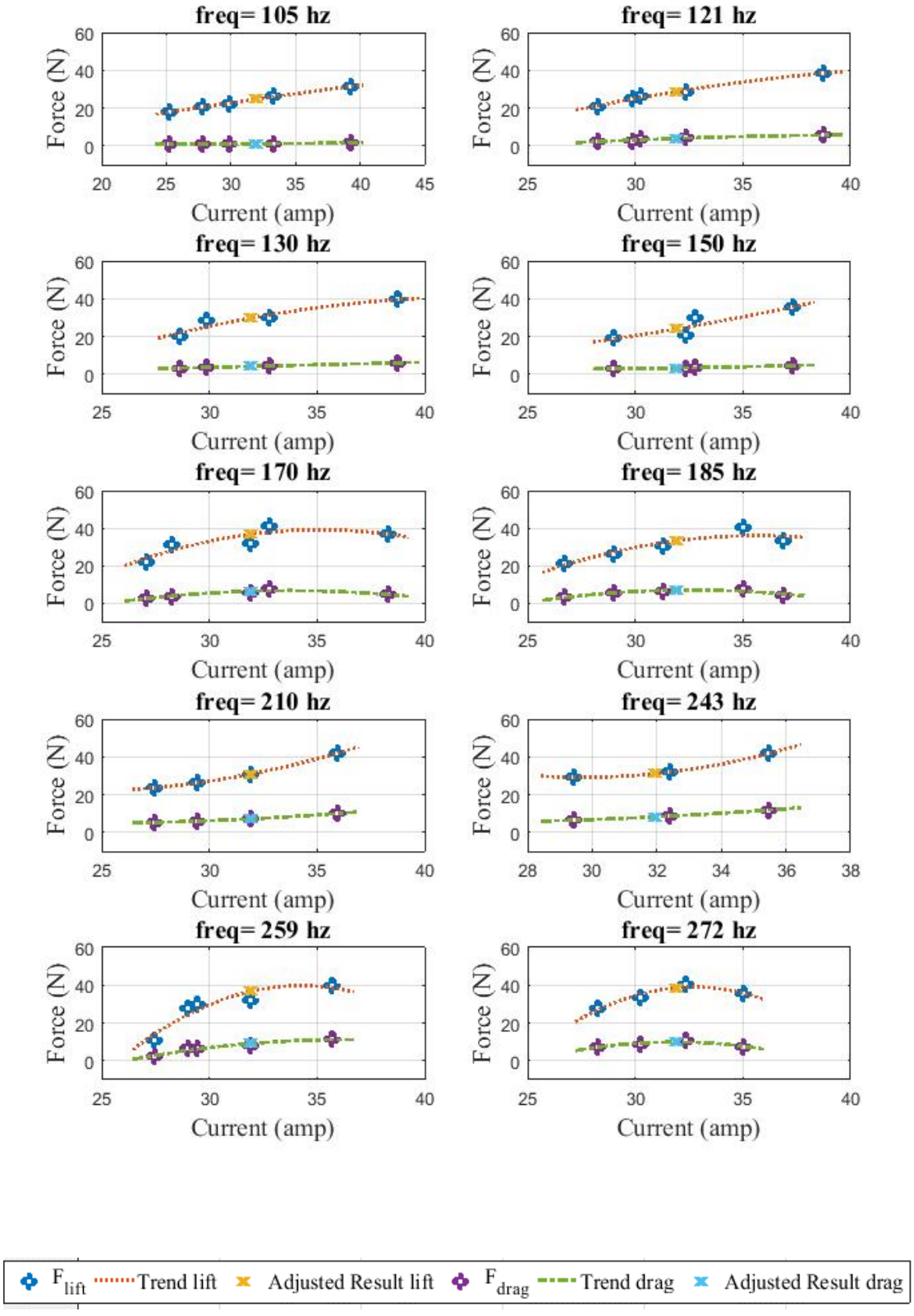

Fig. A.6 2-Layer track results: 105-272 hz

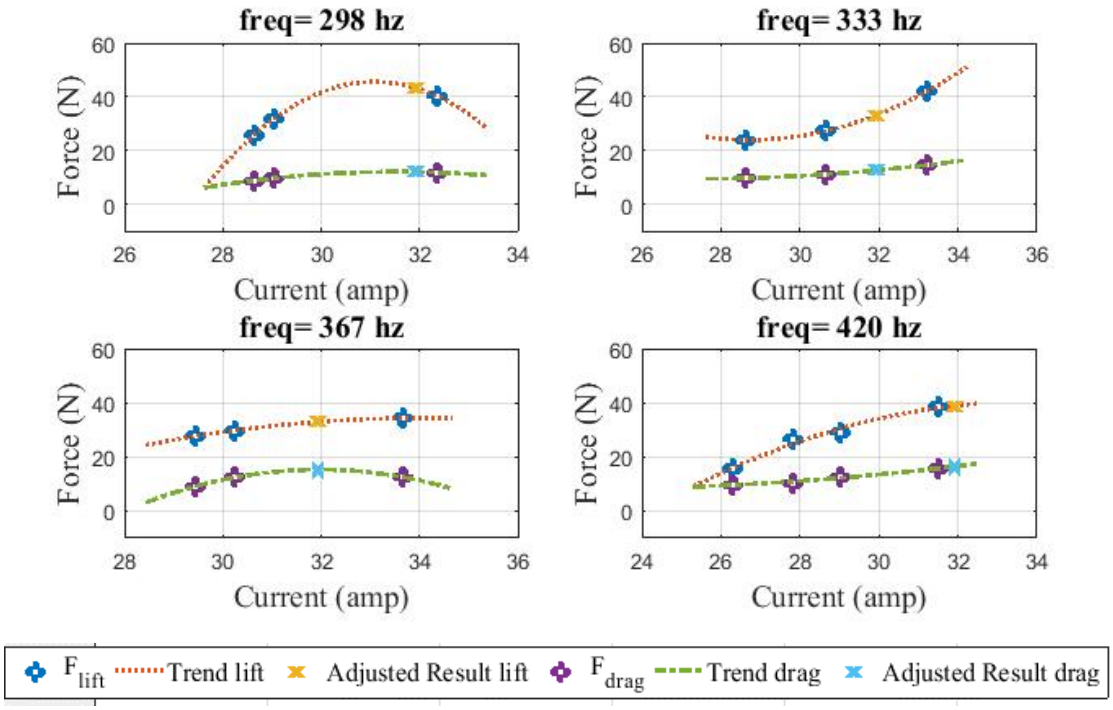

Fig. A.7 2-Layer track results: 298-420 hz

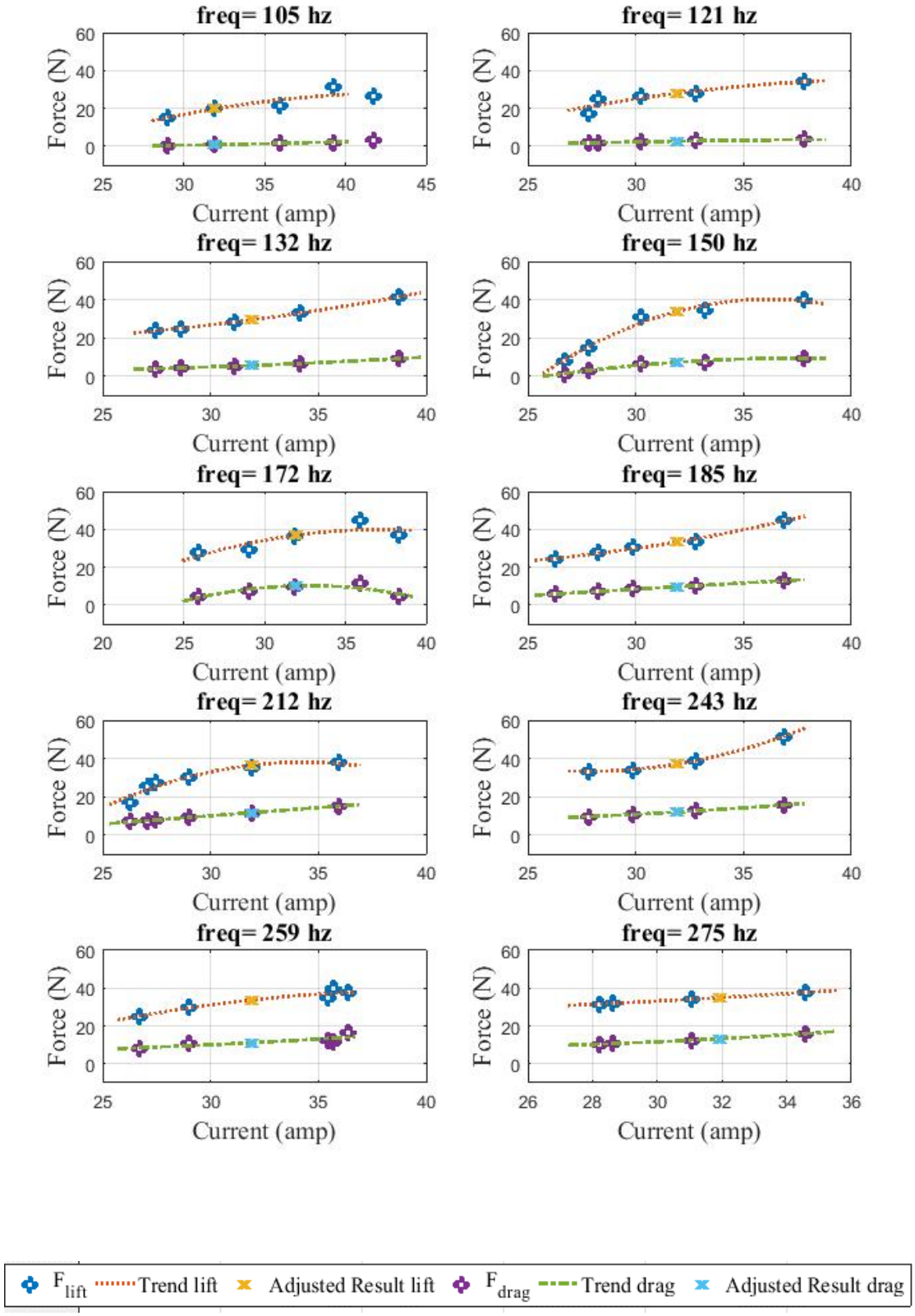

Fig. A.8 3-Layer track results: 105-275 hz

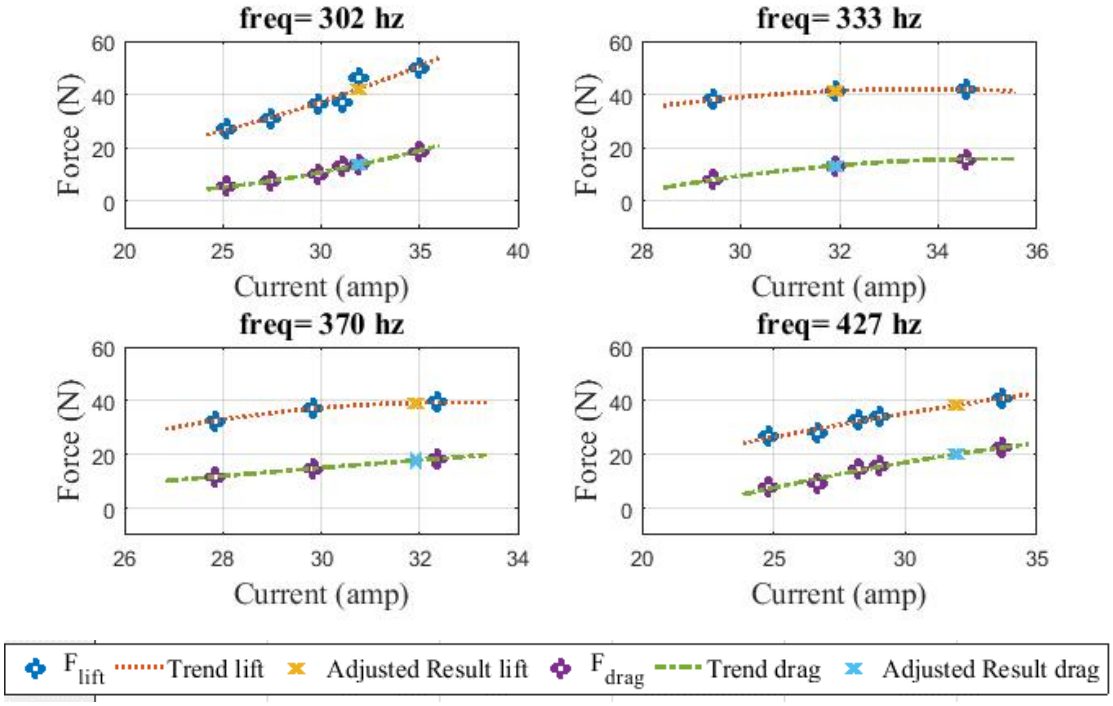

Fig. A.9 3-Layer track results: 302-427 hz

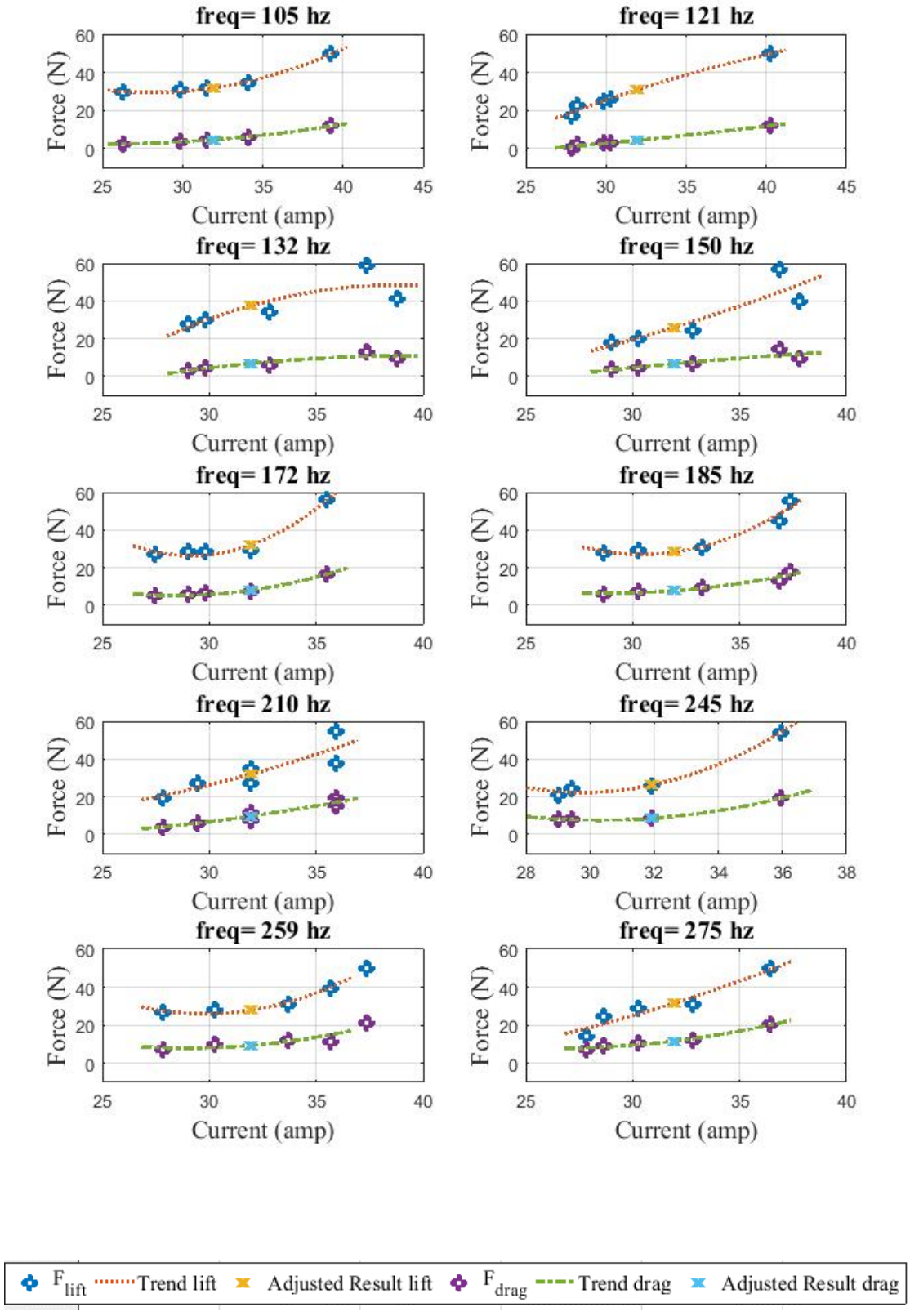

Fig. A.10 4-Layer track results: 105-275 hz

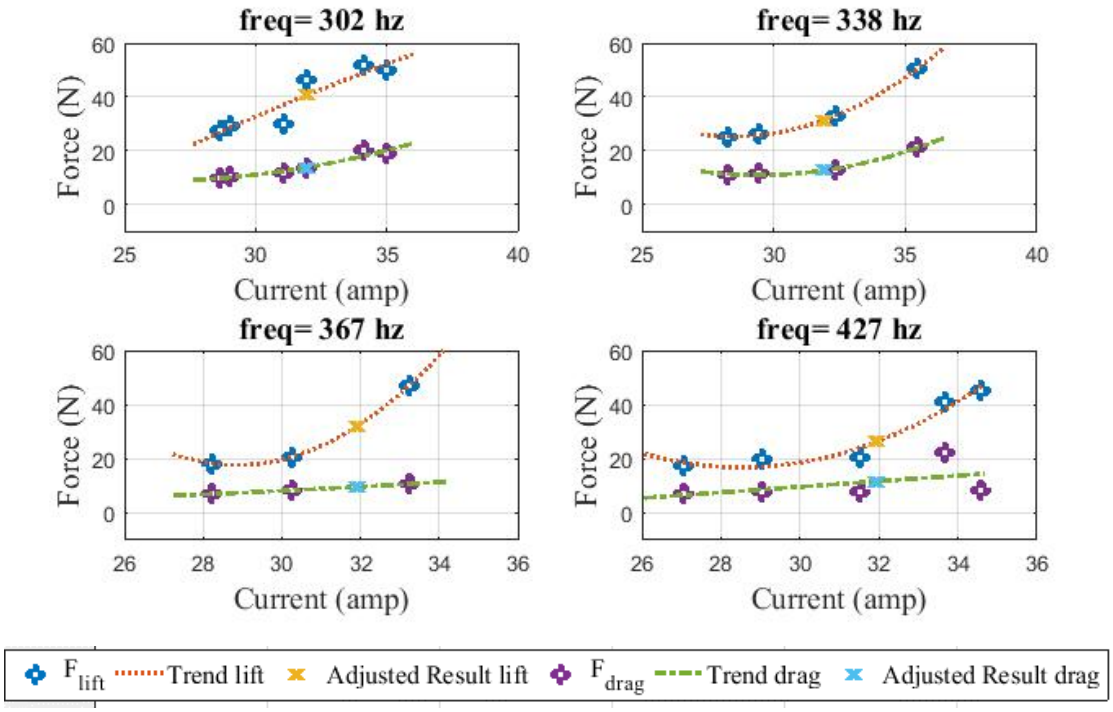

Fig. A.11 4-Layer track results: 302-427 hz

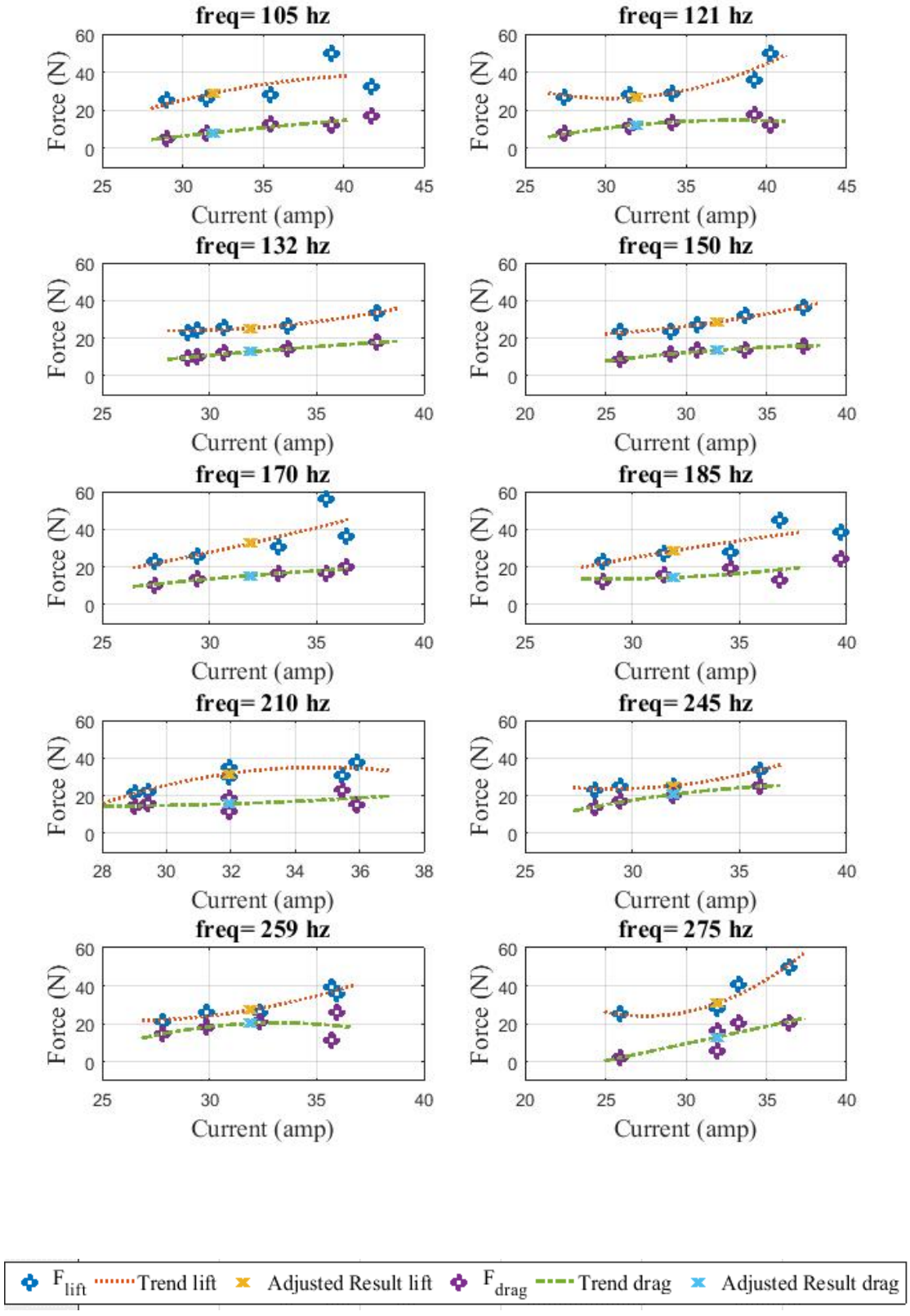

Fig. A.12 5-Layer track results: 105-275 hz

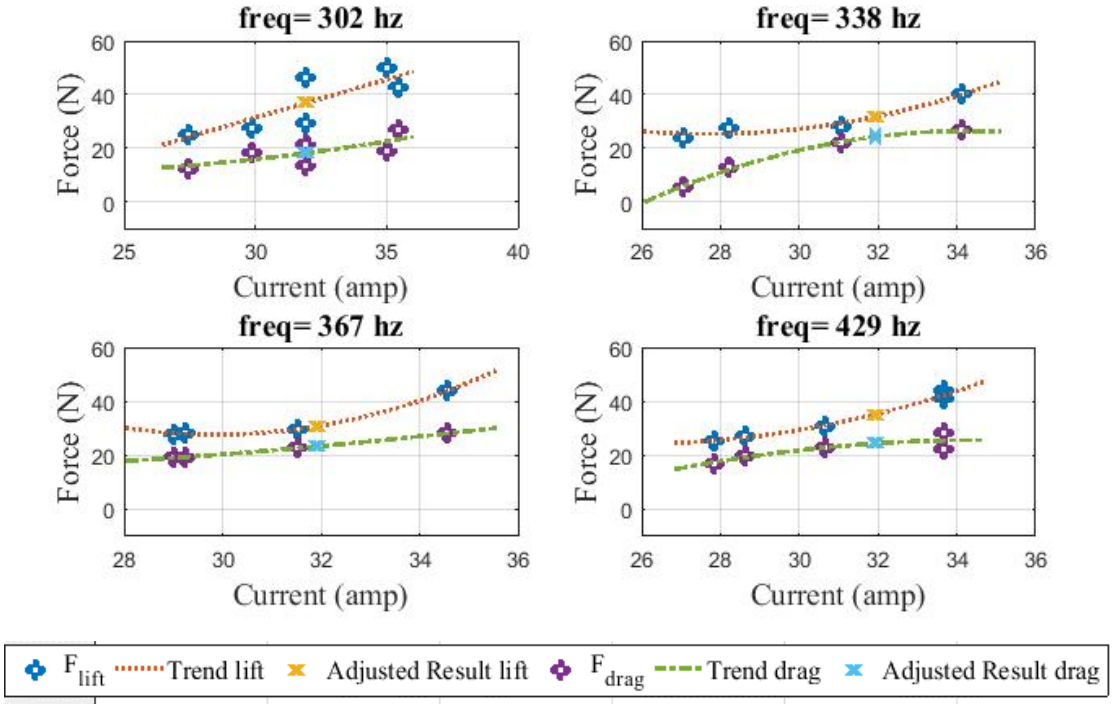

Fig. A.13 5-Layer track results: 302-420 hz

A.2 Capacitor bank connections

TABLE 7-I
CAPACITOR BANK CONNECTIONS 5 TO 30 μF

Diagram	Capacitance (μF)	Diagram	Capacitance (μF)
	5	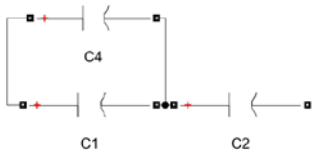	13.3
	6.67	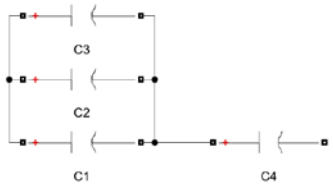	15
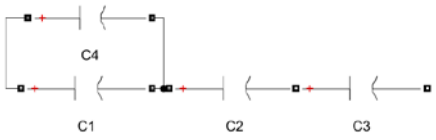	8	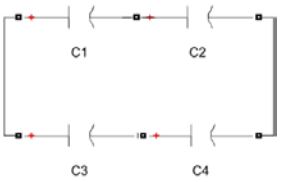	20
	10	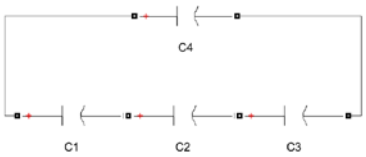	26
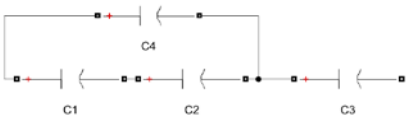	12	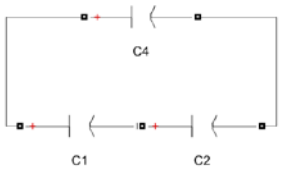	30

TABLE 7-II
CAPACITOR BANK CONNECTIONS 40 TO 80 μ F

Diagram	Capacitance (μF)	Diagram	Capacitance (μF)
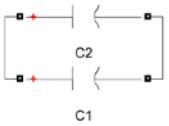	40	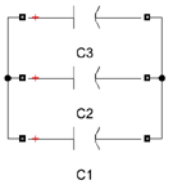	60.
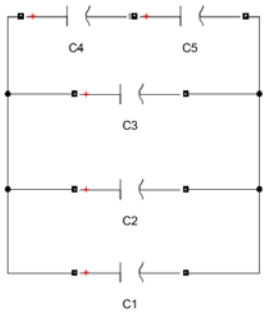	50	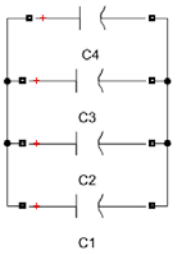	80

A.3 Rectangular coil Halbach array magnetic field mathematical model

As previously stated an accurate mathematical model is being pursued. It has been highlighted in chapter 6 that changing the dimension of the Halbach array elements from cylindrical windings to rectangular-shaped coils can improve the amount of force per square meter. Hence a mathematical model including this dimensions is desired in order to use optimisation programing tools such as genetic algorithms.

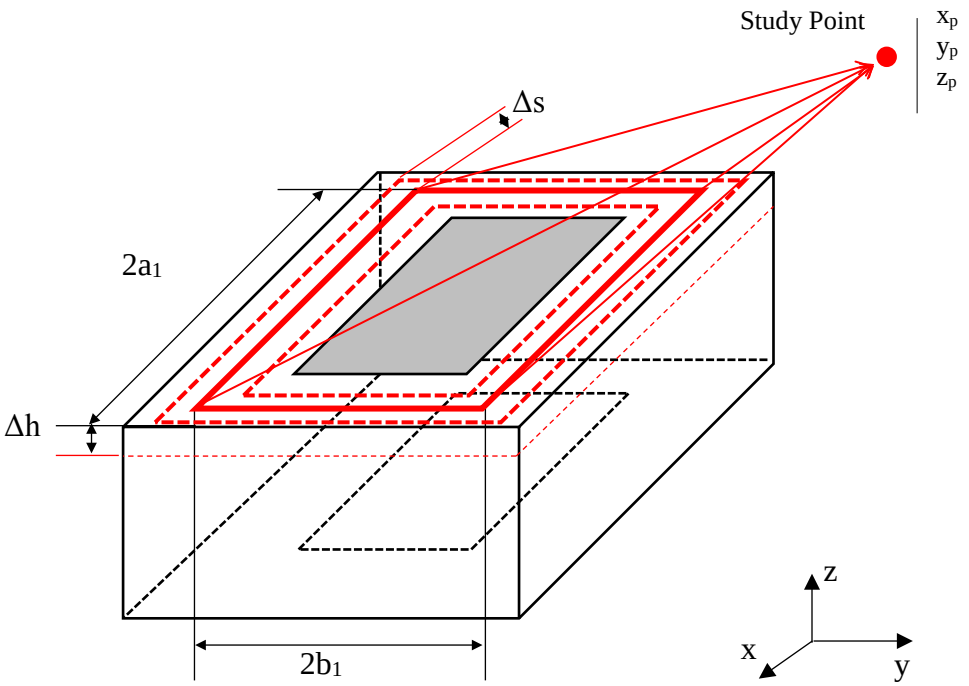

Fig. A.14 Rectangular coils Integration details

In order to obtain the magnetic field acting on a specific point in space from a rectangular shaped coils, the following group of equations utilised based on [192].

$$C_1 = -C_4 = a_1 + x$$

$$C_2 = -C_3 = a_1 - x$$

$$d_1 = d_2 = y + b_1 \qquad \textit{Eq. 7.1}$$

$$d_3 = d_4 = y - b_1$$

$$r_1 = \sqrt{(a_1 + x)^2 + (y + b_1)^2 + z^2}$$

$$r_2 = \sqrt{(a_1 - x)^2 + (y + b_1)^2 + z^2}$$

$$r_3 = \sqrt{(a_1 - x)^2 + (y - b_1)^2 + z^2}$$

$$r_4 = \sqrt{(a_1 + x)^2 + (y - b_1)^2 + z^2}$$

$$B_z = \frac{\mu_0 I}{4\pi} \sum_{\alpha=1}^{4} \left[\frac{(-1)^{\alpha} d_{\alpha}}{r_{\alpha}[r_{\alpha} + (-1)^{\alpha+1} C_{\alpha}]} - \frac{C_{\alpha}}{r_{\alpha}[r_{\alpha} + d_{\alpha}]} \right] \qquad \textit{Eq. 7.2}$$

$$B_x = \frac{\mu_0 I}{4\pi} \sum_{\alpha=1}^{4} \left[\frac{(-1)^{\alpha+1} d_{\alpha} z}{r_{\alpha}[r_{\alpha} + d_{\alpha}]} \right]$$

$$B_y = \frac{\mu_0 I}{4\pi} \sum_{\alpha=1}^{4} \left[\frac{(-1)^{\alpha+1} z}{r_{\alpha}[r_{\alpha} + (-1)^{\alpha+1} C_{\alpha}]} \right]$$

Figure A.3.1 shows the rectangle filament in red. In order to obtain the magnetic field from an entire multi-turn rectangular coil the equations must be integrated in such a way it covers the whole coil geometry.

As well as the two methods explored in section 5, the integration of the above equations were deemed too computationally expensive and so were numerically approximated by Simpson's rule, for ease of evaluation.

In order to explore the accuracy of the mathematical model a script was coded in MatLab. The details for the array geometry (see figure 6.10) can be seen in Table A-III while the results of the magnetic field calculated over a plane are presented in figures A.12-A.15.

TABLE A-III
OPTIMIZED DIMENSIONS GENERATOR

Symbol	Quantity(units)	description	Symbol	quantity	description
$2*a_{r1}$	100(mm)	Air core length. "*x*" axis	$2*a_{r2}$	100(mm)	Air core length. "*x*" axis
$2*b_{ri1}$	5(mm)	Air core length. "*y*" axis	$2*b_{ri2}$	5(mm)	Air core length. "*y*" axis
$2*b_{ro1}$	50 (mm)	Coil thickness. "*y*" axis	$2*b_{ro2}$	50(mm)	Coil thickness. "*y*" axis
$2*c_{r1}$	50(mm)	Coil height "*z*" axis	$2*c_{r2}$	50(mm)	Coil height "*z*" axis
n_1	922	Number turns in coil 1	n_2	922	Number of turns in coil 2

Symbol	Quantity(units)	description	Symbol	Quantity(units)	description	Symbol	quantity	description
I	9(A)	current	f_c	n/a(DC)	frequency	z_g	2(mm)	Gap from levitation track

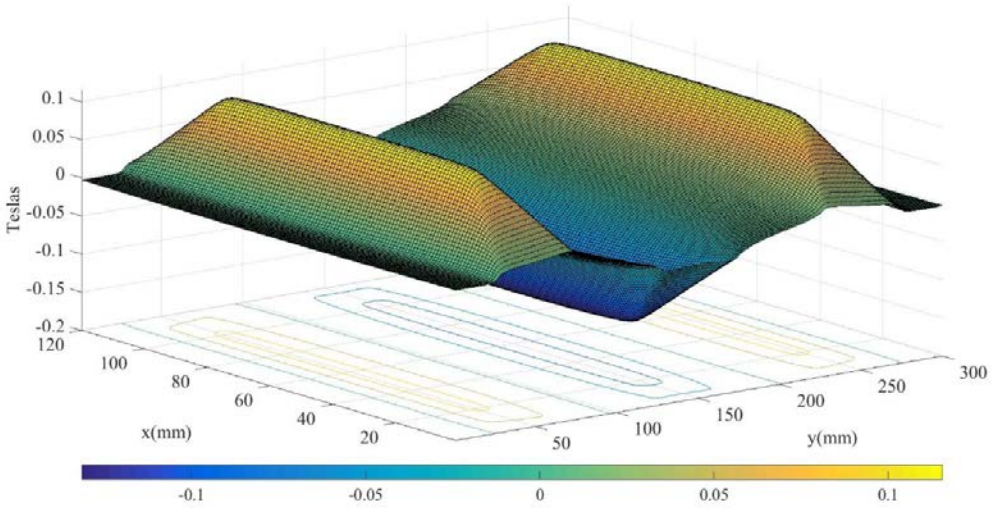

Fig. A.15 MatLab:3D representation of the magnetic field "B_z" on the study plane

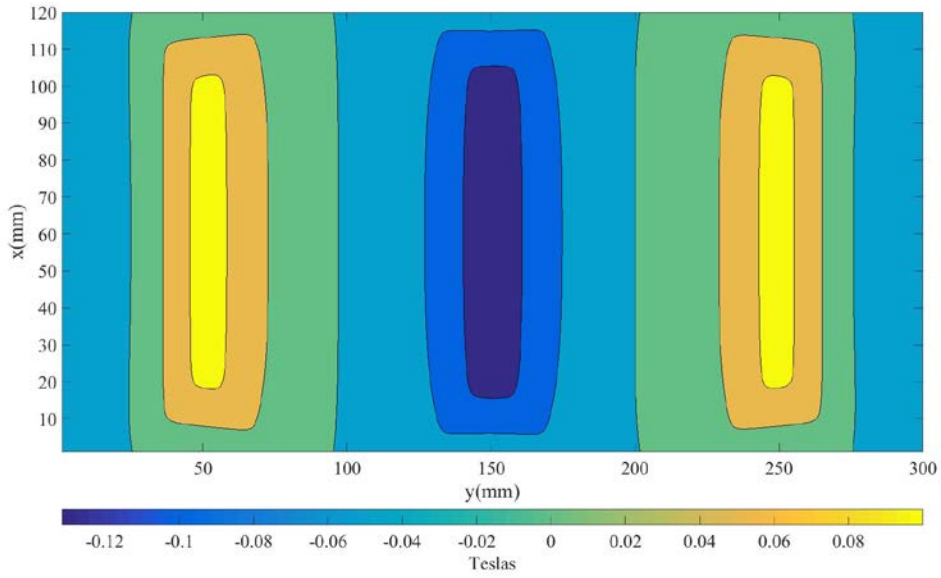

Fig. A.16 MatLab: Projection of the magnetic field "B_z" over the study plane

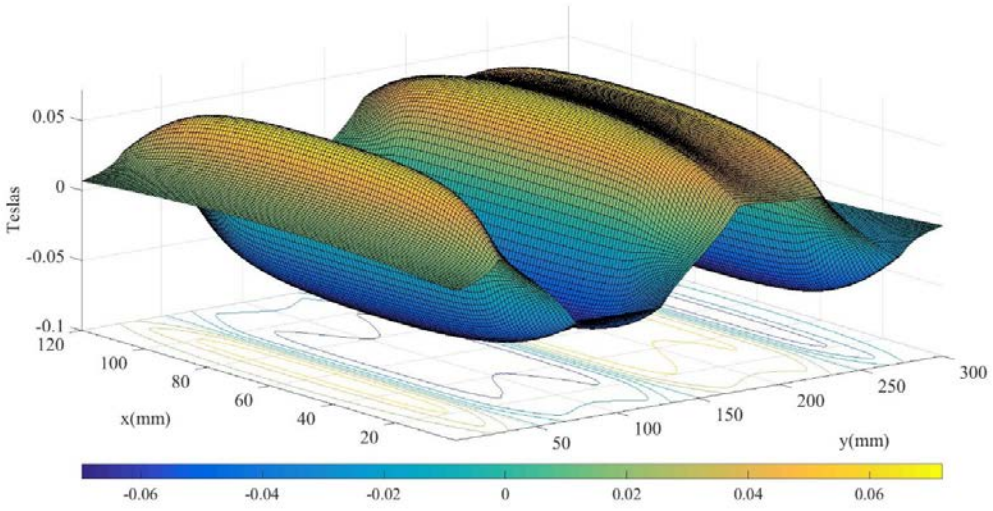

Fig. A.17 MatLab: 3D representation of the magnetic field "B_y" on the study plane

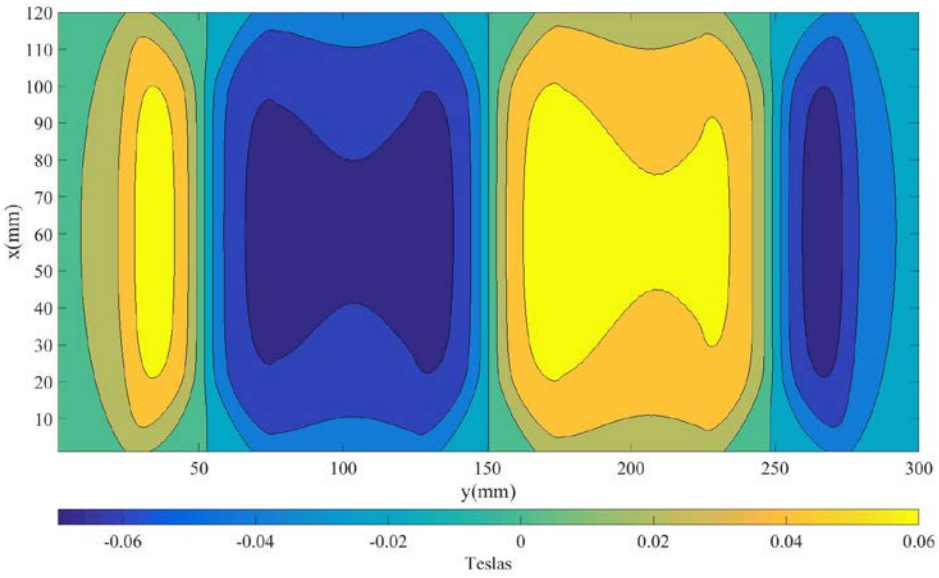

Fig. A.18 MatLab: Projection of the magnetic field "B_y" over the study plane

Subsequently to corroborate the accuracy of the model a simulation of the geometry was created and assessed in COMSOL. These results shown in figures A.16 to A.19. In order to cut down the computational resources used by the finite element software, this simulation was completed using half of the original geometry about arrays line of symmetry.

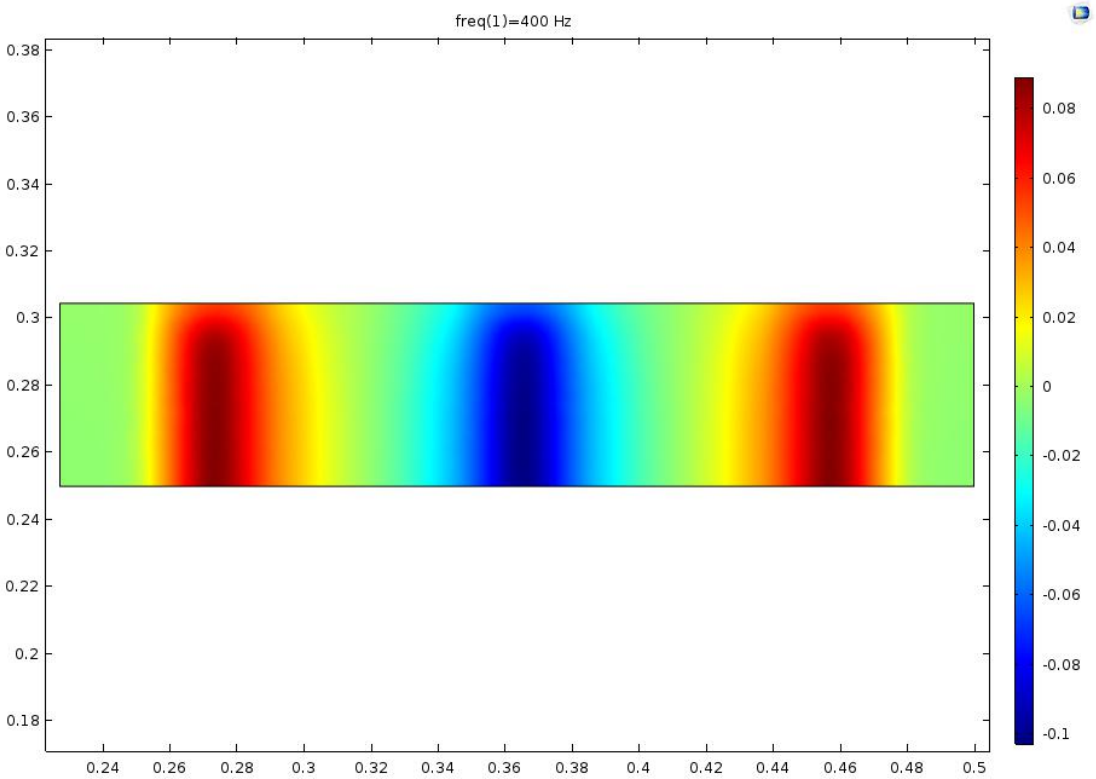

Fig. A.19 COMSOL: Projection of the magnetic field "B_x" over the study plane

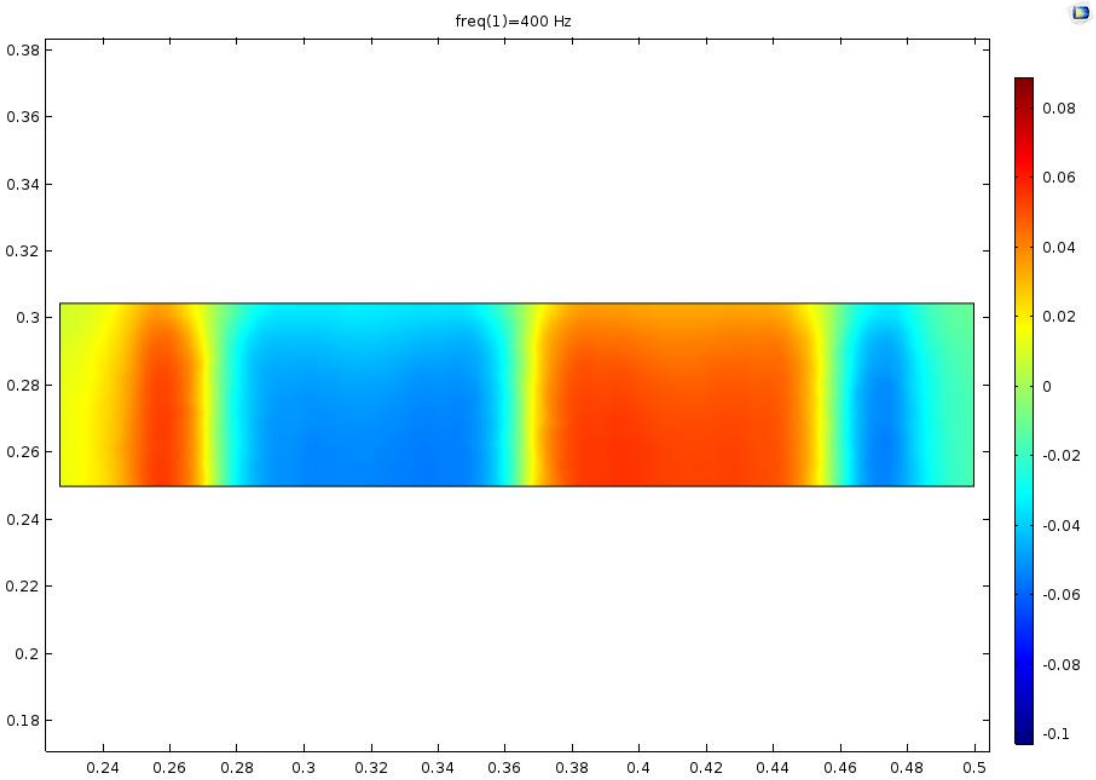

Fig. A.20 COMSOL: Projection of the magnetic field "B_y" over the study plane

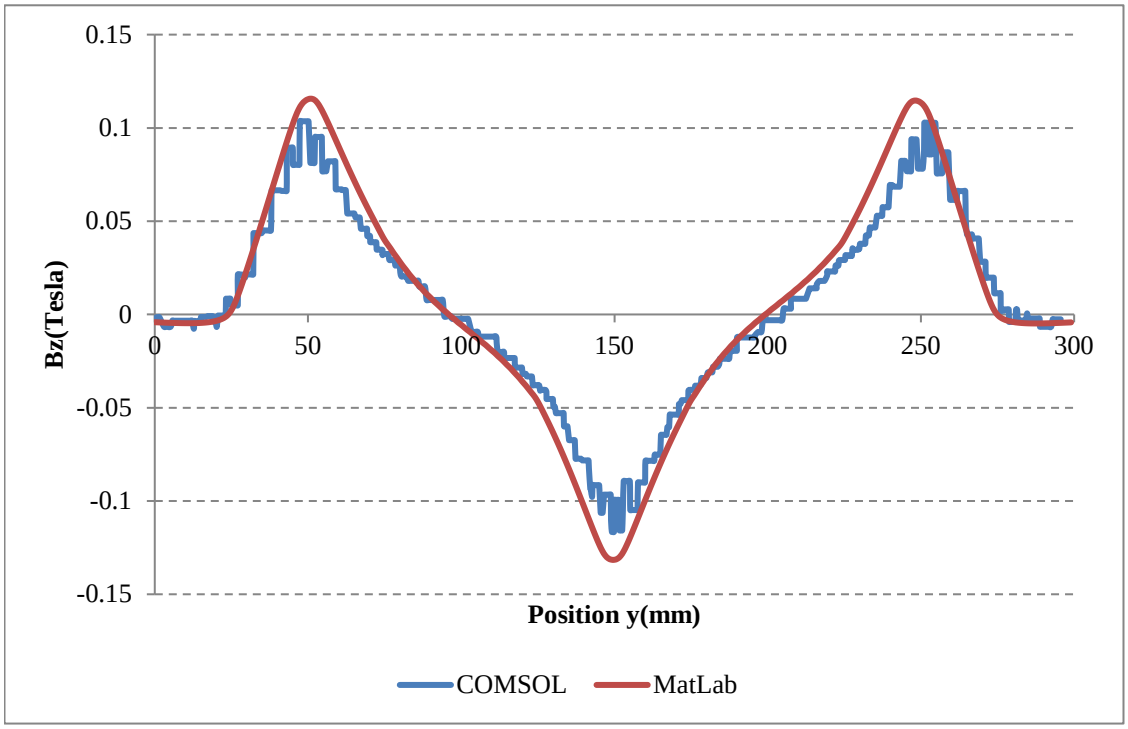

Fig. A.21 Centre of the array "B_z" comparison COMSOL vs MatLab code

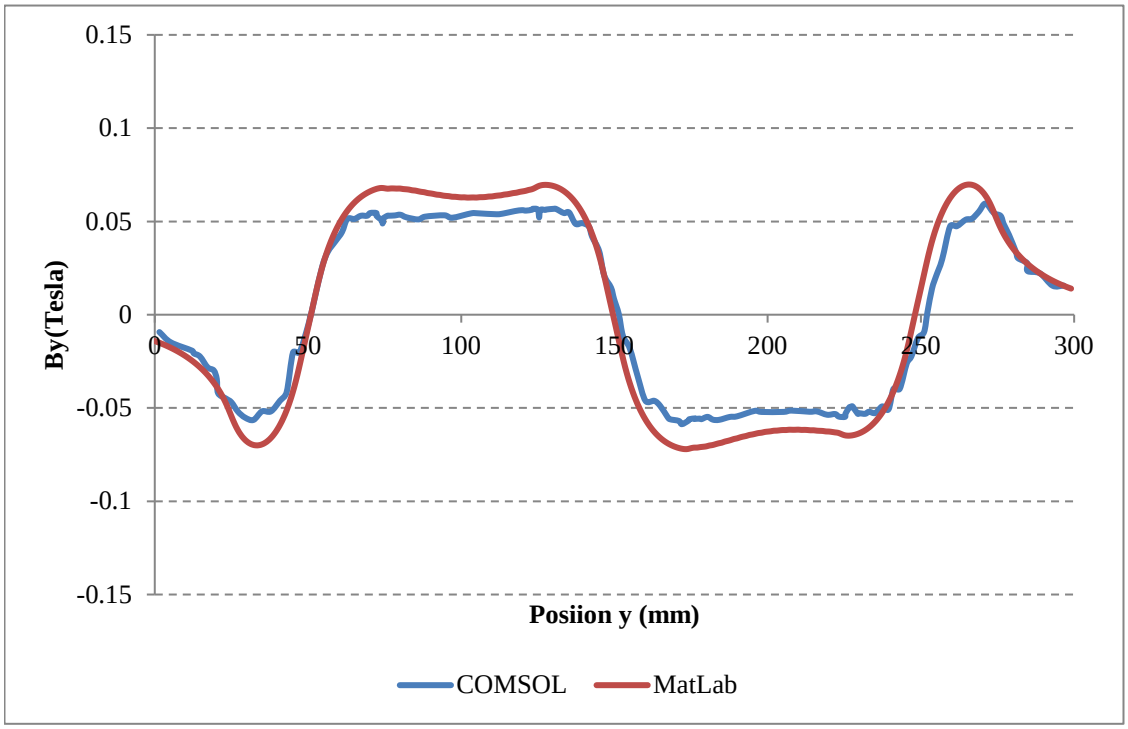

Fig. A.22 Centre of the array "B_y" comparison COMSOL vs MatLab code

The model presented outstanding similarities and it is hoped that this method will be used in the near future in order to improve the design of the device.